Simulations of R-parity Violating SUSY Models

Peter Richardson
Balliol College

Department of Physics · Theoretical Physics
University of Oxford

Thesis submitted in partial fulfillment of the requirements for
the Degree of Doctor of Philosophy at the
University of Oxford

· August 2000 ·

Abstract

In recent years there has been a great deal of interest in R-parity violating supersymmetric models. We explain the motivation for studying these models and explore the various phenomenological consequences of R-parity violation. In particular, we argue that if we are to explore all channels for the discovery of supersymmetry then these models must be investigated.

It has become essential for the experimental study of any new model to have a Monte Carlo event generator which includes the processes predicted by that model. We review the techniques used in the construction of these simulations and show how we have extended the HERWIG event generator to include R-parity violating processes. We discuss how to treat the emission of QCD radiation in these processes including colour coherence effects via the angular-ordered parton shower.

We then make use of this simulation to investigate the discovery potential for resonant slepton production, via either supersymmetric gauge or R-parity violating decay modes, in hadron–hadron collisions. In particular, we show that although the colour coherence properties of the R-parity violating decay modes can be used to improve the extraction of a signal above the QCD background these processes will only be visible for large values of the R-parity violating Yukawa couplings. However a signal, *i.e.* like-sign dilepton production, from the supersymmetric gauge decay modes is visible above the background for much smaller values of the R-parity violating Yukawa couplings.

Finally, we look at the possibility that the KARMEN time anomaly can be explained by the existence of a light neutralino which is produced in the decay of charged pions via R-parity violation. This neutralino then decays inside the KARMEN detector, into three leptons via R-parity violation, explaining the excess of events observed by the KARMEN experiment.

The road goes ever on and on,
down from the door where it began,
now far ahead the road has gone
and I must follow if I can ...

J.R.R. Tolkien

To my parents,

this wouldn't have been possible
without their support and encouragement.

Contents

Acknowledgments **xi**

1 Introduction **1**
1.1 Standard Model . . . 1
1.1.1 Quantum Chromodynamics . . . 5
1.1.2 Electroweak Theory . . . 6
1.1.3 Symmetries of the Standard Model . . . 9
1.2 Supersymmetry . . . 10
1.2.1 Introduction to Supersymmetry . . . 11
1.2.2 Motivations for Supersymmetry . . . 12
1.2.3 Construction of Supersymmetric Lagrangians . . . 15
1.2.4 The Minimal Supersymmetric Standard Model . . . 18
1.3 R-parity Violating Supersymmetry . . . 21
1.3.1 Sparticle Pair Production . . . 23
1.3.2 Single Sparticle Production . . . 24
1.4 Summary . . . 25

2 Monte Carlo Simulations **27**
2.1 Introduction . . . 27
2.2 Hard Processes . . . 29
2.3 Parton Showers . . . 33
2.3.1 Collinear Parton Showers . . . 34
2.3.2 Angular-ordered Parton Showers . . . 40
2.3.3 Monte Carlo Procedure . . . 50
2.3.4 Summary . . . 52
2.4 Hadronization . . . 53
2.5 Monte Carlo Event Generators . . . 54
2.6 Angular Ordering in $\not{R}_p$ . . . 55
2.6.1 Decays . . . 55
2.6.2 Hard Processes . . . 64
2.7 Hadronization of $\not{R}_p$ Processes . . . 66
2.8 Results . . . 71
2.9 Summary . . . 75

3 Resonant Slepton Production in Hadron–Hadron Collisions 77
3.1 Introduction . . . 77
3.2 $\not{R}_p$ Decays of the Resonant Slepton . . . 78
3.3 Gauge Decays of the Resonant Slepton . . . 82
3.3.1 Signal . . . 83
3.3.2 Backgrounds . . . 86
3.3.3 Simulations . . . 92
3.3.4 Mass Reconstruction . . . 116
3.4 Summary . . . 121

4 KARMEN Anomaly 123
4.1 Introduction . . . 123
4.2 The Model . . . 127
4.2.1 Pion Decay Rate . . . 129
4.2.2 Neutralino Lifetime . . . 132
4.2.3 Solutions of the KARMEN Anomaly . . . 133
4.3 Limits on the R-parity Violating Couplings . . . 133
4.4 Experimental Constraints on a Light Neutralino . . . 136
4.4.1 Bounds from $e^+e^- \to \nu\bar{\nu}\gamma$ . . . 136
4.4.2 Bounds from the Invisible Z Width . . . 137
4.4.3 Solutions in the MSSM Parameter Space . . . 138
4.4.4 Limits from Precision Electroweak Measurements . . . 139
4.5 Future Tests . . . 143
4.6 Summary . . . 145

5 Conclusions 147

Addendum 148

A Feynman Rules and Conventions 151
A.1 Introduction . . . 151
A.2 Mixing . . . 151
A.2.1 Charginos . . . 152
A.2.2 Neutralinos . . . 155
A.2.3 Left/Right Sfermion Mixing . . . 157
A.3 Gaugino Interactions with the Sfermions . . . 158
A.4 Gluino Interactions with the Squarks . . . 163
A.5 Gauge Boson Interactions with the Sfermions and Fermions . . . 163
A.6 Higgs Boson Interactions with the Sfermions and Fermions . . . 168
A.7 R-parity Violating Feynman Rules . . . 174

B Decay Rate Calculations 179
B.1 Introduction . . . 179
B.2 Sfermions . . . 180
B.3 Charginos . . . 181
B.4 Neutralinos . . . 185

B.5 Gluinos 187

C Cross-section Calculations **191**
C.1 Introduction 191
C.2 LQD Processes 191
C.2.1 Resonant Slepton Production followed by Weak Decay 191
C.2.2 Resonant Slepton Production followed by $\not{R}_p$ Decay 193
C.2.3 Resonant Slepton Production followed by Higgs Decay 193
C.3 UDD Processes 194
C.3.1 Resonant Squark Production followed by Weak Decay 194
C.3.2 Resonant Squark Production followed by $\not{R}_p$ Decay 196
C.3.3 Resonant Squark Production followed by Higgs Decay 196

Bibliography **199**

List of Figures

1.1 One-loop contributions to the Higgs mass. 13
1.2 Contribution to the Higgs mass from an extra scalar field. 14
1.3 $\not{R}_p$ proton decay. 19
1.4 Different possible resonant sparticle production mechanisms. 24

2.1 Example of a Monte Carlo event. 29
2.2 Feynman diagrams for $e^+e^- \to$ hadrons at next-to-leading order. 34
2.3 Radiation of a collinear gluon. 35
2.4 Feynman diagram and colour flow for $e^+e^- \to q\bar{q}g$. 43
2.5 Emission in angular-ordered cones. 45
2.6 Radiation pattern from the process $e^+e^- \to q\bar{q}g$. 46
2.7 Radiation pattern for the decay $\tilde{q}^* \to qq$. 57
2.8 UDD decays of the $\tilde{\chi}^+$. 58
2.9 UDD decays of the $\tilde{\chi}^0$. 59
2.10 Radiation pattern for the decay $\tilde{\chi}^{0/+} \to qqq$. 60
2.11 UDD decays of the $\tilde{g}$. 61
2.12 Baryon number violating decay of the $\tilde{g}$. 62
2.13 Radiation pattern for $\tilde{g} \to qqq$. 63
2.14 Resonant squark production followed by $\not{B}$ decay. 64
2.15 Radiation pattern for resonant squark production. 65
2.16 Hadronization of a $\not{B}$ neutralino decay. 67
2.17 Hadronization with one $\not{B}$ decay. 68
2.18 Hadronization with two $\not{B}$ decays. 68
2.19 Distributions of the colour-singlet cluster masses. 69
2.20 Masses of the joining and remnant clusters. 70
2.21 Feynman diagrams for $\bar{u}d \to \bar{u}d$ and $\bar{d}d \to \bar{d}d$ via slepton exchange. 72
2.22 Distribution of η_3 for resonant slepton, squark and QCD jet production. . . 74
2.23 Distribution of R for resonant slepton, squark and QCD jet production. . . 74
2.24 Distribution of α for resonant slepton, squark and QCD jet production. . . 74

3.1 Di-jet invariant-mass distribution for $\lambda'_{311} = 0.7$ and $\lambda'_{311} = 0.8$. 79
3.2 Distribution of η_3 for resonant slepton production and the QCD background. 80
3.3 Distribution of R for resonant slepton production and the QCD background. 80
3.4 Distribution of α for resonant slepton production and the QCD background. 80
3.5 Effect of the cuts on the angular-ordering variables as a function of λ'_{311}. . 81
3.6 Invariant-mass distributions after cuts on the angular-ordering variables. . 82

3.7 Production of $\tilde{\chi}^0\ell^+$. 83
3.8 Feynman diagrams for the decay $\tilde{\chi}^0 \to \ell^+ \mathrm{d}\bar{\mathrm{u}}$. 84
3.9 The $\tilde{\chi}_1^0$ and $\tilde{\mu}_L$ masses in the M_0, $M_{1/2}$ plane. 85
3.10 Limits on the coupling λ'_{211} in the M_0, $M_{1/2}$ plane. 87
3.11 Lightest neutralino decay length in the M_0, $M_{1/2}$ plane. 88
3.12 Production cross section for $\tilde{\chi}^0\ell$ at the Tevatron in M_0, $M_{1/2}$ plane. 95
3.13 Cross section for the production of a resonant slepton followed by a supersymmetric gauge decay at the Tevatron in the M_0, $M_{1/2}$ plane. 96
3.14 Effect of the isolation cuts on the $\mathrm{t\bar{t}}$ and $\mathrm{b\bar{b}}$ backgrounds at the Tevatron. . 97
3.15 M_T and $\not\!\!E_T$ in WZ events at the Tevatron. 98
3.16 Effect of the isolation cuts on the WZ and ZZ backgrounds at the Tevatron. 98
3.17 Discovery potential at the Tevatron for the Standard Model backgrounds in the M_0, $M_{1/2}$ plane with different integrated luminosities. 100
3.18 Discovery potential at the Tevatron for the Standard Model backgrounds in the M_0, $M_{1/2}$ plane with different values of λ'_{211}. 101
3.19 Discovery potential for the Tevatron in the M_0, $M_{1/2}$ plane, including all the backgrounds, with different integrated luminosities. 103
3.20 Discovery potential for the Tevatron in the M_0, $M_{1/2}$ plane, including all the backgrounds, for different values of λ'_{211}. 104
3.21 Cross section for the production of $\tilde{\chi}^0\ell$ at the LHC in the M_0, $M_{1/2}$ plane. 106
3.22 Cross section for resonant slepton production followed by a supersymmetric gauge decay at the LHC in the M_0, $M_{1/2}$ plane. 107
3.23 Effect of the isolation cuts on the $\mathrm{t\bar{t}}$ and $\mathrm{b\bar{b}}$ backgrounds at the LHC. . . . 108
3.24 M_T and $\not\!\!E_T$ in WZ events at the LHC. 109
3.25 Effect of the isolation cuts on the WZ and ZZ backgrounds at the LHC. . . 109
3.26 Discovery potential at the LHC for the Standard Model backgrounds in the M_0, $M_{1/2}$ plane with different integrated luminosities. 111
3.27 Discovery potential at the LHC for the Standard Model backgrounds in the M_0, $M_{1/2}$ plane with different values of λ'_{211}. 112
3.28 Discovery potential at the LHC in the M_0, $M_{1/2}$ plane, including all the backgrounds, for different integrated luminosities. 114
3.29 Discovery potential at the LHC in the M_0, $M_{1/2}$ plane, including all the backgrounds, for different values of λ'_{211}. 115
3.30 Reconstructed $\tilde{\chi}_1^0$ mass at the Tevatron for $M_0 = 50$ GeV, $M_{1/2} = 250$ GeV, $\tan\beta = 2$, $\mathrm{sgn}\,\mu > 0$ and $A_0 = 0$ GeV. 117
3.31 Reconstructed $\tilde{\chi}_1^0$ mass at the LHC for $M_0 = 350$ GeV, $M_{1/2} = 950$ GeV, $\tan\beta = 10$, $\mathrm{sgn}\,\mu < 0$ and $A_0 = 0$ GeV. 117
3.32 Reconstructed $\tilde{\mu}_L$ mass at the Tevatron for $M_0 = 50$ GeV, $M_{1/2} = 250$ GeV, $\tan\beta = 2$, $\mathrm{sgn}\,\mu > 0$ and $A_0 = 0$ GeV. 118
3.33 Reconstructed $\tilde{\mu}_L$ mass at the LHC for $M_0 = 350$ GeV, $M_{1/2} = 950$ GeV, $\tan\beta = 10$, $\mathrm{sgn}\,\mu < 0$ and $A_0 = 0$ GeV. 118
3.34 Reconstructed $\tilde{\chi}_1^0$ mass at the LHC for $\lambda'_{211} = 10^{-2}$, $M_0 = 350$ GeV, $M_{1/2} = 350$ GeV, $\tan\beta = 10$, $\mathrm{sgn}\,\mu < 0$ and $A_0 = 0$ GeV. 120
3.35 Reconstructed $\tilde{\mu}_L$ mass at the LHC for $\lambda'_{211} = 10^{-2}$, $M_0 = 350$ GeV, $M_{1/2} = 350$ GeV, $\tan\beta = 10$, $\mathrm{sgn}\,\mu < 0$ and $A_0 = 0$ GeV. 120

4.1 Energy spectrum and time structure of neutrino production in KARMEN. 124
4.2 Time distribution of the events observed by the KARMEN experiment. . . 125
4.3 Radiative $\not{R}_p$ decay of a neutralino. 126
4.4 Pion decay to muon and neutralino. 128
4.5 Branching ratio vs. lifetime required to solve the KARMEN anomaly. . . . 129
4.6 Solutions of the KARMEN anomaly in terms of the $\not{R}_p$ couplings. 134
4.7 Cross section for neutralino production via $e^+e^- \to \tilde{\chi}^0_1\tilde{\chi}^0_1\gamma$. 138
4.8 Solutions in $(M_1, M_2, \mu, \tan\beta)$ parameter space. 139
4.9 Gaugino loops in the gauge boson propagators. 141
4.10 Cross sections for $e^+e^- \to \tilde{\chi}^0_2\tilde{\chi}^0_1$. 144
4.11 $\frac{d\Gamma}{d\theta_{ee}}$ in the KARMEN laboratory frame. 145

A.1 Feynman rules for $q\tilde{q}\tilde{\chi}^+$. 159
A.2 Feynman rules for $\ell\tilde{\ell}\tilde{\chi}^+$. 159
A.3 Feynman rules for $q\tilde{q}\tilde{\chi}^0$. 162
A.4 Feynman rules for $\ell\tilde{\ell}\tilde{\chi}^0$. 162
A.5 Feynman rules for $q\tilde{q}\tilde{g}$. 162
A.6 Feynman rules for the interactions of the squarks and the gauge bosons. . . 165
A.7 Feynman rules for the interactions of the sleptons and the gauge bosons. . 166
A.8 Feynman rules for the interactions of the quarks and the gauge bosons. . . 167
A.9 Feynman rules for the interactions of the Higgs bosons and the squarks. . . 170
A.10 Feynman rules for the interactions of the Higgs bosons and the sleptons. . 172
A.11 Feynman rules for the interactions of the Higgs bosons and the quarks. . . 173
A.12 Feynman rules for LLE. 175
A.13 Feynman rules for LQD. 176
A.14 Feynman rules for UDD. 177

B.1 LLE decays of the $\tilde{\chi}^+$. 181
B.2 LQD decays of the $\tilde{\chi}^+$. 182
B.3 LLE decays of the $\tilde{\chi}^0$. 185
B.4 LQD decays of the $\tilde{\chi}^0$. 187
B.5 LQD decays of the $\tilde{g}$. 188

List of Tables

1.1 Gauge quantum numbers of the Standard Model fermions. 8
1.2 Superfields in the MSSM. 18

2.1 Eikonal current factors. 41

3.1 Decay modes of charged sleptons and sneutrinos. 77
3.2 Backgrounds to like-sign dilepton production at the Tevatron. 99
3.3 Backgrounds to like-sign dilepton production at the LHC. 110
3.4 Reconstructed neutralino and slepton masses. 119

4.1 Coefficients for the fermion-sfermion-neutralino Lagrangian. 130
4.2 Coefficients for the neutralino decay. 132
4.3 Cross sections for the production of $\tilde{\chi}_1^0\tilde{\chi}_1^0\gamma$ at e^+e^- colliders. 137

A.1 Couplings for the chargino Feynman rules. 160
A.2 Couplings for the neutralino Feynman rules. 161
A.3 Couplings for the gluino Feynman rules. 163
A.4 Couplings of squarks, sleptons, quarks and leptons to the Z^0. 164
A.5 Higgs couplings to the squarks. 171
A.6 Higgs couplings to the sleptons. 171
A.7 Higgs couplings to the quarks. 174

B.1 Coefficients for the sfermion $\not{R}_p$ decays. 180

Acknowledgments

Although, in principle, this is all my own work many people have helped along the way. During my time in Cambridge, particularly during my final-year project, I was very lucky to have been taught by Bryan Webber to whom I owe a great debt for awakening my interest in particle physics. Here in Oxford I have increasingly come to realize how fortunate I was in my choice of supervisors. It has been a pleasure to work with both Herbi Dreiner and Mike Seymour. I have benefited from their understanding of their respective fields and while I have learnt a great deal from both of them I hope that they have learnt something as well.

A number of people read this thesis at various stages of the writing process and I am indebted to them for correcting my occasionally poor grammar and making me explain what I meant in what I hope is a clear way. So thank you very much Herbi, Jenny and Mike.

During my time in Oxford I have been able to travel widely due to the support of various funding bodies, in particular PPARC. During my second year I was able to attend, thanks to PPARC, the Tevatron Run II Workshop at Fermilab were I presented some of the results in Chapter 3. I was also able to spend an interesting fortnight at CERN, again thanks to PPARC.

I would like to thank Torbjörn Sjöstrand and Paula Eerola for an invitation to speak at the Nordic LHC physics workshop, and for paying for my trip. At a time when my work was going slowly it was a wonderful experience to meet experimentalists who were running my simulation code and producing interesting results which encouraged me to actually get something finished when I returned, thanks a lot to Christophe Clement and Linda Megner.

In the final year of my D. Phil. I was also able to attend the SUSY Tools workshop in Colmar, thanks to the generosity of PPARC, where again I was lucky to meet a number of experimentalists who had been using my results.

In the middle of writing this thesis I went to the CTEQ summer school at Lake Geneva, in Wisconsin, where I spent an enjoyable ten days. I was also able to visit Fermilab and Argonne after this. So thanks to the Fermilab theory group for their hospitality and to both Fermilab and PPARC for paying for my trip.

Shortly after this trip to Fermilab I attended the SUSY2000 conference, at CERN, where I gave a talk on the results in Chapters 2 and 3. This trip was funded by the physics department and Balliol college.

A large amount of my time has been spent working on the HERWIG Monte Carlo event generator. It has been a pleasure to work with the many authors of HERWIG and they have provided a lot of support and encouragement.

The Cambridge experimental group, in particular Andy Parker, Lee Drage, Debbie Morgan, and Alan Barr, have produced a lot of interesting results on the search for baryon number violating SUSY and I am grateful for their interest in my work and the occasional bugs they found. I look forward to spending the next two years working with them in Cambridge.

The theory group at RAL have also been very helpfully during my time in Oxford and during my occasional visits to the lab.

I have spent an enjoyable three years in Oxford for which I must thank various members of both the physics department and Balliol College. Here in the in the physics department Jenny, Peter, Alex, Ed, Marc, Paul, Ankush, Joern, Todd, Armin, and in college Kyle, Chris, Michaels (all of them), Zoe, Mark, Craig and Joao.

Finally none of this would have been possible without the support of my family. They put up with me when I was very stressed and various deadlines were getting ever closer. So thanks a lot Mam, Dad and Angus.

Publications

Some of the work contained in this thesis has been previously published. The work in Chapter 2 was published in [1], as were the results in Section 3.2. The implementation of the work in Chapter 2 into the HERWIG event generator is described in the release note for the latest version, and the new manual, [2].

The work in Section 3.3 is available in [3] and has been accepted for publication in Phys. Rev. D. This work was also reported in various conference proceedings. Preliminary results of the Tevatron studies were presented at the Tevatron Run II workshop on supersymmetry and Higgs physics and are described in [4] and in the Beyond the MSSM working group report [5]. The results of the LHC studies are available in the summary of the SUSY working group of the 1999 Les Houches workshop [6] and in [7].

The work on the KARMEN anomaly presented in Chapter 4 was published as [8].

Chapter 1

Introduction

For more than twenty years the Standard Model (SM) [9] of particle physics has provided predictions of the results of high energy particle physics experiments. Despite the excellent agreement between the predictions of this theory and the experimental results it is widely believed that the Standard Model cannot be a complete theory of everything. This thesis will be concerned with one possible extension of the Standard Model, R-parity violating ($\not{R}_p$) supersymmetry (SUSY).

In this chapter we will briefly describe the Standard Model, emphasizing the rôle that symmetries play in its construction. This will lead to a discussion of a possible new symmetry of nature, supersymmetry, and the problems in the Standard Model that it solves. In the most naïve supersymmetric extension of the Standard Model lepton and baryon number are violated. This leads to fast proton decay, in conflict with the experimental lower limit on the proton lifetime. This has led to the imposition of a new symmetry called R-parity (R_p), to prevent the decay of the proton. However, we will present other symmetries that can prevent proton decay without the imposition of R-parity. These symmetries lead to the violation of either lepton *or* baryon number but not both simultaneously. These models have been much less studied than those which conserve R-parity. We will therefore briefly discuss the experimental consequences of R-parity violation.

The next chapter discusses the idea of Monte Carlo simulations and presents the necessary calculations to include R-parity violating processes in these simulations. The simulation program produced using these results is then used in Chapter 3 to study resonant slepton production in hadron–hadron collisions. Chapter 4 explores the possibility that the anomaly seen by the KARMEN experiment[1] can be explained by R-parity violation. The conclusions are presented in Chapter 5.

1.1 Standard Model

In the present view of particle physics the symmetries of the theory play a central rôle. In fact, the conventional approach for obtaining the Standard Model Lagrangian is to specify

[1]The KARMEN collaboration has recently announced new results which are discussed in the Addendum.

the particle content of the theory and the symmetries it obeys. We can then write the most general Lagrangian for the particles given the symmetries and the requirement that the theory be renormalizable, *i.e.* that the ultraviolet divergences involved in calculations beyond tree level can be absorbed into the bare parameters of the theory.

In general, we will be considering two types of symmetries. The first is the requirement that the theory be Lorentz invariant, *i.e.* obey the laws of special relativity. All the Lagrangians we will consider will be Lorentz invariant.[2] The other symmetries of the Standard Model are gauge symmetries which lead to gauge field theories. In these theories the forces between the fundamental particles are mediated by the exchange of spin-1 gauge bosons. In the Standard Model the electromagnetic force between charged particles is carried by the photon, the weak force by the W and Z bosons, and the strong force between coloured particles by the gluon.

All of these theories are based on the simplest example, *i.e.* Quantum Electrodynamics (QED). The Dirac Lagrangian for n fermions is given by

$$\mathcal{L}_{\text{Dirac}} = \sum_{i=1}^{n} \bar{\psi}_i (i\partial_\mu \gamma^\mu - m_i)\psi_i, \tag{1.1}$$

where ψ_i are the fermionic fields, γ^μ are the Dirac matrices and m_i is the mass of the fermion i. This Lagrangian is invariant under a global phase change

$$\psi_i \to e^{iq_i\alpha}\psi_i, \tag{1.2}$$

where α is the phase change and q_i is an arbitrary flavour-dependent parameter. If instead we consider a local change of phase, $\alpha \to \alpha(x)$, then the Dirac Lagrangian is no longer invariant under this transformation. The Lagrangian can be made invariant under a local change of phase by introducing a new vector field, A^μ, which has the kinetic term

$$\mathcal{L}_{\text{kinetic}} = -\frac{1}{4} F^{\mu\nu} F_{\mu\nu}, \tag{1.3}$$

where $F_{\mu\nu} = \partial_\mu A_\nu - \partial_\nu A_\mu$. We can introduce an interaction of the vector field with the fermion via the substitution

$$\partial_\mu \to D_\mu = \partial_\mu + iQA_\mu, \tag{1.4}$$

where D_μ is the covariant derivative and Q is the charge operator defined by $Q\psi_i = q_i\psi_i$. The arbitrary constants q_i which we introduced for the case of the global transformation are the couplings of the fermions to the gauge field. If the vector field transforms as

$$A_\mu \to A_\mu - \partial_\mu \alpha, \tag{1.5}$$

[2] In general by invariant we mean that the Lagrangian is invariant up to the addition of a total derivative under the symmetry transformation. As we are really interested in the action, $S = \int d^4x\, \mathcal{L}$, the total derivative will lead to a surface term which will vanish provided the fields go to zero as $x \to \infty$.

under a local change of phase then the Lagrangian,

$$\mathcal{L} = \sum_{i=1}^{n} \bar{\psi}_i (i\partial_\mu \gamma^\mu - m_i)\psi_i + \mathcal{L}_{\text{kinetic}}, \tag{1.6}$$

is invariant under a local change of phase. This gives the interactions of the fermions, *e.g.* the electron, with the electromagnetic field. This is the simplest example of a gauge transformation, namely a $U(1)$ transformation. Here the couplings q_i are the electric charges of the fermions. The gauge theories which form the Standard Model are generalizations of this principle to non-Abelian gauge groups. The non-Abelian gauge transformation is

$$\psi_a(x) \to \psi'_a(x) = \left[e^{i\theta_A(x)\mathbf{t}^A}\right]_{ab} \psi_b(x) \equiv \Omega_{ab}(x)\psi_b(x), \tag{1.7}$$

where $\theta^A(x)$ are the parameters of the transformation and $\mathbf{t}^A$ are the generators of the non-Abelian group in the same representation as the fermions. The generalized covariant derivative has the form

$$D^\mu_{ab} = \delta_{ab}\partial^\mu + ig\mathbf{t}^A_{ab}A^\mu_A, \tag{1.8}$$

where A^μ_A are the gauge bosons in the adjoint representation of the gauge group and g is the coupling of the fermion to the gauge field. The non-Abelian gauge transformation for the gauge field is given by

$$\mathbf{t}^A A^A_\mu \to \mathbf{t}^A A'^A_\mu = \Omega(x)\mathbf{t}^A A^A_\mu \Omega^{-1}(x) + \frac{i}{g}\left(\partial_\mu \Omega(x)\right)\Omega^{-1}(x). \tag{1.9}$$

The Lagrangian for the non-Abelian gauge theory can then be constructed

$$\mathcal{L} = \mathcal{L}_{\text{gauge}} + \mathcal{L}_{\text{fermion}}, \tag{1.10}$$

where

$$\mathcal{L}_{\text{gauge}} = -\frac{1}{4}F^A_{\mu\nu}F^{\mu\nu}_A, \tag{1.11a}$$

$$\mathcal{L}_{\text{fermion}} = \bar{\psi}_a \left(iD_\mu \gamma^\mu - m\right)_{ab} \psi_b. \tag{1.11b}$$

The generalization to a non-Abelian symmetry of the $U(1)$ field strength tensor is given by

$$F^A_{\mu\nu} = \partial_\mu A^A_\nu - \partial_\nu A^A_\mu - g f^{ABC} A^B_\mu A^C_\nu. \tag{1.12}$$

The additional terms due to the non-Abelian structure of the field strength tensor lead to self-interactions of the gauge bosons. These non-Abelian gauge theories form the basis of the Standard Model. There is a problem because a mass term for the gauge boson, *i.e.*

$$\mathcal{L}^{\text{boson}}_{\text{mass}} = \frac{1}{2}m^2 A^\mu_A A^A_\mu, \tag{1.13}$$

is not gauge invariant and therefore cannot be included in the Lagrangian. However in the Standard Model the bosons which mediate the weak force, *i.e.* the W and Z bosons, are massive. There is a way of including a mass for the gauge bosons in a gauge-invariant manner. This is called the Higgs mechanism [10]. It is easiest to illustrate this mechanism by considering the simplest example, *i.e.* a $U(1)$ gauge field coupled to a scalar field with the following Lagrangian

$$\mathcal{L} = \mathcal{L}_{\text{derivative}} - V(\phi) = (D^\mu\phi)^*(D_\mu\phi) - V(\phi), \tag{1.14}$$

where ϕ is a complex scalar field and D^μ is given by Eqn. 1.4. Here the charge operator acts on the scalar field, *i.e.* $Q\phi = q\phi$, where q is the coupling of the gauge field to the scalar field. The most general renormalizable, gauge-invariant potential has the form

$$V(\phi) = \mu^2\phi^*\phi + \lambda(\phi^*\phi)^2. \tag{1.15}$$

The shape of the potential depends on the sign of μ^2:

1. if $\mu^2 > 0$ then the minimum of the potential is at $|\phi| = 0$;
2. if $\mu^2 < 0$ then the minimum of the potential is at $|\phi|^2 = -\frac{\mu^2}{2\lambda} \equiv \frac{v^2}{2}$.

For the case $\mu^2 < 0$ we must consider fluctuations of the field about its ground state, which rather than being $\phi = 0$ is a point on the circle $|\phi| = v/\sqrt{2}$. This breaks the symmetry because while any point on the circle $|\phi| = v/\sqrt{2}$ is equally likely only one of these points gets chosen. We can consider fluctuations by rewriting the field as

$$\phi = \frac{1}{\sqrt{2}}\,(v+\rho)\,e^{i(\xi/v+\theta)}, \tag{1.16}$$

where ρ and ξ are real scalar fields and $ve^{i\theta}/\sqrt{2}$ is the point on the circle $|\phi| = v/\sqrt{2}$ about which we are expanding the field. The covariant derivative part of the Lagrangian can be expanded in terms of these fields,

$$\mathcal{L}_{\text{derivative}} = \frac{1}{2}\left[i\,(v+\rho)\left\{qA_\mu + \frac{1}{v}\partial_\mu\xi\right\} + \partial_\mu\rho\right] \times \left[-i\,(v+\rho)\left\{qA^\mu + \frac{1}{v}\partial^\mu\xi\right\} + \partial^\mu\rho\right]. \tag{1.17}$$

We can then perform a gauge transformation on this Lagrangian,

$$A^\mu \to A^\mu - \frac{1}{qv}\partial^\mu\xi, \tag{1.18}$$

to eliminate all dependence on the field ξ. This choice of gauge is called the unitary gauge. In the unitary gauge the Lagrangian is

$$\begin{aligned}\mathcal{L} \;=\; & -\frac{1}{4}F_{\mu\nu}F^{\mu\nu} + \frac{1}{2}v^2q^2A^\mu A_\mu + \frac{1}{2}\partial_\mu\rho\partial^\mu\rho \\ & + \frac{1}{2}(2v\rho+\rho^2)q^2A^\mu A_\mu - \frac{1}{4}\mu^2v^2 + \mu^2\rho^2 - \lambda v\rho^3 - \frac{\lambda}{4}\rho^4.\end{aligned} \tag{1.19}$$

This Lagrangian represents a massive gauge boson with mass $M_A^2 = q^2v^2$, a massive real scalar field with mass $m_\rho^2 = -2\mu^2$, the self-interactions of the scalar field and its interactions with the gauge boson. This mechanism allows us to introduce a gauge boson mass term in a manifestly gauge-invariant way. In this process the initial complex scalar field ϕ possesses two degrees of freedom, whereas the real scalar field ρ has only one degree of freedom. The second degree of freedom has been 'eaten' to provide the longitudinal polarization of the massive gauge boson, which has three degrees of freedom rather than the two degrees of freedom of a massless gauge boson.

This theory describes a massive $U(1)$ gauge boson, *i.e.* a massive photon. Although in the Standard Model the photon is massless the gauge bosons which mediate the weak force, the W and Z, are massive and their masses are generated by a generalization of this mechanism to non-Abelian symmetries.

We can now discuss the two theories which form the Standard Model in slightly more detail, *i.e.* Quantum Chromodynamics which describes the strong force and the Glashow-Weinberg-Salam model [9] which describes the electroweak force.

1.1.1 Quantum Chromodynamics

Quantum Chromodynamics (QCD) describes the colour force between the quarks which is carried by the exchange of gluons. The Lagrangian is

$$\mathcal{L}_{\mathrm{QCD}} = -\frac{1}{4}F^A_{\mu\nu}F_A^{\mu\nu} + \sum_i \bar{q}^i_a \left(iD_\mu\gamma^\mu - m_i\right)_{ab} q^i_b, \tag{1.20}$$

where $F^A_{\mu\nu}$ is the non-Abelian field strength tensor given by Eqn. 1.12, q^i are the quark fields with mass m_i and the covariant derivative D^μ_{ab} is given by Eqn. 1.8. This is an $SU(3)$ gauge theory based on the general non-Abelian theory we have already considered. The fermions are in the fundamental representation of $SU(3)$ and the gauge bosons, *i.e.* the gluons, in the adjoint representation. There are some subtleties involved in quantizing non-Abelian gauge theories which are discussed in, for example, [11,12]. The major difference between this non-Abelian theory and, for example, QED is the presence of self-interactions of the gauge bosons due to the different structure of the field strength tensor, Eqn. 1.12.

This theory possesses two important features which occur due to the running of the coupling, *i.e.* the fact that after we renormalize the theory the coupling depends on the energy scale at which it is evaluated. This is described in terms of the β-function

$$Q^2\frac{\partial\alpha_S(Q^2)}{\partial Q^2} = \beta(\alpha_S), \tag{1.21}$$

where $\alpha_s = g_s^2/(4\pi)$, g_s is the strong coupling and Q is the energy scale at which the coupling is calculated. To leading order in α_s the β-function is given by

$$\beta(\alpha_s) = -\alpha_s^2\frac{(11C_A - 2n_f)}{12\pi}, \tag{1.22}$$

where C_A is the Casimir in the adjoint representation and n_f is the number of massless quark flavours. The quarks can be considered as effectively massless for energy scales $Q \gg m_i$. The important features of QCD are due to the sign of this β-function. Given that $C_A = 3$ for $SU(3)$, the β-function is negative for less than 17 quark flavours. Six quark flavours have currently been discovered, so even at energy scales above the top quark mass the β-function is negative. This leads to the following properties of QCD:

1. Asymptotic freedom. The coupling decreases as the energy scale at which it is evaluated increases. Hence if we are dealing with high energy processes we can use perturbation theory in the small coupling constant to calculate physical quantities. In general, we can only make use of this fact if the quantity we are calculating is infra-red safe, *i.e.* does not have large corrections due to long-range physics.

2. Confinement. At low energies the coupling becomes large and we can no longer use perturbation theory to perform calculations. No free quarks or gluons have been observed experimentally. All the quarks and gluons are bound together to give the hadrons which are observed. These bound states either contain a valence quark–antiquark pair, a meson, or three valence quarks, a baryon. These bound states also contain gluons which bind the quarks together and a sea of virtual quark–antiquark pairs produced by gluon splitting.

1.1.2 Electroweak Theory

A major success of quantum field theory in general, and gauge theories in particular, is the unification of the electromagnetic and weak forces into a single gauge theory [9]. This theory has the symmetry group $SU(2)_L \times U(1)$. The Lagrangian is given by

$$\mathcal{L}_{\text{electroweak}} = \mathcal{L}_{\text{Higgs}} + \mathcal{L}_{\text{gauge}} + \mathcal{L}_{\text{fermions}}, \tag{1.23}$$

where $\mathcal{L}_{\text{Higgs}}$, $\mathcal{L}_{\text{gauge}}$ and $\mathcal{L}_{\text{fermions}}$ are the Lagrangians for the Higgs field, the gauge fields and the fermions respectively,

$$\mathcal{L}_{\text{Higgs}} = (D_\mu\phi)^\dagger(D^\mu\phi) - \mu^2\phi^\dagger\phi - \lambda(\phi^\dagger\phi)^2, \tag{1.24a}$$

$$\mathcal{L}_{\text{gauge}} = -\frac{1}{4}F^A_{\mu\nu}F_A^{\mu\nu} - \frac{1}{4}B_{\mu\nu}B^{\mu\nu}, \tag{1.24b}$$

$$\mathcal{L}_{\text{fermions}} = \sum_{\text{fermions}} \bar{\psi}_{f,L} i\gamma^\mu D_\mu \psi_{f,L} + \bar{\psi}_{f,R} i\gamma^\mu D_\mu \psi_{f,R} - \bar{\psi}_{f,L} g_{ff'}\phi\psi_{f',R} - \bar{\psi}_{f,R} g^*_{ff'}\phi^\dagger\psi_{f',L}. \tag{1.24c}$$

We have two gauge fields. The first is the $SU(2)_L$ field, W^A_μ, with field strength tensor, $F^A_{\mu\nu}$. This field is in the adjoint of $SU(2)_L$, *i.e.* an $SU(2)_L$ triplet with coupling g. The associated charge is called weak isospin. The second gauge field is the $U(1)$ field, B_μ, with field strength tensor $B_{\mu\nu}$ and coupling g'. The associated $U(1)$ charge is called hypercharge, by analogy with the electric charge of QED. The fields $\psi_{f,L} = \frac{1}{2}(1-\gamma_5)\psi$ are the left-hand components of the fermion fields and are $SU(2)_L$ doublets, as is the Higgs field ϕ. This is because experimentally the W bosons only couple to left-handed fermions.

The fields $\psi_{f,R} = \frac{1}{2}(1+\gamma_5)\psi$ are the right-hand components of the fermion fields and are $SU(2)_L$ singlets, because they do not couple to the W bosons. The coupling, $g_{ff'}$, of the Higgs fields to the fermions f and f' is only non-zero for those combinations of fermions which give a gauge-invariant term in the Lagrangian.

We will first consider the Higgs part of the Lagrangian, $\mathcal{L}_{\text{Higgs}}$. The structure of the Higgs potential is the same as that which we considered for the $U(1)$ case, Eqn. 1.15. Here we take the vacuum state to be

$$\phi = \begin{pmatrix} 0 \\ v \end{pmatrix}, \tag{1.25}$$

and expand about this point in terms of one real field and three angles in $SU(2)_L$ space to give the mass terms for the gauge bosons,

$$\mathcal{L}^{\text{mass}}_{\text{gauge}} = \frac{1}{4}g^2v^2W^+_\mu W^{-\mu} + \frac{1}{4}g^2v^2W^0_\mu W^{0\mu} - \frac{1}{2}gg'v^2W^0_\mu B^\mu + \frac{1}{4}g'^2v^2B_\mu B^\mu. \tag{1.26}$$

After the breaking of the $SU(2)_L$ symmetry there are two neutral gauge bosons, W^0 and B, which mix to give mass eigenstates A and Z^0,

$$A_\mu = \cos\theta_W B_\mu + \sin\theta_W W^0_\mu, \tag{1.27a}$$
$$Z_\mu = -\sin\theta_W B_\mu + \cos\theta_W W^0_\mu, \tag{1.27b}$$

where the weak mixing angle is given by $\tan\theta_W = \frac{g'}{g}$. This gives the mass terms for the gauge bosons in terms of the physical fields,

$$\mathcal{L}^{\text{mass}}_{\text{gauge}} = \frac{1}{4}g^2v^2W^+_\mu W^{-\mu} + \frac{g^2v^2}{4\cos^2\theta_W}Z^0_\mu Z^{0\mu}. \tag{1.28}$$

Hence the gauge boson masses are

$$M^2_{\mathrm{W}} = \frac{1}{2}g^2v^2, \tag{1.29a}$$
$$M^2_{\mathrm{Z}} = \frac{g^2v^2}{2\cos^2\theta_W}, \tag{1.29b}$$
$$M^2_{\mathrm{A}} = 0. \tag{1.29c}$$

So by using the Higgs mechanism masses have been generated for the gauge bosons carrying the weak force, *i.e.* the W and Z, while leaving the photon massless.

As with QCD the second term in Eqn. 1.23, $\mathcal{L}_{\text{gauge}}$, contains the kinetic energy terms for the gauge fields and terms which lead to interactions between the gauge bosons, for example the interaction of the photon with the $\mathrm{W}^\pm$ bosons. These gauge boson interaction terms will not be important for the rest of the discussion of the Standard Model and of supersymmetry.

The final term in the Lagrangian, Eqn. 1.23, gives the interactions of the gauge and Higgs bosons with the Standard Model fermions. Using Eqn. 1.27 we can express the couplings of the fermions to the photon and the Z in terms of their hypercharge and

Fermion	Hypercharge, Y	Isospin	t^3	Charge, Q
d_R	$-\frac{2}{3}$	0	0	$-\frac{1}{3}$
u_R	$+\frac{4}{3}$	0	0	$\frac{2}{3}$
$\begin{pmatrix} u \\ d \end{pmatrix}_L$	$+\frac{1}{3}$	$\frac{1}{2}$	$+\frac{1}{2}$ $-\frac{1}{2}$	$+\frac{2}{3}$ $-\frac{1}{3}$
e_R^-	-2	0	0	-1
$\begin{pmatrix} \nu_e \\ e^- \end{pmatrix}_L$	-1	$\frac{1}{2}$	$+\frac{1}{2}$ $-\frac{1}{2}$	0 -1

Table 1.1: Gauge quantum numbers of the Standard Model fermions.

isospin:

$$\text{photon couplings} \;=\; (t^3 + \frac{1}{2}Y)g\sin\theta_W \equiv Qe, \tag{1.30a}$$

$$\text{Z couplings} \;=\; (t^3\cos^2\theta_W - \frac{1}{2}Y\sin^2\theta_W)\frac{g}{\cos\theta_W} = (t^3 - Q\sin^2\theta_W)\frac{g}{\cos\theta_W}, \tag{1.30b}$$

where t^3 is the third component of the weak isospin, Y is the hypercharge and e is the magnitude of the electron's electric charge. The hypercharge is assigned given the weak isospin and electric charges, Q, of the fermions, *i.e.* $Y = 2(Q - t^3)$. This gives the charges in Table 1.1.

The Feynman rules for the interactions of the Standard Model fermions with the gauge bosons are given in Appendix A. The relevant Lagrangian is given in Eqn. A.48 with the Feynman rules given in Fig. A.8.

This only leaves the problem of generating a mass for the fermions. Simply adding a Dirac mass term, as in Eqn. 1.1, violates the gauge invariance of the theory. We can reexpress the Dirac mass term in terms of the left- and right-handed fields,

$$\mathcal{L}^{\text{mass}}_{\text{Dirac}} = -m\bar{\psi}\psi \equiv -m\left(\bar{\psi}_L\psi_R + \bar{\psi}_R\psi_L\right). \tag{1.31}$$

As the $SU(2)_L$ gauge transformation only acts upon the left-handed fields this term is not gauge invariant. This is the origin of the last two terms in Eqn. 1.24c which couple the Higgs field and the fermions in a gauge-invariant manner. After the breaking of the electroweak symmetry this gives fermion masses,

$$\mathcal{L}^{\text{mass}}_{\text{fermions}} = -g_{ee}v\left(\bar{e}_Le_R + \bar{e}_Re_L\right) - g_{dd}v\left(\bar{d}_Ld_R + \bar{d}_Rd_L\right) - g_{uu}v\left(\bar{u}_Lu_R + \bar{u}_Ru_L\right), \tag{1.32}$$

by defining $m_f = g_{ff}v$ the fermions obtain a mass in a gauge-invariant way. Here we have only considered one generation of fermions. It should be noted that to give mass to both the up- and down-type quarks we have used both the Higgs field ϕ and its hermitian

conjugate $\phi^\dagger$.

In general, with the three generations of fermions which have been discovered experimentally, the mass eigenstates of the fermions and their weak interaction states can be different. We must write down all the possible terms in the Lagrangian which are invariant under the symmetries and are renormalizable. We obtain the following Lagrangian

$$\begin{aligned}
\mathcal{L}^{\text{mass}}_{\text{fermions}} &= -v \begin{pmatrix} \bar{d}_L & \bar{s}_L & \bar{b}_L \end{pmatrix} \begin{pmatrix} g_{dd} & g_{ds} & g_{db} \\ g_{sd} & g_{ss} & g_{sb} \\ g_{bd} & g_{bs} & g_{bb} \end{pmatrix} \begin{pmatrix} d_R \\ s_R \\ b_R \end{pmatrix} \\
&\quad -v \begin{pmatrix} \bar{u}_L & \bar{c}_L & \bar{t}_L \end{pmatrix} \begin{pmatrix} g_{uu} & g_{uc} & g_{ut} \\ g_{cu} & g_{cc} & g_{ct} \\ g_{tu} & g_{tc} & g_{tt} \end{pmatrix} \begin{pmatrix} u_R \\ c_R \\ t_R \end{pmatrix} + \text{h.c.} \qquad (1.33) \\
&= -\bar{D}_L M_d D_R - \bar{U}_L M_u U_R + \text{h.c.}, \qquad (1.34)
\end{aligned}$$

where $D_{L,R}$ is a vector containing the three (left/right) down-type quark fields and $U_{L,R}$ is a vector containing the three (left/right) up-type quark fields. M_d and M_u are the mass matrices for the up- and down-type quarks, respectively. This leads to mixing between the quark generations.[3] The fields in Eqn. 1.34 are the weak interaction eigenstates. We can express Eqn. 1.34 in terms of the mass eigenstates by applying separate rotations to the left- and right-handed components of the quark fields. If we rotate the left-hand components of the field by the unitary matrix L and the right-hand components by the unitary matrix R we can obtain a diagonal mass matrix, $M' = LMR^\dagger$. We will need different rotation matrices for the up- and down-type quarks which we shall denote with the subscripts u and d, respectively. We must also rotate the quark fields in the other terms in the Standard Model Lagrangian. The neutral-current part of the electroweak and the QCD Lagrangians are flavour diagonal in terms of either the mass or weak interaction eigenstates. The only parts of the Lagrangian which are not are those which involve the coupling of the W boson to the quark fields. These terms involve the combination of fields

$$W\bar{U}_L D_L = W\bar{U'}_L L_u L_d^\dagger D'_L \equiv W\bar{U'}_L V D'_L, \qquad (1.35)$$

where $V = L_u L_d^\dagger$ is called the Cabibbo-Kobayashi-Maskawa (CKM) matrix. We can therefore work in a physical, *i.e.* mass, basis for the quarks and simply include the relevant element of the CKM matrix at the vertex coupling the W boson to the quarks. This is the only physical combination of the rotation matrices and can be associated with the down-type quarks.

1.1.3 Symmetries of the Standard Model

In addition to the gauge and Lorentz symmetries of the Standard Model there are a number of other symmetries. These symmetries are consequences of the gauge and Lorentz symmetries and the requirement that the Standard Model be renormalizable.

[3] If the neutrino is massless and the right-handed neutrino does not exist there can be no mixing between the lepton generations. However, as we now believe the neutrinos are massive, it is possible that the leptons also undergo mixing.

In particular there are two symmetries[4] which will be important in the rest of this thesis:

Lepton Number. We assign a quantum number, called lepton number, such that the lepton fields have lepton number $+1$, the antileptons have lepton number -1 and all the other fields have lepton number zero. The electroweak Lagrangian, Eqn. 1.23, conserves this quantum number.

Baryon Number. We assign the baryon number such that the quarks have baryon number $+1/3$, the antiquarks baryon number $-1/3$ and all the other fields have baryon number zero. This is done so that the baryons, *e.g.* the proton, have baryon number $+1$. Both the QCD Lagrangian, Eqn. 1.20, and the electroweak Lagrangian, Eqn. 1.23, respect this symmetry.

The important point to note for the rest of the thesis is that we did not construct the Lagrangian to have these symmetries. It is impossible to write down a term in the Lagrangian which is renormalizable, Lorentz and gauge invariant, but violates these discrete symmetries given the particle content of the Standard Model. This is important as in a supersymmetric theory it is possible to have terms in the Lagrangian which are renormalizable, Lorentz and gauge invariant, but violate either lepton or baryon number.

1.2 Supersymmetry

Despite the great success of the Standard Model in explaining all the current experimental results it is widely believed that it cannot be a complete theory, if for no other reason than that it does not include gravity. The Standard Model is viewed as some low-energy effective theory of some larger theory which may be:

- a grand unified theory (GUT) in which the gauge group of the Standard Model is unified as a part of a larger gauge group, *e.g.* $SU(5)$;
- a string theory which would also include gravity.

This theory would hope to explain, for example, why there are three generations of fermions and predict some of the free parameters of the Standard Model, *e.g.* the particle masses. While supersymmetry does not provide a solution to any of these questions it does provide a solution to other problems in the Standard Model such as the hierarchy problem, which we will discuss in Section 1.2.2.

We will first discuss the idea of supersymmetry, followed by the problems it solves and other reasons for favouring it as a possible extension of the Standard Model. The simplest supersymmetric extension of the Standard Model is then discussed in some detail, concentrating on those parts of the theory which will be important in the rest of this thesis.

[4]These symmetries are violated in the Standard Model by non-perturbative effects [13].

1.2.1 Introduction to Supersymmetry

The basic idea of supersymmetry is that for every bosonic degree of freedom there is a corresponding fermionic one. Therefore the operator Q, which generates the transformation from a boson to a fermion must be a spinor and fermionic, *i.e.*

$$Q|\text{Fermion}\rangle = |\text{Boson}\rangle, \tag{1.36a}$$
$$Q|\text{Boson}\rangle = |\text{Fermion}\rangle. \tag{1.36b}$$

These fermionic generators form part of an extended Poincaré group. In addition to the standard algebra for the generators of the Poincaré group

$$[P^\mu, P^\nu] = 0, \tag{1.37a}$$
$$[M^{\mu\nu}, P^\rho] = i(g^{\nu\rho}P^\mu - g^{\mu\rho}P^\nu), \tag{1.37b}$$
$$\left[M^{\mu\nu}, M^{\rho\lambda}\right] = i(g^{\nu\rho}M^{\mu\lambda} + g^{\mu\lambda}M^{\nu\rho} - g^{\mu\rho}M^{\nu\lambda} - g^{\nu\lambda}M^{\mu\rho}), \tag{1.37c}$$

we have the following relations for the anti-commuting generator Q,

$$[Q_\alpha, P_\mu] = [\bar{Q}_{\dot{\alpha}}, P_\mu] = 0, \tag{1.38a}$$
$$\{Q_\alpha, Q_\beta\} = \{\bar{Q}_{\dot{\alpha}}, \bar{Q}_{\dot{\beta}}\} = 0, \tag{1.38b}$$
$$[M^{\mu\nu}, Q_\alpha] = -i(\sigma^{\mu\nu})_\alpha{}^\beta Q_\beta, \tag{1.38c}$$
$$\left[M^{\mu\nu}, \bar{Q}^{\dot{\alpha}}\right] = -i(\bar{\sigma}^{\mu\nu})^{\dot{\alpha}}{}_{\dot{\beta}}\bar{Q}^{\dot{\beta}}, \tag{1.38d}$$
$$\{Q_\alpha, \bar{Q}_{\dot{\beta}}\} = 2\sigma^\mu{}_{\alpha\dot{\beta}}P_\mu. \tag{1.38e}$$

The generators Q and $\bar{Q}$ are two-component left- and right-handed Weyl spinors, respectively. We use the index α (or β) to denote the component of the left-handed spinors and the index $\dot{\alpha}$ (or $\dot{\beta}$) to denoted the component of the right-handed spinors, since the two types of spinors transform differently under Lorentz transformations.

This gives a closed algebra for the extended Poincaré group with the addition of the fermionic generator Q. As with the Poincaré group we can construct Lagrangians which are invariant under this symmetry. For example the simplest possible supersymmetric Lagrangian contains a complex field ϕ, with two degrees of freedom, and a Weyl fermion ψ, also with two degrees of freedom. The Lagrangian [14]

$$\mathcal{L} = \partial_\mu\phi^*\partial^\mu\phi + i\bar{\psi}\bar{\sigma}^\mu\partial_\mu\psi, \tag{1.39}$$

is invariant under the supersymmetry transformation

$$\delta\phi = \sqrt{2}\xi\psi, \tag{1.40a}$$
$$\delta\psi = i\sqrt{2}\partial_\mu\phi\sigma^\mu\bar{\xi}, \tag{1.40b}$$

where we have a spinor parameter ξ for the transformation. While it is easier to construct the Lagrangian for a supersymmetric theory in two-component notation, using Weyl spinors, to actually derive the Feynman rules we will use the standard four-component notation with Dirac spinors. In this case for every Standard Model Dirac fermion with

four degrees of freedom there will be two corresponding complex scalar fields, each with two degrees of freedom. Similarly the massless gauge bosons of the Standard Model which each have two degrees of freedom, *i.e.* two polarizations, will have as partners a Majorana fermion with two degrees of freedom. The particles and their superpartners will have the same mass, and the masses of the massive gauge bosons and gauginos are generated via the Higgs mechanism.

1.2.2 Motivations for Supersymmetry

As none of the superpartners of the Standard Model fields have been observed supersymmetry cannot be an exact symmetry, *i.e.* it must be broken in such a way that most of the superpartners are more massive than their Standard Model partners.[5] Despite this there are a number of theoretical reasons for favouring a supersymmetric extension of the Standard Model:

1. Coleman-Mandula Theorem.

   Perhaps the most persuasive argument in favour of supersymmetry is based on the Coleman-Mandula theorem [15]. As we saw in Section 1.1 the Standard Model can be constructed by imposing the symmetries of the theory, *i.e.* gauge and Lorentz invariance, and by the requirement that the theory is renormalizable. It is therefore interesting to consider possible extensions of these symmetries, *e.g.* by unifying the gauge groups of the Standard Model into one group. However if we consider possible extensions of the Poincaré group, Coleman and Mandula showed that the addition of any new generators which transform as bosons leads to a trivial S-matrix, *i.e.* in particle scattering experiments the particles could only scatter through certain discrete angles, which is not observed. While extending the Poincaré group with additional bosonic generators is forbidden by this theorem we can extend the group with generators which transform as fermions. It was later shown [16] that supersymmetry is the only possible extension of the Poincaré group which does not lead to a trivial S-matrix.

2. Hierarchy Problem.

   A second argument in favour of supersymmetry can be seen by considering the one-loop corrections to the Higgs mass, given by the diagrams in Fig. 1.1. In particular, if we only consider the fermion loops we get a contribution

   $$\delta M_{Hf}^2 = \Pi_H(M_H^2), \tag{1.41}$$

   where

   $$i\Pi_H(p^2) = -\frac{|g_f|^2}{4}\int \frac{d^4k}{(2\pi)^4}\frac{\mathrm{tr}\left[(\not{k}+\not{p}+m_f)(\not{k}+m_f)\right]}{\left[(k+p)^2-m_f^2\right]\left[k^2-m_f^2\right]} \tag{1.42}$$

[5] Given the current experimental limits apart from the supersymmetric partners of the top quark all the sfermions must be heavier than their Standard Model partners.

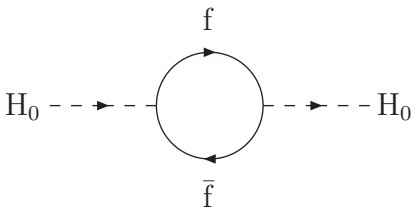

(a) Fermion loops.

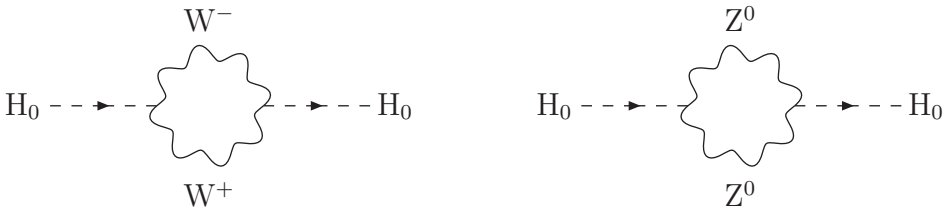

(b) W and Z boson loops.

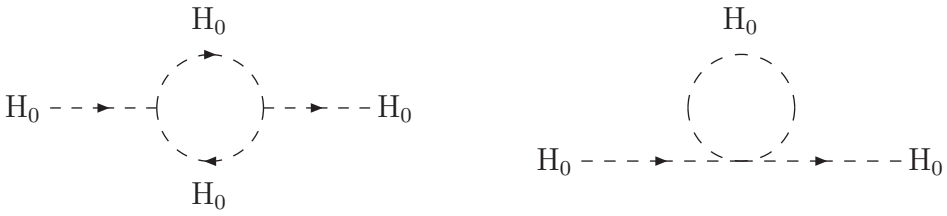

(c) Higgs loops.

Figure 1.1: One-loop contributions to the Higgs mass.

and $g_f = m_f/v$ is the coupling of the fermion to the Higgs field. Naïvely, from power counting, this diagram is quadratically divergent. This divergence can be regulated by imposing a cut-off, Λ, giving the following result

$$\delta M_{Hf}^2 = \frac{|g_f|^2}{16\pi^2}\left[-2\Lambda^2 + 6m_f^2 \ln\left(\Lambda/m_f\right)\right], \tag{1.43}$$

where we have neglected terms which are finite in the limit $\Lambda \to \infty$.

The Standard Model Higgs mass depends quadratically on the cut-off scale, Λ. This is not a problem provided that we renormalize the theory and absorb the divergent terms into a redefinition of the Higgs mass. However if we take the modern view that the Standard Model is only a low-energy effective theory we would expect the cut-off to be the scale of new physics, *e.g.* the GUT or Planck scale. This means that the natural value of the Higgs mass is $10^{14} - 10^{17}$ GeV rather than the upper limit of around 300 GeV suggested by the precision electroweak data. This is the hierarchy

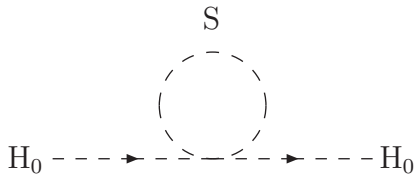

Figure 1.2: Contribution to the Higgs mass from an extra scalar field.

problem, *i.e.* the natural scale for the Higgs mass is the scale of new physics. We would therefore have to tune the bare Higgs mass in the Standard Model,

$$M_H^2 = M_{H\,\mathrm{bare}}^2 + \delta M_H^2, \tag{1.44}$$

in order to obtain a Higgs mass at the electroweak scale. If we require the Higgs mass to be around the electroweak scale the cancellation between M_H^{bare} and δM_H must be ~ 1 part in 10^{12} which requires an enormous fine-tuning to the parameters of the bare Lagrangian.

We can see how this problem is solved by supersymmetry by considering an additional scalar field [17] which interacts with the Higgs boson via the Lagrangian $\mathcal{L} = -\lambda_s \phi_s^2 H^2 S^2$. This gives an extra one-loop contribution, Fig. 1.2, to the Higgs mass

$$\delta M_{H\,S}^2 = \frac{\lambda_s}{16\pi^2}\left(\Lambda^2 - 2M_S^2 \ln\left(\Lambda/M_S\right)\right), \tag{1.45}$$

where we have again neglected terms which are finite in the limit $\Lambda \to \infty$. In supersymmetry, as we have two complex scalar fields for each Dirac fermion, this contribution will cancel the contribution from the fermion loops provided that $\lambda_S = |g_f|^2$, which is the case if supersymmetry is unbroken.

3. Supersymmetric Grand Unified Theories.

   The idea in grand unified theories is that at some high scale the strong and electroweak forces can be unified into a single gauge theory, the simplest example being $SU(5)$. This is supported by the running of the couplings measured by the LEP experiments. If we evolve the couplings from their values at current day collider energies the strong, electromagnetic and weak couplings seem to unify at about 10^{16} GeV. However, in the Standard Model these couplings do not quite unify. If we introduce new particles into the spectrum, as in supersymmetry, this will change the evolution of the couplings with energy and in a supersymmetric theory the couplings do indeed unify. While this may seem to favour SUSY as an extension of the Standard Model, the unification of the couplings can also be achieved by the addition of other kinds of new particles into the spectrum.

While there are many theoretical reasons, *i.e.* the Coleman-Mandula theorem and the hierarchy problem, and perhaps even the suggestion that we need supersymmetry, or

some other new physics if we want the couplings to unify, there is no direct experimental evidence for supersymmetry. Supersymmetry is a very elegant theory but this does not mean that it is realized in nature. However, as one possible extension of the Standard Model, it has a number of attractive theoretical features and we must investigate whether it is indeed a symmetry of nature.

1.2.3 Construction of Supersymmetric Lagrangians

In principle we can start from the particle content of the theory and write the most general Lagrangian consistent with the symmetries and renormalizablity. However for supersymmetric theories it is easier to construct the supersymmetrically-invariant Lagrangian using the superfield formalism rather than the basic bosonic and fermionic fields. A more detailed description of this formalism can be found in, for example, [18–20].

The momentum operator and the generators, Q and $\bar{Q}$, of the SUSY transformations form a sub-group of the extended Poincaré group. This allows us to construct a function $S(x^\mu, \theta, \bar{\theta})$, the superfield, which is a linear representation of this sub-group. The change in this function induced by the action of a member of the sub-group,

$$G(a^\mu, \xi, \bar{\xi}) = \exp i(\xi Q + \bar{\xi}\bar{Q} - a^\mu P_\mu), \tag{1.46}$$

is generated by

$$P_\mu = i\partial_\mu, \tag{1.47a}$$

$$Q_\alpha = -i\frac{\partial}{\partial\theta^\alpha} - \sigma^\mu_{\alpha\dot{\alpha}}\bar{\theta}^{\dot{\alpha}}\partial_\mu, \tag{1.47b}$$

$$\bar{Q}_{\dot{\alpha}} = i\frac{\partial}{\partial\bar{\theta}^{\dot{\alpha}}} + \theta^\alpha\sigma^\mu_{\alpha\dot{\alpha}}\partial_\mu, \tag{1.47c}$$

where ξ, $\bar{\xi}$, θ and $\bar{\theta}$ are anti-commuting Grassmann variables which transform as Weyl spinors. Further derivatives which anti-commute with the generators can also be defined

$$D_\alpha = \frac{\partial}{\partial\theta^\alpha} + i\sigma^\mu_{\alpha\dot{\alpha}}\bar{\theta}^{\dot{\alpha}}\partial_\mu, \tag{1.48a}$$

$$\bar{D}_{\dot{\alpha}} = -\frac{\partial}{\partial\bar{\theta}^{\dot{\alpha}}} - i\theta^\alpha\sigma^\mu_{\alpha\dot{\alpha}}\partial_\mu. \tag{1.48b}$$

The general superfield, $S(x^\mu, \theta, \bar{\theta})$, is a reducible representation of the supersymmetric algebra. However, we can obtain irreducible representations by imposing further conditions:

$$\bar{D}_{\dot{\alpha}}S = 0 \quad \text{chiral superfield;} \tag{1.49a}$$

$$S^\dagger = S \quad \text{vector superfield.} \tag{1.49b}$$

It should be noted that because θ and $\bar{\theta}$ are two-component Grassmann variables the expansion of the superfield as a power series in θ and $\bar{\theta}$ cannot involve terms with more than two powers of θ or $\bar{\theta}$. The chiral superfield can be written as an expansion in terms

of the Grassmann variables θ and $\bar{\theta}$ giving

$$\begin{aligned}\Phi(x^\mu,\theta,\bar{\theta}) &= \phi(x)+\sqrt{2}\theta\psi(x)+\theta\theta F(x)+i\partial_\mu\phi(x)\theta\sigma^\mu\bar{\theta} \\ &\quad -\frac{i}{\sqrt{2}}\theta\theta\partial_\mu\psi(x)\sigma^\mu\bar{\theta}-\frac{1}{4}\partial^\mu\partial_\mu\phi(x)\theta\theta\bar{\theta}\bar{\theta}. \end{aligned} \tag{1.50}$$

This superfield includes a Weyl spinor, ψ, and a complex scalar field, ϕ. The field F is an auxiliary field which can be eliminated using the equations of motion. The component fields transform in the following way under the SUSY transformation:

$$\delta\phi = \sqrt{2}\xi\psi; \tag{1.51a}$$
$$\delta\psi = \sqrt{2}\xi F+i\sqrt{2}\partial_\mu\phi\sigma^\mu\bar{\xi}; \tag{1.51b}$$
$$\delta F = i\sqrt{2}\partial_\mu\psi\sigma^\mu\bar{\xi}. \tag{1.51c}$$

This is the left chiral superfield, the right chiral superfield can be obtained by taking the hermitian conjugate. We refer to the coefficient of the $\theta\theta$ term as the F-term. Eqn. 1.51c shows that the change, under the SUSY transformations, of the F-term is a total derivative. Hence the F-term is suitable for use as a supersymmetrically-invariant Lagrangian.

Similarly, the vector superfield can be expanded in powers of θ and $\bar{\theta}$,

$$\begin{aligned}S(x^\mu,\theta,\bar{\theta}) &= C(x)+i\theta\chi(x)-i\bar{\theta}\bar{\chi}(x)+\frac{i}{2}\theta\theta\left[M(x)+iN(x)\right] \\ &\quad -\frac{i}{2}\bar{\theta}\bar{\theta}\left[M(x)-iN(x)\right]+\theta\sigma^\mu\bar{\theta}V_\mu(x) \\ &\quad +i\theta\theta\bar{\theta}\left[\bar{\lambda}(x)+\frac{i}{2}\bar{\sigma}^\mu\partial_\mu\chi(x)\right]-i\bar{\theta}\bar{\theta}\theta\left[\lambda(x)+\frac{i}{2}\sigma^\mu\partial_\mu\bar{\chi}(x)\right] \\ &\quad +\frac{1}{2}\theta\theta\bar{\theta}\bar{\theta}\left[D(x)-\frac{1}{2}\partial_\mu\partial^\mu C(x)\right], \end{aligned} \tag{1.52}$$

where the real scalar fields C, M, N and the Weyl fermion χ can be eliminated by a SUSY gauge transformation leaving the physical degrees of freedom, *i.e.* the gauge field V_μ and its superpartner gaugino field λ, and the auxiliary field D. The component fields transform in the following way under the SUSY transformations:

$$\delta C = i\left(\xi\chi-\bar{\xi}\bar{\chi}\right); \tag{1.53a}$$
$$\delta\lambda_\alpha = -iD\xi_\alpha-\frac{1}{2}(\sigma^\mu\bar{\sigma}^\nu)_\alpha{}^\beta\xi_\beta\left(\partial_\mu V_\nu-\partial_\nu V_\mu\right); \tag{1.53b}$$
$$\delta V^\mu = i\left(\xi\sigma^\mu\bar{\lambda}-\lambda\sigma^\mu\bar{\xi}\right)-\partial^\mu\left(\xi\chi+\bar{\xi}\bar{\chi}\right); \tag{1.53c}$$
$$\delta D = \partial_\mu\left(-\xi\sigma^\mu\bar{\lambda}+\lambda\sigma^\mu\bar{\xi}\right). \tag{1.53d}$$

Here the variation of the coefficient of the $\theta\theta\bar{\theta}\bar{\theta}$ term, the D-term, is a total derivative and hence this can also be used as a supersymmetrically-invariant Lagrangian.

Using these superfields we can construct supersymmetric Lagrangians. In the supersymmetric extension of the Standard Model we will use left chiral superfields to represent the left-hand components of the Standard Model fermions, together with their super-

partners, and right chiral superfields to represent the right-hand components, and their superpartners. The gauge bosons are represented by vector superfields.

Here we will only consider how to construct the Lagrangian for the chiral superfields as these are the terms in the supersymmetric Lagrangian we are interested in. This can be done by taking products of chiral superfields. In particular the product of two left chiral superfields is also a left chiral superfield. Hence the F-term of a product of left chiral superfields can be used to give a suitable term in the Lagrangian. The product of a left and a right chiral superfield gives a vector superfield. The D-term of the product of a left and a right chiral superfield can therefore also be used to give a term in the Lagrangian. The simplest example of this is a single left chiral superfield. We can form the product of this field with its hermitian conjugate and take the D-term. This gives

$$[\Phi\Phi^\dagger]_{\theta\theta\bar{\theta}\bar{\theta}} = FF^\dagger + \partial_\mu\phi^*\partial^\mu\phi + i\bar{\psi}\bar{\sigma}^\mu\partial_\mu\psi, \tag{1.54}$$

which, after eliminating the auxiliary field F using the equations of motion, is the Lagrangian given in Eqn 1.39. Therefore using the D-term of the product of the superfield and its hermitian conjugate we can form the kinetic term for the fermionic field and its superpartner. We can add interaction and mass terms to this theory by taking products of the left chiral superfields. This can be done by forming the superpotential for the theory. For example, in a theory with only one chiral superfield,

$$\mathbf{W}(\Phi) = \frac{m}{2}\Phi\Phi + \frac{\lambda}{3}\Phi\Phi\Phi. \tag{1.55}$$

In general we can only include terms which are at most cubic in the superfields in order for the theory to be renormalizable. This gives the interaction Lagrangian

$$\begin{aligned} \mathcal{L} &= [W(\Phi)]_{\theta\theta} + \text{h.c.}, & (1.56)\\ &= m(\phi F - \frac{1}{2}\psi\psi) + \lambda(\phi^2 F - \phi\psi\psi) + \text{h.c.}. & (1.57) \end{aligned}$$

We can then write the full Lagrangian for this theory and use the equations of motion to eliminate the auxiliary field F,

$$F^\dagger = -m\phi - \lambda\phi^2, \tag{1.58}$$

giving the result

$$\begin{aligned} \mathcal{L} &= [\Phi\Phi^\dagger]_{\theta\theta\bar{\theta}\bar{\theta}} + ([W(\Phi)]_{\theta\theta} + \text{h.c.}), & (1.59)\\ &= \partial_\mu\phi^*\partial^\mu\phi + i\bar{\psi}\bar{\sigma}^\mu\partial_\mu\psi - |\lambda\phi^2 + m\phi|^2 - \Big(\frac{m}{2}\psi\psi + \lambda\psi\psi\phi + \text{h.c.}\Big). & (1.60) \end{aligned}$$

By taking the relevant combinations of the chiral superfields, the kinetic terms and the interactions of the chiral fields with each other can be constructed. In general the superpotential gives the Yukawa-type interactions and part of the scalar potential of the theory. Similarly the kinetic energy terms of the gauge fields and their supersymmetric partners can be constructed, as well as the interactions of the vector and chiral superfields. In the next section we will construct a supersymmetric extension of the Standard Model using these superfield techniques.

Superfields		Bosonic Fields	Fermionic Fields	$SU(3)_C$	$SU(2)_L$	Y
Field	Type					
Gauge Multiplets						
G^a	Vector	Gluons	Gluinos	Octet	Singlet	0
W^a	Vector	W	Winos	Singlet	Triplet	0
B^a	Vector	B	Bino	Singlet	Singlet	0
Matter Multiplets						
L_i	Left Chiral	$(\tilde{\nu}_L, \tilde{\ell}_L^-)$	(ν_L, ℓ_L)	Singlet	Doublet	-1
E_i	Right Chiral	$\tilde{\ell}_R^-$	ℓ_R	Singlet	Singlet	-2
Q_i	Left Chiral	$(\tilde{u}_L, \tilde{d}_L)$	(u_L, d_L)	Triplet	Doublet	$1/3$
U_i	Right Chiral	$\tilde{u}_R$	u_R	Triplet	Singlet	$4/3$
D_i	Right Chiral	$\tilde{d}_R$	d_R	Triplet	Singlet	$-2/3$
Higgs Multiplets						
H_1	Left Chiral	(H_1^1, H_1^2)	$(\tilde{H}_1^0, \tilde{H}_1^-)_L$	Singlet	Doublet	-1
H_2	Left Chiral	(H_2^1, H_2^2)	$(\tilde{H}_2^+, \tilde{H}_2^0)_L$	Singlet	Doublet	1

Table 1.2: Superfields in the Minimal Supersymmetric Standard Model (MSSM). The subscript $i = 1, 2, 3$ gives the generation of the matter fields.

1.2.4 The Minimal Supersymmetric Standard Model

We can construct the minimal supersymmetric extension of the Standard Model by including the superpartners of the Standard Model particles and then using the superfield formalism to construct the most general renormalizable supersymmetrically- and gauge-invariant Lagrangian. In the supersymmetric version of the Standard Model we cannot use the same Higgs boson to give mass to both the up- and down-type quarks. Hence we need two $SU(2)_L$ doublet Higgs fields to give all the particles in the theory mass. This gives the particle content in Table 1.2.

The Standard Model is extended by including the superpartners of all the Standard Model particles. As with the Standard Model we should write down the most general Lagrangian consistent with the symmetries of the theory and renormalizablity. This means we should write down the most general renormalizable supersymmetrically-invariant theory consistent with the gauge symmetries. The most general renormalizable gauge-invariant superpotential is given by

$$\mathbf{W} = \mathbf{W}_{\text{MSSM}} + \mathbf{W}_{\not{\mathbf{R}}_\mathbf{p}}, \tag{1.61}$$

where

$$\mathbf{W}_{\text{MSSM}} = -h_{ij}^E \varepsilon_{ab} L_i^a H_1^b \overline{E}_j - h_{ij}^D \varepsilon_{ab} Q_i^a H_1^b \overline{D}_j + h_{ij}^U \varepsilon_{ab} Q_i^a H_2^b \overline{U}_j + \mu \varepsilon_{ab} H_1^a H_2^b, \tag{1.62}$$

$$\mathbf{W}_{\not{\mathbf{R}}_\mathbf{p}} = \frac{1}{2}\lambda_{ijk}\varepsilon^{ab} L_a^i L_b^j \overline{E}^k + \lambda'_{ijk}\varepsilon^{ab} L_a^i Q_b^j \overline{D}^k + \frac{1}{2}\lambda''_{ijk}\varepsilon^{c_1 c_2 c_3} \overline{U}_{c_1}^i \overline{D}_{c_2}^j \overline{D}_{c_3}^k + \kappa_i \varepsilon^{ab} L_a^i H_b^2, \tag{1.63}$$

using the superfields given in Table 1.2. Here $a, b = 1, 2$ are the $SU(2)_L$ indices,

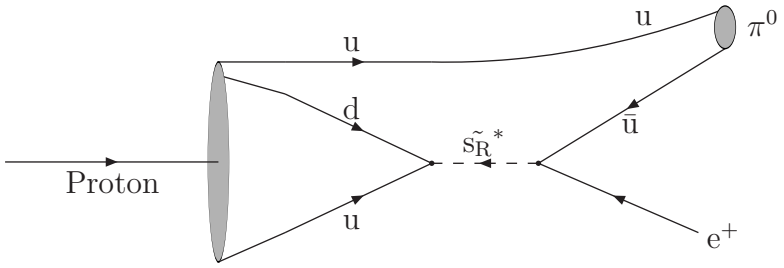

Figure 1.3: $\not{R}_p$ proton decay, $p \to \pi^0 e^+$.

$c_1, c_2, c_3 = 1, 2, 3$ are the $SU(3)_C$ indices and $i, j, k = 1, 2, 3$ are the generations of the matter fields. As we can only include left chiral superfields in the superpotential we must take the hermitian conjugate, denoted with a bar, of the right chiral superfields. Another consequence of the requirement that we can only use left chiral superfields in the superpotential is that we cannot use the conjugate of the Higgs field to give mass to both the up- and down-type quarks, as in the Standard Model, and we therefore need two Higgs doublets to give mass to both types of quark. The first term in this superpotential, $\mathbf{W}_{\text{MSSM}}$, gives the Yukawa terms of the Standard Model and the additional terms required by supersymmetry. However the second term[6] $\mathbf{W}_{\not{\mathbf{R}}_\mathbf{p}}$ gives additional interactions. A recent summary of the bounds on the couplings in Eqn. 1.63 can be found in [21]. This superpotential gives, for example from the third term, interactions of a squark and two quarks or of four squarks. When combined with the MSSM superpotential, $\mathbf{W}_{\text{MSSM}}$, there are also terms involving the interactions of three squarks/sleptons with a Higgs boson. The presence of this second term in the superpotential, $\mathbf{W}_{\not{\mathbf{R}}_\mathbf{p}}$, leads to a problem with the supersymmetric extension of the Standard Model. If we consider the second two terms of Eqn. 1.63 the proton can decay by the process shown in Fig. 1.3.

We can use the experimental limit on the proton lifetime [22]

$$\tau\left(\text{Proton} \longrightarrow e^+\pi^0\right) > 10^{32}\,\text{yr}, \tag{1.64}$$

to obtain a bound on the product of the couplings at the two vertices in Fig. 1.3, as a function of the exchanged squark mass,

$$\lambda'_{11k}\lambda''_{11k} \lesssim 2 \times 10^{-27}\left(\frac{M_{\tilde{\mathrm{d}}_{kR}}}{100\ \text{GeV}}\right). \tag{1.65}$$

Hence as we require that $M_{\tilde{\mathrm{d}}_{kR}} \lesssim 1\,\text{TeV}$ to solve the hierarchy problem the only natural way to satisfy this bound is to have one of these couplings set to zero. The standard way to achieve this is to introduce a new multiplicatively conserved quantum number called

[6] It should be noted that some authors choose to define this superpotential without the factors of one half in the LLE and UDD terms. This will lead to differences in the Feynman rules, but the results with this second convention can always be obtained by taking λ or λ'' to be twice their value in our convention.

R-parity which is defined as [23]

$$\mathrm{R_p} = (-1)^{3\mathrm{B}+\mathrm{L}+2\mathrm{S}}, \tag{1.66}$$

where L is the lepton number, B is the baryon number and S is the spin of the particle. This new quantum number is $+1$ for the Standard Model particles and -1 for their SUSY partners. This prevents proton decay by forbidding all the terms in Eqn. 1.63 but not the terms in Eqn. 1.62. The conservation of R-parity in addition to the symmetries, *i.e.* supersymmetry and the Standard Model gauge symmetries, and particle content defines the Minimal Supersymmetric Standard Model (MSSM). Another symmetry which has the same effect, but is easier to see at the superfield level, is called matter parity. Here we change the sign of the matter, *i.e.* quark and lepton, superfields but not the Higgs or gauge superfields

$$(Q_i, \bar{U}_i, \bar{D}_i, L_i, \bar{E}_i) \rightarrow -(Q_i, \bar{U}_i, \bar{D}_i, L_i, \bar{E}_i), \qquad (H_1, H_2) \rightarrow (H_1, H_2). \tag{1.67}$$

This also forbids all the terms in Eqn. 1.63 but none of the terms in Eqn. 1.62.

The Lagrangian of the theory can then be specified by taking the relevant combinations of the superfields and extracting the terms which are invariant under supersymmetry. In general these Lagrangians are given in [18,24]. The Feynman rules for this new theory can be found in [18, 24] and the Feynman rules for those interactions that will be important in this thesis are given in a more general form in Appendix A.

The problem is that in a theory with unbroken supersymmetry the Standard Model particles and their superpartners would have the same mass. However the superpartners of the known fundamental particles have not been detected experimentally. Thus if supersymmetry is realized in nature it must be broken.

There are mechanisms, based on either the F- or D-terms developing a non-zero vacuum expectation value, which spontaneously break supersymmetry. However in these models there are generally mass sum rules, for example, the supertrace in models with F-term supersymmetry breaking [25] ,

$$\mathrm{Str}\, M^2 \equiv \sum_J (-1)^{2J}(2J+1)m_J^2 = 0, \tag{1.68}$$

where the supertrace, $\mathrm{Str}\, M^2$, denotes the trace of the mass-squared matrix over the real fields, of spin J. This formula can be modified by radiative corrections. However at tree level it implies that while one of the superpartners of the Standard Model fermions would be heavier than the fermion the other would be lighter. This is not observed. Given this tree-level result, realistic models of broken supersymmetry based on either F- or D-term supersymmetry breaking are difficult to construct.

The approach which is taken in the MSSM is to add by hand all terms that violate supersymmetry in such a way that the quadratic divergences, *e.g.* in the Higgs mass, are not reintroduced. This is called soft supersymmetry breaking. However soft SUSY breaking is "ad-hoc" and leads to over one hundred additional parameters [26]. Given the number of free parameters which must be specified it is also of limited use in experimental searches.

Another approach is to break supersymmetry in some "hidden-sector" which only couples to the MSSM fields via either non-renormalizable operators [19, 27] or loop diagrams [28].

In general the supersymmetry breaking in the "hidden-sector" can be due to either F-term supersymmetry breaking or the production of gaugino condensates [29]. The two types of models differ in how this supersymmetry breaking is transmitted from the "hidden-sector" to the "visible-sector", *i.e.* the MSSM fields.

In supergravity models the supersymmetry breaking is transmitted to the "visible-sector" through gravitational interactions, represented by non-renormalizable terms suppressed by inverse powers of the Planck mass. In gauge-mediated models of supersymmetry breaking new vector fields are introduced which transmit the supersymmetry breaking between the "hidden-" and "visible-sectors".

In this thesis we will not be concerned with the details of the supersymmetry-breaking mechanism. While in principle we could perform all our analyses within the framework of the MSSM, *i.e.* by specifying all the soft SUSY-breaking parameters, it is much easier to work with a smaller set of parameters. We will therefore use the standard supergravity (SUGRA) scenario where the soft SUSY-breaking masses for the gauginos ($M_{1/2}$) and scalars (M_0), and the trilinear SUSY-breaking terms (A_0) are universal at the GUT scale. In addition we will require that electroweak symmetry is radiatively broken [30], *i.e.* the Higgs mass squared becomes negative due to its renormalization group evolution. This gives five parameters: the soft masses and trilinear SUSY-breaking terms $M_{1/2}$, M_0, A_0, the ratio of the Higgs vacuum expectation values of the two Higgs doublets $\tan\beta$ and $\operatorname{sgn}\mu$. The absolute value of the μ term in Eqn. 1.62 is fixed by the requirement of radiative electroweak symmetry breaking.

1.3 R-parity Violating Supersymmetry

In the Standard Model the Lagrangian is constructed by writing down all the terms consistent with the gauge symmetries, renormalizablity and the particle content of the theory. The discrete symmetries, *i.e.* lepton and baryon number, then emerge as consequences of the other symmetries of the theory. However in the construction of the MSSM we were forced to impose a new discrete symmetry, $\mathrm{R_p}$, to prevent the decay of the proton.

There is no reason to impose R-parity as a symmetry, all that is required is a symmetry such that either the second or third terms in Eqn. 1.63 are forbidden. We can achieve this for example by imposing baryon parity,

$$(Q_i, \bar{U}_i, \bar{D}_i) \rightarrow -(Q_i, \bar{U}_i, \bar{D}_i), \qquad (L_i, \bar{E}_i, H_1, H_2) \rightarrow (L_i, \bar{E}_i, H_1, H_2), \tag{1.69}$$

which prevents the third term in Eqn. 1.63. This leads to lepton number violation but no baryon number violation and hence prevents the decay of the proton. Similarly there are symmetries, *e.g.* lepton parity

$$(L_i, \bar{E}_i) \rightarrow -(L_i, \bar{E}_i), \qquad (Q_i, \bar{U}_i, \bar{D}_i, H_1, H_2) \rightarrow (Q_i, \bar{U}_i, \bar{D}_i, H_1, H_2), \tag{1.70}$$

which forbids the second term in Eqn. 1.63 giving baryon number violation with no lepton

number violation and preventing the decay of the proton.

As we are imposing, by hand, a new multiplicative symmetry on the theory there is no reason to favour imposing either R-parity or, for example, baryon parity. As there is no reason for favouring either of these models, if we are to search for supersymmetry both must be studied. This is particularly important as there are major differences in the experimental signatures of these processes.

The conservation of R_p in the MSSM gives a number of effects:

- as the initial state in any collider experiment contains only Standard Model particles SUSY particles must be produced in pairs;
- the lightest supersymmetric particle (LSP) is stable;
- cosmological bounds on electric- or colour-charged stable relics imply that a stable LSP must be a neutral colour singlet [31].

This leads to a classical signature for supersymmetry in all collider experiments. As the lightest SUSY particle is stable, any SUSY particle produced will tend to cascade decay to the LSP. The LSP, which is weakly interacting, will then escape from the detector without interacting giving missing energy and momentum. This type of signature is part of most search channels which have been used by experiments to look for R_p-conserving SUSY.

However when R_p is violated the following can happen:

- single sparticles can be produced;
- the LSP can decay to Standard Model particles;
- the LSP can be any SUSY particle and need not be neutral;
- either lepton or baryon number is violated.

This leads to different approaches for searching for the experimental signatures of these models. In particular as the LSP can decay, depending on the $\not{R}_p$ couplings, inside the detector the standard missing energy and momentum signatures of the MSSM no longer exist. In general there have been two types of studies of these models: the first has studied the production of sparticle pairs by R_p-conserving processes followed by $\not{R}_p$ decays, usually of the LSP; the second has studied the possibility of single sparticle production via $\not{R}_p$ processes.

There has been a great deal of interest in these models in recent years motivated by the possible explanations of various experimental discrepancies, *e.g.* [32–40]. It has become clear that if we are to explore all possible channels for the discovery of supersymmetry then $\not{R}_p$ models must be investigated. Recent reviews of R-parity violating models can be found in [41]. We will now briefly discuss the phenomenology of these two different scenarios and review the studies which have been made.

1.3.1 Sparticle Pair Production

In this case the sparticles are produced by MSSM processes, hence the production cross sections only depend on the parameters of the MSSM. There are a number of possible scenarios depending on the size of the $\not{R}_p$ couplings and the lifetime of the lightest supersymmetric particle:

- For large values of the $\not{R}_p$ couplings it is possible that particles other than the LSP will have significant branching ratios for $\not{R}_p$ decay modes.
- For small values of the $\not{R}_p$ couplings the main effect is the decay of the LSP. The experimental situation will depend on the lifetime of the LSP:
  1. If the lifetime of the LSP is such that it is stable on collider time scales it can escape the detector before it decays. The experimental search strategy depends on the nature of the LSP. If it is the lightest neutralino the searches are identical to those for the MSSM. However if the LSP is charged it can be also be detected. In this case, it would look like a muon in the detector apart from losing energy due to ionization at a different rate, due to the different mass. There have been a number of searches for these heavy stable charged particles [42].
  2. The LSP lifetime can be such that while it decays inside the detector it can travel a significant distance away from the primary interaction point before decaying. There has been little study of this case.
  3. If the LSP lifetime is sufficiently short it will decay at the primary interaction point. This is the case which has been most studied.

The signatures in the case where the LSP decays inside the detector depend on whether lepton or baryon number is violated and we will briefly consider both of these cases:

- If lepton number is violated the typical experimental signature now involves large numbers of high transverse momentum leptons in the final state which can be easily detected by collider experiments. In some ways more information can potentially be extracted in these models experimentally. As the decay products of the LSP can be detected it is possible that the LSP mass can be reconstructed. This is impossible in the MSSM because the LSP escapes the detector.

  There have been a number of searches for these processes by both the LEP [43–52] and Tevatron [53,54] experiments, and studies of the range of parameters which can be discovered by the LHC [55].

- If, however, baryon number is violated the situation is much worse and this is considered a potential "worst case" scenario for the discovery of SUSY. In this case instead of the clean missing transverse momentum signatures of the MSSM the LSP will decay giving jets of hadrons. Extracting this signal of SUSY from the QCD backgrounds in hadron colliders will prove to be a challenging experimental problem. These models have been much less studied experimentally.

1.3.2 Single Sparticle Production

There have been many theoretical and experimental studies of single sparticle production. The cross sections for these processes depend on the $\not{R}_p$ couplings, in addition to the parameters of the MSSM. The kinematic reach of these processes is typically twice that of sparticle pair production. While there have been some studies of non-resonant sparticle production [56] most of the studies have been of resonant sparticle production.

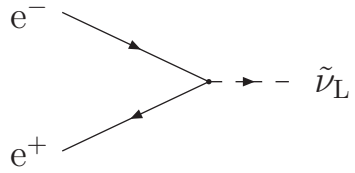

(a) Resonant sneutrino production in e^+e^- collisions.

(b) Resonant squark production in electron-proton collisions.

(c) Resonant slepton production in hadron–hadron collisions.

(d) Resonant squark production in hadron–hadron collisions.

Figure 1.4: Different possible resonant sparticle production mechanisms. While the produced sparticles can be of any generation the incoming particles will usually be first generation.

The terms in Eqn. 1.63 lead to different resonant production mechanisms in various collider experiments, which are shown in Fig. 1.4. The first term leads to resonant sneutrino production in e^+e^- collisions [57–62], Fig. 1.4a. The second term gives both resonant squark production in ep collisions [37, 38, 40, 63, 64], Fig. 1.4b, and resonant slepton production in hadron–hadron collisions [5, 6, 65–68], Fig. 1.4c. The third term gives resonant squark production in hadron–hadron collisions [5, 65, 69–72], Fig. 1.4d.

In general the search strategies depend on the decay modes of the sparticle. Most of the studies have concentrated on the $\not{R}_p$ decay modes of the resonant sparticles, although there have also been a number of studies of the gauge decay modes in various collider experiments.

1.4 Summary

In this chapter we have introduced the concept of supersymmetry and the theoretical reasons for favouring it as a possible extension of the Standard Model. We then argued that models in which R_p is conserved are no better motivated than those in which R-parity is violated and therefore both should be studied if we are to discover supersymmetry.

Despite the interest in $\not{R}_p$ SUSY models, and the potential experimental problems, there have been few experimental studies particularly at hadron colliders. The first systematic study of $\not{R}_p$ signatures at hadron colliders was presented in [73]. More recent overviews of the search potential at the LHC and Run II of the Tevatron have been presented in [5, 74]. These studies have been limited by the fact that few simulations have been available. In hadron–hadron collisions the only available Monte Carlo event generator is ISAJET [75] where the $\not{R}_p$ decays can be implemented using the `FORCE` command, *i.e.* the decay mode of a given particle, *e.g.* the LSP, can be specified by hand. However there has been no simulation which includes all the decay modes and the single sparticle production processes.

We shall therefore present in this thesis the calculations required to produce a simulation of the $\not{R}_p$ processes and decays together with some results from these simulations looking at the possibility of detecting $\not{R}_p$ SUSY processes. We also look at the latest experimental anomaly which can be explained by $\not{R}_p$ SUSY.

We present in Chapter 2 an introduction to the techniques of parton-shower Monte Carlo simulations followed by the calculations required to apply these techniques to $\not{R}_p$ SUSY.

Chapter 3 then uses these simulations to look at the production of resonant sleptons via $\not{R}_p$ SUSY in hadron–hadron colliders and some ways of detecting these processes.

Chapter 4 considers a possible $\not{R}_p$ SUSY explanation of the results of the KARMEN experiment.

Chapter 2

Monte Carlo Simulations

2.1 Introduction

If we wish to examine the experimental signatures of any model of beyond the Standard Model physics we need a Monte Carlo event generator which includes the processes predicted by that model. This is particularly important in experimental studies so that the effects of the cuts applied and the resolution of the detector can be included. There is currently only one Monte Carlo event generator, ISAJET [75], which can simulate $\not{R}_p$ processes in hadron–hadron collisions. However these processes are only included in an ad-hoc way via the `FORCE` command which allows the decay modes of a given particle, for example the LSP, to be specified by hand. It does not contain any hard resonant $\not{R}_p$ production processes or a calculation of the $\not{R}_p$ decay rates. If we wish to study these processes, in particular resonant sparticle production, we must add these processes to a Monte Carlo event generator. This chapter will start by discussing the physics used in Monte Carlo simulations and then go on to show how $\not{R}_p$ processes can be added.

In principle it should be possible to calculate all the observables measured experimentally using perturbative QCD, or the electroweak theory if they do not involve particles which interact via the strong force. There are however two problems with this approach:

1. In practice most observables have been calculated to at most next-to-leading order in perturbative QCD. A few inclusive observables have been calculated to higher orders, *e.g.* the cross section for $e^+e^- \to$ hadrons. Given the complexity of QCD calculations beyond leading order it is unlikely that many higher orders will be calculated in the near future. Even the calculation of final states including more partons is very difficult, *e.g.* the first general next-to-leading order calculation of three-jet observables in e^+e^- collisions [76] was performed in 1980, while it is only recently that the four-jet calculations [77] were completed.

2. An experiment observes hadrons not the quarks and gluons of a perturbative QCD calculation. It is currently impossible to calculate the hadronization process in QCD and we must use various phenomenological models with adjustable parameters which are fitted to data.

The idea of the Monte Carlo procedure is to provide a full description of the events which are seen in modern particle physics experiments. To do this we need some way of

starting with a given hard process and obtaining the hadrons which are observed by the detector as a result of that process. This is done by considering the regions of phase space where the emission of QCD radiation is enhanced and taking these into account to all orders in perturbation theory. This leads to the idea of a parton shower where we take a parton at some high scale and then evolve this down to a lower scale with the emission of QCD radiation. Finally at some low scale typical of the hadronization process we resort to a non-perturbative model for the hadronization process to give the observed hadrons.

In general the Monte Carlo event generation process can be divided into main three phases:

1. The hard process where the particles in the hard collision and their momenta are generated, usually according to the leading-order matrix element. This can be of either the incoming fundamental particles in lepton collisions or of a parton extracted from a hadron in hadron-initiated processes. In the example event shown in Fig. 2.1 the hard process is $e^+e^- \to q\bar{q}$.

2. The parton-shower phase where the coloured particles in the event are perturbatively evolved from the hard scale of the collision to the infrared cut-off. This is done for both the particles produced in the collision, the final-state shower, and the initial partons involved in the collision for processes with incoming hadrons, the initial-state shower. This is shown by the gluon radiation in Fig. 2.1. The emission of electromagnetic radiation from charged particles can be handled in the same way.

3. A hadronization phase in which the partons left after the perturbative evolution are formed into the observed hadrons. For processes with hadrons in the initial state after the removal of the partons in the hard process we are left with a hadron remnant. This remnant is also formed into hadrons by the hadronization model. In the example shown in Fig. 2.1 the cluster model, which is used in HERWIG, is shown.

There are usually two additional stages, one between the parton-shower and hadronization phases and the other after the hadronization phase, which are conceptually less important but are necessary for a full simulation of a hard collision process. In these phases those particles which are produced, but are unstable, decay. These secondary decays are handled in different ways depending on whether the particle decays before or after hadronization:[1]

1. Those particles which decay before hadronizing, *e.g.* the top quark, are decayed before the hadronization phase. Any coloured particles produced in these decays are then evolved by the parton-shower algorithm. The hadronization phase occurs after all such particles have been decayed. These decays are usually performed according to a calculated branching ratio and often, *e.g.* in top decay, use a matrix element to give the momenta of the decay products.

2. Those unstable hadrons which are produced in the hadronization phase must also be decayed. These decays are usually performed using the experimentally measured branching ratios and a phase-space distribution for the momenta of the decay

[1] The stage at which the various secondary decays occur is different in the different event generators and the procedure we discuss here is that adopted in the HERWIG Monte Carlo event generator.

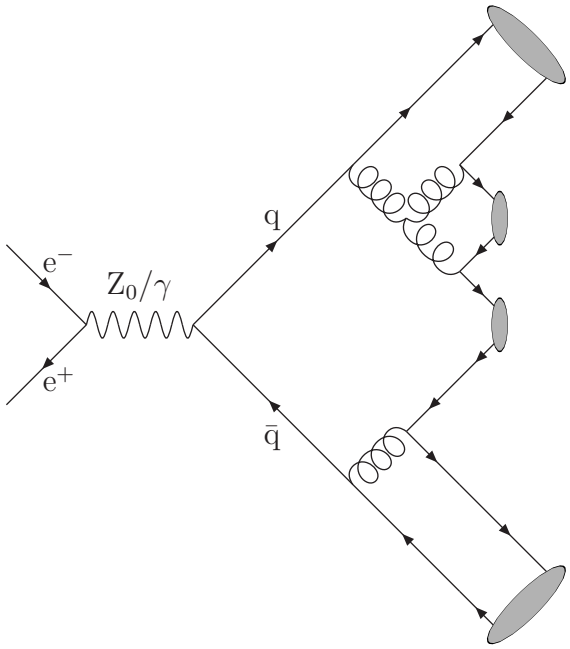

Figure 2.1: Example of a Monte Carlo event.

products. It is at this stage that those unstable fundamental particles which are not coloured, and hence do not hadronize, are decayed. For example the W and Z boson decays occur at this stage of the event generation process, however the decays of the colourless SUSY particles are handled by the previous secondary decay stage because unstable coloured sparticles are often produced in these decays. Any coloured particles produced in these decays are then evolved according to the parton-shower algorithm and hadronized. This procedure is repeated until all the unstable particles have been decayed.

We will describe the three main phases in some detail, concentrating on those used in the HERWIG event generator [2] but mentioning the other available approaches. We then study the extension of these simulations to include $\not{R}_p$ hard processes and decays.

2.2 Hard Processes

The first stage of the Monte Carlo event generator is to generate the momenta of the particles involved in the hard process. Usually these momenta are generated according to the leading-order cross section. As we will mainly be dealing with hadron–hadron collisions we will look at the procedure here in more detail.

The cross section, for example, for a two-to-two process in hadron–hadron collisions is given by

$$\sigma = \int_0^1 dx_1 \int_0^1 dx_2 \int_{-1}^1 d\cos\theta \int_0^{2\pi} d\phi \sum_{ij} \frac{d\hat{\sigma}_{ij}}{d\Omega}\left(\hat{s},\theta,\phi,\mu^2\right) f_i(x_1,\mu^2) f_j(x_2,\mu^2), \qquad (2.1)$$

where $\frac{d\hat{\sigma}_{ij}}{d\Omega}(\hat{s},\theta,\phi,\mu^2)$ is the differential cross section for the partons i and j to go to whatever final state we are interested in and $f_i(x,\mu^2)$ is the parton distribution function, *i.e.* the probability of finding a parton i with a fraction x of the incoming hadron's momentum. The parton distributions are also dependent on the factorization scale, μ. Partons which are emitted from those partons involved in the hard collision and have transverse momenta below this scale are treated as part of the hadron structure whereas those with momenta above this scale are part of the hard collision process. In principle the cross section should not depend on this scale. If we only perform the calculation to leading order however there can be a sizable factorization-scale dependence. This dependence is usually reduced if higher-order corrections are included. The cross-section integral can then be performed using the Monte Carlo method.

The Monte Carlo procedure is based on the following result. For a simple one-dimensional integral,

$$\int_{x_1}^{x_2} f(x)dx = (x_2 - x_1)\langle f(x)\rangle. \tag{2.2}$$

The average, $\langle f(x)\rangle$, can be approximated by calculating $f(x)$ at N randomly chosen points, in the interval (x_1, x_2), *i.e.*

$$\langle f(x)\rangle \simeq \frac{1}{N}\sum_{i=1}^{N} f(x_i) = \overline{f_N}, \tag{2.3}$$

giving an estimate, $\overline{f_N}$, of the average. This method is particularly useful as we can also calculate an error on the estimate by computing the standard deviation and applying the central limit theorem

$$\langle f(x)\rangle = \overline{f_N} \pm \frac{\sigma_N}{\sqrt{N}}, \tag{2.4}$$

where $\sigma_N = \sqrt{\overline{f_N^2} - \overline{f_N}^2}$ and $\overline{f_N^2} = \frac{1}{N}\sum_{i=1}^{N} f^2(x_i)$.

The convergence of this method for numerically evaluating the integral goes as $1/\sqrt{N}$ with the number of function evaluations, N. This is slower than other commonly used techniques for numerical integration, *e.g.* the trapezium rule converges as $1/N^2$ and Simpson's rule as $1/N^4$. While the convergence of these other methods becomes far slower for higher dimensional integrals, *e.g.* the trapezium rule converges as $1/N^{2/d}$ and Simpson's rule as $1/N^{4/d}$ where d is the dimension of the integral, the Monte Carlo method will always converge as $1/\sqrt{N}$.

Hence for the performance of high-dimensional integrals the Monte Carlo technique is more efficient. This is particularly important in particle physics where we need to perform high dimensional phase-space integrals. The Monte Carlo procedure is also well suited to integrating over complex regions, which are difficult with other methods, and often occur in particle physics, *e.g.* due to experimental cuts. Another advantage of this method is that we can evaluate a number of different quantities, *e.g.* differential distributions, at

the same time whereas with other methods each distribution would have to be calculated separately.

The convergence of the Monte Carlo technique can be improved by reducing the standard deviation, σ_N. In principle if the integral can be performed analytically a Jacobian transform can be used to reduce the standard deviation to zero. In practice we can use a simple function which approximates the shape of the function we are integrating to improve the convergence of the integral, thus considerably reducing the time required for the numerical computation of the integral.

In the cross sections for the $\not{R}_{\rm p}$ processes we are studying there are Breit-Wigner resonances. These lead to a large variance in the calculation of the cross section, which can be improved by applying a Jacobian transformation. First we consider the case of only one resonance. The cross section can be rewritten as

$$\sigma = \int_{\tau_0}^{1} d\tau \int_{\tau}^{1} \frac{dx_1}{x_1} \int_{-1}^{1} d\cos\theta \int_{0}^{2\pi} d\phi \sum_{ij} \frac{d\hat{\sigma}_{ij}}{d\Omega}\left(\hat{s},\theta,\phi,\mu^2\right) f_i(x_1,\mu^2) f_j\left(\frac{\tau}{x_1},\mu^2\right), \tag{2.5}$$

where $\tau = x_1 x_2$, $\tau_0 = (m_3+m_4)^2/s$, s is the hadron–hadron centre-of-mass energy squared, and m_3 and m_4 are the masses of the final-state particles. The parton-level centre-of-mass energy squared is given by $\hat{s} = \tau s$. The form of the Breit-Wigner peak in the cross section is

$$\frac{d\hat{\sigma}_{ij}}{d\Omega}\left(\hat{s},\theta,\phi,\mu^2\right) \sim \frac{1}{\left(\hat{s}-M^2\right)^2 + \Gamma^2 M^2}, \tag{2.6}$$

where M is the mass of the resonant particle and Γ is its width. We can perform a change of variables

$$\tau = \tau_M + \sqrt{\tau_M \tau_\Gamma}\tan\left(\rho\sqrt{\tau_M\tau_\Gamma}\right), \tag{2.7}$$

where $\tau_M = M^2/s$ and $\tau_\Gamma = \Gamma^2/s$. This gives an integral over ρ,

$$\begin{aligned} \sigma \;=\; & \int_{\rho_0}^{\rho_1} d\rho \int_{\tau}^{1} \frac{dx_1}{x_1} \int_{-1}^{1} d\cos\theta \int_{0}^{2\pi} d\phi \\ & \left[\tau_M\tau_\Gamma + (\tau-\tau_M)^2\right] \sum_{ij} \frac{d\hat{\sigma}_{ij}}{d\Omega}\left(\hat{s},\theta,\phi,\mu^2\right) f_i(x_1,\mu^2) f_j\left(\frac{\tau}{x_1},\mu^2\right), \end{aligned} \tag{2.8}$$

where

$$\rho_0 \;=\; \frac{1}{\sqrt{\tau_M\tau_\Gamma}}\tan^{-1}\left(\frac{\tau_0-\tau_M}{\sqrt{\tau_M\tau_\Gamma}}\right), \tag{2.9a}$$

$$\rho_1 \;=\; \frac{1}{\sqrt{\tau_M\tau_\Gamma}}\tan^{-1}\left(\frac{1-\tau_M}{\sqrt{\tau_M\tau_\Gamma}}\right). \tag{2.9b}$$

If the only dependence of the cross section on $\hat{s}$ was the Breit-Wigner resonance the ρ integral would be the integral of a constant, *i.e.* the variance would be zero. In practice there is some remaining $\hat{s}$ dependence in the integrand but this is far smoother than the

Breit-Wigner resonance and hence the variance is dramatically reduced.

In the $\not{R}_p$ cross sections there can be more than one accessible resonance depending on the number of non-zero $\not{R}_p$ couplings. In this case we can use a multi-channel Monte Carlo integration technique. The cross section can be rewritten in the following way

$$\begin{aligned}\sigma &= \int_{\tau_0}^{1} d\tau \int_{\tau}^{1} \frac{dx_1}{x_1} \int_{-1}^{1} d\cos\theta \int_{0}^{2\pi} d\phi \sum_{k}^{N} \frac{W_k}{F(\tau)\left[(\hat{s}-M_k^2)^2+\Gamma_k^2 M_k^2\right]} \\ &\quad \sum_{ij} \frac{d\hat{\sigma}_{ij}}{d\Omega}(\hat{s},\theta,\phi,\mu^2)\; f_i(x_1,\mu^2) f_j\left(\frac{\tau}{x_1},\mu^2\right),\end{aligned} \tag{2.10}$$

where

$$F(\tau) = \sum_{i}^{N} \frac{W_i}{(\hat{s}-M_i^2)^2+\Gamma_i^2 M_i^2}, \tag{2.11}$$

and M_i and Γ_i are the mass and width of the ith resonance. The weight, W_i, is chosen to approximate the contribution of the ith resonance to the total cross section. We can perform a Jacobian transform for these integrals treating each of the terms in the sum as we did before for the single resonance. This allows us to perform a change of variables for each of the integrals in the sum

$$\tau = \tau_M^k + \sqrt{\tau_M^k \tau_\Gamma^k}\tan\left(\rho_k \sqrt{\tau_M^k \tau_\Gamma^k}\right), \tag{2.12}$$

where $\tau_M^k = M_k^2/s$ and $\tau_\Gamma^k = \Gamma_k^2/s$. This gives a set of integrals over the new variables ρ_k,

$$\sigma = \int_{-1}^{1} d\cos\theta \int_{0}^{2\pi} d\phi \sum_{k}^{N} \int_{\rho_0^k}^{\rho_1^k} d\rho_k \frac{W_k}{F(\tau)} \frac{1}{s^2} \int_{\tau}^{1} \frac{dx_1}{x_1} \sum_{ij} \frac{d\hat{\sigma}_{ij}(\hat{s})}{d\Omega} f_i(x_1,\mu^2) f_j\left(\frac{\tau}{x_1},\mu^2\right), \tag{2.13}$$

where

$$\rho_0^k = \frac{1}{\sqrt{\tau_M^k \tau_\Gamma^k}} \tan^{-1}\left(\frac{\tau_0 - \tau_M^k}{\sqrt{\tau_M^k \tau_\Gamma^k}}\right), \tag{2.14a}$$

$$\rho_1^k = \frac{1}{\sqrt{\tau_M^k \tau_\Gamma^k}} \tan^{-1}\left(\frac{1 - \tau_M^k}{\sqrt{\tau_M^k \tau_\Gamma^k}}\right). \tag{2.14b}$$

The use of this technique significantly increases the efficiency of the Monte Carlo simulation. Each different hard collision process must be studied separately and a Jacobian transformation applied to reduce the variance. In, for example, QCD jet and heavy quark production the cross section falls like p_T^{-4}, where p_T is the transverse momentum of the partons produced in the hard collision, and we must therefore use a Jacobian transform to smooth this fall-off. In other processes, for example Drell-Yan, a multi-channel approach

must be used because in addition to a power law fall-off, like $\hat{s}^{-2}$, of the cross section due to photon exchange there is a Breit-Wigner resonance due to Z exchange.

We can then use the parton-level centre-of-mass energy and angles which we randomly generate while performing the cross-section integral to construct the four-momenta of the particles involved in the hard collision. In the next section we will describe how these particles can be evolved from the high scale of the parton–parton collision to some low scale typical of the hadronization process.

2.3 Parton Showers

In the previous section we described how to generate the momenta of the particles involved in the hard scattering process. This scattering process usually involves coloured particles in either the initial or final state. After the hard collision these coloured particles must be evolved from the high-energy scale of the collision to some lower scale with the emission of QCD radiation. The exact calculation of the matrix elements for processes with large numbers of final-state partons is not possible and we must therefore treat the regions of phase space for which the emission of QCD radiation is enhanced and take these into account to all orders in perturbation theory. There are two regions of phase space where the emission of QCD radiation is enhanced:

1. Collinear Emission;

2. Soft Emission.

This can be seen by considering the process $\mathrm{e^+e^-} \to \mathrm{q(p_1)\bar{q}(p_2)g(p_3)}$, shown in Fig. 2.2b. The leading-order cross section for this process is given by [78]

$$\sigma_{q\bar{q}g} = N_c \sigma_0 \sum_q Q_q^2 \int dx_1 dx_2 C_F \frac{\alpha_s}{2\pi} \frac{x_1^2 + x_2^2}{(1-x_1)(1-x_2)}, \tag{2.15}$$

where $\sigma_0 = 4\pi\alpha^2/(3s)$ is the leading-order cross section for $\mathrm{e^+e^-} \to \mu^+\mu^-$. The energy of the final-state partons in the laboratory frame is E_i, and $x_i = 2E_i/\sqrt{s}$, where $\sqrt{s}$ is the centre-of-mass energy of the $\mathrm{e^+e^-}$ collision. Momentum conservation therefore leads to $x_1 + x_2 + x_3 = 2$. $C_F = (N_c^2 - 1)/(2N_c)$ is the Casimir in the fundamental representation, where N_c is the number of colours. If we look at Eqn. 2.15 the cross section diverges when either x_1, x_2, or both tend to one. We can now consider the physical origins of these divergences:

1. $(1 - x_1) = \frac{E_2 E_3}{Q^2}(1 - \cos\theta_{2g})$, where θ_{2g} is the angle between the antiquark and the gluon. The singularity as $x_1 \to 1$ therefore occurs as the antiquark and the gluon become collinear. Similarly the singularity as $x_2 \to 1$ occurs as the quark and the gluon become collinear. This is the collinear singularity.

2. As $x_1 \to 1$ and $x_2 \to 1$ energy conservation implies that $x_3 \to 0$, *i.e.* the energy of the gluon tends to zero. This is the soft singularity.

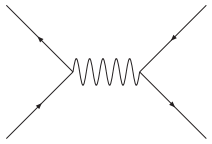

(a) Leading-order diagram.

(b) Real emission diagrams.

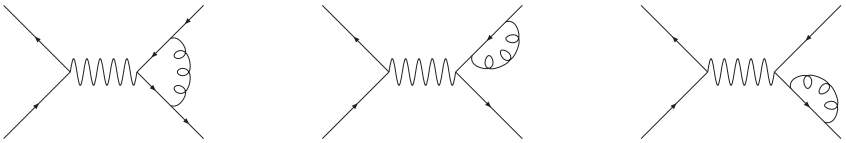

(c) Loop diagrams.

Figure 2.2: Feynman diagrams for $e^+e^- \to$ hadrons at next-to-leading order in α_s.

If we were to perform the full next-to-leading-order calculation of the cross section for $e^+e^- \to$ hadrons these singularities would cancel with the singularities that occur in the loop diagrams. The real emission diagrams in Fig. 2.2b give a contribution to the cross section which is of order α_s, Eqn. 2.15. The product of the loop diagrams, Fig. 2.2c, and the leading-order diagram, Fig. 2.2a, also gives a contribution of the same order in α_s, and the singularities in this term exactly cancel those in the real emission diagrams.

However for less inclusive observables, *e.g.* the thrust in e^+e^- events, it can be the case that after this cancellation large logarithms remain. The aim of the parton-shower phase is to resum these logarithms to all orders in perturbation theory. In general the simplest algorithm for the parton shower only resums the leading collinear logarithms [79] whereas with a slight modification [80, 81] both the leading soft and collinear logarithms are resummed. We will first describe how the collinear logarithms can be resummed and then generalize this to include the soft logarithms as well. Good reviews of the parton-shower algorithm can be found in [12, 79].

2.3.1 Collinear Parton Showers

We will start by considering the simplest type of process, *i.e.* the emission of a collinear gluon by a final-state quark. The matrix element for the radiation of an additional gluon

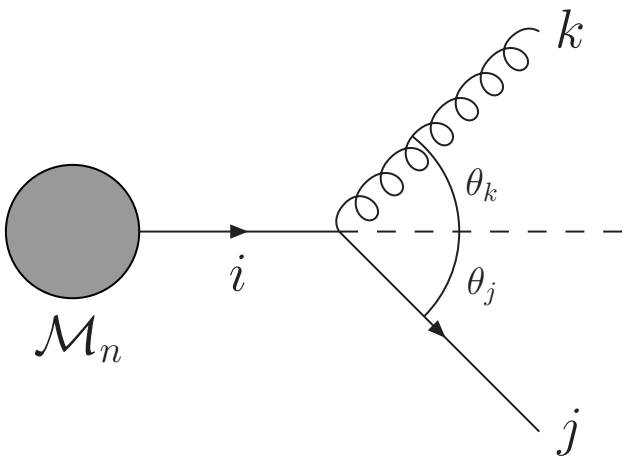

Figure 2.3: Radiation of a collinear gluon k by a quark i giving the quark j.

from a final-state quark, Fig. 2.3, can be written as

$$\mathcal{M}_{n+1} = \frac{g_s}{t}\mathbf{t}^a \bar{u}(p_j)\gamma^\mu \not{p}_i \mathcal{M}'_n \varepsilon^*_\mu, \tag{2.16}$$

where $\mathbf{t}^a$ is the colour generator of $SU(3)$ in the fundamental representation, p_i is the momentum of the quark before the gluon is radiated, p_j is the momentum of the quark after the gluon radiation, p_k is the momentum of the radiated gluon, ε_μ is the polarization vector of the gluon and $\mathcal{M}'_n$ represents the matrix element, without the spinor for the quark i, before the gluon radiation. The initial quark i is off mass-shell, $t = p_i^2$, while both the gluon and the quark after the branching are on mass-shell. We will assume that the quarks are massless.

We can square this matrix element and sum over the final-state spins giving,

$$\sum_{\text{spins}} |\mathcal{M}_{n+1}| = \frac{g_s^2 C_F}{2t^2}\text{tr}\left(\mathcal{M}'^{\,\dagger}_n \not{p}_i\gamma_\nu\not{p}_j\gamma_\mu\not{p}_i\mathcal{M}'_n\right)\left(-g^{\mu\nu} + \frac{p_k^\mu l^\nu + p_k^\nu l^\mu}{p_k\cdot l}\right), \tag{2.17}$$

where we have used an axial gauge for the gluon propagator. The four-vector l^μ is an arbitrary light-like four-vector which must not be collinear with any of the momenta.

We can evaluate this expression in the collinear limit. The traces in this expression can be treated individually. The first term gives

$$\begin{aligned} -\,\text{tr}\left(\mathcal{M}'^{\,\dagger}_n \not{p}_i\gamma_\nu\not{p}_j\gamma_\mu\not{p}_i\mathcal{M}'_n\right) g^{\mu\nu} &= 2\,\text{tr}\left(\mathcal{M}'^{\,\dagger}_n \not{p}_i\not{p}_j\not{p}_i\mathcal{M}'_n\right), \\ &= 2\,\text{tr}\left(\mathcal{M}'^{\,\dagger}_n \not{p}_k\not{p}_j\not{p}_k\mathcal{M}'_n\right), \end{aligned} \tag{2.18}$$

where the first line comes from the properties of the Dirac matrices and the second line from momentum conservation, *i.e.* $p_i = p_j + p_k$, and $p_j^2 = 0$. As the gluon is on mass-shell, *i.e.* $p_k^2 = 0$, we can make use of the following identity,

$$\not{p}_k = \sum_{\text{spins}} u_s(p_k)\bar{u}_s(p_k), \tag{2.19}$$

giving

$$-\mathrm{tr}\left(\mathcal{M}_n'^{\dagger}\not{p}_i\gamma_\nu\not{p}_j\gamma_\mu\not{p}_i\mathcal{M}_n'\right)g^{\mu\nu} = 8p_j\cdot p_k\,\mathrm{tr}(\mathcal{M}_n'^{\dagger}\not{p}_k\mathcal{M}_n'). \tag{2.20}$$

Finally p_k can be replaced by $p_k = (1-z)p_i$ in the collinear limit, where $z = E_j/E_i$ is the fraction of the initial quark i's energy carried by the quark j after the gluon emission, giving

$$-\mathrm{tr}\left(\mathcal{M}_n^{\dagger}\not{p}_i\gamma_\nu\not{p}_j\gamma_\mu\not{p}_i\mathcal{M}_n\right)g^{\mu\nu} = 4t(1-z)\sum_{\text{spins}}|\mathcal{M}_n|^2, \tag{2.21}$$

where $\mathcal{M}_n$ is the full matrix element for the process before the emission of the collinear gluon. The remaining terms can be calculated in the same way giving

$$\sum_{\text{spins}}|\mathcal{M}_{n+1}|^2 = \frac{2g_s^2}{t}\,C_F\frac{1+z^2}{1-z}\sum_{\text{spins}}|\mathcal{M}_n|^2. \tag{2.22}$$

The matrix element squared for the emission of a collinear gluon *factorizes* into the matrix element squared for the process without the collinear gluon and a universal, *i.e.* process independent, Altarelli-Parisi splitting function [82] for the radiation of a gluon from a quark, *i.e.*

$$P_{qq} = C_F\frac{1+z^2}{1-z}. \tag{2.23}$$

In general, if we consider a process involving n partons the amplitude squared for a process with the emission of an extra collinear parton can be written in terms of the matrix element for the n parton process and a universal splitting function

$$\sum_{\text{spins}}|\mathcal{M}_{n+1}|^2 = \frac{2g_s^2}{t}P_{ji}(z)\sum_{\text{spins}}|\mathcal{M}_n|^2, \tag{2.24}$$

where P_{ji} are the unregularized Altarelli-Parisi splitting functions. P_{qq} is given above for gluon radiation from a quark and

$$P_{gg} = \quad C_A\left[\frac{1-z}{z}+\frac{z}{1-z}+z(1-z)\right], \tag{2.25}$$

$$P_{qg} = \qquad T_R\left[z^2+(1-z)^2\right], \tag{2.26}$$

for gluon radiation from a gluon and for a gluon splitting into a quark–antiquark pair, respectively. $T_R = \frac{1}{2}$ and $C_A = N_c$ is the Casimir in the adjoint representation of $SU(3)$. There is an additional splitting function, $P_{gq}(z)$, which describes the splitting of a quark to give a gluon with a fraction z of its energy. This splitting function can be obtained by making the replacement $z \to 1-z$ in Eqn. 2.23.

The phase space for this splitting also factorizes. The phase space for the n body

process before the gluon radiation is given by

$$d\Phi_n = d\Gamma \, \frac{d^3p_i}{2E_i(2\pi)^3}, \tag{2.27}$$

where $d\Gamma$ represents the phase-space integrals over all the particles apart from the quark i which radiates the gluon. The phase space for the process after the gluon radiation can be written as

$$d\Phi_{n+1} = d\Gamma \, \frac{d^3p_j}{2E_j(2\pi)^3} \, \frac{d^3p_k}{2E_k(2\pi)^3}. \tag{2.28}$$

As momentum is conserved, *i.e.* $p_i = p_j + p_k$, at fixed p_j this implies $d^3p_k = d^3p_i$. We therefore obtain

$$d\Phi_{n+1} = d\Phi_n \frac{1}{(1-z)} \, \frac{d^3p_j}{2E_j(2\pi)^3}, \tag{2.29}$$

using $E_k = (1-z)E_i$ in the collinear limit. The phase-space integral over the momentum of the quark j can be expanded in the small angle limit giving

$$\begin{aligned} d\Phi_{n+1} &= d\Phi_n \frac{1}{2(2\pi)^3} \frac{1}{(1-z)} E_j dE_j \theta_j d\theta_j d\phi, \\ &= d\Phi_n \frac{1}{2(2\pi)^3} \, E_j dE_j \, \theta_j d\theta_j \, d\phi dt \delta\left(t - \frac{E_j E_k \theta_j^2}{(1-z)^2}\right) \, \frac{dz}{(1-z)} \delta\left(z - \frac{E_j}{E_i}\right), \end{aligned} \tag{2.30}$$

where we have inserted the definitions of t and z, and θ_j is angle between the directions of the partons i and j as shown in Fig. 2.3. In the small angle limit

$$t = (p_j + p_k)^2 = 2E_jE_k(1 - \cos\theta) \simeq E_jE_k\theta^2, \tag{2.31}$$

where θ is the angle between j and k. Using transverse momentum conservation gives $z\theta_j = (1-z)\theta_k$. As $\theta = \theta_j + \theta_k$ we obtain $\theta = \theta_j/(1-z)$. Hence the virtual mass of the initial quark is

$$t \simeq \frac{E_jE_k\theta_j^2}{(1-z)^2}. \tag{2.32}$$

We can now use the δ-functions in Eqn. 2.30 to integrate out the dependence on the energy of the quark, E_j, and its angle, θ_j, giving

$$d\Phi_{n+1} = d\Phi_n \frac{1}{4(2\pi)^3} \, d\phi \, dt \, dz. \tag{2.33}$$

Therefore, using the equations for the collinear factorization of the matrix element,

Eqn. 2.24, and for the phase space, Eqn. 2.33, we obtain

$$d\sigma_{n+1} = d\sigma_n \frac{dt}{t}\, dz \frac{\alpha_s}{2\pi} P_{ji}(z), \tag{2.34}$$

where we have averaged over the azimuthal angle of the emitted parton. The same equation also holds for the radiation of a gluon from an incoming parton in processes involving hadrons in the initial state [12].

So for the emission of QCD radiation in the collinear limit, after azimuthal averaging, the cross section obeys a factorization theorem. The cross section for a process in which one parton pair is much more collinear than any other pair can be written as the convolution of a universal splitting function and the cross section for the same process where the collinear pair is replaced by a single parton of the corresponding flavour. This functional form allows us to apply the procedure to the next most collinear pair in the final state, and so on. We thus have an iterative rule which leads to a description of multi-parton final states as a Markov chain.

This can be reexpressed as an evolution in some energy-like scale, such as the virtuality, where a parton at a high scale is evolved by successive branchings to a lower scale. The normal approach [12] is to consider the evolution of the parton density, $f_i(x,t)$, *i.e.* the probability of finding a parton of type i with a given fraction x of the momentum of an incoming hadron at a given scale t. As we will mainly be dealing with partons in the final state we will instead consider the evolution of the fragmentation function, $d_i^h(x,t)$, *i.e.* the probability of a parton of type i giving a hadron of type h with a fraction x of the parton's momentum at a given scale t.

We can use Eqn. 2.34 to write the evolution of the fragmentation function at a given virtual mass-squared and momentum fraction, $d(x,t)$. For simplicity we will only consider one type of branching, *i.e.* the radiation of a gluon by a quark, and one type of hadron, but the results generalize easily.

The change in the fragmentation function consists of two parts: firstly there is an increase due to partons branching to give a parton with a momentum fraction greater than x,

$$\begin{aligned} \delta d(x,t)_{\text{in}} &= \frac{\delta t}{t} \int_x^1 dx' dz \frac{\alpha_s}{2\pi} P(z) d(x',t) \delta(x - zx'), \\ &= \frac{\delta t}{t} \int_0^1 \frac{dz}{z} \frac{\alpha_s}{2\pi} P(z) d(x/z,t); \end{aligned} \tag{2.35}$$

secondly there is a decrease due to partons radiating to give partons with momentum fractions smaller than x,

$$\begin{aligned} \delta d(x,t)_{\text{out}} &= \frac{\delta t}{t} d(x,t) \int_0^x dx' dz \frac{\alpha_s}{2\pi} P(z) \delta(x' - zx), \\ &= \frac{\delta t}{t} d(x,t) \int_0^1 dz \frac{\alpha_s}{2\pi} P(z). \end{aligned} \tag{2.36}$$

The fragmentation function, $d(x,t)$, is zero for $x > 1$ and therefore the integral in Eqn. 2.35

is zero for $z < x$. Hence the evolution of the fragmentation function with the virtual mass-squared is given by

$$\frac{\partial}{\partial t} d(x,t) = \frac{1}{t} \int_0^1 dz \frac{\alpha_s}{2\pi} P(z) \left[\frac{1}{z} d(x/z,t) - d(x,t) \right]. \tag{2.37}$$

In the standard treatment of the evolution of the fragmentation function, or the parton distribution function, we would now regulate the Altarelli-Parisi splitting functions to obtain the DGLAP equation [82] for the evolution of the fragmentation function. However, it is more convenient for us to continue to work with the unregulated splitting functions and to reexpress the evolution equation in a more useful way using the Sudakov form factor [83] which we will regularize below. The Sudakov form factor is given by

$$\Delta(t) = \exp\left[- \int_{t_0}^t \frac{dt'}{t'} \int_0^1 dz \frac{\alpha_s}{2\pi} P(z) \right], \tag{2.38}$$

where t_0 is the low scale at which we stop the evolution of the fragmentation function. Using the Sudakov form factor we can rewrite Eqn. 2.37 in the following way

$$t \frac{\partial}{\partial t} \left(\frac{d}{\Delta} \right) = \frac{1}{\Delta} \int_0^1 \frac{dz}{z} \frac{\alpha_s}{2\pi} P(z) d(x/z,t). \tag{2.39}$$

This differential equation can be solved to give an integral equation for the fragmentation function, $d(x,t)$, in terms of its initial value, $d(x,t_0)$, at some low scale t_0,

$$d(x,t) = \Delta(t) d(x,t_0) + \int_{t_0}^t \frac{dt'}{t'} \frac{\Delta(t)}{\Delta(t')} \int_0^1 \frac{dz}{z} \frac{\alpha_s}{2\pi} P(z) d(x/z,t'). \tag{2.40}$$

This equation can be interpreted in the following way. The first term is the contribution from those partons which do not branch between the scales t and t_0. The second term is the contribution from partons which last branched at the scale t'. This suggests that we can interpret the ratio of Sudakov form factors, $\Delta(t)/\Delta(t')$, as the probability of evolving down from the scale t to t' without any branching. This is consistent with the first term in Eqn. 2.40 as $\Delta(t_0) = 1$. We can therefore interpret $\Delta(t)$ as the probability of no emission between the scales t and t_0.

The Sudakov form factor can be generalized to include more than one type of parton, by defining the Sudakov form factor for parton type i

$$\Delta_i(t) = \exp\left[- \sum_j \int_{t_0}^t \frac{dt'}{t'} \int_0^1 dz \frac{\alpha_s}{2\pi} P_{ji}(z) \right]. \tag{2.41}$$

The evolution equation for more than one type of parton can be written as

$$t \frac{\partial}{\partial t} \left(\frac{d_i}{\Delta_i} \right) = \frac{1}{\Delta_i} \sum_j \int_0^1 \frac{dz}{z} \frac{\alpha_s}{2\pi} P_{ij}(z) d_j(x/z,t). \tag{2.42}$$

There is however still a problem because the splitting functions, $P_{ij}(z)$, contain the collinear singularity as $z \to 1$ which needs to be regularized. We can do this by introducing an infrared cut-off, $z < 1 - \epsilon$. We then classify branchings above this cut-off as unresolvable. This means that the regularized Sudakov form factor,

$$\Delta_i(t) = \exp\left[-\sum_j \int_{t_0}^{t} \frac{dt'}{t'} \int_{\epsilon}^{1-\epsilon} dz \frac{\alpha_s}{2\pi} P_{ji}(z)\right], \tag{2.43}$$

gives the probability of evolving between two scales without resolvable emission. This implicitly resums the virtual contributions as well as the real emissions we have been considering to all orders. This is because the virtual contributions will affect the probability of no branching and are hence included by unitarity, *i.e.* because we have imposed

$$\mathrm{P}(\text{no resolvable emission}) + \mathrm{P}(\text{resolvable emission}) = 1. \tag{2.44}$$

This correctly resums the leading collinear singularities to all orders in perturbation theory [79]. The infrared cut-off can be chosen as a cut-off, t_0, on the virtuality of the parton i, by defining

$$\epsilon = \frac{t_0}{t}. \tag{2.45}$$

The value of t_0 used in simulations is typically of order 1 GeV^2.

In this section we have seen how we can resum the collinear singularities to all orders in perturbation theory using the Sudakov form factor. In the next section we will discuss how the soft singularities can be resummed as well.

2.3.2 Angular-ordered Parton Showers

We can consider the emission of QCD radiation in the soft limit in much the same way as we did for the collinear emission in Section 2.3.1. The matrix element for the emission of a gluon from an outgoing quark is given by

$$\mathcal{M}_{n+1} = \frac{g_s}{(p_i^2 - m^2)} \mathbf{t}^a_{\beta\alpha} C_\alpha \bar{u}_\beta(p_j) \gamma^\mu \left(\not{p}_i + m\right) \mathcal{M}_n \varepsilon^*_\mu, \tag{2.46}$$

where we are considering the splitting $i \to jk$ as in Fig. 2.3. C_α represents the colour structure of the leading-order process without the soft gluon and m is the mass of the quark. The quark has colour α before the emission of the gluon and colour β afterwards. As the gluon and the quark j, after the splitting, are on mass-shell we can rewrite the denominator as $p_i^2 - m^2 = 2p_j \cdot p_k$. We can then use the anti-commutation relations for the Dirac matrices to obtain

$$\mathcal{M}_{n+1} = \frac{g_s}{2p_j \cdot p_k} \mathbf{t}^a_{\beta\alpha} C_\alpha \bar{u}_\beta(p_j) \left[2p_i^\mu + (m - \not{p}_i)\gamma^\mu\right] \mathcal{M}_n \varepsilon^*_\mu. \tag{2.47}$$

Radiating Parton	Colour Matrix	
	incoming	outgoing
quark	$-\mathbf{t}^c_{\beta\alpha}$	$\mathbf{t}^c_{\alpha\beta}$
antiquark	$\mathbf{t}^c_{\alpha\beta}$	$-\mathbf{t}^c_{\beta\alpha}$
gluon	$-if^{abc}$	$-if^{abc}$

Table 2.1: Colour matrices for the eikonal current. As the eikonal current is independent of the spin of the emitting parton the colour factors for squarks are the same as those for quarks and those for gluinos the same as those for gluons. In the case of radiation from quarks the colour of the external parton is α and the colour of the parton in the hard process is β. Similarly for gluons the colour of the external parton is a and the colour of the gluon participating in the hard process is b. In both cases the colour of the radiated gluon is c. f^{abc} is the $SU(3)$ colour generator in the adjoint representation.

In the soft limit $p_i \approx p_j$ and we can therefore use the Dirac equation $\bar{u}(p_j)(\not{p}_j - m) = 0$ to give

$$\mathcal{M}_{n+1} = \frac{g_s p_j^\mu}{p_j \cdot p_k} \mathbf{t}^a_{\beta\alpha} C_\alpha \bar{u}_\beta(p_j) \mathcal{M}_n \varepsilon^*_\mu. \tag{2.48}$$

In general, a factorization theorem exists for the emission of QCD radiation in the soft limit. However, this theorem applies to the amplitude for the process, rather than the cross section. The amplitude for a process in which one gluon is much softer than the other energy scales in the process can be written as a product of a universal eikonal current and the amplitude for the same process without the soft gluon. The matrix element including the emission of an extra soft gluon is given by

$$\mathcal{M} = g_s \mathbf{m} \cdot \mathbf{J}(q), \tag{2.49}$$

where $\mathcal{M}$ is the matrix element for the process including the emission of an extra soft gluon, $\mathbf{m}$ is the tree-level amplitude for the underlying process and $\mathbf{J}(q)$ is the non-Abelian semi-classical current for the emission of the soft gluon with momentum q from the hard partons. In general the eikonal current $\mathbf{J}(q)$ is given by

$$\mathbf{J}(q) = \varepsilon^*_\mu \sum_{\substack{\text{external} \\ \text{partons}}} C^b_\alpha P^{ab}_\alpha \left(\frac{p_{\text{parton}}}{p_{\text{parton}} \cdot q} \right)^\mu \tag{2.50}$$

for the emission of a soft gluon with momentum q. C^b_α represents the colour structure of the leading-order process without the soft gluon and P^{ab}_α the colour matrix for the emission of a gluon with colour a. These colour matrices are given in Table 2.1 for the various possible radiating partons.

After we square the amplitude and sum over the spins of the external partons we

obtain a result which depends on the momenta of all the external partons. It therefore seems unlikely that we can recover a factorization theorem for the cross section as in the previous section. The surprising result [80, 81] is that, after azimuthal averaging, these effects can be incorporated into a collinear algorithm by simply using a different choice for the evolution scale, *i.e.* the opening angle.

We can illustrate this with a simple example, *i.e.* the process $\mathrm{e}^+\mathrm{e}^- \to \mathrm{q}\,\bar{\mathrm{q}}\,\mathrm{g}_1$, shown in Fig. 2.4. The semi-classical eikonal current can be used to study the emission of an extra soft gluon in this process, *i.e.* the process $\mathrm{e}^+\mathrm{e}^- \to \mathrm{q}\,\bar{\mathrm{q}}\,\mathrm{g}_1\,\mathrm{g}_2$ where the second gluon is much softer than the other partons. The matrix element including the emission of the extra soft gluon is given by

$$\mathcal{M}(k_1, k_2, p_1, p_2, p_3; q) = g_s \mathbf{m}(k_1, k_2, p_1, p_2, p_3) \cdot \mathbf{J}(q), \tag{2.51}$$

where

- $\mathbf{m}(k_1, k_2, p_1, p_2, p_3)$ is the tree-level amplitude for the underlying process, $\mathrm{e}^+(k_1)\,\mathrm{e}^-(k_2) \to \mathrm{q}(p_1)\,\bar{\mathrm{q}}(p_2)\,\mathrm{g}_1(p_3)$.
- $\mathcal{M}(k_1, k_2, p_1, p_2, p_3; q)$ is the matrix element for the process $\mathrm{e}^+(k_1)\,\mathrm{e}^-(k_2) \to \mathrm{q}(p_1)\,\bar{\mathrm{q}}(p_2)\,\mathrm{g}_1(p_3)\,\mathrm{g}_2(q)$, *i.e.* including the emission of an extra soft gluon, g_2, with momentum q.
- $\mathbf{J}(q)$ is the non-Abelian semi-classical current for the emission of the soft gluon with momentum q from the hard partons.

Explicitly in our example the current, $\mathbf{J}(q)$, is given by

$$\mathbf{J}(q) = \sum_{s=1,2} \mathbf{J}^{b,\mu}(q)\varepsilon^*_{\mu,s}, \tag{2.52}$$

where

$$\mathbf{J}^{b,\mu}(q) = \mathbf{t}^{b,\mathrm{q}}_{c_1 c_1'}\mathbf{t}^{a}_{c_1' c_2}\left(\frac{p_1^\mu}{p_1\cdot q}\right) - \mathbf{t}^{a}_{c_1 c_2'}\mathbf{t}^{b,\bar{\mathrm{q}}}_{c_2' c_2}\left(\frac{p_2^\mu}{p_2\cdot q}\right) - if^{aa'b}\mathbf{t}^{a'}_{c_1 c_2}\left(\frac{p_3^\mu}{p_3\cdot q}\right). \tag{2.53}$$

If we now define the radiation functions, as was done in [84], we can express the square of this current in a useful way. We can define the dipole radiation function

$$\frac{2}{\omega^2}W_{ij}(q) = -\left(\frac{p_i}{p_i\cdot q} - \frac{p_j}{p_j\cdot q}\right)^2 = \frac{2}{\omega^2}\left(\frac{\xi_{ij}}{\xi_i\xi_j} - \frac{1}{2\gamma_i^2\xi_i^2} - \frac{1}{2\gamma_j^2\xi_j^2}\right), \tag{2.54}$$

where ω is the energy of the soft gluon, $\xi_{ij} = \frac{p_i\cdot p_j}{E_iE_j} = 1 - v_iv_j\cos\theta_{ij}$, $\xi_i = 1 - v_i\cos\theta_i$, $\gamma_i = E_i/m_i = 1/\sqrt{(1-v_i^2)}$, v_i is the velocity of parton i, θ_i is the angle between the direction of motion of the soft gluon and the parton i, and θ_{ij} is the angle between the partons i and j.

In general this dipole radiation function can be used to express the current squared

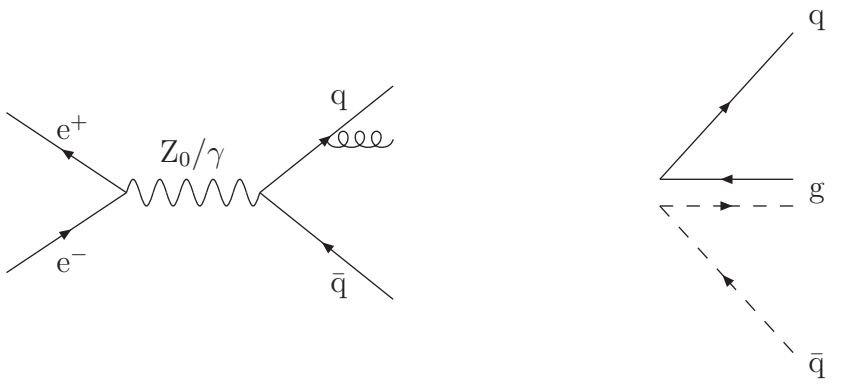

(a) Feynman Diagram (b) Colour Flow

Figure 2.4: Feynman diagram and colour flow for $e^+e^- \to q\bar{q}g$.

for a process in the form

$$\mathbf{J}^2(q) = \frac{C_{\mathbf{m}}}{\omega^2} W(\Omega_q), \tag{2.55}$$

where $C_{\mathbf{m}}$ is the colour factor for the tree-level process, Ω_q is the direction of the gluon and $W(\Omega_q)$ is the soft gluon radiation pattern. For the example we are considering $C_{\mathbf{m}} = C_F N_c$ and the radiation pattern is given by

$$W_{q\bar{q}g}(\Omega_q) = C_A \left[W_{qg}(\Omega_q) + W_{\bar{q}g}(\Omega_q) \right] - \frac{1}{N_c} W_{q\bar{q}}(\Omega_q). \tag{2.56}$$

This corresponds to emission of a soft gluon from a colour dipole, *i.e.* W_{qg} is emission from the dipole formed by the quark and the anticolour line of the gluon, $W_{\bar{q}g}$ is emission from the colour line of the gluon and the antiquark, and $W_{q\bar{q}}$ is emission from the quark and antiquark. This then shows that the $q\bar{q}$ dipole is negative, which is a problem if we wish to use a probabilistic approach to treat the soft gluon radiation.

These dipole radiation functions can be split into two parts as was done in [84], *i.e.*

$$W_{ij}(\Omega_q) = W^i_{ij}(\Omega_q) + W^j_{ij}(\Omega_q), \tag{2.57}$$

where

$$W^i_{ij} = \frac{1}{2\xi_i} \left(1 - \frac{1}{\gamma_i^2 \xi_i} + \frac{\xi_{ij} - \xi_i}{\xi_j} \right). \tag{2.58}$$

This allows us to rewrite the square of the current for $e^+e^- \to q\bar{q}g$, Eqn. 2.53, using these radiation functions, in the following form,

$$\begin{aligned} W_{q\bar{q}g}(\Omega_q) = \; & 2C_F \left(W^q_{qg} + W^{\bar{q}}_{\bar{q}g} \right) + C_A \left(W^g_{g\bar{q}} + W^g_{gq} \right) \\ & + \tfrac{1}{N_c} \left(W^q_{qg} - W^q_{q\bar{q}} + W^{\bar{q}}_{\bar{q}g} - W^{\bar{q}}_{\bar{q}q} \right). \end{aligned} \tag{2.59}$$

The last term in Eqn. 2.59, and other terms of this type, can be neglected for two reasons:

firstly it is suppressed by $1/N_c^2$ with respect to the leading-order term; and secondly it is dynamically suppressed because it does not contain a collinear singularity in the massless limit. Typically the size of these suppressed terms is at most a few percent of the size of the non-N_c suppressed terms.

The function W_{ij}^i has a number of important properties which we will now consider:

1. In the massless limit it contains the collinear singularity as $\theta_i \to 0$, [84]. This can be seen by taking the massless limit of Eqn. 2.58,

$$W_{ij}^i = \frac{1}{2\left(1-\cos\theta_i\right)}\left(1+\frac{\cos\theta_i-\cos\theta_{ij}}{1-\cos\theta_j}\right). \tag{2.60}$$

   This shows that the radiation function is singular in the collinear limit, *i.e.* as $\theta_i \to 0$, and not in the other collinear limit $\theta_j \to 0$ since $\theta_i \to \theta_{ij}$ as $\theta_j \to 0$.

2. After averaging over the azimuthal angle of the soft gluon about the parton i the function W_{ij}^i corresponds to emission in a cone about the direction of the parton i up to the direction of j [80, 81]. This can be seen by writing the angular integral in terms of the polar and azimuthal angles of the gluon with respect to the parton i. We can then consider the integral of the radiation functions over the azimuthal angle

$$\left\langle W_{ij}^i \right\rangle = \int_0^{2\pi} \frac{d\phi_i}{2\pi} W_{ij}^i = \frac{v_i}{2\xi_i}\int_0^{2\pi}\frac{d\phi_i}{2\pi}\left[\frac{v_i-\cos\theta_i}{1-v_i\cos\theta_i}+\frac{\cos\theta_i-v_j\cos\theta_{ij}}{1-v_j\cos\theta_j}\right]. \tag{2.61}$$

   The only dependence of the integrand on the azimuthal angle is contained in the term $1/(1-v_j\cos\theta_j)$. We can rewrite θ_j in terms of the other angles in the problem. It is easiest to take the z-axis along the direction of the parton i and define the xz plane to be the plane containing j. In this co-ordinate system unit vectors along the direction of the parton j and the gluon are given by

$$\underline{\hat{j}} = (\sin\theta_{ij},\ 0,\ \cos\theta_{ij}), \tag{2.62a}$$
$$\underline{\hat{g}} = (\cos\phi_i\sin\theta_i,\ \sin\phi_i\sin\theta_i,\ \cos\theta_i). \tag{2.62b}$$

   This allows us to express θ_j in terms of the other angles by taking the scalar product,

$$\cos\theta_j = \underline{\hat{j}}\cdot\underline{\hat{g}} = \cos\phi_i\sin\theta_i\sin\theta_{ij}+\cos\theta_i\cos\theta_{ij}. \tag{2.63}$$

   The only ϕ_i dependent part of the integral can be written as

$$I = \int_0^{2\pi}\frac{d\phi_i}{2\pi}\frac{1}{1-v_j\cos\theta_j} = \int_0^{2\pi}\frac{d\phi_i}{2\pi}\frac{1}{a-b\cos\phi_i}, \tag{2.64}$$

   where $a = 1-v_j\cos\theta_i\cos\theta_{ij}$ and $b = v_j\sin\theta_i\sin\theta_{ij}$, as was done in [12] for the massless case. This integral can be performed via contour integration [12] giving

$$I = \frac{1}{\sqrt{a^2-b^2}} = \frac{1}{\sqrt{\left(\cos\theta_i-v_j\cos\theta_{ij}\right)^2+\left(\sin\theta_i/\gamma_j\right)^2}}. \tag{2.65}$$

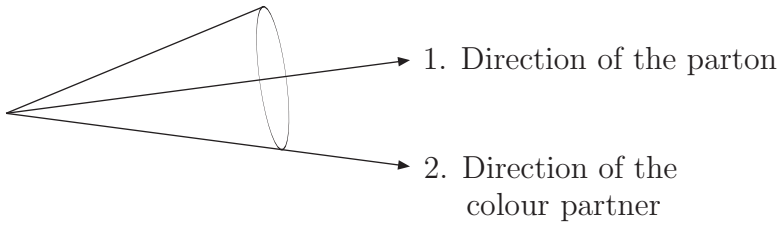

Figure 2.5: Emission in angular-ordered cones.

This allows us to perform the azimuthal average for the radiation function giving

$$\left\langle W_{ij}^{i}\right\rangle = \frac{v_i}{2\left(1-v_i\cos\theta_i\right)}\left[\frac{A_i}{\left(v_iA_i+\gamma_i^{-2}\right)}+\frac{B_i}{\sqrt{B_i^2+(\sin\theta_i/\gamma_j)^2}}\right], \tag{2.66}$$

where $A_i = v_i - \cos\theta_i$ and $B_i = \cos\theta_i - v_j\cos\theta_{ij}$. This result was first derived in [84] for massive partons. If we now take the massless limit of this function we obtain

$$\left\langle W_{ij}^{i}\right\rangle = \frac{1}{2\left(1-\cos\theta_i\right)}\left[1+\frac{\cos\theta_i-\cos\theta_{ij}}{|\cos\theta_i-\cos\theta_{ij}|}\right], \tag{2.67}$$

which can be rewritten as

$$\begin{aligned}\left\langle W_{ij}^{i}\right\rangle = &\quad \frac{1}{1-\cos\theta_i} && \text{if } \theta_i < \theta_{ij},\\ = &\quad 0 && \text{otherwise.}\end{aligned} \tag{2.68}$$

We have therefore shown that, after azimuthally averaging, the emission of a soft gluon from the parton i can only occur in a cone about the direction of i, with the opening angle of the cone given by the direction of j.

3. If the parton i is massive we should use the full azimuthally averaged radiation function, given in Eqn. 2.66, rather than massless result. This gives two main effects: firstly the step function at $\cos\theta_i = \cos\theta_{ij}$ moves to $\cos\theta_i = v_j\cos\theta_{ij}$ and the fall-off of the radiation is smoothed, *i.e.* rather than being a step-function the fall-off occurs over a region in $\cos\theta_i$ of order γ_j^{-1}. Secondly soft radiation in the direction of the parton is reduced, *i.e.* emission within an angle of order $\theta \sim m_i/E_i$ vanishes [84]. Again rather than a step function the soft gluon radiation distribution goes to zero at $\cos\theta_i = v_i$ with a width, in $\cos\theta_i$, of order γ_i^{-2}. This full radiation function cannot be implemented numerically and therefore in practice we use the massless form of the function together with the 'dead-cone' prescription [84] in which there is no emission of soft gluons for angles $\theta < m_i/E_i$.

4. While W_{ij}/ω^2 is Lorentz invariant the individual functions W_{ij}^{i}/ω^2 and W_{ij}^{j}/ω^2 are not.

If we first define the concept of a *colour connected* parton we can then use the properties of the radiation functions to look at the radiation pattern from $e^+e^- \to q\bar{q}g$. Two partons

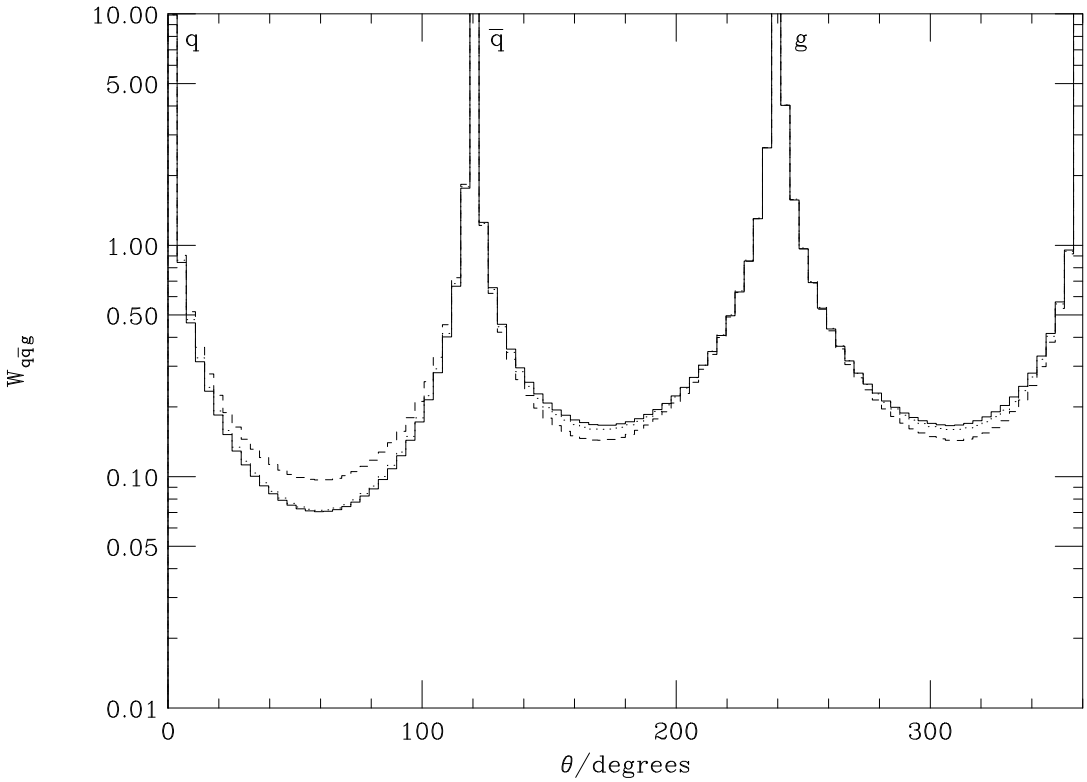

Figure 2.6: Soft gluon radiation pattern from the process $e^+e^- \to q\bar{q}g$. The hard quark, anti-quark and gluon directions were fixed at $\theta = 0^0$, $\theta = 120^0$ and $\theta = 240^0$ respectively. The solid line gives the full radiation pattern and the dashed line gives the angular-ordered radiation pattern after the $1/N_c^2$-suppressed terms have been neglected. The dotted line gives the improved angular-ordered approximation.

are considered to be colour connected if they share the same colour line. The colour flow, in the large N_c limit, for the process $e^+e^- \to q\bar{q}g$ is shown in Fig. 2.4b. The $\bar{q}$ and g are colour connected and the q and g are colour connected, while the $\bar{q}$ and q are not colour connected. Each quark only has one colour-connected partner in a given Feynman diagram and each gluon has two. Colour-connected partners are defined at each stage of the iterative parton-shower procedure. If the final-state q were to emit another gluon, g_2, the new final-state q would be colour connected to g_2 and no longer to g. The gluons g and g_2 would then also be colour connected.

We see from Eqn. 2.59 that after neglecting the final term, using the properties of the function W_{ij}^i, and averaging over the azimuthal angle of the gluon about a parton, the radiation can only occur in a cone about the direction of the parton up to the direction of its colour partner. This is shown in Fig. 2.5. We can draw a cone around parton one with half-angle given by the angle between the momenta of partons one and two. The emission from parton one within the cone defined by its colour-connected partner, parton two, is called angular-ordered emission.

The radiation pattern for the process $e^+e^- \to q\bar{q}g$ is shown in Fig. 2.6. The solid histogram gives the full radiation pattern for the soft gluon given in Eqn. 2.59 using the

non-azimuthally averaged radiation functions given in Eqn. 2.58. The dashed line gives the radiation pattern in the angular-ordered approximation where we have dropped the $1/N_c^2$-suppressed terms in Eqn. 2.59 and used the azimuthal-averaged radiation function. Azimuthal correlations can be included inside the angular-ordered cones after the full parton shower has been generated [85]. This leads to the improved angular-ordered approximation where we use the full radiation function, Eqn. 2.58, inside the angular ordered cone and the azimuthal average, *i.e.* zero, outside the cone. This gives the replacement [81]

$$W_{ij}^i \longrightarrow W_{ij}^i \Theta\left(\theta_i - \theta_{ij}\right). \tag{2.69}$$

This is shown by a dotted line in Fig. 2.6.

The angular-ordering procedure is one way of implementing the phenomenon of *colour coherence*. The idea of colour coherence is that if we consider a pair of partons and a soft gluon at a large angle to them, with respect to the angle between the parton pair, then this gluon can only resolve the total colour charge of the pair of smaller angle partons. It is therefore as if the larger-angle soft gluon was emitted before the smaller angle branchings. There have been a number of experimental studies of colour coherence effects. In particular the "string effect" in e^+e^- collisions [86], where there is a suppression of soft QCD radiation between the two quark jets in three jet events, has been studied. Fig. 2.6 shows that both angular-ordering approximations reproduce the "string effect", *i.e.* the large dip in the soft gluon radiation about $\theta = 60^0$. There have also been studies of colour coherence effects between the initial and final states in hadron–hadron collisions [87, 88].

In general, in the soft limit the matrix element can be written as

$$\sum_{\text{spins}} |\mathcal{M}_{n+1}|^2 = \frac{g_s^2}{\omega^2} \sum_{\text{spins}} |\mathcal{M}_n|^2 \sum_{i,j\neq i}^{n} C_{ij}^i W_{ij}^i, \tag{2.70}$$

where C_{ij}^i are the colour factors and W_{ij}^i the dipole radiation functions. After neglecting the $1/N_c^2$-suppressed terms the colour factors are $C_{qj}^q = 2C_F$ for a quark and its colour partner, $C_{gj}^g = C_A$ for a gluon and its colour partner and zero otherwise. The tree-level colour factor $C_{\mathbf{m}}$ has been absorbed into the tree-level matrix element squared $|\mathcal{M}_n|^2$. We have now obtained a factorized form for the matrix element squared for the emission of a soft gluon by neglecting the $1/N_c^2$-suppressed terms.

As in the collinear limit, we also need to consider the factorization of the phase space. As before the phase space for the leading-order process is given by Eqn. 2.27 and the phase space for the process after the radiation of a soft gluon by Eqn. 2.28. In the soft limit the momentum of the quark before and after the radiation of the gluon are the same and therefore

$$\frac{d^3p_i}{2E_i(2\pi)^3} \overset{w\to 0}{=} \frac{d^3p_j}{2E_j(2\pi)^3}. \tag{2.71}$$

The momentum of the radiated soft gluon can be written in terms of its energy giving

$$\frac{d^3p_k}{2E_k(2\pi)^3} = \omega d\omega \frac{d\Omega}{16\pi^3}. \tag{2.72}$$

Hence, as in the collinear limit, the phase space factorizes giving

$$d\Phi_{n+1} = d\Phi_n \omega d\omega \frac{d\Omega}{16\pi^3}. \tag{2.73}$$

This allows us to write the cross section for the emission of a soft gluon in the following factorized form using Eqns. 2.70 and 2.73,

$$d\sigma_{n+1} = d\sigma_n \frac{\alpha_s}{2\pi} \frac{d\omega}{\omega} \sum_{i,j\neq i} \frac{d\Omega_i}{2\pi} C_{ij}^i W_{ij}^i. \tag{2.74}$$

After averaging over the azimuthal direction

$$d\sigma_{n+1} = d\sigma_n \frac{\alpha_s}{2\pi} \frac{d\omega}{\omega} d\cos\theta \sum_{i,j\neq i} C_{ij}^i \left\langle W_{ij}^i \right\rangle. \tag{2.75}$$

Now if we use the angle for the evolution, or as is done in practice

$$\zeta = \frac{p_j \cdot p_k}{E_j E_k} \simeq 1 - \cos\theta, \tag{2.76}$$

for the branching $i \to jk$, in the collinear limit we can replace dt/t with $d\zeta/\zeta$ in Eqn. 2.34. If we take the soft limits of the splitting functions we obtain

$$\lim_{z\to 1} P_{qq} = \frac{2C_F}{1-z}, \tag{2.77a}$$

$$\lim_{z\to 1} P_{gg} = \frac{C_A}{1-z}. \tag{2.77b}$$

Hence both of these splitting functions are singular in the soft limit, *i.e.* as $z \to 1$. However the splitting function for $g \to q\bar{q}$ is non-singular in the soft limit. The energy of the soft gluon is given by $\omega = (1-z)E_i$ where E_i is the momentum of the particle before the gluon radiation. Hence $d\omega/\omega = dz/(1-z)$. This means we can replace $C_{ij}^i d\omega/\omega$ in Eqn. 2.75 with $P(z)dz$ in the soft limit. We can therefore combine Eqn. 2.34 and Eqn. 2.75 to give the following equation which correctly includes both the soft and collinear singularities:

$$d\sigma_{n+1} = d\sigma_n \frac{d\zeta}{\zeta} \frac{\alpha_s}{2\pi} P_{ji}(z) dz. \tag{2.78}$$

The evolution equation, Eqn. 2.40, can be written in terms of these angular variables instead of the virtualities we used before,

$$d(x,\zeta) = \Delta(\zeta) d(x_0,\zeta_0) + \int_{\zeta_0}^{\zeta} \frac{d\zeta'}{\zeta'} \frac{\Delta(\zeta)}{\Delta(\zeta')} \int_0^1 dz \frac{\alpha_s}{2\pi} P(z) d(x/z,\zeta'). \tag{2.79}$$

The new Sudakov-like form factor defined in terms of angles is given by

$$\Delta(\zeta) = \exp\left[-\int_{\zeta_0}^{\zeta}\frac{d\zeta'}{\zeta'}\int_0^1 dz\frac{\alpha_s}{2\pi}P(z)\right]. \tag{2.80}$$

As before, we need to choose an infra-red cut-off to regularize the integral, *i.e.* the Sudakov form factor becomes

$$\Delta(\zeta) = \exp\left[-\int_{\zeta_0}^{\zeta}\frac{d\zeta'}{\zeta'}\int_\epsilon^{1-\epsilon} dz\frac{\alpha_s}{2\pi}P(z)\right]. \tag{2.81}$$

Whereas in the collinear case we imposed a cut-off on the virtuality of the parton, here we impose a cut-off on the minimum angle of the emission. It is easier however to impose a cut-off on some energy-like variable and we therefore choose the variable

$$\tilde{t} = E^2\zeta, \tag{2.82}$$

as the evolution variable. It was shown in [84] that for particles with a mass m_i and energy E_i there is no soft radiation for angles $\theta \lesssim m_i/E_i$. This corresponds to

$$\tilde{t} \lesssim m_i^2. \tag{2.83}$$

Hence if we wish to impose a cut-off, t_0, on the virtuality of the particle we can impose

$$\tilde{t} \geq t_0. \tag{2.84}$$

This is the simplest choice of the cut-off, however by using a different choice we can include the next-to-leading-log terms (at least for large x) as well [89]. To do this we must impose a cut-off on the transverse momentum [80]

$$p_T^2 = \frac{\mathbf{q}_j^2\mathbf{q}_k^2\sin^2\theta}{\mathbf{q}_i^2} = \frac{\left[\mathbf{q}_j^2\mathbf{q}_k^2 - E_j^2E_k^2(1-\zeta)^2\right]}{\mathbf{q}_i^2} \geq t_0, \tag{2.85}$$

where $\mathbf{q}_i$, $\mathbf{q}_j$ and $\mathbf{q}_k$ are the three-momenta of the partons i, j and k, respectively. If we now assume that the particles produced in the branching are massless, this implies

$$z, (1-z) > \sqrt{\frac{t_0}{2\tilde{t}}}. \tag{2.86}$$

To next-to-leading-log accuracy we can neglect the factor of $1/\sqrt{2}$ which gives the following cut-off condition for z,

$$\sqrt{t_0/\tilde{t}} < z < 1 - \sqrt{t_0/\tilde{t}}. \tag{2.87}$$

These two limits only allow some phase space for the branching if $\tilde{t} \geq 4t_0$. This gives the

Sudakov form factor in terms of this new variable

$$\Delta_i(\tilde{t}) = \exp\left[-\sum_j \int_{4t_0}^{\tilde{t}} \frac{d\tilde{t}'}{\tilde{t}'} \int_{\sqrt{t_0/\tilde{t}'}}^{1-\sqrt{t_0/\tilde{t}'}} \frac{dz}{2\pi}\alpha_s\big(z^2(1-z)^2\tilde{t}'\big)\, P_{ji}(z)\right]. \tag{2.88}$$

Although we have averaged over the azimuthal angle for the emission of the gluon in both the soft and collinear cases, azimuthal effects, *e.g.* due to spin correlations, can be included [85] after the full parton shower has been generated.

In processes where there is more than one Feynman diagram it is possible for the colour flows in the diagrams to be different. This leads to so called "non-planar" terms from the interference between diagrams with different colour flows. These are not positive definite and hence cannot be interpreted in a probabilistic way for implementation in the Monte Carlo procedure. The "non-planar" terms are always suppressed by inverse powers of N_c. A procedure must be adopted to split up the "non-planar" parts of the tree-level matrix element to give redefined planar terms with positive-definite coefficients that can be used in the Monte Carlo procedure. Such a procedure was proposed in [81] and shown to work correctly for all QCD processes. However, as shown in [90], this is inadequate for MSSM processes and hence a new procedure was proposed, which we adopt here. In this procedure the "non-planar" parts of the matrix element are split up according to

$$|\overline{M}|^2_{\text{full},i} = \frac{|\overline{M}|^2_i}{|\overline{M}|^2_{\text{planar}}}|\overline{M}|^2_{\text{tot}}, \tag{2.89}$$

where $|\overline{M}|^2_i$ is the matrix element squared for the ith colour flow, $|\overline{M}|^2_{\text{planar}}$ is the sum of the matrix elements squared for the planar colour flows, and $|\overline{M}|^2_{\text{tot}}$ is the total matrix element squared. This ensures that the redefined planar terms, $|\overline{M}|^2_{\text{full},i}$, are positive definite and have the correct pole structure. This can be implemented numerically.

In this section we have explained how by using a Markov branching procedure we can resum both the soft and collinear singularities in QCD. In the next section we will discuss how this procedure can be implemented numerically.

2.3.3 Monte Carlo Procedure

The ratio of Sudakov form factors $\Delta(t_1)/\Delta(t_2)$ gives the probability of evolving downwards from the scale t_1 to the scale t_2 without resolvable emission. We can therefore implement the parton-shower algorithm numerically by solving

$$\frac{\Delta(t_1)}{\Delta(t_2)} = \mathcal{R}, \tag{2.90}$$

where $\mathcal{R}$ is a random number uniformly distributed between 0 and 1.[2] Using Eqn. 2.90, given the initial scale t_1, we can generate the scale of the next branching. If the value of $\mathcal{R}$ is smaller than $\Delta(t_1)$ there is no solution of Eqn. 2.90 for $t_2 > t_0$. This is because

[2]This interval includes both of the end points, *i.e.* $0 \leq \mathcal{R} \leq 1$.

$\Delta(t)$ increases as the scale decreases and $\Delta(t_0) = 1$. This procedure correctly gives the probability that there is no resolvable branching.

If a solution $t_2 > t_0$ exists we need to generate the momentum fraction $z = x_2/x_1$ of the parton after the branching. This is done by solving

$$\int_{\sqrt{t_0/\tilde{t}'}}^{z} dz' \frac{\alpha_s}{2\pi} P(z') = \mathcal{R}' \int_{\sqrt{t_0/\tilde{t}'}}^{1-\sqrt{t_0/\tilde{t}'}} dz' \frac{\alpha_s}{2\pi} P(z'), \tag{2.91}$$

where $\mathcal{R}'$ is a second uniformly distributed random number in the interval $[0, 1]$.

We have discussed the parton-shower procedure for the final state, *e.g.* in $e^+e^- \to q\bar{q}$. However in processes involving hadrons in the initial state the QCD radiation from the incoming partons must also be generated, *e.g.* in Drell-Yan $q\bar{q} \to \ell^+\ell^-$. There are two ways in which this can be achieved:

Forward Evolution. Starting at the cut-off scale with the parton distribution function, $f(x_0, t_0)$, which is evolved to the scale of the hard collision. This starts with the initial momentum fraction x_0 and generates the momentum fraction x_n of the partons in the hard collisions after n branchings.

Backward Evolution. Starting with the momentum fractions of the partons involved in the hard collision the partons are evolved backwards to give the parton branchings from which they came.

The problem is that forward evolution will often generate momentum fractions, x_n, which give a small contribution to the total cross section and are therefore rejected, *i.e.* forward evolution is inefficient. However with backward evolution we can generate those momentum fractions which give large contributions to the cross section, hence this is more efficient.

The backward evolution is set up in the following way. First we can write an evolution equation for the parton distribution functions in the same way as for the fragmentation functions in Eqn. 2.40,

$$t\frac{\partial}{\partial t}\left(\frac{f}{\Delta}\right) = \frac{1}{\Delta}\int_0^1 \frac{dz}{z}\frac{\alpha_s}{2\pi} P(z) f(x/z, t), \tag{2.92}$$

$$f(x,t) = \Delta(t) f(x, t_0) + \int_{t_0}^{t} \frac{dt'}{t'}\frac{\Delta(t)}{\Delta(t')}\int_0^1 \frac{dz}{z}\frac{\alpha_s}{2\pi} P(z) f(x/z, t'). \tag{2.93}$$

We can now define $df(x, t_2)$ as the fraction of partons with momentum fraction x and scale t_2 which came from branchings between the scale t and $t + \delta t$. This gives the probability of no branching between the scales t_1 and t_2,

$$\Pi = 1 - \int_{t_1}^{t_2} df. \tag{2.94}$$

Now from the evolution equation, Eqn. 2.93,

$$f(x,t_2)df = \frac{\delta t}{t}\frac{\Delta(t_2)}{\Delta(t)}\int_0^1 \frac{dz}{z}\frac{\alpha_s}{2\pi}P(z)f(x/z,t), \quad (2.95)$$

$$= \delta t\frac{\partial}{\partial t}\left[\frac{\Delta(t_2)}{\Delta(t)}f(x,t)\right]. \quad (2.96)$$

Hence we can substitute into Eqn. 2.94 for df and perform the integral to give the probability of no branching between the scales t_1 and t_2, Π, in a more useful form

$$\Pi = \frac{f(x,t_1)\Delta(t_2)}{f(x,t_2)\Delta(t_1)}. \quad (2.97)$$

Therefore instead of the Sudakov form factor for the backwards evolution we should use $\Delta(t)/f(x,t)$. We can then generate the correct scale for the branching by solving Eqn. 2.90 with this modified Sudakov form factor, *i.e.* by solving $\Pi = \mathcal{R}$ where $\mathcal{R}$ is a random number uniformly distributed between 0 and 1.

As in the forward evolution case after we have generated the scale of the next branching we need to find the momentum fractions of the partons produced in the branching. In the forward evolution case this is done by solving Eqn. 2.91. This equation is modified for the backwards evolution algorithm to give

$$\int_{\sqrt{t_0/\tilde{t}'}}^{z} dz'\frac{\alpha_s}{2\pi}\frac{P(z')}{z'}f(x_2/z',t_1) = \mathcal{R}'\int_{\sqrt{t_0/\tilde{t}'}}^{1-\sqrt{t_0/\tilde{t}'}} dz'\frac{\alpha_s}{2\pi}\frac{P(z')}{z'}f(x_2/z',t_1), \quad (2.98)$$

where again $\mathcal{R}'$ is a random number uniformly distributed between 0 and 1.

2.3.4 Summary

We have explained how the cross section for $n+1$ partons factorizes in both the collinear and soft limits into a universal splitting term and the cross section for n partons. Both of these limits can be implemented by using angles as the evolution variable in a Markov branching procedure. We start at the hard cross section, normally with a two-to-two process. The maximum angle of emission from a parton is set by the direction of the colour partner. We then generate some smaller angle parton, *e.g.* a gluon from a quark. Then we repeat the procedure, *e.g.* the gluon's colour partner is now the colour partner of the original quark, and its anticolour partner the quark, and the colour partner of the quark is the gluon. One of the partons will now radiate with the maximum angle given by the direction of the new colour partner and so on until the cut-off below which emission does not occur is reached. This procedure resums both the leading soft and collinear singularities. If the initial state contains partons the radiation from these incoming partons can be generated by using a backward evolution algorithm which is more efficient than forward evolution in this case.

After the parton-shower phase we are left with partons with a low virtuality which must then form the observed hadrons. In the next section we will discuss the various phenomenological models for the hadronization process which are currently used in Monte

Carlo event generators.

2.4 Hadronization

There are a number of different phenomenological models of the hadronization process which are used in different Monte Carlo event generators:[3]

Independent Fragmentation. This was the first proposed hadronization model [91] and is the simplest scheme. In this method, for example for the hadronization of a quark, a quark–antiquark pair is created from the vacuum, the original quark and the antiquark then form a meson. The procedure is then repeated for the quark which was created and so on until the energy of the remaining quark falls below some cut-off. This model leads to violations of energy and momentum conservation which must be corrected after the hadronization phase is finished. The colours and flavours of the left-over partons must also be neutralized at this stage.

String Model. In this model [92] the quark and antiquark produced in e^+e^- collisions are assumed to be joined by a relativistic string. As the quark and antiquark move apart the string breaks via the production of a $q\bar{q}$ pair in the colour field of the string. The original quark is now connected by a string to the produced antiquark and the original antiquark to the produced quark. This procedure is repeated until there is insufficient energy to break the colour strings any further. The $q\bar{q}$ pairs connected by the strings then give the observed hadrons.

Cluster Model. This model is based on the idea of colour preconfinement [93]. This suggests that if we consider the pairs of colour-connected partons left after the parton-shower phase they have a mass spectrum which falls rapidly at high masses, is independent of Q^2 and universal (see Fig. 2.19a). The model then decays these clusters into the observed hadrons. As this is the model used in the HERWIG event generator we will now discuss it in more detail.

The cluster model proceeds in the following way. The gluons left after the end of the parton-shower phase are non-perturbatively split into $q\bar{q}$ pairs. The colour-connected quarks and antiquarks are then formed into colour-singlet clusters. The cluster mass spectrum is shown in Fig. 2.19a. The exact form of this spectrum will depend on the QCD scale Λ, the cut-off scale t_0 and the mechanism used to split the gluons into $q\bar{q}$ pairs. Fig. 2.19a shows the spectrum for a low value of the cut-off t_0. Most clusters have masses of a few GeV and it is therefore reasonable to assume they are superpositions of the known hadrons. In general, as the clusters are too massive to be any of the observed hadrons they are assumed to decay into a pair of hadrons, either two mesons or a baryon and an antibaryon, with the type of hadron determined by the available density of states, *i.e.* phase space times the spin degeneracy.

A simple extension of this model is used for hadron remnants. If we consider the example of a collision in which a valence quark in the proton participates in a hard

[3] A more detailed review of the various hadronization models can be found in [12, 79].

process, the two remaining valence quarks are left in the final state. These valence quarks are paired up into a "diquark" which, in the planar approximation, carries an anticolour index and can be treated like an antiquark. The resulting cluster has baryonic quantum numbers and decays into a baryon and a meson.

The procedure for selecting the hadrons produced in these cluster decays works as follows [94]. We will consider the procedure for a cluster containing a quark–antiquark pair $q_1\bar{q}_2$, where $1, 2$ are any of the quark flavours d, u, s, c and b which hadronize before decaying. If the cluster is too light to decay into two hadrons it is taken to represent the lightest single hadron of its flavour. Its mass is shifted to the appropriate value by an exchange of momentum with a neighbouring cluster in the jet. Those clusters massive enough to decay into two hadrons decay into pairs of hadrons selected in the following way. Another flavour q_3 or d_3 is randomly selected where $q_3 =$ u, d, s is one of the three light quark flavours and d_3 is one of the six corresponding diquarks, *i.e.* dd, du, ds, uu, us, ss. The flavours of the decay products are taken to be either $q_1\bar{q}_3$ and $q_3\bar{q}_2$, a two-meson decay, or $q_1 d_3$ and $\bar{d}_3\bar{q}_2$, a baryon–antibaryon decay. Each decay product is then randomly selected from a list of resonances with the correct flavours. A weight, W, for a given pair of resonances is calculated by taking the available phase space weighted with the spin degeneracy. This is compared with a random number, *i.e.* the pair of hadrons is accepted if

$$W \geq \mathcal{R} \times W_{\max}, \tag{2.99}$$

where $W_{\max}$ is the maximum possible weight and $\mathcal{R}$ is a uniformly distributed random number in the range $[0, 1]$. If this weight is rejected the whole procedure is repeated. In the original model [94, 95] each cluster was assumed to decay isotropically in the rest frame of the cluster into a pair of hadrons. However, in the current implementation of the model [2] hadrons containing quarks from the perturbative stage of the event continue in the same direction, in the cluster rest frame, as the original quark.

While it is reasonable to assume that low mass clusters are superpositions of hadron resonances there is a small fraction of high mass clusters for which this is not a reasonable approximation. These clusters must first be split using a string-like mechanism [94], into lighter clusters, before they are decayed into hadrons.

2.5 Monte Carlo Event Generators

There are a number of Monte Carlo event generators currently available which implement different hadronization models and treat the parton-shower phase in different ways. In general there are three main types of Monte Carlo event generator depending on which hadronization model is used.

The ISAJET event generator [75] uses the original independent fragmentation model of [91]. However the treatment of the parton-shower phase does not include colour coherence effects. This model was successful in explaining moderate energy e^+e^- data but gives poor agreement with the current LEP and Tevatron data. ISAJET is still commonly used, particularly for studies of supersymmetric processes, due to the large number of SUSY production processes and decays which are implemented.

The JETSET event generator [96] uses the string hadronization model and a final-state parton shower which includes colour coherence effects. However, colour coherence effects are only partially included in the initial-state parton shower via a veto algorithm. This simulation is in impressive agreement with the experimental measurements of hadronic final states, particularly in e^+e^- collisions, up to the highest energies currently studied. JETSET is used to perform the hadronization for a range of event generators, PYTHIA [96], LEPTO [97] and ARIADNE [98], which uses a different formalism for the parton-shower phase. There is also a supersymmetric extension, SPYTHIA [99], and a simulation of SUSY in e^+e^- collisions, SUSYGEN [100], which use JETSET to perform the parton-shower and hadronization phases.

The HERWIG event generator uses a cluster hadronization model with full treatment of colour coherence effects in both the initial- and final-state parton showers. The agreement with the e^+e^- data is not as good as with the string hadronization model used in JETSET, however there are fewer adjustable parameters in the model. HERWIG provides better agreement, in hadron–hadron collisions, for observables which are sensitive to colour coherence effects.

In the next two sections we will discuss how to implement $\not{R}_p$ SUSY processes into the HERWIG event generator.

2.6 Angular Ordering in $\not{R}_p$

In Standard Model and MSSM processes, apart from complications involving processes where there are "non-planar" terms [90], the angular-ordering procedure is relatively straightforward to implement. However in $\not{R}_p$ SUSY there are additional complications.

The lepton number violating processes, which come from the first two terms in the superpotential, Eqn. 1.63, have colour flows which are the same as those which occur in the MSSM. On the other hand the baryon number violating interactions, which come from the third term in Eqn. 1.63, have a very different colour structure involving the totally antisymmetric tensor, $\epsilon^{c_1c_2c_3}$. We look first at the colour structure of the various baryon number violating decays which we include in the Monte Carlo simulation and then at the structure of the various hard scattering processes.

2.6.1 Decays

From the point of view of the colour structure there are three types of baryon number violating decays which we include in the Monte Carlo simulation:

1. two-body $\not{B}$ decay of an antisquark to two quarks or a squark to two antiquarks;
2. three-body $\not{B}$ decay of a colourless sparticle, *i.e.* neutralino and chargino, to three quarks or antiquarks;
3. three-body $\not{B}$ decay of the gluino to three quarks or antiquarks.

In general it is possible to consider, for example, the decay of a neutralino to three quarks as either a three-body decay or two sequential two-body decays, of the neutralino

to an antisquark and a quark, and then of the antisquark to two quarks. If either of the two sequential two-body decays are kinematically forbidden, *i.e.* they can only proceed if the internal particle in the three-body decay is off-shell, we consider the decay to be three-body, otherwise we treat the decay as two sequential two-body decays.

The problem is how to implement the angular-ordering procedure for these processes. We shall consider these processes using the eikonal current with an arbitrary number of colours as was done in Section 2.3.2 for the process $e^+e^- \to q\bar{q}g$. In these $\not{R}_p$ processes this means we need to consider the decay of an antisquark to (N_c-1) quarks and of the neutralino, chargino and gluino to N_c quarks. We also have to use the generalization to N_c colours of the antisymmetric tensor, *i.e.* $\epsilon^{c_1\ldots c_{N_c}}$.

2.6.1.1 Squark Decays

For the decay of an antisquark to (N_c-1) quarks the leading infrared contribution to the soft gluon distribution has the factorized form

$$\mathcal{M}(p_0,p_1,p_2,\ldots,p_{N_c-1};q) = g_s\mathbf{m}(p_0,p_1,p_2,\ldots,p_{N_c-1})\cdot\mathbf{J}(q), \tag{2.100}$$

where

- $\mathbf{m}(p_0,p_1,p_2,\ldots,p_{N_c-1})$ is the tree-level matrix element for an antisquark, with momentum p_0, to decay to N_c-1 quarks, with momenta $p_1,\ldots,p_{N_c-1}$.
- $\mathcal{M}(p_0,p_1,p_2,\ldots,p_{N_c-1};q)$ is the tree-level matrix element for the decay of an antisquark to N_c-1 quarks including the emission of an extra soft gluon with momentum q.
- $\mathbf{J}(q)$ is the non-Abelian semi-classical current for the emission of the soft gluon, with momentum q, from the hard partons.
- c_0 is the colour of the decaying antisquark and $c_1,\ldots,c_{N_c-1}$ are the colours of the quarks.

Again the current, $\mathbf{J}(q)$, is given by, $\mathbf{J}(q) = \sum_{s=1,2}\mathbf{J}^{b,\mu}(q)\varepsilon^*_{\mu,s}$ where

$$\mathbf{J}^{b,\mu}(q) = \left(\frac{p_0^\mu}{p_0\cdot q}\right)\mathbf{t}^{b,\tilde{\mathrm{q}}^*}_{c_0c_0'}\epsilon^{c_0'c_1\ldots c_{N_c-1}} + \sum_{i=1}^{N_c-1}\left(\frac{p_i^\mu}{p_i\cdot q}\right)\mathbf{t}^{b,\mathrm{q}_i}_{c_ic_i'}\epsilon^{c_0\ldots c_i'\ldots c_{N_c-1}}, \tag{2.101}$$

b and μ are the colour and Lorentz indices of the emitted gluon, and $\mathbf{t}^{b,\tilde{\mathrm{q}}^*}$ and $\mathbf{t}^{b,\mathrm{q}_i}$ are the colour matrices of the antisquark and quarks, respectively.

We can now obtain the soft gluon distribution simply by squaring the current,

$$\mathbf{J}^2(q) = -C_FN_c(N_c-2)!\left[\sum_{i=1}^{N_c-1}\left(\frac{p_0}{p_0\cdot q}-\frac{p_i}{p_i\cdot q}\right)^2 + \sum_{i=1}^{N_c-2}\sum_{j>i}^{N_c-1}\left(\frac{p_i}{p_i\cdot q}-\frac{p_j}{p_j\cdot q}\right)^2\right]. \tag{2.102}$$

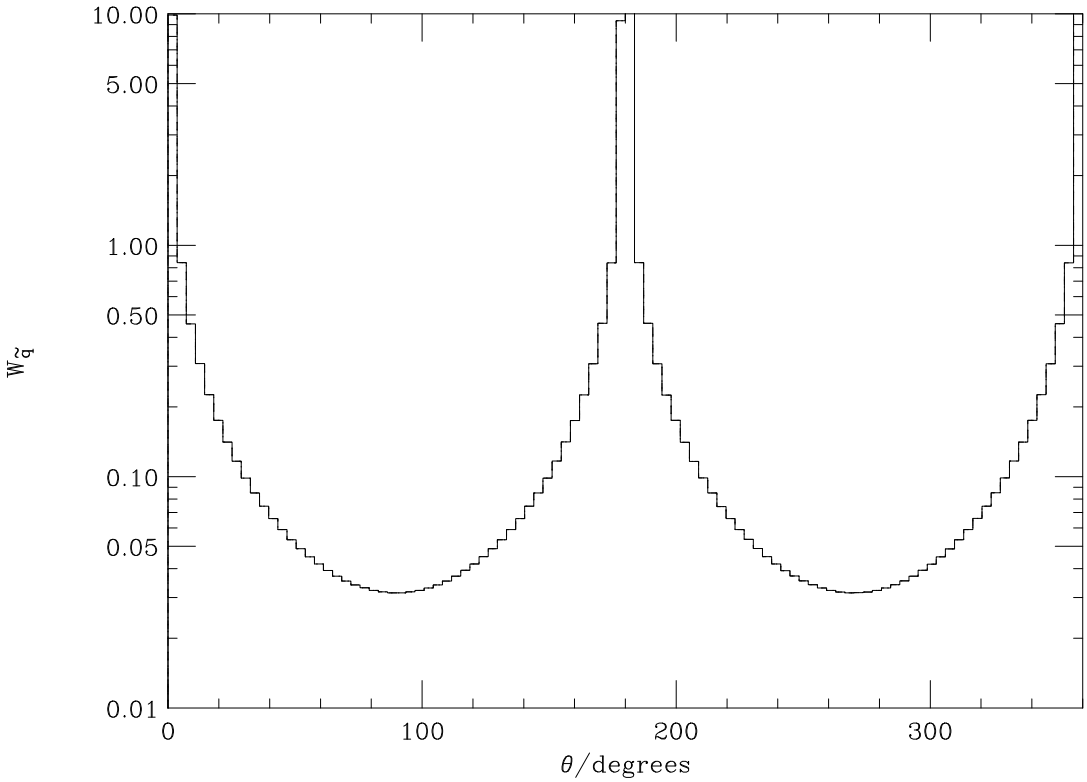

Figure 2.7: Radiation pattern for the decay $\tilde{q}^* \to qq$. The quarks produced in the decay are in the directions $\theta = 0^0$ and $\theta = 180^0$. In this case the lines for the two different angular-ordering approximations are indistinguishable from the full result.

This can be expressed in terms of the radiation functions, as in Eqn. 2.55. The tree-level colour factor is now $C_{\mathbf{m}} = \epsilon^{c_0 \ldots c_{N_c-1}} \epsilon^{c_0 \ldots c_{N_c-1}} = N_c!$, where we have not averaged over the initial colours, and the radiation pattern is given by

$$W(\Omega_q) = \frac{-\omega^2 C_F}{(N_c-1)} \left[\sum_{i=1}^{N_c-1} \left(\frac{p_0}{p_0 \cdot q} - \frac{p_i}{p_i \cdot q} \right)^2 + \sum_{i=1}^{N_c-2} \sum_{j>i}^{N_c-1} \left(\frac{p_i}{p_i \cdot q} - \frac{p_j}{p_j \cdot q} \right)^2 \right]. \qquad (2.103)$$

We can reexpress this result in terms of the functions given in [84],

$$W(\Omega_q) = \frac{2C_F}{(N_c-1)} \sum_{i=0}^{N_c-1} \sum_{j \neq i}^{N_c-1} W_{ij}^i. \qquad (2.104)$$

This is exactly the same result as was obtained in [101], in the context of baryon number violation in the Standard Model, except that the massless radiation functions of [101] are replaced by the massive functions here.

We can now consider the radiation pattern given by this result. If we average over the azimuthal angle for the emission of the soft gluon about one of the final-state quarks we have two contributions to the radiation from this quark: the first is from radiation in a cone about the direction of the quark up to the direction of the decaying squark;

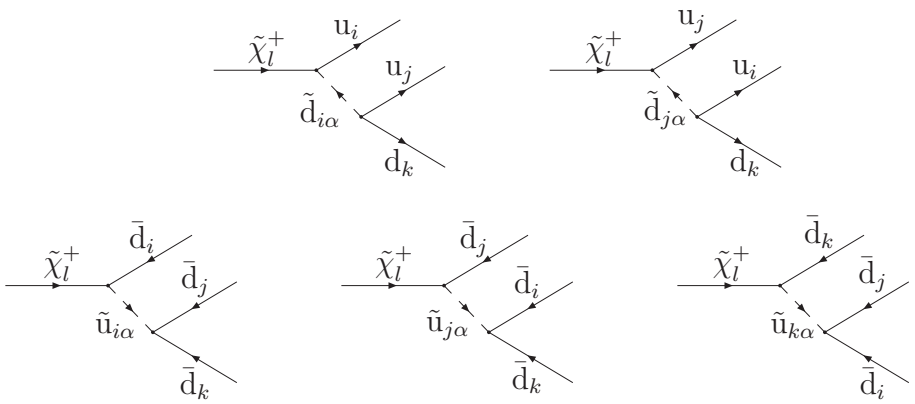

Figure 2.8: UDD decays of the $\tilde{\chi}^+$. The index $l = 1, 2$ gives the mass eigenstate of the chargino, the indices $i, j, k = 1, 2, 3$ give the generation of the fermions and sfermions, and the index $\alpha = 1, 2$ gives the mass eigenstate of the sfermion. The conventions for the mixings of the sfermions and electroweak gauginos are discussed in Appendix A.

the second is from radiation in a cone up to the direction of the other quark produced in the decay, if we only consider three colours. The coefficient of the radiation functions describing the radiation into these cones is suppressed by a factor of $1/(N_c-1) = 1/2$ with respect to the Standard Model case where the quark can only radiate up to the direction of its colour partner. If we wish to include these decays in the parton shower we need to have one maximum angle for the emission of QCD radiation from the quark, to give the initial conditions for the parton-shower algorithm. This leads to the following approach for treating the soft gluon radiation from this process: the quarks from the decay are randomly colour connected to either the decaying antisquark or the other quark. The direction of this colour partner gives the maximum angle for the QCD radiation from the quark. On average, this correctly treats the soft gluon radiation from the decay products. We cannot treat this radiation pattern correctly on an event-by-event basis, a parton can only have one colour partner whose direction gives the maximum angle for the emission of QCD radiation. However if we consider all the events the radiation is treated correctly because we have picked the colour partners with the correct probabilities, *i.e.* the coefficients in Eqn. 2.104, $1/(N_c - 1) = 1/2$. A similar situation also occurs in Standard Model events where the gluon has both a colour and an anticolour partner. When we perform the evolution of the gluon we must pick one of these, with equal probability, to give the maximum angle for the radiation from the gluon.

It should be noted that this is only the colour connection for the angular-ordering procedure. The colour connections for the hadronization of these events will be discussed in Section 2.7. The radiation pattern for this process is shown in Fig. 2.7 in the rest frame of the decaying antisquark. This shows radiation between the two quarks produced in the antisquark decay as there is no QCD radiation from the antisquark in its rest frame.

In general the QCD radiation from sparticles, which are in the initial state here, is neglected in HERWIG. We would expect this approximation to be valid for two reasons: firstly the sparticles will usually have a short lifetime and secondly, due to their heavy masses, the QCD radiation will also be suppressed unless they have momenta much greater than their masses. However for the decays we are considering, we can include the effects

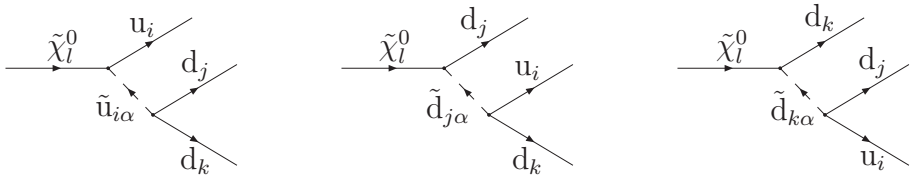

Figure 2.9: UDD decays of the $\tilde{\chi}^0$. The indices i, j, k and α are defined in the caption of Fig. 2.8. Here the index $l = 1, \ldots, 4$ gives the mass eigenstate of the neutralino.

of radiation from the decaying sparticles. This is done by treating the radiation in the rest frame of the decaying squark where there is no radiation from the decaying sparticle, which HERWIG would not generate anyway. However, as stated in Section 2.3.2, while the radiation from individual partons, *i.e.* W_{ij}^i, is not Lorentz invariant the dipole radiation functions are. Hence the total radiation pattern is Lorentz invariant and therefore, by treating the decay in the rest frame of the decaying particle, we correctly include the QCD radiation from the decaying particle when we boost back to the laboratory frame.

2.6.1.2 Neutralino and Chargino Decays

The charginos decay via the processes shown in Fig. 2.8 and the neutralinos via the processes in Fig. 2.9. If we consider the QCD radiation from the decay of a colour-neutral object which decays, for an arbitrary number of colours N_c, to N_c quarks, then we see that there is only one possible colour flow for this process. The squarks appearing in these processes, $\tilde{q}_{i\alpha}$, can be either of the states $\alpha = 1, 2$ resulting from the mixing of $\tilde{q}_{iL}$ and $\tilde{q}_{iR}$. This is discussed in more detail in Appendix A.

In fact, the colour structure of this process is very similar to that of the squark decay and the matrix element in the soft limit can be written in the same factorized form as before. Again we can express the current as in Eqn. 2.55, where here the tree-level colour factor $C_{\mathbf{m}} = \epsilon^{c_0 \ldots c_{N_c-1}} \epsilon^{c_0 \ldots c_{N_c-1}} = N_c!$, and the radiation function is given by

$$W(\Omega_q) = \frac{2C_F}{(N_c - 1)} \sum_{i=1}^{N_c} \sum_{j \neq i}^{N_c} W_{ij}^i. \tag{2.105}$$

This result can be interpreted in the same way as for the squark decay considered in the previous section. If we now only consider three colours, this radiation pattern gives two contributions to the radiation from a given final-state quark, after averaging over the azimuthal angle of the radiated gluon about that quark. For this process both of these contributions are from radiation in cones up to the directions of either of the other quarks produced in the decay, for three colours. The contribution from the radiation into these cones in suppressed by a factor of $1/(N_c - 1) = 1/2$ relative to the case where the quark has a unique colour partner. Hence we can interpret this radiation pattern as saying that a quark in the final state should be randomly connected to any of the other quarks from the neutralino or chargino decay. Again this is only the colour connection for the angular-ordering procedure, the colour connections for the hadronization phase are discussion in Section 2.7.

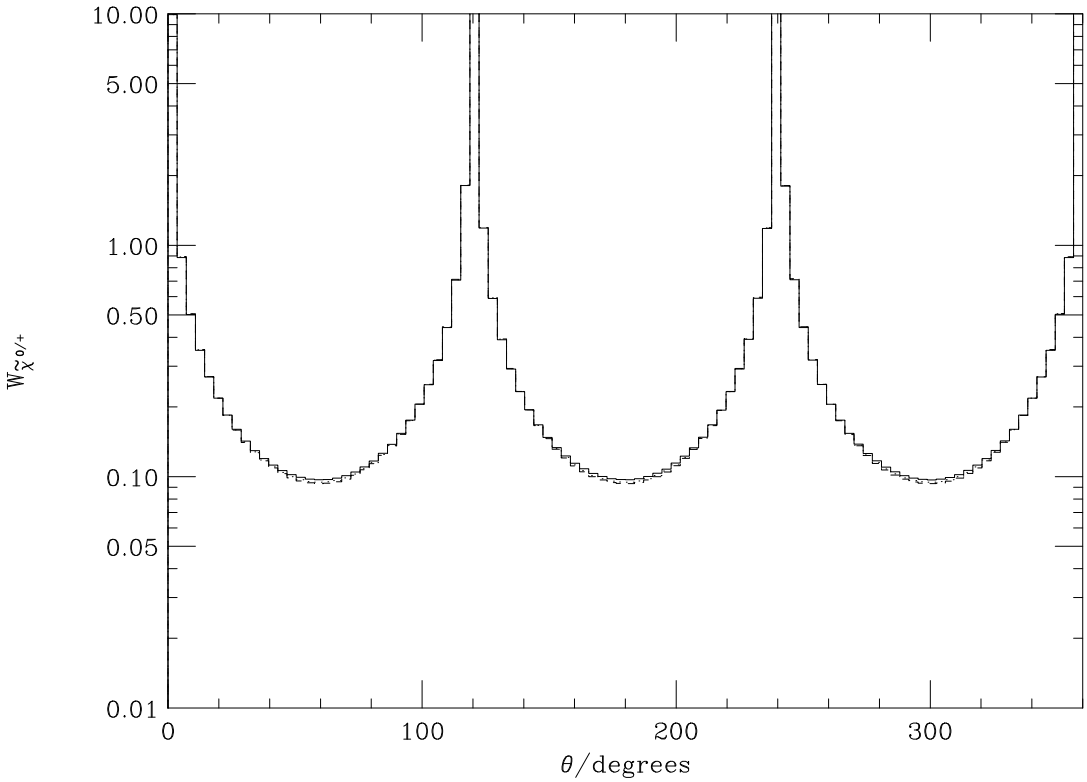

Figure 2.10: Radiation pattern for the radiation of a soft gluon in the decay $\tilde{\chi}^{0/+} \to qqq$. The decay is in the rest frame of the gaugino and the quarks are along the directions $\theta = 0^0$, $\theta = 120^0$ and $\theta = 240^0$. The solid line gives the full radiation pattern, the dashed line the angular-ordered approximation and the dotted line the improved angular-ordered approximation.

The radiation pattern for this process is shown in Fig. 2.10. As can been seen this pattern is more symmetric than the radiation from the process $e^+e^- \to q\bar{q}g$, Fig. 2.6. In particular there is an equal amount of soft gluon radiation between all the quarks, due to the random colour connection structure at the $\not{B}$ vertex, rather than the reduced radiation between the quark and antiquark in $e^+e^- \to q\bar{q}g$ which occurs because the quark and the antiquark are not colour connected.

2.6.1.3 Gluino Decays

The colour structure of the gluino decay is very different from that of the colourless objects or the squarks which we have already considered, the diagrams for this process are shown in Fig. 2.11. Again if we consider an arbitrary number of colours, N_c, the gluino will decay to N_c quarks. In this case there will be N_c possible colour flows, corresponding to the Feynman diagrams and colour flows shown in Fig. 2.12. These different colour flows will lead to "non-planar" terms which must be dealt with.

The leading infrared contribution to the soft gluon distribution can be written in the

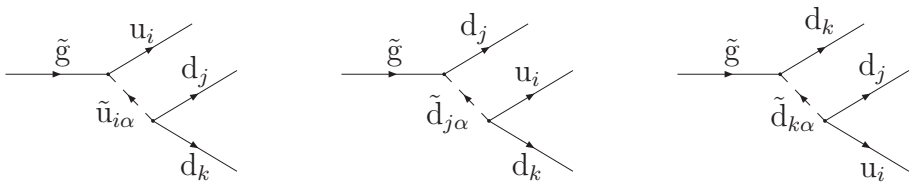

Figure 2.11: UDD decays of the $\tilde{g}$. As before, the indices $i, j, k = 1, 2, 3$ are the generations of the fermions and sfermions.

factorized form,

$$\mathcal{M}(p_0, p_1, p_2, \ldots, p_{N_c}; q) = g_s \sum_{i=1}^{N_c} \mathbf{m}_i(p_0, p_1, p_2, \ldots, p_{N_c}) \cdot \mathbf{J}_i(q), \tag{2.106}$$

where

- $\mathbf{m}_i(p_0, p_1, p_2, \ldots, p_{N_c})$ is the tree-level matrix element for the three-body gluino decay for the ith possible colour flow.
- $\mathcal{M}(p_0, p_1, p_2, \ldots, p_{N_c}; q)$ is the tree-level matrix element for the three-body gluino decay including the emission of an extra soft gluon of momentum q.
- $\mathbf{J}_i(q)$ is the non-Abelian semi-classical current for the emission of a soft gluon, with momentum q, from the hard partons for the ith possible colour flow.

Again the current has the form $\mathbf{J}_i(q) = \sum_{s=1,2} \mathbf{J}_i^{b,\mu}(q)\varepsilon^*_{\mu,s}$, where in this case

$$\begin{aligned}\mathbf{J}_i^{b,\mu}(q) &= i\left(\frac{p_0^\mu}{p_0 \cdot q}\right) \mathbf{f}^{ba'a} \mathbf{t}^{a'}_{c_i c_i'} \epsilon^{c_1 \ldots c_i' \ldots c_{N_c}} + \left(\frac{p_i^\mu}{p_i \cdot q}\right) \mathbf{t}^{b}_{c_i c_i'} \mathbf{t}^{a}_{c_i' c_i''} \epsilon^{c_1 \ldots c_i'' \ldots c_{N_c}} \\ &\quad + \sum_{j=1, j\neq i}^{N_c} \left(\frac{p_j^\mu}{p_j \cdot q}\right) \mathbf{t}^{b}_{c_j c_j'} \mathbf{t}^{a}_{c_i c_i'} \epsilon^{c_1 \ldots c_i' \ldots c_j' \ldots c_{N_c}}.\end{aligned} \tag{2.107}$$

The first term describes the radiation of a gluon by the decaying gluino and the second two terms describe radiation from the quarks produced in the gluino decay.

We can write the matrix element squared for this process as

$$\begin{aligned}|\mathcal{M}(p_0, p_1, p_2, \ldots, p_{N_c}; q)|^2 &= g_s^2 \sum_{i=1}^{N_c} |\mathbf{m_i}(p_0, p_1, p_2, \ldots, p_{N_c})|^2 \cdot |\mathbf{J}_i(q)|^2 \\ &\quad + g_s^2 \sum_{i=1}^{N_c} \sum_{j=1, j\neq i}^{N_c} \mathbf{m_i} \mathbf{m_j^*} \cdot \mathbf{J}_i(q) \cdot \mathbf{J}_j^*(q).\end{aligned} \tag{2.108}$$

The procedure of [90], which was described in Section 2.3.2, can be used with the matrix elements for this process, given in Appendix B, to deal with the "non-planar" terms. We will now consider the radiation pattern of the planar terms. The current can

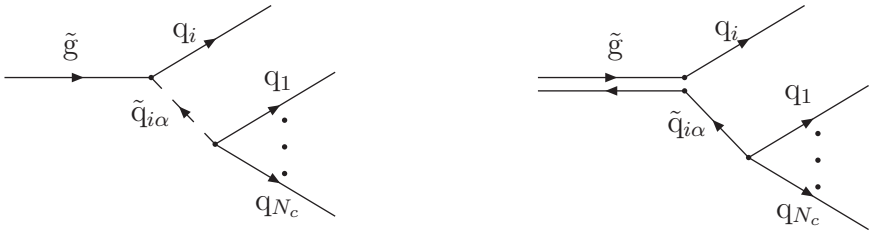

(a) Feynman Diagram (b) Colour Flow

Figure 2.12: Baryon number violating decay of the $\tilde{g}$. There are $N_c - 1$ quarks coupling to the squark at the lower vertex, *i.e.* all the quarks produced in the gluino decay apart from the quark i.

be written as in Eqn. 2.55 where here the tree-level colour factor

$$C_{\mathbf{m}} = \mathbf{t}^b_{c_i c'_i} \epsilon^{c_1 \ldots c'_i \ldots c_{N_c}} \mathbf{t}^b_{c''_i c_i} \epsilon^{c_0 \ldots c''_i \ldots c_{N_c}} = C_F N_c!. \tag{2.109}$$

We have not averaged over the initial colours and the radiation function is given by

$$\begin{aligned} W(\Omega_q) \;=\; & C_A W^0_{0i} + 2C_F W^i_{i0} + \frac{2C_F}{(N_c-1)} \sum_{j\neq i, k\neq j}^{N_c} W^j_{jk} + \frac{1}{(N_c-1)} \sum_{j\neq i}^{N_c} \left(C_A W^0_{0j} + 2C_F W^j_{j0} \right) \\ & + \frac{1}{N_c} W^i_{i0} + \frac{1}{N_c(N_c-1)} \sum_{j\neq i}^{N_c} \left(W^j_{j0} - W^i_{ij} - W^j_{ji} \right). \end{aligned} \tag{2.110}$$

This planar part of the soft radiation pattern gives us the result we would naïvely expect. The radiation pattern, Eqn. 2.110, contains terms, the second line of Eqn. 2.110, which are of order $1/N_c^2$ with respect to the leading-order terms which we shall neglect as in Section 2.3.2. The first term, in Eqn. 2.110, describes radiation from the gluino up to the direction of the ith quark. The second term describes radiation from the direction of the ith quark up to the direction of the gluino. Hence the colour line of the gluino and the ith quark should be colour connected as for MSSM processes.

As for both the squark and electroweak gaugino decays we have already considered we must now assign colour partners, with the correct probabilities, for the remaining quarks and the anticolour line of the gluino. The third term, in Eqn. 2.110, after azimuthal averaging, describes radiation from the direction of one of the final-state quarks, which is not connected to the colour line of the gluino, up to the directions of all the other final-state quarks, apart from the quark which is connected to the colour line of the gluino. The next term then describes radiation from the anticolour line of the gluino in cones up to the directions of all the final-state quarks, apart from the quark which is connected to the colour line of the gluino. The final, non-suppressed, term describes radiation from one of the final-state quarks, not connected to the colour line of the gluino, up to the direction of the gluino. We can therefore treated the anticolour line of the gluino and

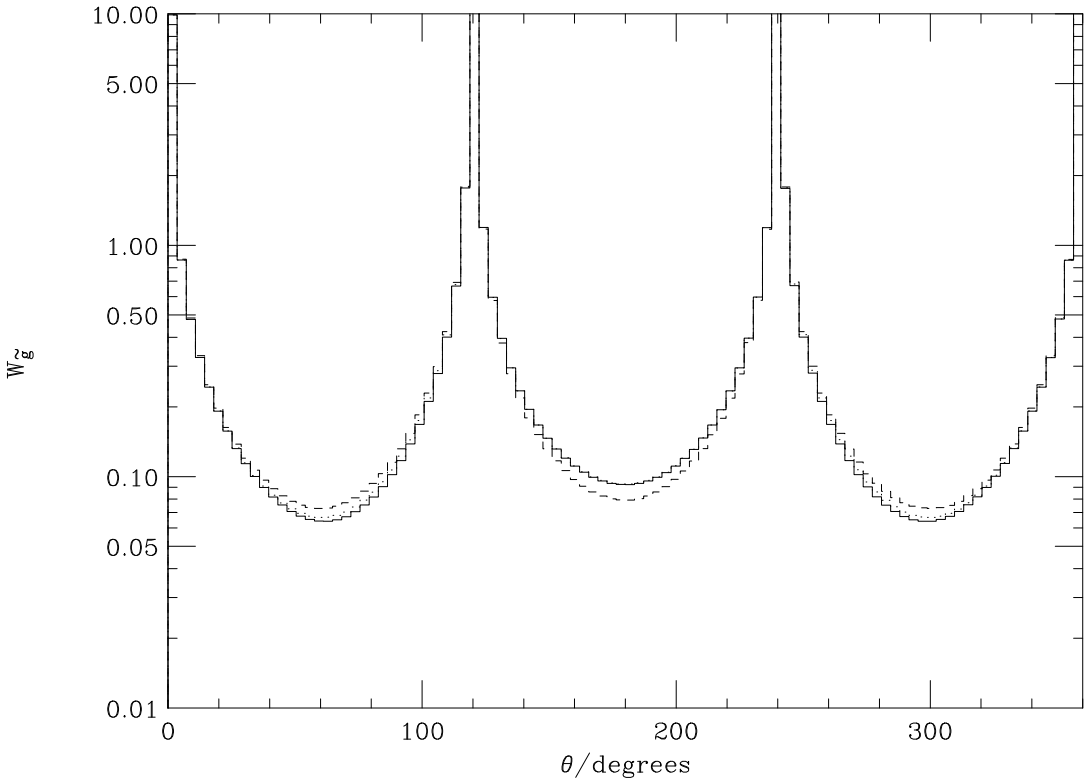

Figure 2.13: Soft gluon radiation pattern for $\tilde{g} \to qqq$. The decay is in the rest frame of the gluino and the quarks are along the directions $\theta = 0^0$, $\theta = 120^0$ and $\theta = 240^0$. The quark at $\theta = 0^0$ is colour connected to the gluino in the standard MSSM way while the other two quarks are colour connected to the gluino via the $\not{B}$ vertex. As before, the solid line gives the full radiation pattern, the dashed line the angular-ordered radiation pattern and the dotted line the improved angular-ordered radiation pattern.

the remaining quarks in the same way as a decaying antisquark. The anticolour line of the gluino should be randomly connected to one of the quarks which is not connected to the colour line of the gluino and the final-state quarks which are not connected to the colour line of the gluino should be connected at random to either the anticolour line of the gluino or the other final-state quark which is not connected to the colour line of the gluino. This assigns the colour partners with the correct probabilities. This is only the procedure for one of the N_c possible planar diagrams.

If we now consider all the possible planar colour flows the correct procedure is to connect the ith quark to the colour line of the gluino in the standard MSSM way with probability given by $\frac{|\overline{M}|^2_{\text{full},i}}{|\overline{M}|^2_{\text{tot}}}$, where $|\overline{M}|^2_{\text{full},i}$ is given by Eqn. 2.89. We can then treat the anticolour line of the gluino and the remaining quarks as an antisquark decaying to quarks.

The soft gluon radiation pattern for one of the possible planar diagrams is shown in Fig. 2.13. There is slightly less radiation between the quark at $\theta = 0^0$ and the other two quarks as the quark at $\theta = 0^0$ is not colour connected to either of the other two quarks. There is however more radiation between the other two quarks which are colour connected.

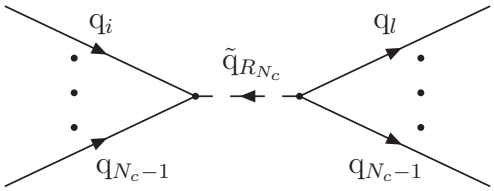

Figure 2.14: Resonant squark production followed by $\not{B}$ decay for an arbitrary number of colours N_c.

2.6.2 Hard Processes

In addition to the decays which we have already discussed there are a number of baryon number violating hard subprocesses which we include in the simulation. All of the colour structures of the hard processes which actually violate baryon number have already been discussed, as these processes are merely crossed versions of the various decays discussed above. However, in addition to these processes there are some hard processes which occur via the third term in the superpotential but involve no net baryon number violation, *e.g.* Fig. 2.14.

In this section we will only discuss this type of process which cannot be obtained by crossing the previous results.

2.6.2.1 Resonant Squark production followed by $\not{B}$ Decay

As before, we will consider the process in Fig. 2.14 for an arbitrary number of colours, N_c. We can write the matrix element for the emission of an extra soft gluon in the form

$$\mathcal{M}(p_1,\ldots,p_{N_c-1}:k_1,\ldots,k_{N_c-1};q) = g_s\mathbf{m}(p_1,\ldots,p_{N_c-1}:k_1,\ldots,k_{N_c-1}),\cdot\mathbf{J}(q), \quad (2.111)$$

where

- $\mathbf{m}(p_1,\ldots,p_{N_c-1}:k_1,\ldots,k_{N_c-1})$ is the tree-level matrix element for the (N_c-1) quarks to (N_c-1) quarks scattering.
- $\mathcal{M}(p_1,\ldots,p_{N_c-1}:k_1,\ldots,k_{N_c-1};q)$ is the tree-level matrix element for the (N_c-1) quarks to (N_c-1) quarks scattering with the emission of an extra soft gluon with momentum q.
- $\mathbf{J}(q)$ is the non-Abelian semi-classical current for the emission of the soft gluon, with momentum q, from the hard partons.
- $p_1,\ldots,p_{N_c-1}$ are the momenta of the partons in the initial state.
- $k_1,\ldots,k_{N_c-1}$ are the momenta of the partons in the final state.

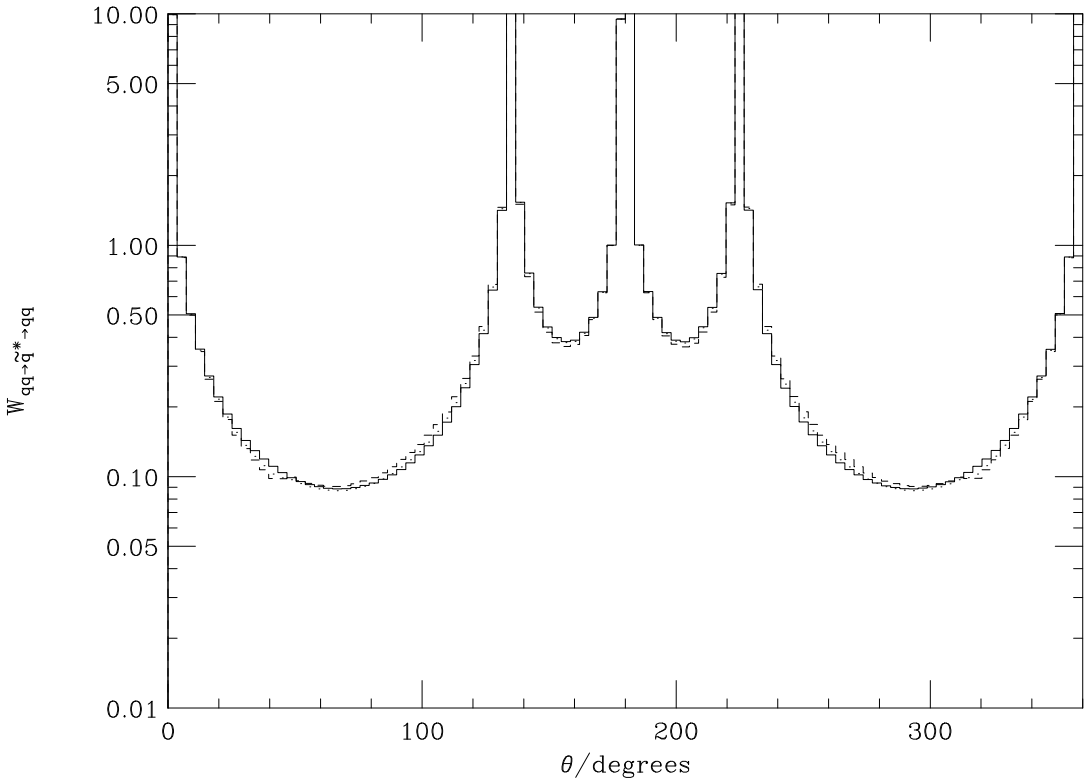

Figure 2.15: Soft gluon radiation pattern for $qq \to \tilde{q}^* \to qq$. The incoming quark directions are $\theta = 0^0$ and $\theta = 180^0$. The outgoing quark directions are $\theta = 135^0$ and $\theta = 225^0$. This process is shown in a frame which is boosted along the beam direction as will usually occur in hadron–hadron collisions. The solid line gives the full radiation pattern, the dashed line the angular-ordered approximation and the dotted line the improved angular-ordered approximation.

Again the current has the form $\mathbf{J}(q) = \sum_{s=1,2} \mathbf{J}^{b,\mu}(q)\varepsilon^*_{\mu,s}$, where in this case

$$\begin{aligned} \mathbf{J}^{b,\mu}(q) &= -\sum_{i=1}^{N_c-1} \left(\frac{p_i^\mu}{p_i \cdot q}\right) \mathbf{t}^b_{c'_i c_i} \epsilon^{c_1 \ldots c'_i \ldots c_{N_c}} \epsilon^{d_1 \ldots d_{N_c-1} c_{N_c}} \\ &\quad + \sum_{i=1}^{N_c-1} \left(\frac{k_i^\mu}{k_i \cdot q}\right) \mathbf{t}^b_{d_i d'_i} \epsilon^{c_1 \ldots c_{N_c-1} d_{N_c}} \epsilon^{d_1 \ldots d'_i \ldots d_{N_c}}, \end{aligned} \tag{2.112}$$

where b and μ are the colour and Lorentz indices of the emitted gluon, respectively.

We can obtain the soft gluon distribution by squaring the current. The result can be rewritten using Eqn. 2.55 where the tree-level colour factor is given by $C_{\mathbf{m}} = N_c!(N_c-1)!$. We have not averaged over the initial colours, and the radiation

function is given by

$$W(\Omega_q) = \frac{2C_F}{(N_c-1)}\sum_{i=1}^{N_c-1}\sum_{j\neq i}W_{ij}^{i} + \frac{2C_F}{(N_c-1)}\sum_{l=1}^{N_c-1}\sum_{m\neq l}W_{lm}^{l} + \frac{2C_F}{(N_c-1)^2}\sum_{i=1}^{N_c-1}\sum_{l=1}^{N_c-1}\left(W_{li}^{i}+W_{il}^{l}\right), \quad (2.113)$$

where the partons i and j are in the initial state and the partons l and m are in the final state.

If we now only consider three colours, the first term in this radiation pattern describes radiation from one of the initial-state quarks in cones up to the direction of the other initial-state quark, after azimuthal averaging. Similarly, the second term describes radiation from the direction of one of the final-state quarks up to the direction of the other final-state quark. Both of these have probability $1/(N_c-1) = 1/2$ relative to the case of a quark and its Standard Model colour partner. The remaining terms describe radiation from one of the final-state quarks up to the direction of either of the initial-state quarks and radiation from one of the initial-state quarks up to the direction of either of the final-state quarks. The probability for radiation from one of the final-state quarks up to the direction of one of the incoming quarks is $1/(N_c-1)^2 = 1/4$ relative to the Standard Model case.

This radiation pattern gives quite an unusual angular-ordering procedure. If we consider one of the quarks in the initial state, this quark should be randomly connected to any of the other quarks in the initial state or to the intermediate squark. If the quark is connected to the intermediate squark it should then be randomly connected to any of the final-state quarks. Similarly the final-state quarks are connected at random to any of the other final-state quarks or the intermediate squark, and again quarks connected to the intermediate squark are then randomly connected to any of the initial-state quarks. This correctly assigns the probabilities of the colour partners described above.

The radiation pattern for this process is shown in Fig. 2.15. There is less radiation between the two outgoing quarks and the quark at $\theta = 0^0$ than between the outgoing quarks and the quark at $\theta = 180^0$. This is because, while there are some colour connections between the incoming and outgoing quarks, due to the random nature of the colour connection at the $\not{B}$ vertex, the main colour connection is between the two quarks in the initial state and the two quarks in the final state. As the angular distance between the two outgoing quarks is smaller about $\theta = 180^0$ there is more radiation in this direction.

2.7 Hadronization of $\not{R}_p$ Processes

As we saw in Section 2.6, it is possible to angular order the baryon number violating decays and hard processes. It is then necessary to decide how to hadronize these events using the cluster hadronization model [94] in order to include a full simulation of these processes in the HERWIG event generator. The procedure described in Section 2.4 also works for the MSSM provided that the lifetime of the coloured sparticles does not exceed

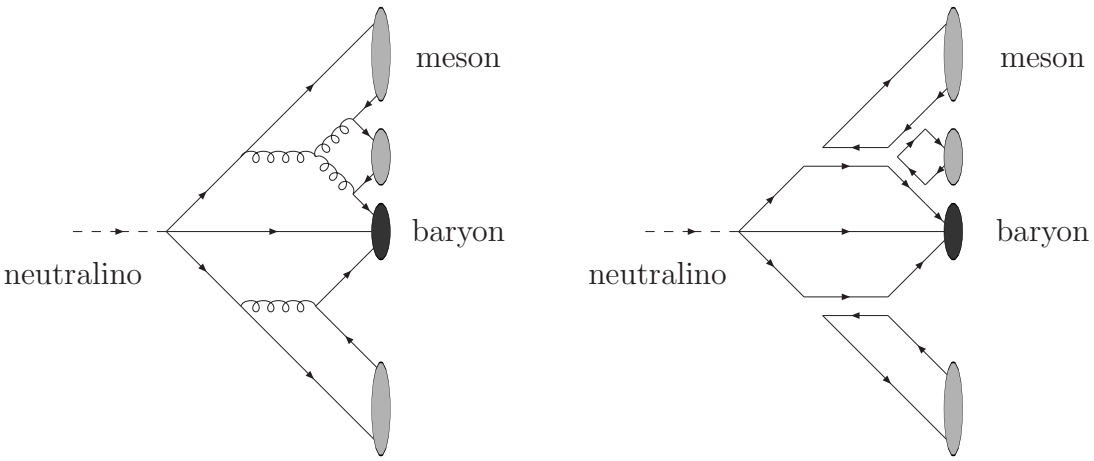

(a) Feynman diagram (b) Colour flow

Figure 2.16: The Feynman diagram and colour flow for the hadronization of a $\not{B}$ neutralino decay. No QCD radiation from the central quark has been shown for simplicity, in general this quark can also radiate.

the hadronization time-scale. However, some modifications to this model are required for $\not{R}_p$ processes.

In the Standard Model and MSSM cases the colour partner for the colour coherence effects and for the hadronization phase are always the same. However in the $\not{B}$ decays and hard processes we see for the first time cases where the colour connection for the angular ordering and for the hadronization can be different. This is because while the colour connection for the angular-ordering procedure is determined by the eikonal current, the colour connection for the hadronization phase is defined by the colour flow in the leading-order diagram. When baryon number is conserved these are identical, however when baryon number is violated, there are cases where the two are different.

First we consider the simplest type of decay, *i.e.* a neutralino or chargino decaying to three quarks. The method described in Section 2.6 correctly implements the angular-ordering procedure. After the parton-shower phase (and the splitting of the remaining gluons into quark–antiquark pairs) we will be left with pairs of colour-connected partons forming colour singlets as well as three further quarks. An example of this is shown in Fig. 2.16. These three remaining quarks form a colour singlet with baryonic quantum numbers, a baryonic cluster. To handle baryonic clusters HERWIG needs the constituents to be labelled as one quark and one diquark rather than three quarks, so we randomly pair two of them into a diquark. In our example in Fig. 2.16 the three quarks in the middle together form a colour singlet. Two of these quarks are paired into a diquark which combines with the remaining quark to form a baryonic cluster. The mesonic clusters will decay to give either two mesons, or a baryon–antibaryon pair, while the baryonic cluster will decay to give a meson and a baryon.

This procedure is relatively easy to implement in the case of electroweak gaugino decays. However it becomes more difficult in the case of the $\not{B}$ decay of an antisquark

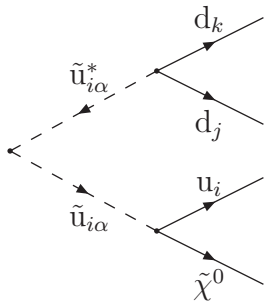

Figure 2.17: Hadronization with one $\not{B}$ decay.

to two quarks. If the anticolour partner of the decaying antisquark is a particle which decays via a baryon number conserving process then the two quarks and the particle which gets the colour of the second decaying particle can be clustered as in the neutralino case, *e.g.* in Fig. 2.17 the u_i, d_j, and d_k should be formed into a baryonic cluster. In general, we do not form these quarks into the colour-singlet baryonic cluster but the parton produced in the parton shower of these partons which inherits the colour of the showering parton, as in Fig. 2.16.

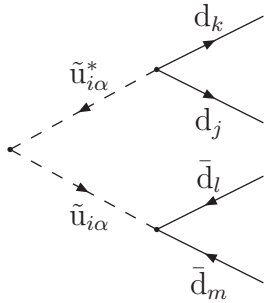

Figure 2.18: Hadronization with two $\not{B}$ decays.

However, if this second particle decays via $\not{B}$ then the procedure must be different, as shown in Fig. 2.18. Here, instead of forming one baryonic cluster, we form two mesonic clusters. This is done by pairing the d_k randomly with either the $\bar{\mathrm{d}}_l$ or $\bar{\mathrm{d}}_m$ into a standard colour-singlet cluster, the remaining quark and antiquark are also paired into a colour-singlet cluster. This is not the colour connection for the angular ordering procedure but the colour connection for the hadronization phase, which is different in this case and determined by the colour flow in the tree-level diagram.

This leaves the case of the gluino decay which looks more complicated but can be considered by treating the colour line as normal and the anticolour line like a decaying antisquark. If the anticolour partner of the gluino is a Standard Model particle or decays via a baryon number conserving MSSM decay mode we form the three quarks into a baryonic cluster. However if the anticolour partner decays via a $\not{B}$ mode we then form two mesonic clusters.

There is one further type of colour flow to be considered, which is the production of a resonant squark via baryon number violation which then also decays via $\not{B}$. The correct hadronization procedure in this case is similar to that adopted for the case of

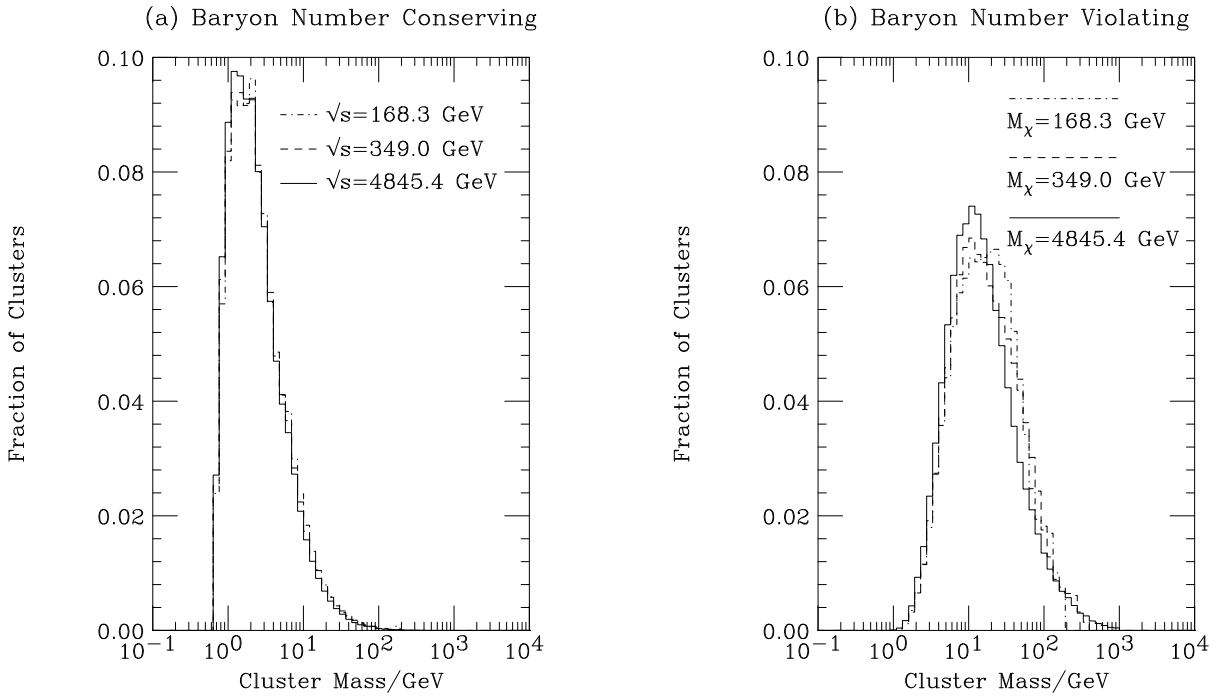

Figure 2.19: Distributions of the colour-singlet cluster masses. The baryon number conserving clusters come from e^+e^- events at the given centre-of-mass energy, $\sqrt{s}$, whereas the baryon number violating clusters come from decays of neutralinos at the given masses.

two colour connected $\not{B}$ decays. We randomly connect one of the final-state quarks to the colour partners of either of the initial-state quarks to form a colour-singlet cluster. The remaining final-state quark can then be paired with the colour partner of the other initial-state quark. This gives two colour-singlet clusters. Again the colour partner for hadronization is determined by the colour flow in the tree-level diagram.

Using the procedures we have outlined above it is possible to hadronize any of the $\not{B}$ decays or hard processes. There is however one potential problem. The cluster model is based on the idea of colour preconfinement. In $\not{B}$ processes we see a very different spectrum for the baryonic clusters formed from the baryon number violation to that seen for clusters in Standard Model events.

Fig. 2.19 shows the spectra for both normal and $\not{B}$ clusters. The spectrum for the baryon number violating clusters peaks at a much higher mass than the baryon number conserving clusters and has a large tail at high masses. This therefore means that before these clusters are decayed to hadrons most of them must be split into lighter clusters. The baryon number conserving clusters in these events have the same spectrum as in Standard Model events. Fig. 2.19 contains the mass spectrum of pairs of colour-connected partons after the parton-shower phase and the non-perturbative splitting of the gluons into quark–antiquark pairs. The baryon number conserving clusters, Fig. 2.19a, contains all the clusters in e^+e^- events at the given centre-of-mass energies, whereas the baryon number violating clusters, Fig. 2.19b, only contains those clusters which contain the three quarks left after all the other quarks are paired into colour singlets from neutralino decays

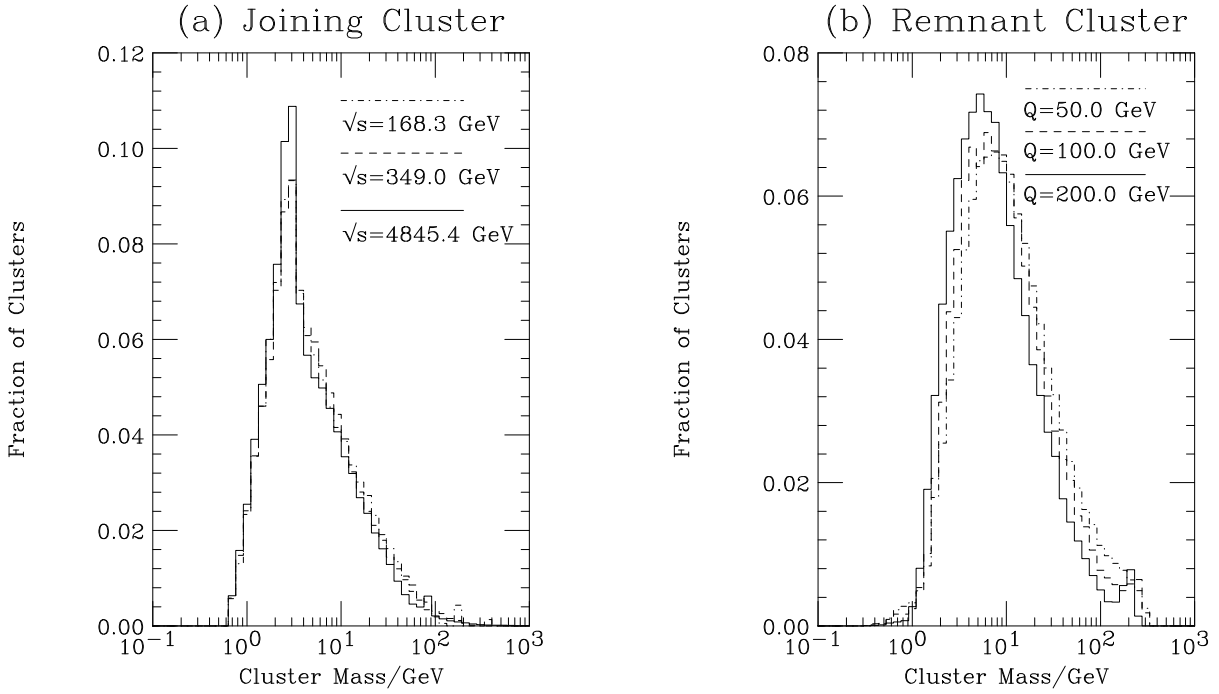

Figure 2.20: Masses of the joining and remnant clusters. The joining clusters are from e^+e^- events at the given centre-of-mass energy, $\sqrt{s}$. The remnant clusters were generated in e^-p events with 30 GeV electrons and 820 GeV protons with the given scale as the minimum value of the momentum transfer, Q.

at the given mass.

Fig. 2.20a shows the joining clusters, *i.e.* the clusters in e^+e^- events with a quark from the parton shower of the quark and an antiquark from the parton shower of the antiquark. The remnant clusters, Fig. 2.20b, come from the cluster in deep-inelastic scattering events which contains the diquark, formed from two of the valence quarks.

We would expect the baryon number violating clusters to be heavier than the standard baryon number conserving clusters because:

1. The baryonic cluster is formed from three quarks originating from three different jets, as shown in Fig. 2.19 from the neutralino decay. In normal, *i.e.* baryon number conserving, $e^+e^- \rightarrow$ hadrons events the clusters joining partons from different jets, *i.e.* containing a parton from each jet, are heavier than the clusters which come entirely from partons from one jet, Fig. 2.20a.

2. The $\not{B}$ cluster contains a diquark and in general the clusters containing diquarks, in for example the hadron remnant in deep-inelastic scattering, are heavier than the quark–antiquark clusters, Fig. 2.20b.

As these clusters are heavier they will be more sensitive to the fine details of the hadronization model. In particular, these clusters are sensitive to the maximum cluster mass before the clusters are split into lighter clusters and the details of this splitting mechanism. This is also true for the clusters which join jets in $e^+e^- \rightarrow 3$ jet events and it is these clusters

which contribute to the "string effect", which is well described by HERWIG. The mass distribution of the remnant in deep-inelastic scattering events at HERA is also reasonably well described by the cluster model.

2.8 Results

We have implemented R-parity violating decays and hard processes into the HERWIG Monte Carlo event generator according to the algorithms given in Sections 2.6 and 2.7. They are available in the current version HERWIG 6.1 [2]. Having taken care to implement colour coherence effects, it is of immediate interest to see whether they have a significant influence on observable final-state distributions. To this end we have studied some jet production processes and compared the final-state distributions with those from standard QCD di-jet events. It was observed in [88] that certain variables can be constructed which are particularly sensitive to colour coherence effects. In particular these variables are sensitive to the presence of colour connections that link the initial and final states. To investigate these effects for the different colour-connection structures of the $\not{R}_p$ models, we will study these variables for jet production via resonant sparticle production in hadron–hadron collisions. We essentially follow the details of the analysis of [88].

As examples, we study the processes:

- $\bar{u}d \to \bar{u}d$ via a resonant stau, and $\bar{d}d \to \bar{d}d$ via a resonant tau sneutrino. These occur via the coupling λ'_{311}. The Feynman diagrams for these processes are shown in Fig. 2.21. This process involves lepton number violating couplings but no baryon number violating vertices.

- Resonant squark production via the coupling λ''_{212}. This leads to resonant down, strange and charm squark production. The resonant diagram for this process is shown in Fig. 2.14.

These processes were chosen to try to maximize the cross section at the Tevatron given the current low energy limits on the couplings. The coupling λ'_{311} has an upper bound, at the 2σ level, given by [5]

$$\lambda'_{311} < 0.11 \left(\frac{M_{\tilde{d}_R}}{100 \text{ GeV}} \right). \tag{2.114}$$

While the bounds on other LQD couplings are weaker, they involve higher generation quarks and hence the cross sections will be suppressed by the parton luminosities. As we will see in Chapter 3, for the values of the couplings which are still allowed by the current experimental limits [5], these processes may not be visible above the large QCD background.

Similarly for resonant squark production, the couplings which couple to two first generation quarks would in principle give the highest cross sections. However, the limits on these couplings are so strict that we used the λ''_{212} coupling which is only limited by perturbativity [5]. At the Tevatron these processes have a very low cross section due to the requirement for two quarks to be carrying a high fraction of the incoming proton or

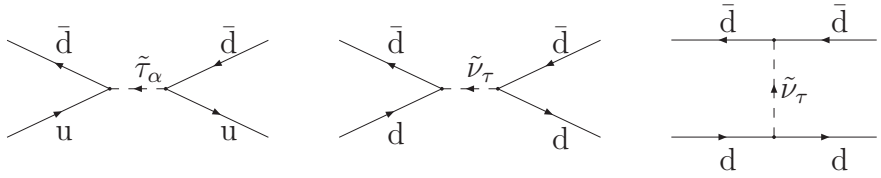

Figure 2.21: Feynman diagrams for $\bar{u}d \to \bar{u}d$ via resonant charged slepton production and $\bar{d}d \to \bar{d}d$ via resonant sneutrino production and t-channel sneutrino exchange.

anti-proton's momentum in the initial state. This means that resonant squark production followed by a $\not{B}$ decay will never by visible above the QCD background. Here we will simply look at the difference in the observables used in [88] for the two different processes and the QCD background.

We would expect very different results for the variables which are sensitive to the initial–final state colour connections for these two processes. In particular the first process only has this type of connection for the t-channel sneutrino diagram, which gives a small contribution close to the resonance, whereas the second process does have initial–final state colour connections, due to the random colour structure at the $\not{B}$ vertex, for the resonant production mechanism.

We looked at both processes and QCD di-jet production using events generated with the program described in [2]. The cone algorithm, with a cone-size in (η, ϕ) of 0.7 radians, was used to define the jets for this study. The actual algorithm used is very similar to that used by CDF apart from taking the midpoint between two particles as a seed for the algorithm in addition to the particles themselves. The inclusion of the midpoints as seeds improves the infra-red safety of the cone algorithm. The only cut was to require the presence of at least one jet with transverse energy, E_T, greater than 200 GeV in the event. A parton-level cut requiring the transverse momentum, p_T, of the two final-state partons to be greater than 150 GeV was used to reduce the number of events we needed to simulate, however this should not affect the results. The signal points were generated using the following SUGRA parameters:

Resonant Slepton $M_0 = 600$ GeV, $M_{1/2} = 200$ GeV, $A_0 = 0$ GeV, $\tan\beta = 10$, $\operatorname{sgn}\mu = +$ and $\lambda'_{311} = 0.8$;

Resonant Squark $M_0 = 430$ GeV, $M_{1/2} = 200$ GeV, $A_0 = 0$ GeV, $\tan\beta = 10$, $\operatorname{sgn}\mu = +$ and $\lambda''_{212} = 1.0$.

These points were chosen so that the resonant sleptons and squarks have approximately the same mass. At the first point the slepton masses are $M_{\tilde{\tau}_1} = 599$ GeV, $M_{\tilde{\tau}_2} = 617$ GeV and $M_{\tilde{\nu}_\tau} = 610$ GeV, while at the second point the squark masses are $M_{\tilde{d}_R, \tilde{s}_R, \tilde{c}_R} = 602$ GeV.

We can now study the events about the resonance by imposing a cut 580 GeV $\leq M_{jj} \leq$ 640 GeV and plotting the variables that are sensitive to angular ordering for these events. These variables depend on the distribution of a third jet in

the events which is generated in the simulation by the parton-shower algorithm. Three variables, η_3, R and α were considered. They are defined in the following way [88]:

- If we define the jets in the event in order of their E_T, with jet 1 being the hardest jet in the event, then η_3 is the pseudo-rapidity of the third jet.
- Defining $\Delta\eta = \eta_3 - \eta_2$ and the difference in polar angles $\Delta\phi = \phi_3 - \phi_2$, then the variable R is the distance between the second and third jets in (η, ϕ) space, *i.e.* $R = \sqrt{\Delta\eta^2 + \Delta\phi^2}$.
- If we define $\Delta H = \text{sgn}(\eta_2)\Delta\eta$, we can consider the polar angle in $(|\Delta\phi|, \Delta H)$ space, $\alpha = \tan^{-1}(\Delta H/|\Delta\phi|)$.

In the analysis of [88] additional cuts had to be imposed, which we also use here:

1. a pseudo-rapidity cut on the highest two p_T jets in the event, $|\eta_1|, |\eta_2| < 0.7$;
2. requiring the two leading jets to be back-to-back $||\phi_1 - \phi_2| - 180^0| < 20^0$;
3. third jet transverse energy $E_{T_3} > 10$ GeV to avoid background from the underlying event;
4. a final cut used only for the study of α is that $1.1 < R < \pi$ to avoid problems with the jet clustering algorithm.

We can now study these variables for resonant slepton and squark production, and for QCD di-jet events. The results in all the graphs correspond to the number of events at the Run II Tevatron centre-of-mass energy of 2 TeV and integrated luminosity of 2 fb^{-1}.

There are a number of differences in the observables η_3, R and α for resonant slepton production and QCD jet production. In particular, in the η_3 distributions instead of a dip in the distribution at $\eta_3 = 0$ for the QCD jet production, Fig. 2.22c, there is a bump for the resonant slepton production, Fig. 2.22a. This dip in the QCD jet production was observed in [88], and is a feature of the initial–final state colour connections which are present in QCD jet production, but not in resonant slepton production.

The distribution of the distance in $(\Delta\eta, \Delta\phi)$ space, R, is very similar for both resonant slepton production, Fig 2.23a, and QCD jet production, Fig 2.23c . In the study of [88] all the event generators, even those which do not include angular ordering, gave good agreement with the data for this observable. The distribution of the polar angle α also shows a difference between resonant slepton production, Fig. 2.24a, and QCD jet production, Fig. 2.24c, with the resonant slepton production not showing the dip in the middle which is again an effect of the initial–final state colour connections which are present in QCD jet production but not in resonant slepton production.

There is less difference for the variables η_3, R and α between resonant squark production and QCD jet production shown in Figs. 2.22, 2.23 and 2.24. The distributions for the two resonant production processes are different. The distribution for resonant squark production shows the dip at $\eta_3 = 0$ and the rise as $\alpha \to \frac{\pi}{2}$ which is due to the colour connections in these processes between the initial and final states. The effect of the colour flow between the initial and final states is less for this process than for QCD

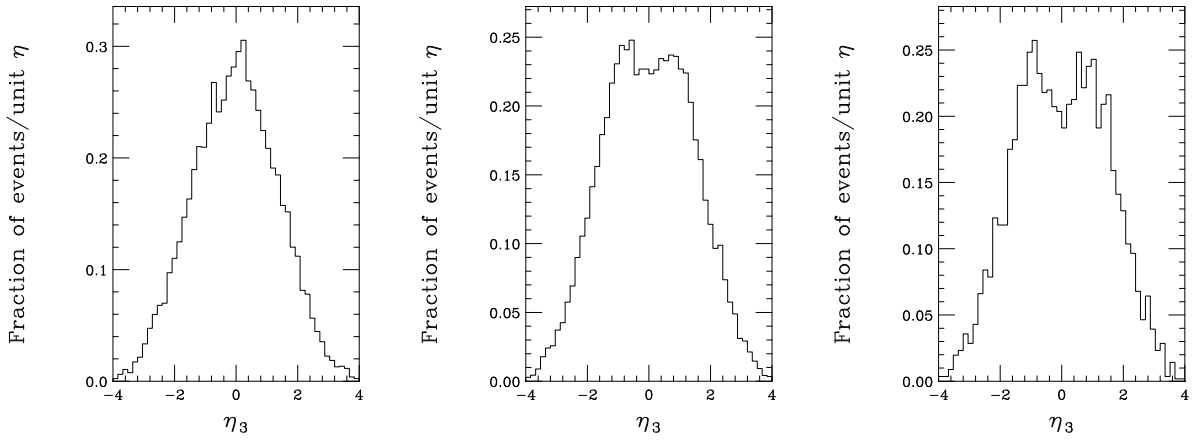

(a) Resonant slepton (b) Resonant squark (c) QCD di-jet

Figure 2.22: Distribution of η_3 for resonant slepton, resonant squark and QCD jet production.

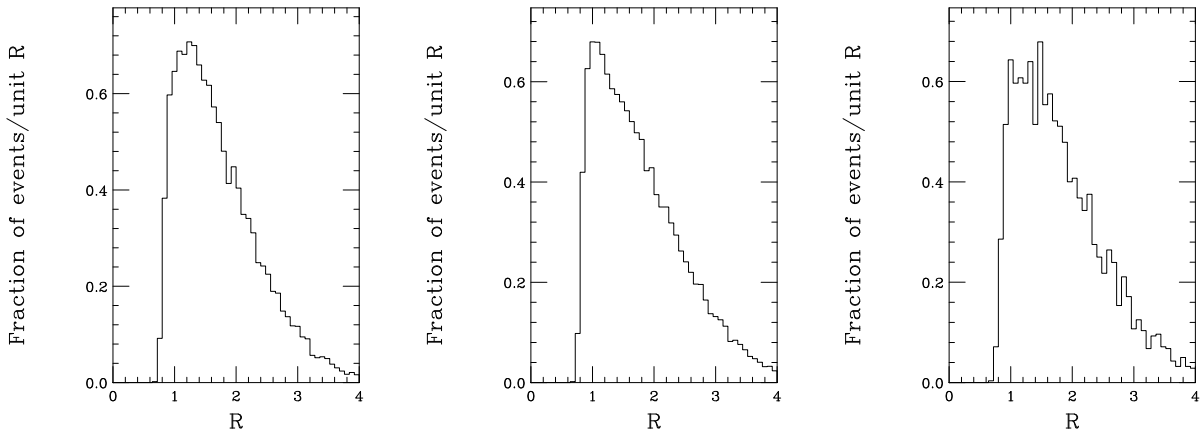

(a) Resonant slepton (b) Resonant squark (c) QCD di-jet

Figure 2.23: Distribution of R for resonant slepton, resonant squark and QCD jet production.

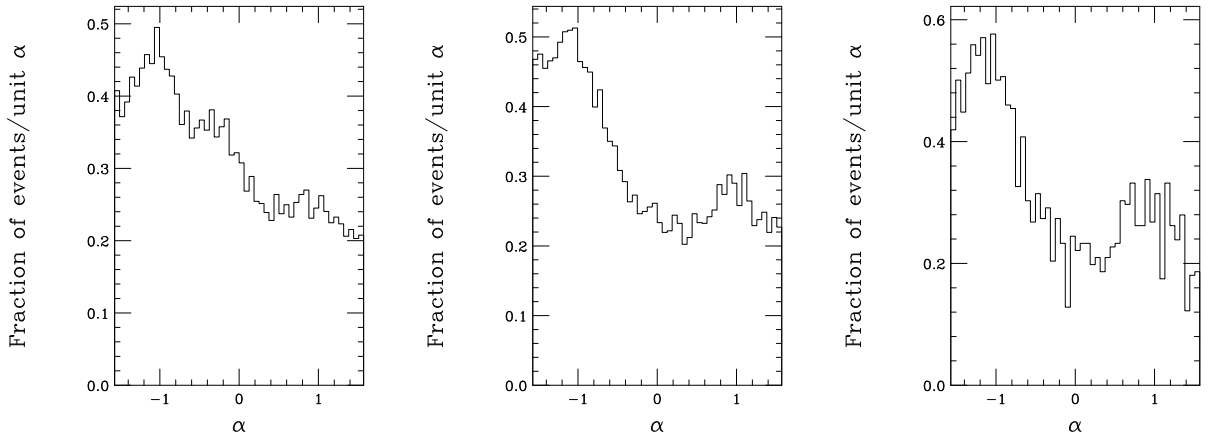

(a) Resonant slepton (b) Resonant squark (c) QCD di-jet

Figure 2.24: Distribution of α for resonant slepton, resonant squark and QCD jet production.

jet production as there are combinatorially fewer such connections for resonant squark production.

The fact that the final-state distributions of the resonant slepton and resonant squark production processes are so different, despite the identities and kinematics of the jets themselves being so similar, clearly shows that colour coherence plays an important rôle in determining the properties of R-parity violating processes. Even if this is not used as a tool to enhance the signal, it is likely that it will effect the efficiency of any cuts that are applied, so it is essential that any experiments looking for R-parity violating processes take into account colour coherence in their simulations of the signal.

Even if R-parity violating hard processes were added to ISAJET [75], this event generator would not be expected to describe the final state well, as it is based on the incoherent parton shower and independent fragmentation models. Thus, in our case for example, resonant slepton and resonant squark processes would have very similar properties. It is worth noting that ISAJET gives a poor description of the CDF data [88] on η_3 and α in standard QCD di-jet events.

2.9 Summary

We have presented a procedure for implementing colour coherence effects via the angular-ordering procedure in $\not{R}_p$ SUSY models. We find that the $\not{B}$ processes have a random colour connection structure for angular ordering. In these processes we see, for the first time, differences in the colour partners for the colour coherence effects and those used, with the idea of colour preconfinement, for hadronization in the cluster model.

A full set of decays and hadron–hadron cross sections have now been implemented in the HERWIG Monte Carlo event generator [2, 102], using the matrix elements given in Appendices B and C. The first preliminary results for these processes show that the inclusion of colour coherence is important. In the next chapter we will look at the possibility of using these colour coherence properties to improve the extraction of a resonant slepton signature at the Tevatron.

These simulations have allowed the first experimental studies of the possibility of discovering $\not{R}_p$ supersymmetry via the baryon number violating decay of the neutralino at the LHC [103].

Chapter 3

Resonant Slepton Production in Hadron–Hadron Collisions

3.1 Introduction

In the previous chapter we discussed how to include R-parity violating processes into a Monte Carlo simulation. We then briefly looked at the differences in the final states for resonant squark and slepton production, which were solely due to the different colour structures of the two different processes. In this chapter we will look at resonant slepton production in hadron colliders and ways in which it can be detected using the simulations described in the previous chapter. In hadron colliders, as we saw in the previous chapter, sleptons can be produced on resonance via the $\not{R}_{\rm p}\ L_iQ_j\overline{D}_k$ term in the superpotential, Eqn. 1.63.

Resonant slepton production in hadron–hadron collisions has previously been considered in [5, 6, 65–68]. The signature of this process depends on the decay mode of the resonant slepton. The various possible decay channels are given in Table 3.1. The cross

	Charged Sleptons	Sneutrinos
Supersymmetric Gauge Decays	$\tilde{\ell}_{i\alpha} \to \ell_i^- \tilde{\chi}^0$	$\tilde{\nu}_i \to \nu_i \tilde{\chi}^0$
	$\tilde{\ell}_{i\alpha} \to \nu_i \tilde{\chi}^-$	$\tilde{\nu}_i \to \ell_i^- \tilde{\chi}^+$
$\not{R}_{\rm p}$ Decays	$\tilde{\ell}_{i\alpha} \to \bar{\rm u}_j {\rm d}_k$	$\tilde{\nu}_i \to \bar{\rm d}_j {\rm d}_k$
	$\tilde{\ell}_{i\alpha} \to \bar{\nu}_j \ell_k^-$	$\tilde{\nu}_i \to \ell_j^+ \ell_k^-$
Weak Decays	$\tilde{\ell}_{i\alpha} \to \tilde{\nu}_i {\rm W}^-$	$\tilde{\nu}_i \to \tilde{\ell}_{i\alpha} {\rm W}^+$
	$\tilde{\ell}_{i2} \to \tilde{\ell}_{i1} {\rm Z}_0$	
Higgs Decays	$\tilde{\ell}_{i\alpha} \to \tilde{\nu}_i {\rm H}^-$	$\tilde{\nu}_i \to \tilde{\ell}_{i\alpha} {\rm H}^+$
	$\tilde{\ell}_{i2} \to \tilde{\ell}_{i1} {\rm h}_0, {\rm H}_0, {\rm A}_0$	

Table 3.1: Decay modes of charged sleptons and sneutrinos. The index $i, j, k = 1, 2, 3$ gives the generation of the fermion or sfermion and the index $\alpha = 1, 2$ the mass eigenstate of the sfermion as described in Appendix A.

sections for resonant slepton production followed by these decay modes are given in Appendix C. Most of the previous studies have only considered the $\not{R}_p$ decays of the resonant slepton to either leptons via the first term in Eqn. 1.63 [5, 65–67], or to quarks via the second term in Eqn. 1.63 [5, 65, 67].

We shall first consider the $\not{R}_p$ decay modes and look at the use of the angular-ordering properties of these processes to improve the extraction of a signal over the QCD background in Section 3.2.

There has been little study of the supersymmetric gauge decays of the resonant sleptons. The cross sections for these processes were first presented in [65][1] where there was a discussion of the possible experimental signatures, however the signal we will consider was not discussed and there was no calculation of the Standard Model background. The supersymmetric gauge decays of the sneutrinos have been studied [6, 68]. These studies were performed using a detector-level Monte Carlo simulation for both the signal and background processes. These analyses looked at the trilepton signature for resonant sneutrino production, which comes from the decay chain $\tilde{\nu} \to \ell^- \tilde{\chi}^+$, followed by a decay of the chargino, $\tilde{\chi}^+ \to \ell^+ \nu_\ell \tilde{\chi}_1^0$, and the decay of the neutralino to a lepton and a quark–antiquark pair. A study of the supersymmetric gauge decays of the sleptons is presented in Section 3.3, where we look at the like-sign dilepton signature for these processes.

There has been no study of either the weak or Higgs decay modes for which, in general, the resonance is not kinematically accessible, although for completeness these have been included in the HERWIG event generator [2] and the cross sections are presented in Appendix C.

3.2 $\not{R}_p$ Decays of the Resonant Slepton

There are two types of $\not{R}_p$ decay modes of the resonant sleptons:

1. The first requires that in addition to the $\not{R}_p$ Yukawa coupling which allows the resonant slepton production there is a second non-zero coupling, λ_{ijk}, allowing the decays $\tilde{\ell}_{i\alpha} \to \bar{\nu}_j \ell_k^-$ and $\tilde{\nu}_i \to \ell_j^+ \ell_k^-$. This has been extensively studied [5, 65–67]. As there is only initial-state QCD radiation, from the quarks involved in the hard collision, in these processes the parton-level results of [5,65–67] should not be significantly affected by the addition of a full simulation. We therefore have not considered these processes.

2. It is also possible that the resonant slepton decays back to the initial state via the same coupling required for the resonant slepton production. We studied the colour coherence properties of these processes in the previous chapter and we will discuss them in more detail here.

We considered resonant slepton production followed by an $\not{R}_p$ decay using the same cuts which were applied in Section 2.8. We also used the same SUGRA point

[1] The cross sections for the resonant processes were only presented in the narrow-width approximation and the interference between the resonant and t-channel diagrams was neglected. Neutralino and chargino mixing was also neglected, and there were errors in the calculations of the non-resonant diagrams.

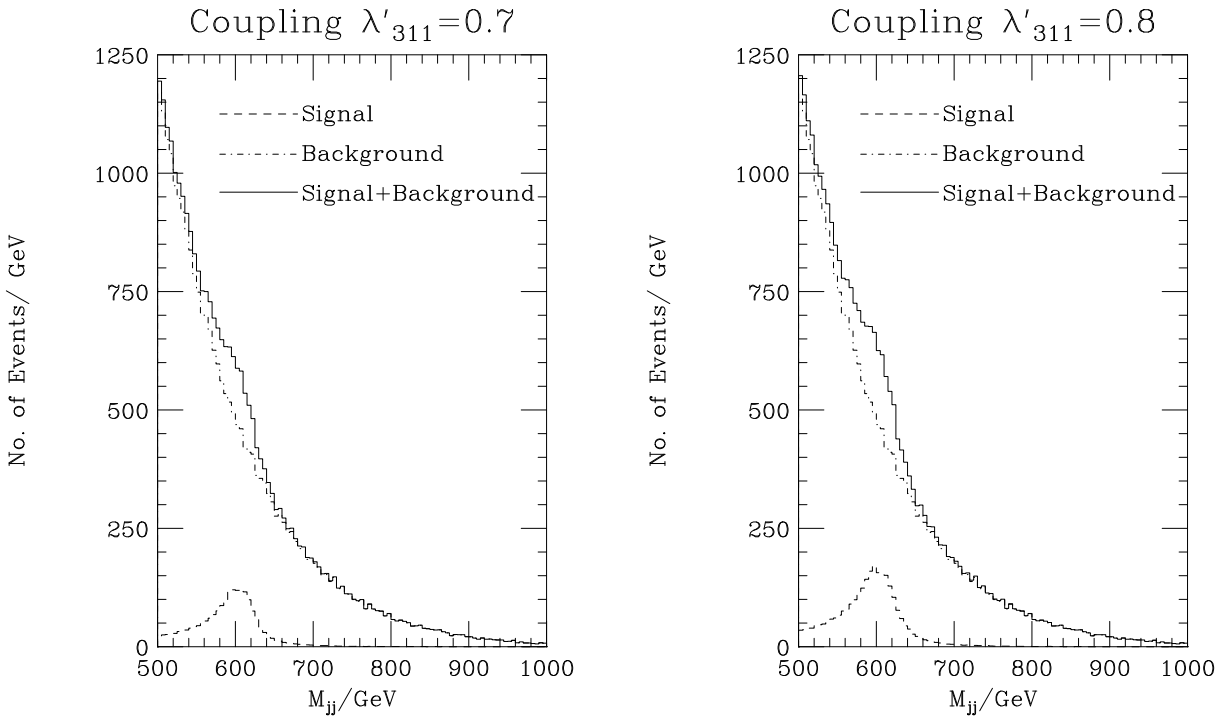

Figure 3.1: Di-jet invariant-mass distribution for $\lambda'_{311} = 0.7$ and $\lambda'_{311} = 0.8$.

$M_0 = 600$ GeV, $M_{1/2} = 200$ GeV, $A_0 = 0$ GeV, $\tan\beta = 10$ and $\mathrm{sgn}\,\mu = +$. The results in all the graphs correspond to the number of events at Run II of the Tevatron, with centre-of-mass energy of 2 TeV and integrated luminosity of 2 fb^{-1}. Again we used a cone algorithm with radius parameter of 0.7 radians to define the jets.

At this SUGRA point the right sdown mass is 728 GeV which corresponds to a limit on the coupling of $\lambda'_{311} < 0.80$, from Eqn. 2.114. As can been seen in Fig. 3.1, the results for two different values of the coupling show that there is a bump in the di-jet invariant-mass distribution, M_{jj}, from the resonant slepton production for large values of the coupling.

We can now consider the events around the bump, 580 GeV $\leq M_{jj} \leq$ 640 GeV, in the distribution and plot the variables that are sensitive to angular ordering for these events. These variables depend on the distribution of a third jet in the events which is generated in the simulation by the parton-shower algorithm. The definitions of the variables and the cuts used are the same as in Section 2.8.

We can now study the distributions for the signal, background, and signal plus background for resonant slepton production with coupling $\lambda'_{311} = 0.8$. As we saw in the previous chapter, there are significant differences between the signal and the background for this process which we will briefly recall here. In the η_3 distributions, Fig. 3.2, instead of a dip in at $\eta_3 = 0$ there is a bump in the signal. This dip in the QCD background was observed in [88], and is a feature of the initial-final state colour connection. In our study it is present in the background, but not the signal. The distribution of events in α, Fig. 3.4, also shows a difference between the signal and the background, with the signal not showing the dip in the middle. This is again an effect of the initial-final state colour connection which is present in the background but not in the signal.

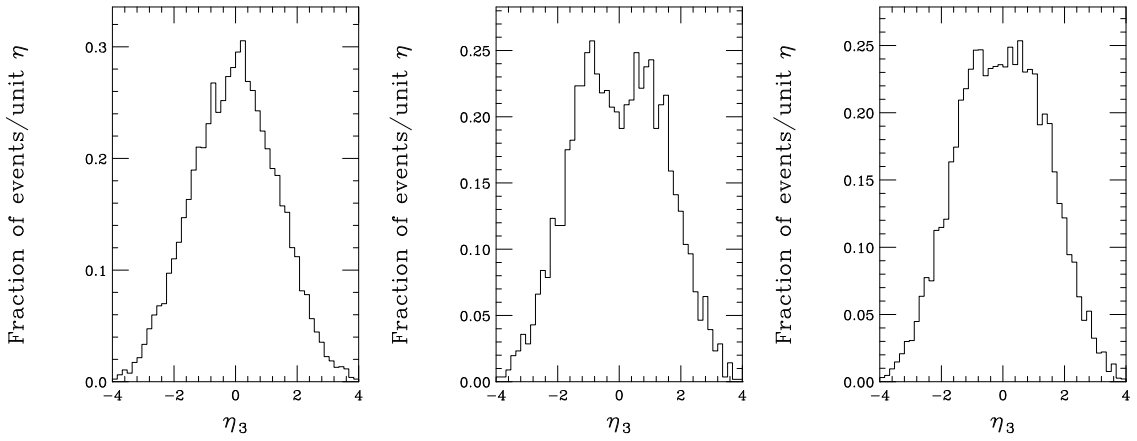

(a) Signal (b) QCD Background (c) Signal+Background

Figure 3.2: Distribution of events in η_3 for resonant slepton production and the QCD background.

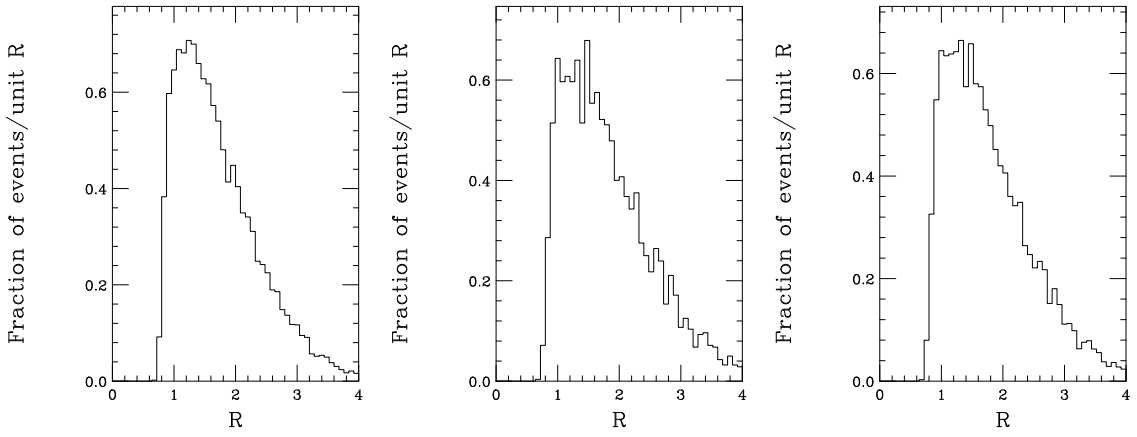

(a) Signal (b) QCD Background (c) Signal+Background

Figure 3.3: Distribution of events in R for resonant slepton production and the QCD background.

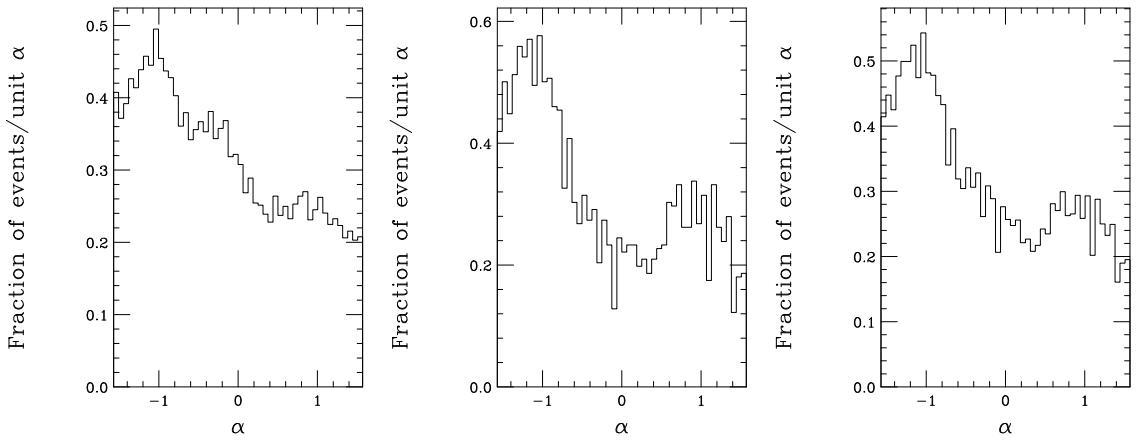

(a) Signal (b) QCD Background (c) Signal+Background

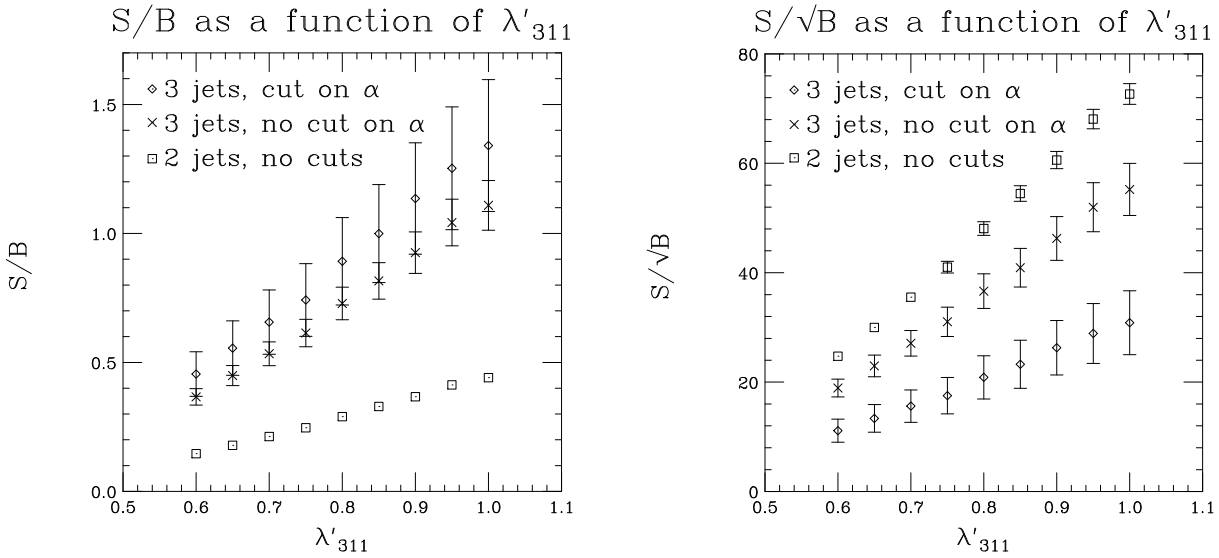

Figure 3.5: Effect of the cuts on the angular-ordering variables as a function of λ'_{311}.

As can be seen in all the distributions, apart from the disappearance of the dip at $\eta_3 = 0$, once the signal and background are added the effect of the signal is minimal. While there are differences between the signal and background it is hard to see how cuts can be applied on these variables to improve the extraction of a signal over the QCD background. The only major difference which can be cut on is the difference in the distribution of α. We consider two approaches to increase the ratio of signal to background, S/B:

1. Accept all the events with at least three jets, provided they pass the cuts described in Section 2.8 from the analysis of [88].

2. Reject all the two-jet events and only accept the events with more than two jets provided that $|\alpha| \leq \alpha_{\rm cut}$. We apply a cut of $\alpha_{\rm cut} = 0.4$ for these jet events.

These cuts were chosen to maximize S/B while not reducing $S/\sqrt{B}$ below five. As can been seen in Fig. 3.5 both of these cuts significantly increase the S/B. The effects of the second cut on the invariant-mass distribution is shown in Fig. 3.6. In the invariant-mass distribution the signal is now more visible over the background.

This shows that by using the colour coherence effects we can improve the extraction of a signal. Obtaining a large S/B is important for this process because we do not have an accurate prediction for the QCD background. However given the limits on the coupling, λ'_{311}, the signal will only be visible above the background at the highest values of the coupling currently allowed by low-energy experiments. In [5, 67] it was suggested that by using the sidebands to normalize the background, resonant slepton production could be probed to much smaller values of the $\not{R}_p$ coupling. Indeed the $S/\sqrt{B}$ numbers in Fig. 3.5 suggest that without any of our additional cuts the signal is visible at a much lower coupling. The results in [5, 67] were obtained using the narrow-width limit for the production cross section and did not included the effects of QCD radiation. Our results suggest that after including these effects the signal will only be visible for large values of

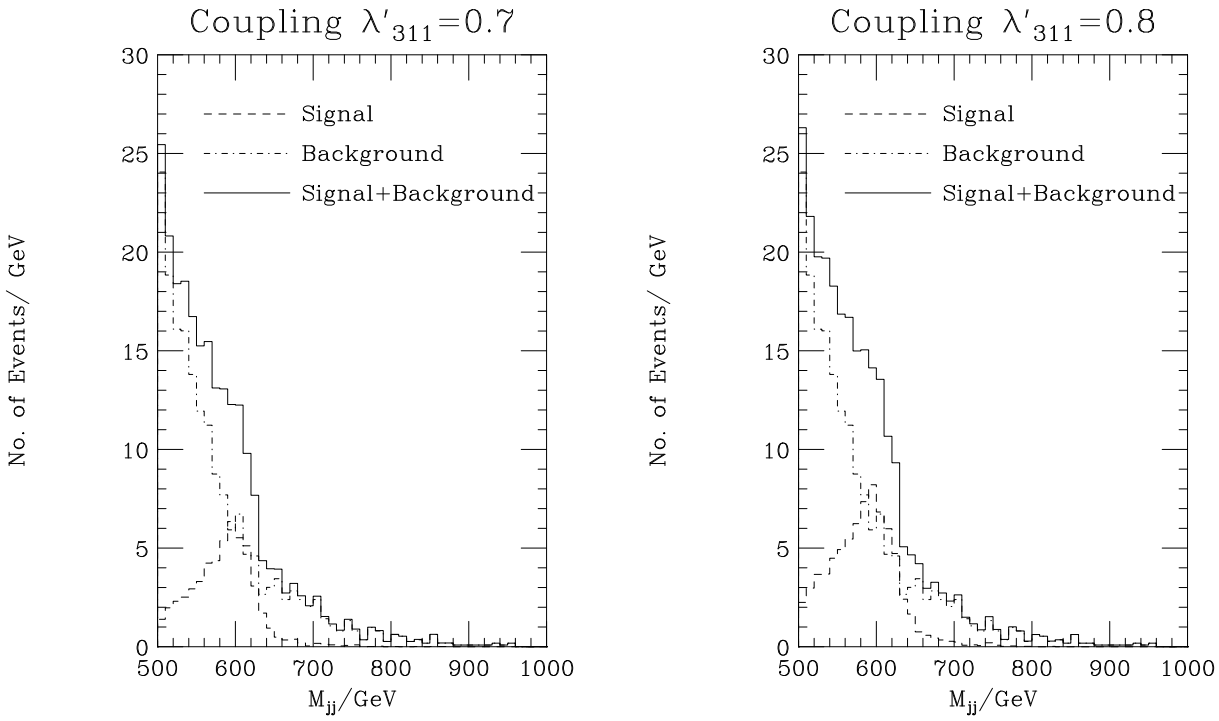

Figure 3.6: Invariant-mass distribution for $\lambda'_{311} = 0.7$ and $\lambda'_{311} = 0.8$ after cuts on the angular-ordering variables.

the coupling. It may be possible to use the sidebands which we have removed with our cuts to normalize this background, as in [5, 67], to improve the extraction of the signal. However this may not be possible due to the increased width of the resonance, Fig. 3.1, due to QCD radiation. The situation will hopefully improve with the availability of a next-to-leading order calculation for the QCD background. At present, if we require a S/B ratio of 25% in addition to $S/\sqrt{B} > 5$, then looking at the di-jet invariant masses will only allow a coupling of $\lambda'_{311} > 0.75$ to be probed. However, by using the cuts we described, based on the colour structure, couplings as low as $\lambda'_{311} > 0.55$ can be probed.

3.3 Gauge Decays of the Resonant Slepton

As we saw in the previous section, due to the large QCD background, the $\not{R}_p$ decay modes of the resonant sleptons can only be observed above the QCD background for large values of the $\not{R}_p$ Yukawa couplings. If we are to observe resonant slepton production we must therefore examine other possible decay modes of the resonant sleptons which have a lower background from Standard Model processes. One possibility is the decay of the slepton via the $\not{R}_p$ operator $L_i L_j \overline{E}_k$. Another which we shall consider here is a supersymmetric gauge decay of the resonant slepton.

We will consider a specific signature, *i.e.* like-sign dilepton production, for these processes rather than any one given resonant production mechanism. We would expect like-sign dilepton production to have a low background from Standard Model processes.

In Section 3.3.1 we will consider the signal processes in more detail, followed by a

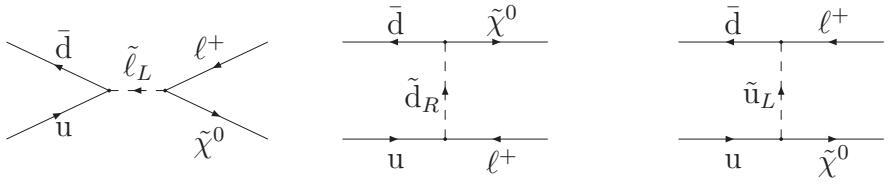

Figure 3.7: Production of $\tilde{\chi}^0\ell^+$.

discussion of the various processes which contribute to the background in Section 3.3.2. We will also discuss the different cuts which can be used to reduce the background. In Section 3.3.3 we will then consider the discovery potential at both Run II of the Tevatron and the LHC. We also consider the possibility of reconstructing the neutralino and slepton masses using their decay products.

3.3.1 Signal

There are a number of different possible production mechanisms for a like-sign dilepton pair via resonant slepton production. The dominant production mechanism is the production of a charged slepton followed by a supersymmetric gauge decay of the charged slepton to a neutralino and a charged lepton. The neutralino can then decay via the crossed process to give a second charged lepton which, due to the Majorana nature of the neutralino, can have the same charge as the lepton produced in the slepton decay. The production of a charged lepton and a neutralino via the LQD term in the $\not{R}_p$ superpotential, Eqn. 1.63, occurs at tree-level via the Feynman diagrams given in Fig. 3.7. The decay of the neutralino occurs at tree-level via the diagrams given in Fig. 3.8.

Like-sign dileptons can also be produced in resonant charged slepton production with a supersymmetric gauge decay of the slepton to a chargino and neutrino, $\tilde{\ell}^+ \to \tilde{\chi}_1^+\nu_\ell$. The chargino can then decay $\tilde{\chi}_1^+ \to \ell^+\nu_\ell\tilde{\chi}_1^0$. Again given the Majorana nature of the neutralino it can decay to give a like-sign dilepton pair.

The production of like-sign dileptons is also possible in resonant sneutrino production followed by a supersymmetric gauge decay to a chargino and a charged lepton, $\tilde{\nu} \to \ell^-\tilde{\chi}_1^+$. This can be followed by $\tilde{\chi}_1^+ \to q\bar{q}'\tilde{\chi}_1^0$, the neutralino can then decay as in Fig. 3.8 to give a like-sign dilepton pair.

All the resonant $\not{R}_p$ production mechanisms and the decays of the SUSY particles have been included in the HERWIG event generator [2]. The implementation of both R-parity conserving and R-parity violating SUSY is described in [102]. The matrix elements used for the various $\not{R}_p$ processes are given in Appendices B and C.

We will only consider one of the $\not{R}_p$ Yukawa couplings to be non-zero at a time, either λ'_{111} or λ'_{211}, which lead to resonant selectron and smuon production, respectively. The cross section depends quadratically on the $\not{R}_p$ Yukawa coupling. These couplings have upper bounds from low energy experiments. The bound on the coupling λ'_{111} from neutrino-less double beta decay is very strict [21, 104]. We therefore consider smuon

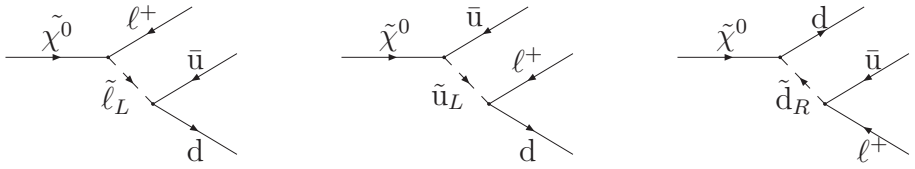

Figure 3.8: Feynman diagrams for the decay $\tilde{\chi}^0 \to \ell^+ \mathrm{d}\bar{\mathrm{u}}$. The neutralino is a Majorana fermion and decays to the charge conjugate final state as well. There is a further decay mode $\tilde{\chi}^0 \to \nu \mathrm{d}\bar{\mathrm{d}}$.

production via the coupling λ'_{211}, which has a much weaker bound,

$$\lambda'_{211} < 0.059 \times \left(\frac{M_{\tilde{d}_R}}{100 \text{ GeV}} \right), \tag{3.1}$$

from the ratio $R_\pi = \Gamma(\pi \to \mathrm{e}\nu_\mathrm{e})/\Gamma(\pi \to \mu\nu_\mu)$ [21, 58]. Our results will however apply for resonant selectron production if the coupling λ'_{111} is large enough to give an observable signal while still satisfying the bound from neutrino-less double beta decay.

As we are considering a dominant λ'_{211} coupling the leptons produced in the neutralino decays and the hard processes will be muons. We will therefore require throughout that both leptons are muons because this reduces the background, where electrons and muons are produced with equal probability, with respect to the signal. This typically reduces the Standard Model background by a factor of four while leaving the dominant signal process almost unaffected. It will lead to some reduction of the signal from channels where some of the leptons are produced in cascade decays from the decay of a W or Z boson.

The signal has a number of features, in addition to the presence of a like-sign dilepton pair, which will enable us to extract it above the background:

- Provided that the difference between the slepton and the neutralino/chargino masses is large enough both the leptons will have a high transverse momentum, p_T, and be well isolated.

- As the neutralino decays inside the detector, for this signature, there will be little missing transverse energy, $\not\!\!E_T$, in the event. Any $\not\!\!E_T$ will come from semi-leptonic hadron decays or from cascade decays following the production of a chargino or one of the heavier neutralinos.

- The presence of a third lepton can only come from semi-leptonic hadron decays, or in SUSY cascade decays if a chargino or one of the heavier neutralinos is produced.

- The presence of two hard jets from the decay of the neutralino.

The cross section for the signal processes and the acceptance[2] will depend upon the various SUSY parameters. We have performed a scan in M_0 and $M_{1/2}$ with $A_0 = 0$ GeV for two different values of $\tan\beta$ and both values of $\mathrm{sgn}\,\mu$. The masses of the left-handed smuon and the lightest neutralino are shown in Fig. 3.9. There are regions in these plots which we have not considered either due to the lack of radiative electroweak symmetry breaking,

[2]We define the acceptance to be the fraction of signal events which pass the cuts.

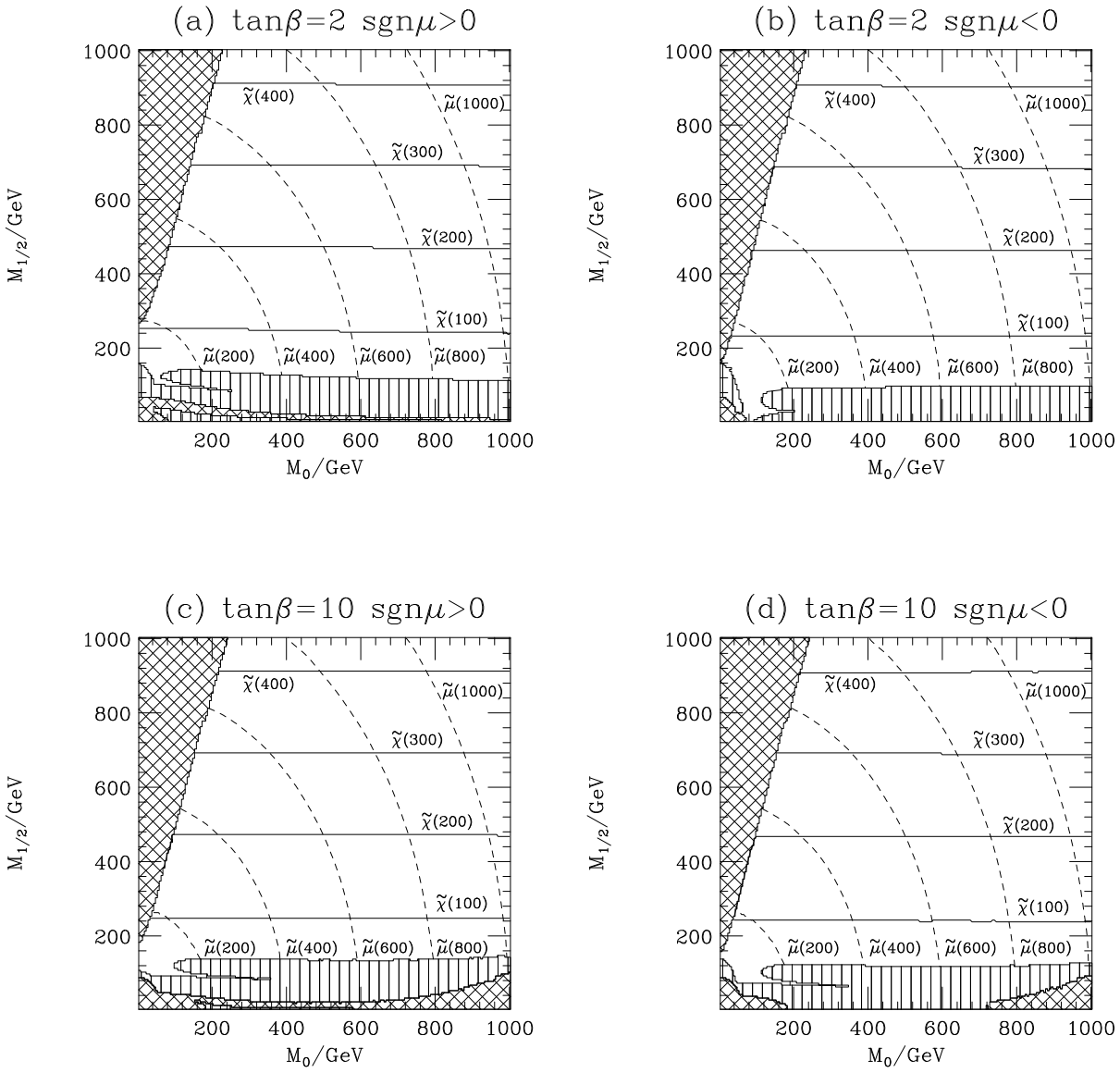

Figure 3.9: Contours showing the lightest neutralino mass, solid lines, and the $\tilde{\mu}_L$ mass, dashed lines, in the M_0, $M_{1/2}$ plane with $A_0 = 0$ GeV for different values of $\tan\beta$ and $\mathrm{sgn}\,\mu$. The hatched regions at small M_0 are excluded by the requirement that the $\tilde{\chi}_1^0$ be the LSP. The region at large M_0 and $\tan\beta$ is excluded because there is no radiative electroweak symmetry breaking. The vertically-striped region is excluded by the LEP experiments. This region was obtained using the limits on the chargino [44] and smuon [45] production cross sections, and the chargino mass [50]. This analysis was performed using ISAJET 7.48 [75].

or because the lightest neutralino is not the lightest supersymmetric particle (LSP). In the MSSM, the LSP must be a neutral colour singlet [31], from cosmological bounds on electric- or colour-charged stable relics. However if R-parity is violated the LSP can decay and these bounds no longer apply. We should therefore consider cases where one of the other SUSY particles is the LSP. We have only considered the case where the neutralino is the LSP for two reasons:

1. Given the unification of the SUSY-breaking parameters at the GUT scale it is hard to find points in parameter space where the lightest neutralino is not the LSP without the lightest neutralino becoming heavier than the sleptons, which tend to be the lightest sfermions in these models. If the neutralino is heavier than the sleptons the resonance will not be accessible for the supersymmetric gauge decay modes we are considering and the slepton will decay via $\not{R}_p$ modes.

2. The ISAJET code for the running of the couplings and the calculation of the MSSM decay modes only works when the neutralino is the LSP.

The plots in Fig. 3.9 also include the current experimental limits on the SUSY parameters from LEP. This experimentally excluded region comes from two sources: the region at large M_0 is excluded by the limit on the cross section for chargino pair production [44] and the limit on the chargino mass [50]; the region at small M_0 is excluded by the limit on the production of smuons [45]. There is also a limit on the neutralino production cross section [44]. However, for most of the SUGRA parameter space this is weaker than the limit on chargino pair production. The gap in the excluded region between M_0 of about 50 GeV and 100 GeV is due to the presence of a destructive interference between the t-channel sneutrino exchange and the s-channel photon and Z exchanges in the chargino production cross section in e^+e^- collisions.

The limit on the coupling λ'_{211} is shown in Fig. 3.10. As can be seen from Figs. 3.9 and 3.10 the limit on the coupling is fairly weak for large regions of parameter space, even when the smuon is relatively light. This is due to the squark masses, upon which the limit depends, being larger than the slepton masses in the SUGRA models.

The signature we are considering requires the neutralino to decay inside the detector. In practice, if the neutralino decays more than a few centimeters from the primary interaction point a different analysis including displaced vertices would be necessary. The neutralino decay length is shown in Fig. 3.11 and is small for all the currently allowed values of the SUGRA parameters. There will, however, be a lower limit on the $\not{R}_p$ couplings which can be probed using this process as the decay length $\sim 1/\lambda'^2_{211}$ [105].

3.3.2 Backgrounds

3.3.2.1 Standard Model Backgrounds

The dominant Standard Model backgrounds to like-sign dilepton production come from:

- Gauge boson pair production, *i.e.* production of WZ or ZZ followed by leptonic decays with some of the leptons not being detected.

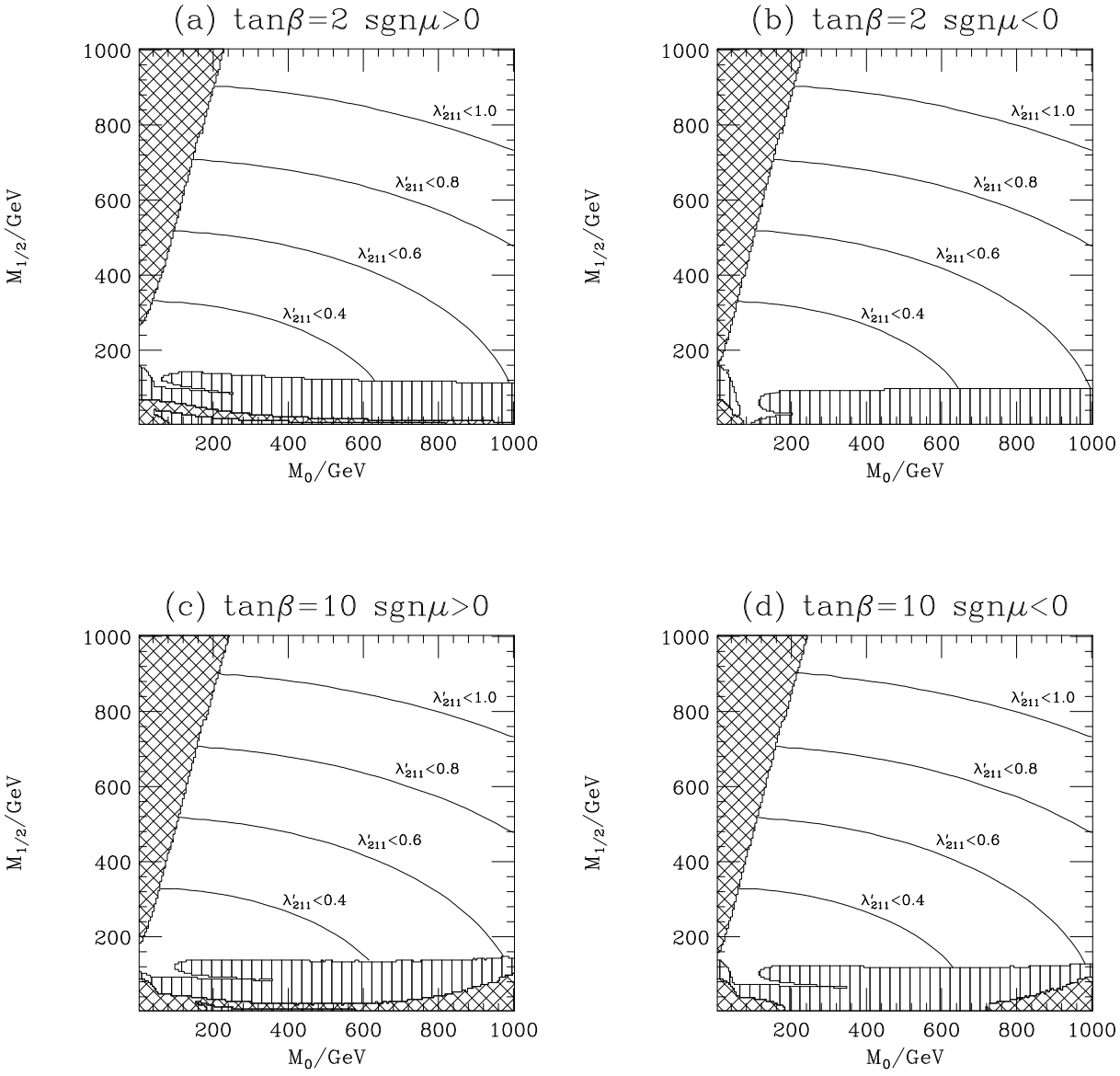

Figure 3.10: Contours showing the limit on the $\not{R}_{\rm p}$ Yukawa coupling λ'_{211} in the M_0, $M_{1/2}$ plane for $A_0 = 0$ GeV and different values of $\tan\beta$ and $\mathrm{sgn}\,\mu$. The striped and hatched regions are described in the caption of Fig. 3.9.

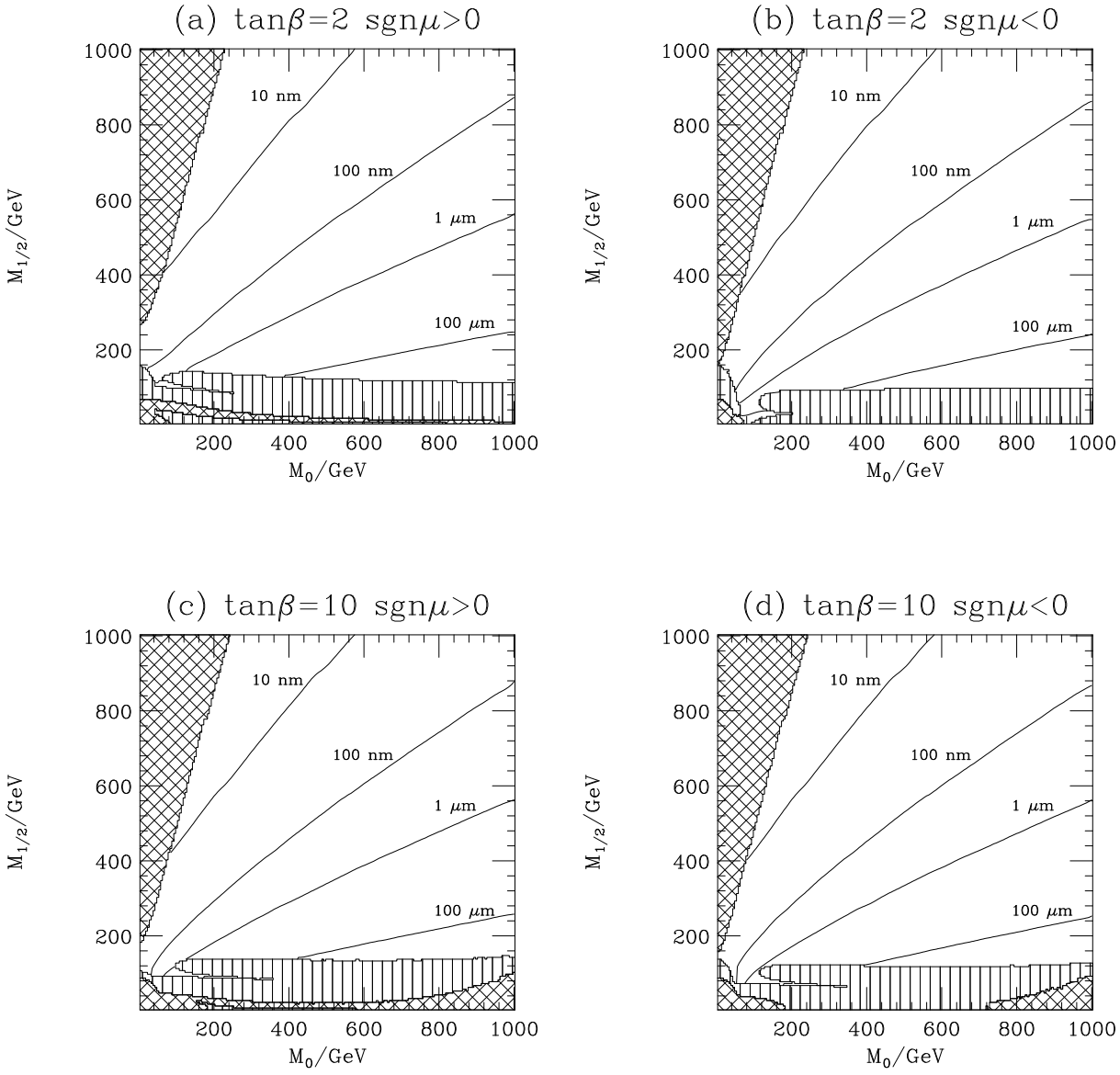

Figure 3.11: Contours showing the decay length of a neutralino produced in the decay of an on-mass-shell slepton in the M_0, $M_{1/2}$ plane for $A_0 = 0$ GeV, $\lambda'_{211} = 10^{-2}$ and different values of $\tan\beta$ and $\mathrm{sgn}\,\mu$. The striped and hatched regions are described in the caption of Fig. 3.9.

- $t\bar{t}$ production. Either the t or $\bar{t}$ decays semi-leptonically, giving one lepton. The second top decays hadronically. A second lepton with the same charge can be produced in a semi-leptonic decay of the bottom hadron formed in the decay of the second top, *i.e.*

$$\begin{aligned} t &\rightarrow W^+ b \rightarrow \mu^+ \bar{\nu}_\mu b, \\ \bar{t} &\rightarrow W^- \bar{b} \rightarrow q\bar{q}\bar{b}, \quad \bar{b} \rightarrow \mu^+ \bar{\nu}_\mu \bar{c}. \end{aligned} \tag{3.2}$$

- $b\bar{b}$ production. If either of these quarks hadronizes to form a $B^0_{d,s}$ meson this can mix to give a $\bar{B}^0_{d,s}$. This means that both the bottom hadrons in the event will contain a b quark, if a $B^0_{d,s}$ undergoes mixing, or both bottom hadrons will contain a $\bar{b}$, if a $\bar{B}^0_{d,s}$ mixes. Thus if both the bottom hadrons decay semi-leptonically the leptons will have the same charge as they are both coming from either b or $\bar{b}$ decays.

- Single top production. A single top quark can be produced together with a $\bar{b}$ quark by either an *s*- or *t*-channel W exchange. This can give one charged lepton from the top decay, and a second lepton with the same charge from the decay of the meson formed after the b quark hadronizes.

- Non-physics backgrounds. There are two major sources: (i) from misidentifying the charge of a lepton, *e.g.* in Drell-Yan production, and (ii) from incorrectly identifying an isolated hadron as a lepton. This means that there is a major source of background from W production with an additional jet faking a lepton.

These processes have been extensively studied [106–113] as they are also the major backgrounds to the production of like-sign dileptons in the MSSM. The first studies of like-sign dilepton production at the LHC [107] only considered the background from heavy quark production, *i.e.* $t\bar{t}$ and $b\bar{b}$ production. More recent studies for both the LHC [108, 109] and Run II of the Tevatron [110–113] have also considered the background from gauge boson pair production. In addition, the Tevatron studies [110–113] have included the non-physics backgrounds. We have considered all the physics backgrounds, from both heavy quark production and gauge boson pair production, but have neglected the non-physics backgrounds which would require a full simulation of the detector.

In these studies a number of different cuts have been used to suppress the backgrounds. These cuts can be split into two groups. The first of these sets of cuts is designed to reduce the background from heavy quark production:

- A cut on the p_T of the leptons requiring

$$p_T^{\text{lepton}} > p_T^{\text{CUT}}. \tag{3.3}$$

  The values of p_T^{CUT} for Tevatron studies have been between 5 and 20 GeV. Higher values, between 20 and 50 GeV, have usually been used in LHC simulations.

- A cut requiring that the leptons are isolated, *i.e.* imposing a cut on the transverse energy, E_T^{IC}, of the particles other than the lepton in a cone about the direction of

the lepton such that

$$E_T^{IC} < E_0. \tag{3.4}$$

E_0 has been taken to be less than 5 GeV for Tevatron simulations and between 5 and 10 GeV for LHC studies. The radius of the cone is usually taken to be

$$\Delta R = \sqrt{\Delta\phi^2 + \Delta\eta^2} < 0.4, \tag{3.5}$$

where $\Delta\phi$ is the azimuthal angle and $\Delta\eta$ the pseudo-rapidity of the particles with respect to the lepton.

It was shown in [107] that these cuts can reduce the background from heavy quark production by several orders of magnitude. Any high-p_T lepton from a bottom hadron decay must come from a high-p_T hadron. This is due to the small mass of the bottom hadron relative to the lepton p_T which means the lepton will be travelling in the same direction as the other decay products [114]. Hence the isolation and p_T cuts remove the majority of these events.

The analyses of [109–113] then imposed further cuts to reduce the backgrounds from gauge boson pair production, which is the major contribution to the SM background after the imposition of the isolation and p_T cuts:

- A cut on the invariant mass, $m_{\ell^+\ell^-}$, of any pair of opposite sign same flavour (OSSF) leptons to remove those leptons coming from Z decays, *i.e.*

  $$|M_{\rm Z} - m_{\ell^+\ell^-}| < m_{\ell^+\ell^-}^{\rm CUT}, \tag{3.6}$$

  was used in [110, 112, 113].

- Instead of a cut on the mass of OSSF lepton pairs, some analyses considered a veto on the presence of an OSSF lepton pair in the event.

- In [111, 113] a cut on the transverse mass was imposed to reject leptons which come from the decays of W bosons. The transverse mass, M_T, of a lepton–neutrino pair is given by

  $$M_T^2 = 2|p_{T_\ell}||p_{T_\nu}|(1 - \cos\Delta\phi_{\ell\nu}), \tag{3.7}$$

  where p_{T_ℓ} is the transverse momentum of the charged lepton, p_{T_ν} is the transverse momentum of the neutrino (assumed to be the total missing transverse momentum in the event) and $\Delta\phi_{\ell\nu}$ is the azimuthal angle between the lepton and the neutrino (the direction of the neutrino is taken to be the direction of the missing momentum in the event).

  This cut is applied to both of the like-sign leptons in the event to reject events in which either of them came from the decay of a W boson. A cut removing events with 60 GeV $< M_T <$ 85 GeV was used in [113] to reduce the background from WW and WZ production.

- For the MSSM signatures considered in [110–113] there is missing transverse energy, $\not{E}_T$, due to the LSP escaping from the detector. This allowed them to impose a cut on the $\not{E}_T$, $\not{E}_T > E_T^{\rm CUT}$, to reduce the background.

There are, however, differences between the MSSM signatures which were considered in [110–113] and the $\not{R}_{\rm p}$ processes we are considering here. In particular as the LSP decays, there will be little missing transverse energy in the $\not{R}_{\rm p}$ events. This means that instead of a cut requiring the $\not{E}_T$ to be above some value we will consider a cut requiring the $\not{E}_T$ to be less than some value, *i.e.*

$$\not{E}_T < E_T^{\rm CUT}. \tag{3.8}$$

This cut will remove events from some of the possible resonant production mechanisms, *i.e.* those channels where a neutrino is produced in either the slepton decay or the cascade decay of a chargino, or one of the heavier neutralinos, to the lightest neutralino. However it will not affect the decay of a charged slepton to the lightest neutralino which is the dominant production mechanism over most of the SUSY parameter space.

Similarly, the signal we are considering in general will not contain more than two leptons. Further leptons can only come from cascade decays following the production of either a chargino or one of the heavier neutralinos, or from semi-leptonic hadron decays. This means that instead of the cut on the invariant mass of OSSF lepton pairs we will only consider the effect of a veto on the presence of OSSF pairs. This veto was considered in [110, 111] but for the MSSM signal considered there it removed more signal than background.

3.3.2.2 SUSY Backgrounds

So far we have neglected what may be the major source of background to this process, *i.e.* supersymmetric particle pair production. If we only consider small $\not{R}_{\rm p}$ couplings the dominant effect in sparticle pair production is that the LSP produced at the end of the cascade decays of the other SUSY particles will decay. For large $\not{R}_{\rm p}$ couplings the cascade decay chains can also be affected by the heavier SUSY particles decaying via $\not{R}_{\rm p}$ modes. We will not consider this effect here.[3] The LSP will decay giving a quark–antiquark pair and either a charged lepton or a neutrino. There will usually be two LSPs in each event, one from the decay chain of each of the sparticles produced in the hard collision. This means that they can both decay to give leptons with the same charge. Leptons can also be produced in the cascade decays. These processes will therefore be a major background to like-sign dilepton production via resonant slepton production.

The cuts which were intended to reduce the Standard Model background will also significantly reduce the background from sparticle pair production. However we will need to impose additional cuts to suppress this background. In the signal events there will be at least two high-p_T jets from the neutralino decay and there may be more jets from either initial-state QCD radiation or radiation from quarks produced in the neutralino decay. In the dominant production mechanism, *i.e.* $\tilde{\mu} \to \mu^- \tilde{\chi}_1^0$, this will be the only source of

[3] These additional decays are included in HERWIG 6.1 and the matrix elements are given in Appendix B.

jets, however additional jets can be produced in the cascade SUSY decays if a chargino or one of the heavier neutralinos is produced. In the SUSY background there will be at least four high-p_T jets from the neutralino decays, plus other jets formed in the decays of the coloured sparticles which are predominantly formed in hadron–hadron collisions. This suggests two possible strategies for reducing the sparticle pair production background:

1. A cut such that there are at most 2 or 3 jets (allowing for some QCD radiation) above a given p_T. This will reduce the SUSY background which typically has more than four high-p_T jets.

2. A cut such that there are exactly two jets, or only two or three jets above a given p_T. This will reduce the gauge boson pair production background where typically the only jets come from initial-state radiation, as well as the background from sparticle pair production.

In practice we would use a much higher momentum cut in the first case, as we only need to ensure that the cut is sufficiently high that most of the sparticle pair production events give more than 2 or 3 jets above the cut. However with the second cut we need to ensure that the jets in the signal have sufficiently high-p_T to pass the cut as well. In practice we found that the first cut significantly reduced the sparticle pair production background while having little effect on the signal, while the second cut dramatically reduced the signal as well. In the next section we will consider the effects of these cuts on both the signal and background at Run II of the Tevatron and the LHC.

3.3.3 Simulations

HERWIG 6.1 [2] was used to simulate the signal and the backgrounds from sparticle pair, $t\bar{t}$, $b\bar{b}$ and single top production. HERWIG does not include gauge boson pair production in hadron–hadron collisions and we therefore used PYTHIA 6.1 [96] to simulate this background. The simulation of the signal includes all the R-parity conserving decay modes given in Table 3.1. We used the cone algorithm described in the previous chapter for all the jet reconstructions, although for this study we took the radius of the cone to be 0.4 radians rather than the value of 0.7 radians used in both the previous section and the last chapter.

Due to the large cross sections for some of the Standard Model backgrounds before any cuts, we imposed parton-level cuts and forced certain decay modes, *i.e.* we required that certain particles decay via a particular channel, in order to simulate a sufficient number of events with the resources available. We designed these cuts in such a way that hopefully they are weaker than any final cut we apply, so that we do not lose any of the events that would pass the final cuts. We imposed the following cuts for the various backgrounds:

- $b\bar{b}$ production. We forced the B hadrons produced by the hadronization to decay semi-leptonically. This neglects the production of leptons in charm decays which has a higher cross section but which we would expect to have a lower p_T and be less well isolated than those leptons produced in bottom decays. If there was only one $B^0_{d,s}$ meson in the event this was forced to mix. When there was more than one $B^0_{d,s}$ meson then one of them was forced to mix and the others were forced not to

mix. Similarly we imposed a parton-level cut on the transverse momentum of the initial b and $\bar{\mathrm{b}}$, $p_T^{\mathrm{b},\bar{\mathrm{b}}} \geq p_T^{\mathrm{parton}}$. This parton level cut should not affect the background provided that we impose a cut on the transverse momentum of the leptons produced in the decay, $p_T^{\mathrm{lepton}} \geq p_T^{\mathrm{parton}}$.

- $\mathrm{t\bar{t}}$ production. While not as large as the $\mathrm{b\bar{b}}$ production cross section the cross section for $\mathrm{t\bar{t}}$ is large, particularly at the LHC. We improved the efficiency by forcing one of the top quarks in each event to decay semi-leptonically, again this neglects events in which there are leptons from charm decay. However we did not impose a cut on the p_T of the top quarks as, due to the large top quark mass, even relatively low p_T top quarks can give high-p_T leptons.

- Single top production. While the cross section for this process is relatively small compared to the heavy quark pair production cross sections, we forced the tops to decay semi-leptonically to reduce the number of events we needed to simulate.

- Gauge boson pair production. The cross sections for these processes are relatively small and it was not necessary to impose any parton level cuts, or force particular decay modes.

Where possible, the results of the Monte Carlo simulations have been normalized by using next-to-leading-order cross sections for the various background processes. We used the next-to-leading-order calculation of [115] for gauge boson pair production. The $\mathrm{t\bar{t}}$ simulations were normalized using the next-to-leading-order, with next-to-leading-log resummation, calculation from [116].

The calculation of a next-to-leading-order cross section for $\mathrm{b\bar{b}}$ production is more problematic due to the parton-level cuts we imposed on the simulated events. There are a range of possible options for applying the p_T cut we imposed on the bottom quark at next-to-leading order. At leading order the transverse momenta of the quarks are identical and therefore the cut requires them both to have transverse momentum $p_T > p_T^{\mathrm{CUT}}$. However at next-to-leading order, due to gluon radiation, the transverse momenta of the quarks are no longer equal. Therefore a cut on, for example, the p_T of the hardest quark, $p_{T_1} > p_T^{\mathrm{CUT}}$, together with a cut on the lower p_T quark, $p_{T_2} > p_T^{\mathrm{CUT}} - \delta$, with any positive value of $\delta < p_T^{\mathrm{CUT}}$, is the same as the leading-order cut we applied. Given that we need a high transverse momentum bottom hadron to give a high-p_T lepton and only events with two such high-p_T leptons will contribute to the background, a cut requiring both bottom quarks to have $p_T > p_T^{\mathrm{CUT}}$, *i.e.* $\delta = 0$, is most appropriate. However at this point perturbation theory is unreliable [117] and for the cuts we applied the next-to-leading-order cross section is smaller than the leading-order result. We therefore applied the cut $p_{T_1} > p_T^{\mathrm{CUT}}$ with no cut on the softer bottom as this avoids the point at which the perturbative expansion is unreliable, *i.e.* $\delta = p_T^{\mathrm{CUT}}$. We used the program of [118] to calculate the next-to-leading-order cross section with these cuts.

All of the simulations and SUSY cross section calculations used the latest MRS parton distribution set [119], as did the calculation of the single top production cross section. The parton distribution sets used in the various next-to-leading-order cross sections are described in the relevant papers.

We can now study the signal and background in more detail for both the Tevatron and the LHC. This is followed by a discussion of the methods used to reconstruct the masses of both the lightest neutralino and the resonant slepton.

3.3.3.1 Tevatron

The cross section for the production of a neutralino and a charged lepton, which is the dominant like-sign dilepton production mechanism, is shown in Fig. 3.12 in the M_0, $M_{1/2}$ plane with $A_0 = 0$ GeV and $\lambda'_{211} = 10^{-2}$ for two different values of $\tan\beta$ and both values of $\mathrm{sgn}\,\mu$. The total cross section for resonant slepton production followed by supersymmetric gauge decays is shown in Fig 3.13. As can be seen from these figures, the total cross section closely follows the slepton mass contours shown in Fig. 3.9, whereas the neutralino–lepton cross section falls off more quickly at small $M_{1/2}$ where the charginos and heavier neutralinos can be produced. This cross section must be multiplied by the acceptance, *i.e.* the fraction of signal events which pass the cuts, to give the number of events detected in the experiment.

We will first discuss the cuts applied to reduce the various Standard Model backgrounds and then present the discovery potential at the Tevatron if we only consider these backgrounds. This is followed by a discussion of the additional cuts needed to reduce the background from sparticle pair production.

Standard Model Backgrounds

We have applied the following cuts to reduce the Standard Model backgrounds:

1. A cut requiring all the leptons to be in the central region of the detector, $|\eta| < 2.0$.

2. A cut on the transverse momentum of each of the like-sign leptons, $p_T^{\mathrm{lepton}} \geq 20$ GeV. This is the lowest cut we could apply given our parton level cut of $p_T^{\mathrm{parton}} = 20$ GeV for the $\mathrm{b\bar{b}}$ background.

3. An isolation cut on the like-sign leptons so that the transverse energy in a cone of radius $\Delta R = \sqrt{\Delta\phi^2 + \Delta\eta^2} = 0.4$ about the direction of the lepton is less than 5 GeV.

4. We reject events with 60 GeV $< M_T <$ 85 GeV (*c.f.* Eqn. 3.7). This cut is applied to both of the like-sign leptons.

5. A veto on the presence of a lepton in the event with the same flavour but opposite charge as either of the leptons in the like-sign pair if the lepton has $p_T > 10$ GeV and passes the same isolation cut as the like-sign leptons.

6. A cut on the missing transverse energy, $\not{E}_T < 20$ GeV. In our analysis we have assumed that the missing transverse energy is solely the due to the momenta of the neutrinos produced.

The first two cuts are designed to reduce the background from heavy quark production, which is the major source of background before any cuts. Fig. 3.14 shows that the cut

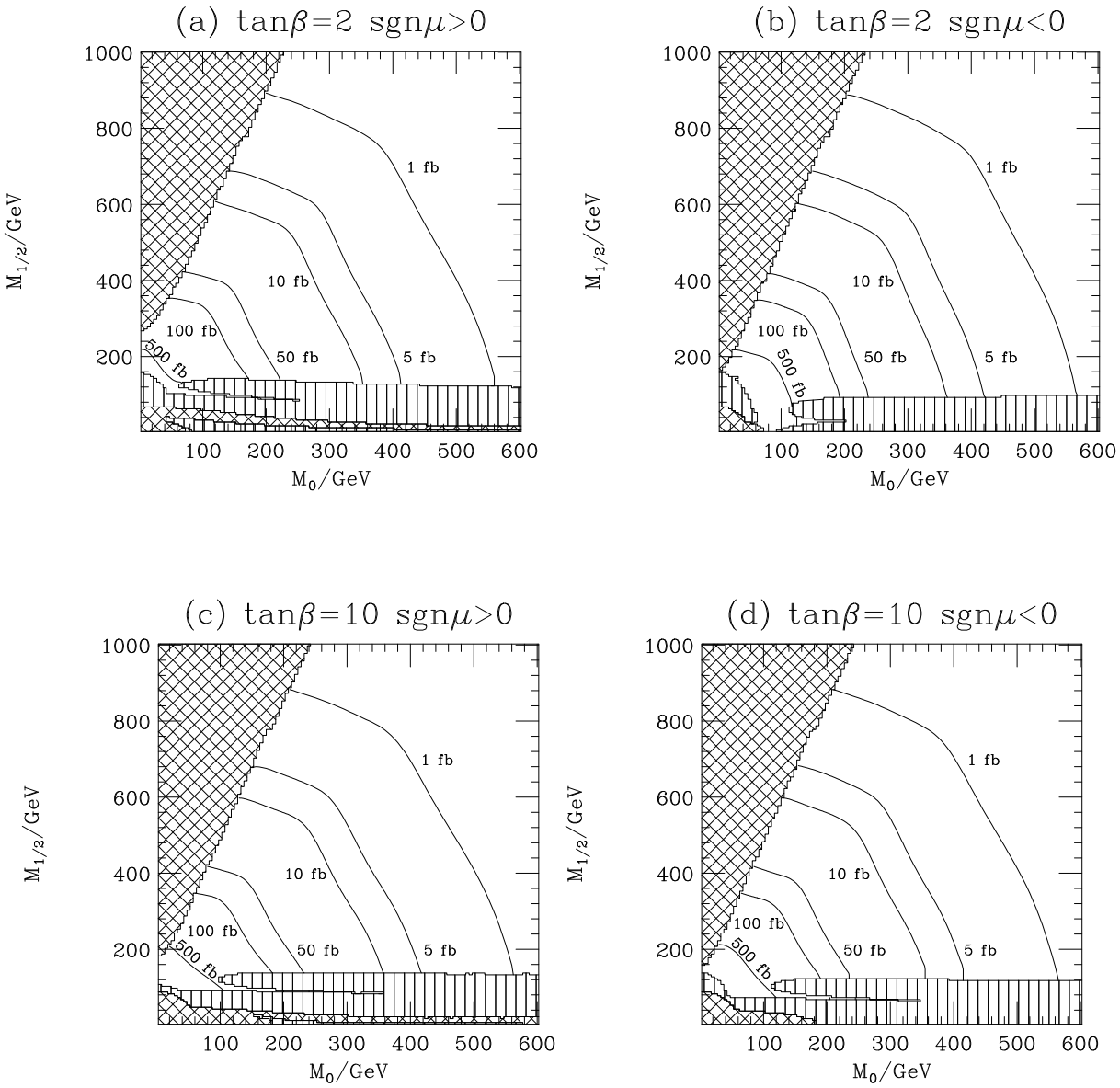

Figure 3.12: Contours showing the cross section for the production of a neutralino and a charged lepton at Run II of the Tevatron in the M_0, $M_{1/2}$ plane for $A_0 = 0$ GeV and $\lambda'_{211} = 10^{-2}$ with different values of $\tan\beta$ and $\mathrm{sgn}\,\mu$. The striped and hatched regions are described in the caption of Fig. 3.9.

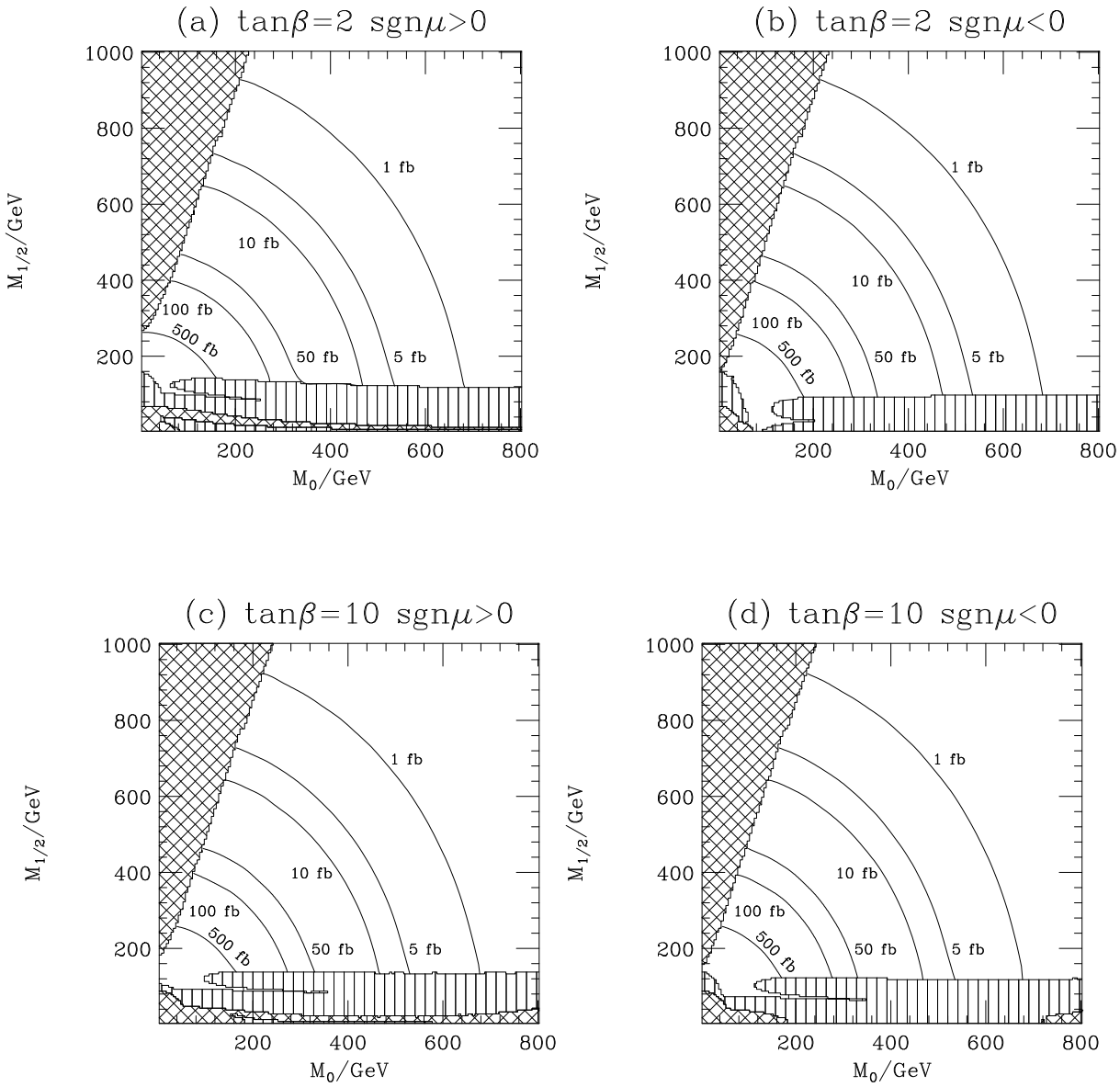

Figure 3.13: Contours showing the cross section for the production of a slepton followed by a supersymmetric gauge decay at Run II of the Tevatron in the M_0, $M_{1/2}$ plane for $A_0 = 0$ GeV and $\lambda'_{211} = 10^{-2}$ with different values of $\tan\beta$ and $\mathrm{sgn}\,\mu$. The striped and hatched regions are described in the caption of Fig. 3.9.

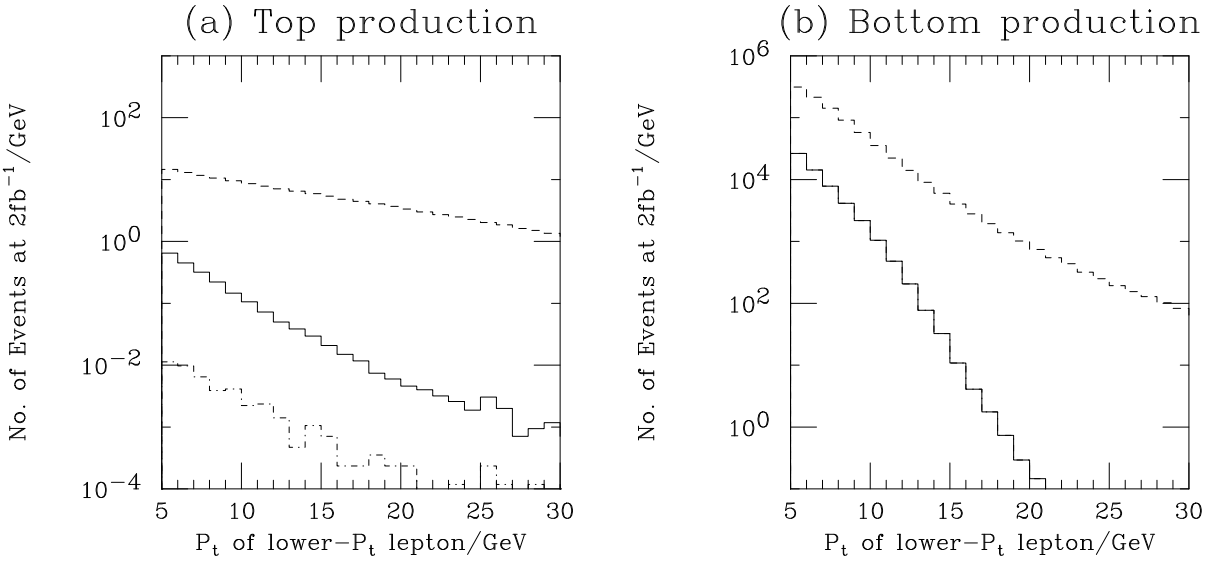

Figure 3.14: Effect of the isolation cuts on the $t\bar{t}$ and $b\bar{b}$ backgrounds at Run II of the Tevatron. The dashed line gives the background before any cuts and the solid line shows the effect of the isolation cut described in the text. The dot-dash line gives the effect of all the cuts, including the cut on the number of jets (for the $b\bar{b}$ background this is indistinguishable from the solid line). As a parton-level cut of 20 GeV was used in simulating the $b\bar{b}$ background the results below 20 GeV for the lepton p_T do not correspond to the full number of background events. The distributions have been normalized to an integrated luminosity of 2 fb^{-1}.

on the transverse momentum, $p_T > 20$ GeV, reduces the background by several orders of magnitude and the addition of the isolation cut reduces this background to less than one event at Run II of the Tevatron.

The remaining cuts reduce the background from gauge boson pair production which dominates the Standard Model background after the imposition of the isolation and p_T cuts. Fig. 3.15a shows that the cut on the transverse mass, *i.e.* removing the region 60 GeV $< M_T <$ 85 GeV, for each of the like-sign leptons will reduce the background from WZ production, which is the largest of the gauge boson pair production backgrounds. Similarly the cut on the missing transverse energy, $\not{E}_T < 20$ GeV, will significantly reduce the background from WZ production. This is shown in Fig. 3.15b. The effect of these cuts is shown in Fig. 3.16. Our simulations do not include Wγ production which was recently found to be a major source of background to like-sign dilepton production in the MSSM [111]. However, we would expect this to be less important here due to the different cuts we have applied. In particular, in the analysis of [111] a cut on the invariant mass of OSSF lepton pairs was imposed to reduce the background from Z production, rather than the veto on the presence of OSSF leptons which we have used. The veto and missing transverse energy cut will reduce the number of events from Wγ production while the cut on the invariant mass will not suppress this background.

The effect of all these cuts on the background is given in Table 3.2. While the dominant background is from WZ production, the dominant contribution to the error comes from

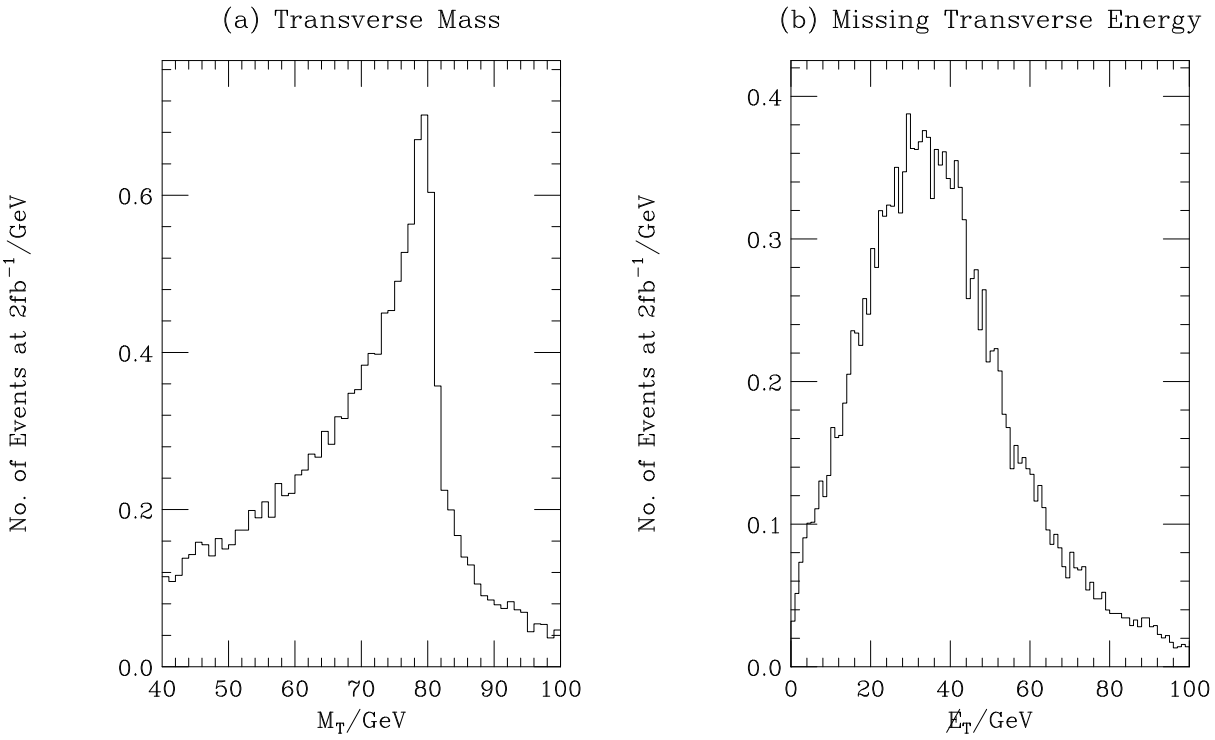

Figure 3.15: The transverse mass and missing transverse energy in WZ events at Run II of the Tevatron. The distributions are normalized to an integrated luminosity of 2 fb^{-1}.

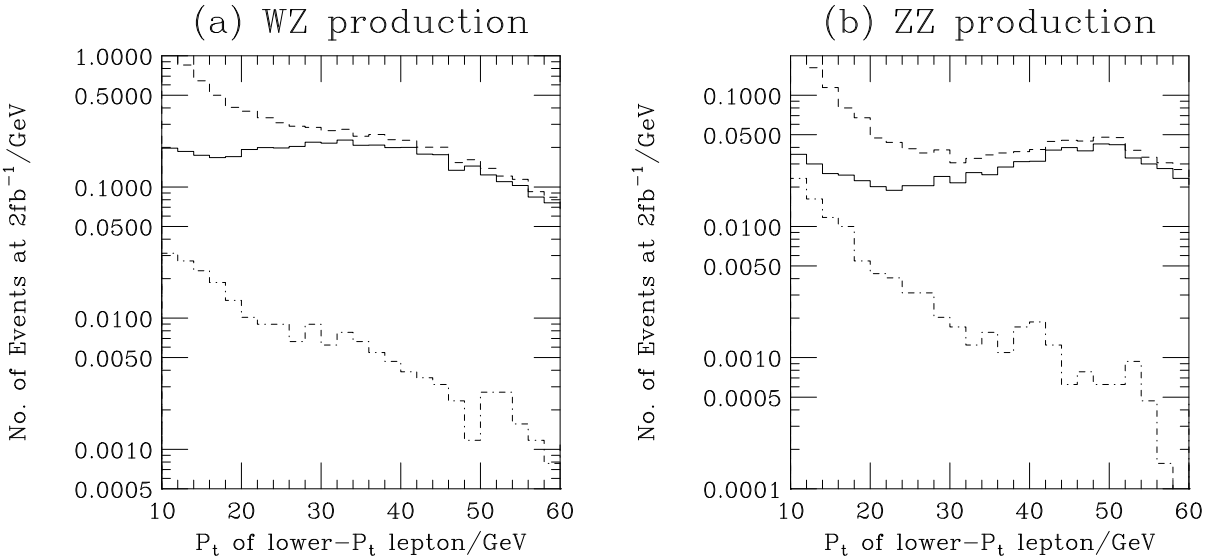

Figure 3.16: Effect of the isolation cuts on the WZ and ZZ backgrounds at Run II of the Tevatron. The dashed line gives the background before any cuts and the solid line shows the effect of the isolation cut described in the text. The dot-dash line gives the effect of all the cuts, including the cut on the number of jets. The distributions are normalized to an integrated luminosity of 2 fb^{-1}.

Background process	Number of Events			
	After p_T cut	After isolation and p_T cuts	After isolation, p_T, M_T, $\not{E}_T$ cuts and OSSF lepton veto.	After all cuts
WW	0.23 ± 0.02	0.0 ± 0.003	0.0 ± 0.003	0.0 ± 0.003
WZ	9.96 ± 0.09	7.93 ± 0.08	0.21 ± 0.01	0.21 ± 0.01
ZZ	2.05 ± 0.03	1.61 ± 0.02	0.069 ± 0.005	0.069 ± 0.005
$t\bar{t}$	34.1 ± 1.6	0.028 ± 0.002	0.0032 ± 0.0006	0.0016 ± 0.0004
$b\bar{b}$	$(3.4 \pm 1.3) \times 10^3$	0.15 ± 0.16	0.15 ± 0.16	0.15 ± 0.16
Single top	1.77 ± 0.01	0.0014 ± 0.0003	0.0001 ± 0.0001	0.0001 ± 0.0001
Total	$(3.4 \pm 1.3) \times 10^3$	9.72 ± 0.18	0.43 ± 0.16	0.43 ± 0.16

Table 3.2: Backgrounds to like-sign dilepton production at Run II of the Tevatron. The numbers of events are based on an integrated luminosity of 2 fb^{-1}. We have calculated an error on the cross section by varying the scale between half and twice the hard scale, apart from the gauge boson pair production cross section where we do not have this information and the effect of varying the scale is expected to be small anyway. The error on the number of events is the error on the cross section and the statistical error from the Monte Carlo simulation added in quadrature. If no events passed the cut the statistical error was taken to be the same as if one event had passed the cuts.

$b\bar{b}$ production. This can only be reduced with a significantly more elaborate simulation.

We also need to calculate the acceptance of these cuts for the signal. To estimate the acceptance of the cuts we simulated twenty thousand events at each of one hundred points in the M_0, $M_{1/2}$ plane. The acceptance was then interpolated between the points and multiplied by the cross section to give the number of signal events passing the cuts. This can be used to find the discovery potential by comparing the number of signal events with a 5σ statistical fluctuation of the background.

Fig. 3.17 shows the discovery potential, for different integrated luminosities and a fixed value of the coupling $\lambda'_{211} = 10^{-2}$, if we only consider the Standard Model backgrounds and apply the cuts we described to suppress these backgrounds. Fig. 3.18 shows the effect of varying the $\not{R}_p$ coupling for 2 fb^{-1} integrated luminosity with the same assumptions.

We have taken a conservative approach where the background is taken to be one standard deviation above the central value, *i.e.* we take the background to be 0.59 events. Due to the small number of events we must use Poisson statistics. For the Standard Model background given in Table 3.2, 7 events corresponds to the same probability as a 5σ statistical fluctuation for a Gaussian distribution.

For small couplings there are regions, for low $M_{1/2}$, which cannot be observed even for small smuon masses. For larger couplings, however, we can probe masses of up to 430 (500) GeV for a coupling $\lambda'_{211} = 0.05$ with 2 (10) fb^{-1} integrated luminosity. Masses of up to 520 (600) GeV can be observed for a coupling of $\lambda'_{211} = 0.1$ with 2 (10) fb^{-1} integrated luminosity.

We have neglected the non-physics background. This mainly comes from fake leptons

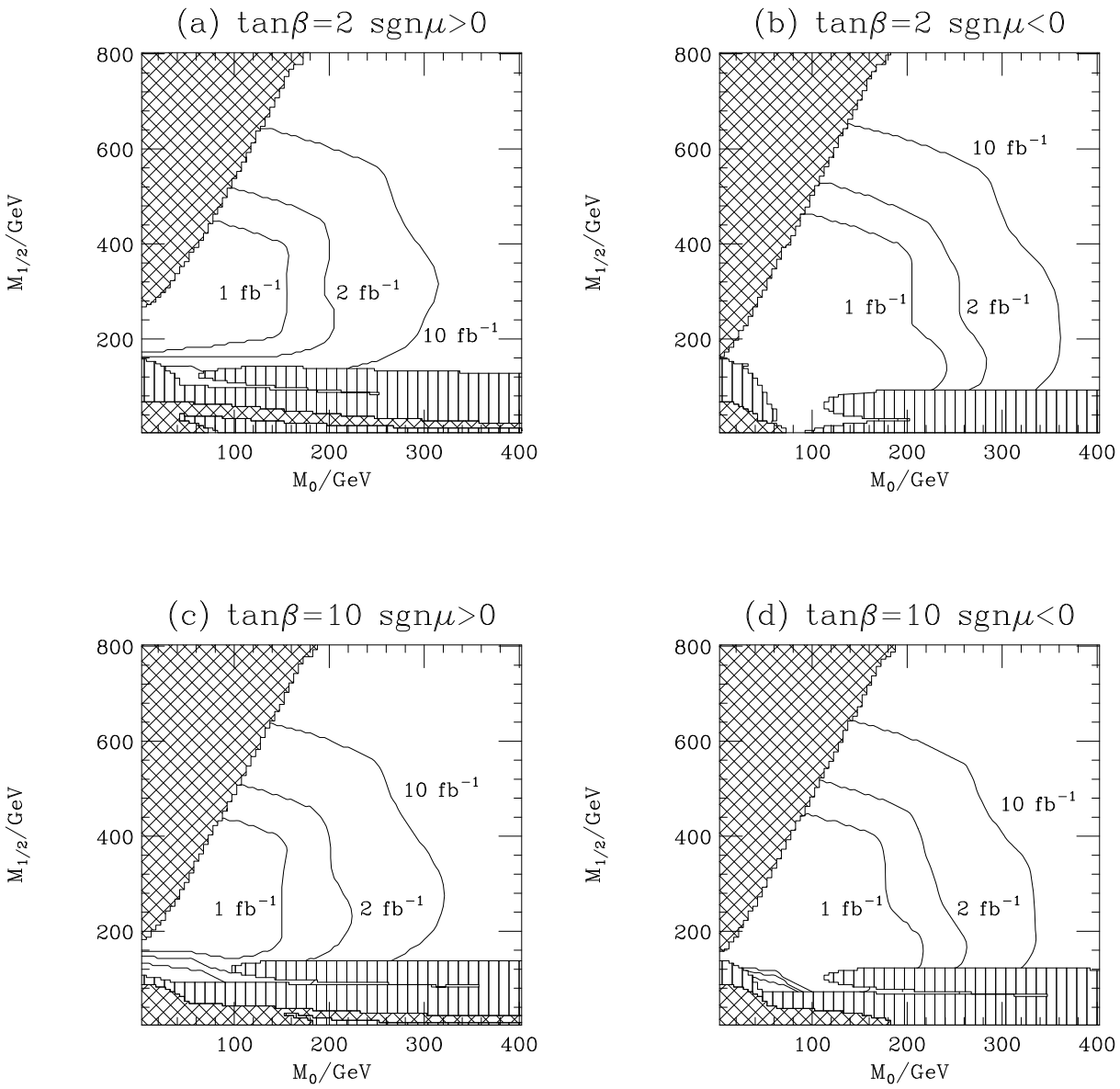

Figure 3.17: Contours showing the discovery potential of the Tevatron in the M_0, $M_{1/2}$ plane for $\lambda'_{211} = 10^{-2}$ and $A_0 = 0$ GeV. These contours are a 5σ excess of the signal above the background. Here we have imposed the cuts on the isolation and p_T of the leptons, the transverse mass and the missing transverse energy described in the text, and a veto on the presence of OSSF leptons. We have only considered the Standard Model background. The striped and hatched regions are described in the caption of Fig. 3.9.

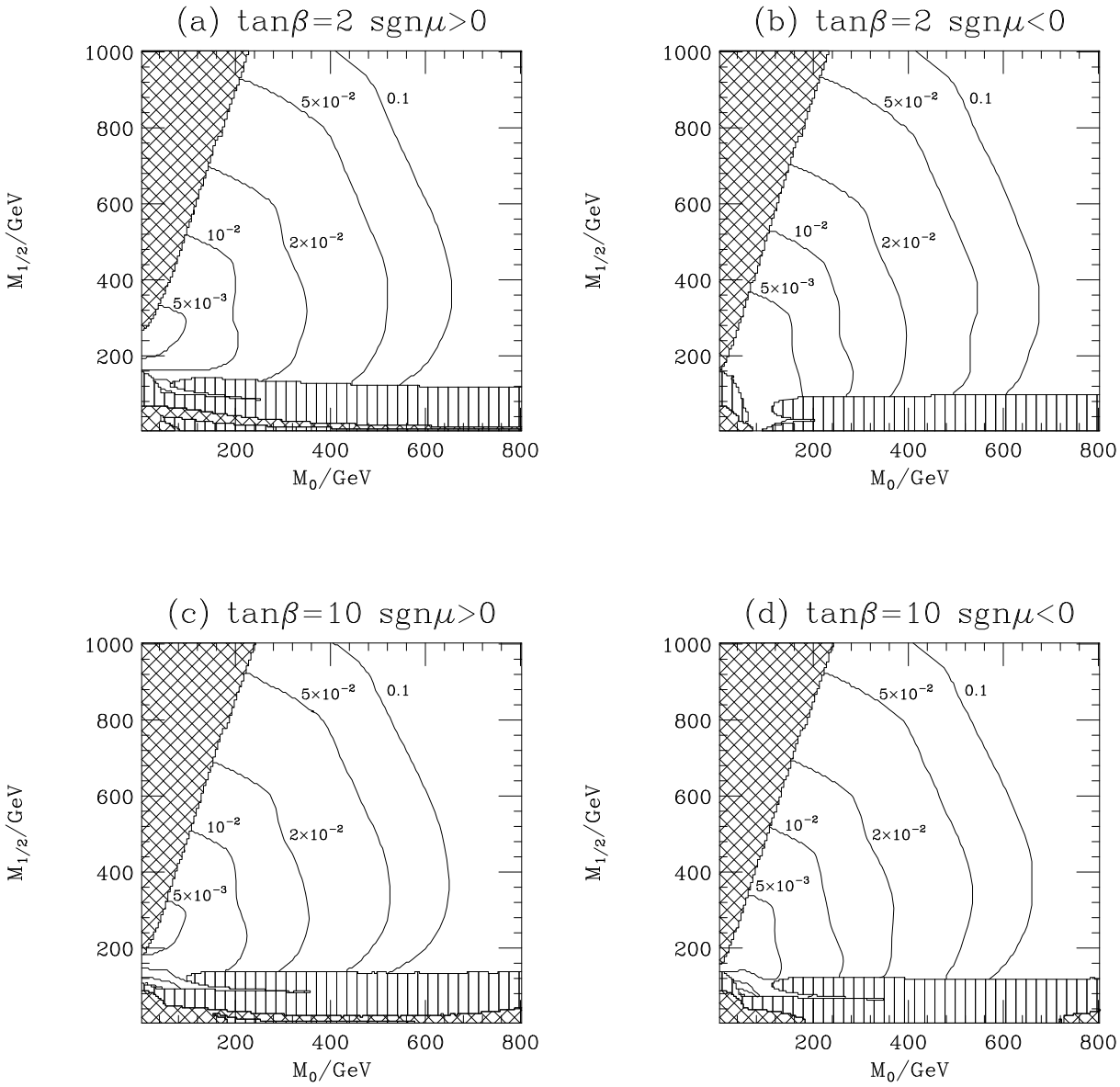

Figure 3.18: Contours showing the discovery potential of the Tevatron in the M_0, $M_{1/2}$ plane for $A_0 = 0$ GeV and 2 fb^{-1} integrated luminosity for different values of λ'_{211}. These contours are a 5σ excess of the signal above the background. Here we have imposed the cuts on the isolation and p_T of the leptons, the transverse mass and the missing transverse energy described in the text, and a veto on the presence of OSSF leptons. We have only considered the Standard Model background. The striped and hatched regions are described in the caption of Fig. 3.9.

in W production. The cuts we have applied to reduce the gauge boson pair production backgrounds, in particular the cuts on the missing transverse energy and the transverse mass, will significantly reduce this background. It was noted in [110] that the cross section falls extremely quickly with the p_T of the fake lepton, and hence the large p_T cut we have imposed will suppress this background. A proper treatment of the non-physics background requires a simulation of the detector and this is beyond the scope of this work.

In Figs. 3.17 and 3.18 the background from sparticle pair production is neglected. This is reasonable in an initial search where presumably an experiment would be looking for an excess of like-sign dilepton pairs, rather than worrying about precisely which model was giving the excess. If such an excess were observed, it would then be necessary to establish which physical processes were producing the excess. In the $\not{R}_{\rm p}$ MSSM there are two possible mechanisms which could produce such an excess: either resonant sparticle production; or sparticle pair production followed by the decay of the LSP. We will now consider additional cuts which will suppress the background to resonant slepton production from sparticle pair production and hopefully allow these two scenarios to be distinguished.

SUSY Backgrounds

We have seen that by imposing cuts on the transverse momentum and isolation of the like-sign dileptons, the missing transverse energy, the transverse mass and the presence of OSSF leptons the Standard Model backgrounds can be significantly reduced. However a significant background from sparticle pair production still remains. We therefore imposed the following additional cut to reduce this background:

- Vetoing all events when there are more than two jets each with $p_T > 20$ GeV.

While this cut only slightly reduces the signal it dramatically reduces the background from sparticle pair production. We performed a scan of the SUGRA parameter space at the four values of $\tan\beta$ and $\mathrm{sgn}\,\mu$ considered in Section 3.3.1. We generated fifty thousand events at each of one hundred points in the M_0, $M_{1/2}$ plane at each value of $\tan\beta$ and $\mathrm{sgn}\,\mu$, and then interpolated between these points as for the signal process. This allowed us to estimate an acceptance for the cuts which we multiplied by the sparticle pair production cross section to give a number of background events.

The effect of all the cuts on the total background, *i.e.* the Standard Model background and the sparticle pair production background is shown in Fig. 3.19 for different integrated luminosities with $\lambda'_{211} = 10^{-2}$ and in Fig. 3.20 for an integrated luminosity of 2 fb^{-1} with different values of λ'_{211}.

The effect of including the sparticle pair production background is to reduce the 5σ discovery regions. These regions are reduced for two reasons: for large $M_{1/2}$ the additional cut removes more signal events and hence reduces the statistical significance of the signal; at small values of $M_{1/2}$ there is a large background from sparticle pair production, relative to the SM background, which also reduces the statistical significance of the signal. However even for this relatively small value of the coupling there are large regions of parameter space in which a signal is visible above the background. The ratio of signal to background is still larger than one for most of the region where the signal is detectable above the background. For $\mathrm{sgn}\,\mu > 0$ there is only a very small region at low $M_{1/2}$ where

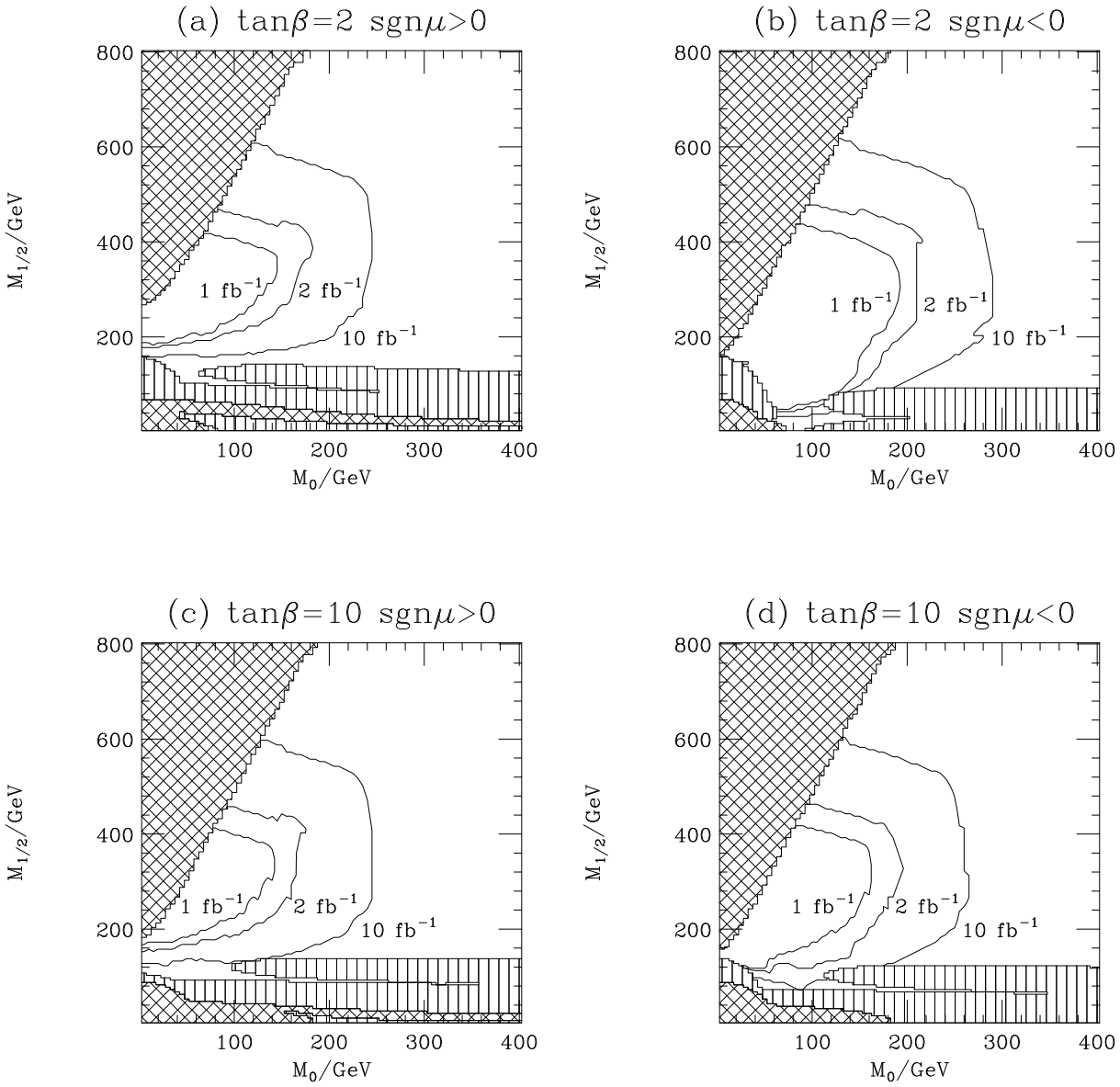

Figure 3.19: Contours showing the discovery potential of the Tevatron in the M_0, $M_{1/2}$ plane for $\lambda'_{211} = 10^{-2}$ and $A_0 = 0$ GeV. These contours are a 5σ excess of the signal above the background. Here, in addition to the cuts on the isolation and p_T of the leptons, the transverse mass and the missing transverse energy described in the text, and a veto on the presence of OSSF leptons we have imposed a cut on the presence of more than two jets. This includes the sparticle pair production background as well as the Standard Model backgrounds. The striped and hatched regions are as described in the caption of Fig. 3.9.

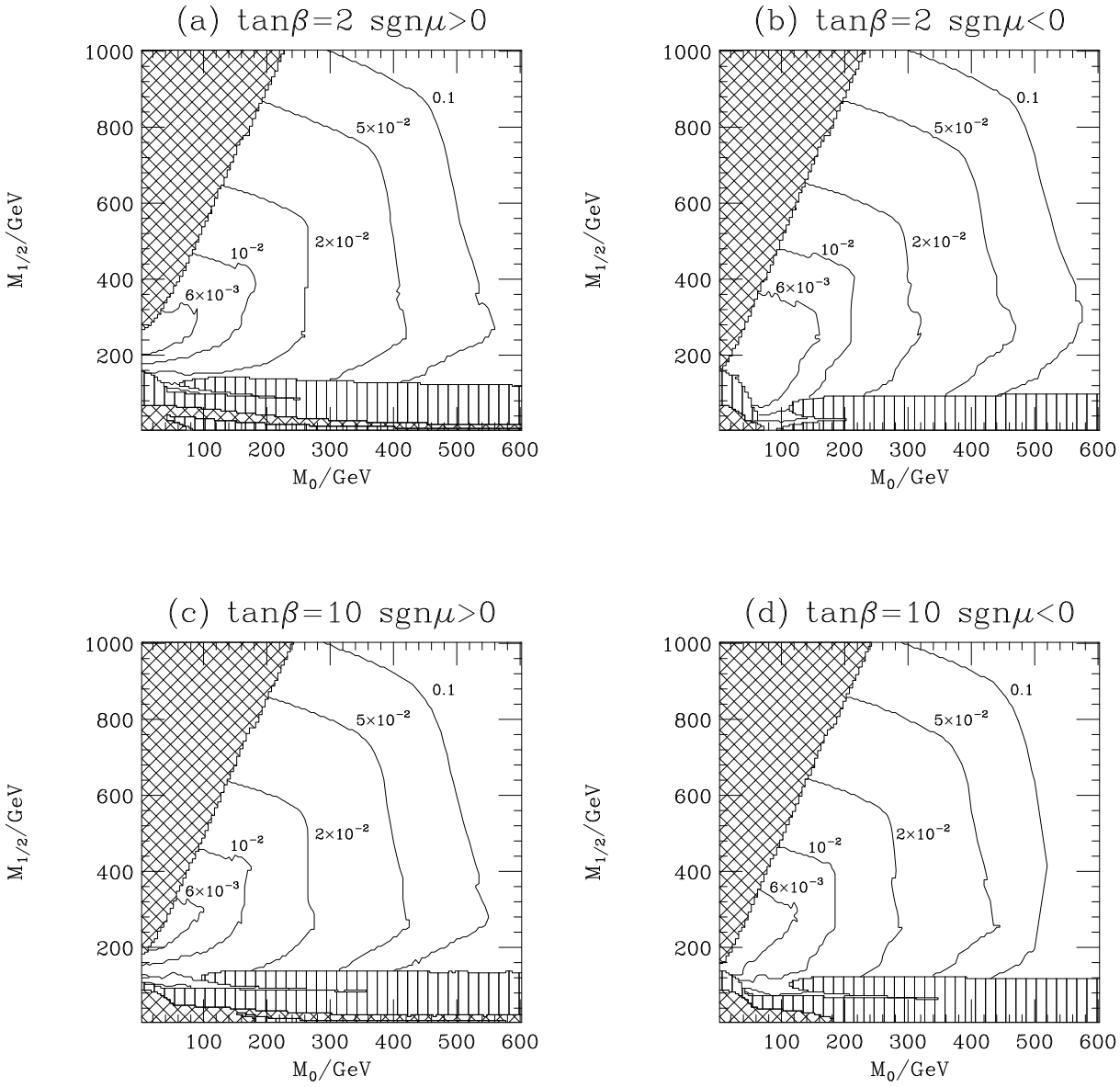

Figure 3.20: Contours showing the discovery potential of the Tevatron in the M_0, $M_{1/2}$ plane for $A_0 = 0$ GeV and an integrated luminosity of 2 fb^{-1} for different values of λ'_{211}. These contours are a 5σ excess of the signal above the background. Here, in addition to the cuts on the isolation and p_T of the leptons, the transverse mass and the missing transverse energy described in the text, and a veto on the presence of OSSF leptons we have imposed a cut on the presence of more than two jets. This includes the sparticle pair production background as well as the Standard Model backgrounds. The striped and hatched regions are as described in the caption of Fig. 3.9.

S/B drops below one and even here $S/B > 0.5$. However for $\operatorname{sgn}\mu < 0$ there are regions of low S/B for small values of $M_{1/2}$. The discovery range for these $\not{R}_p$ processes extends to larger values of $M_{1/2}$ than the 5σ discovery curve for sparticle pair production as only one sparticle is produced which requires a much lower parton–parton centre-of-mass energy than sparticle pair production.

Again even for small smuon masses with low values of the $\not{R}_p$ Yukawa coupling there are regions where a signal of resonant slepton production is not visible above the background. However for large couplings the signal in these regions is visible above the background. For a coupling of $\lambda'_{211} = 0.05$ a smuon mass of 310 (330) GeV is visible above the background with 2 (10) fb^{-1} integrated luminosity, and for a coupling of $\lambda'_{211} = 0.1$ a smuon mass of 400 (430) GeV is visible above the background with 2 (10) fb^{-1} integrated luminosity.

3.3.3.2 LHC

The cross section for the production of a charged lepton and a neutralino, which is again the dominant production mechanism, at the LHC is shown in Fig. 3.21 in the M_0, $M_{1/2}$ plane with $A_0 = 0$ GeV and $\lambda'_{211} = 10^{-2}$ for two different values of $\tan\beta$ and both values of $\operatorname{sgn}\mu$. The total cross section for resonant slepton production followed by a supersymmetric gauge decay is shown in Fig. 3.22. As for the Tevatron, the total resonant slepton cross section closely follows the slepton mass contours whereas the cross section for neutralino–lepton production falls off more quickly at small $M_{1/2}$ because the branching ratio for $\tilde{\mu}_L \to \mu\tilde{\chi}^0_1$ is reduced due to the production of charginos and the heavier neutralinos. We adopted the same procedure described in Section 3.3.3.1 to estimate the acceptance of the cuts we imposed. We will again first consider the cuts required to reduce the Standard Model backgrounds and then the additional cut used to suppress the sparticle pair production background.

Standard Model Backgrounds

We applied the following cuts to reduce the Standard Model backgrounds:

1. A cut requiring all the leptons to be in the central region of the detector $|\eta| < 2.0$.

2. A cut on the transverse momentum of the like-sign leptons, $p_T^{\text{lepton}} \geq 40$ GeV. This is the lowest cut we could apply given our parton-level cut of $p_T^{\text{parton}} = 40$ GeV, for the $b\bar{b}$ background.

3. An isolation cut on the like-sign leptons so that the transverse energy in a cone of radius, $\Delta R = \sqrt{\Delta\phi^2 + \Delta\eta^2} = 0.4$, about the direction of the lepton is less than 5 GeV.

4. We reject events with 60 GeV $< M_T <$ 85 GeV (*c.f.* Eqn. 3.7). This cut is applied to both of the like-sign leptons.

5. A veto on the presence of a lepton in the event with the same flavour but opposite charge as either of the leptons in the like-sign pair if the lepton has $p_T > 10$ GeV and passes the same isolation cut as the like-sign leptons.

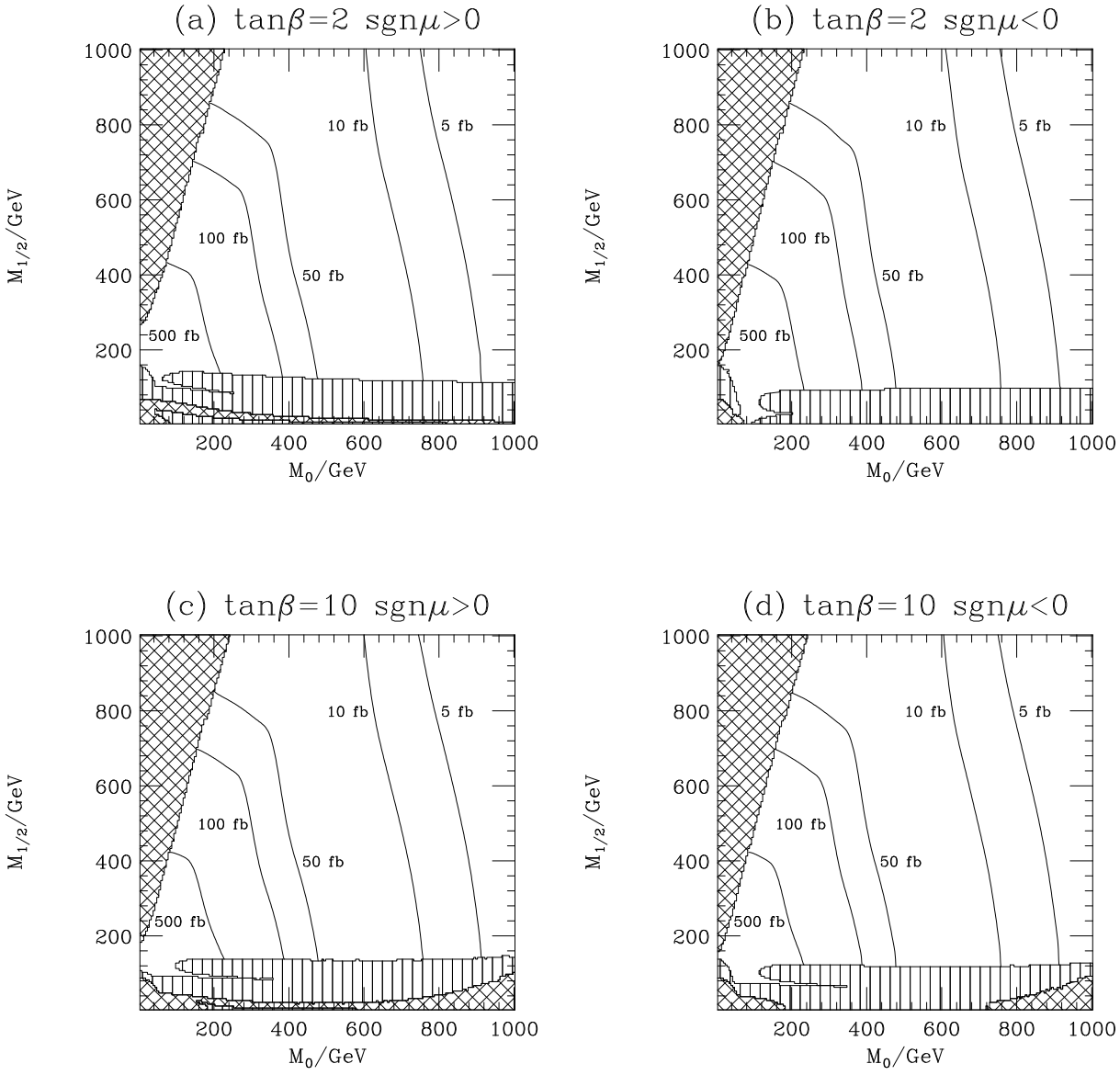

Figure 3.21: Contours showing the cross section for the production of a neutralino and a charged lepton at the LHC in the M_0, $M_{1/2}$ plane for $A_0 = 0$ GeV and $\lambda'_{211} = 10^{-2}$ with different values of $\tan\beta$ and $\mathrm{sgn}\,\mu$. The striped and hatched regions are described in the caption of Fig. 3.9.

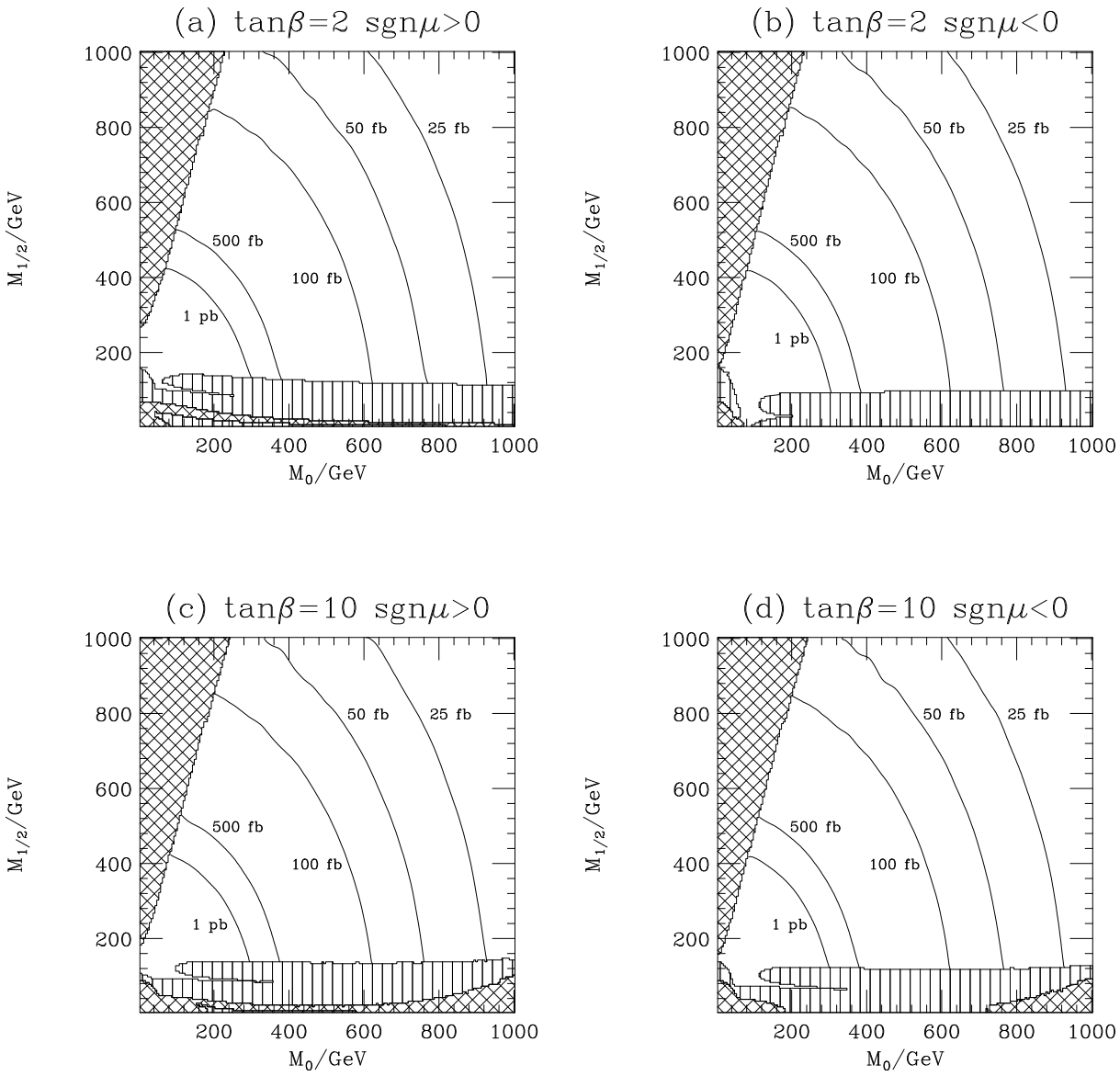

Figure 3.22: Contours showing the cross section for resonant slepton production followed by a supersymmetric gauge decay at the LHC in the M_0, $M_{1/2}$ plane for $A_0 = 0$ GeV and $\lambda'_{211} = 10^{-2}$ with different values of $\tan\beta$ and $\mathrm{sgn}\,\mu$. The striped and hatched regions are described in the caption of Fig. 3.9.

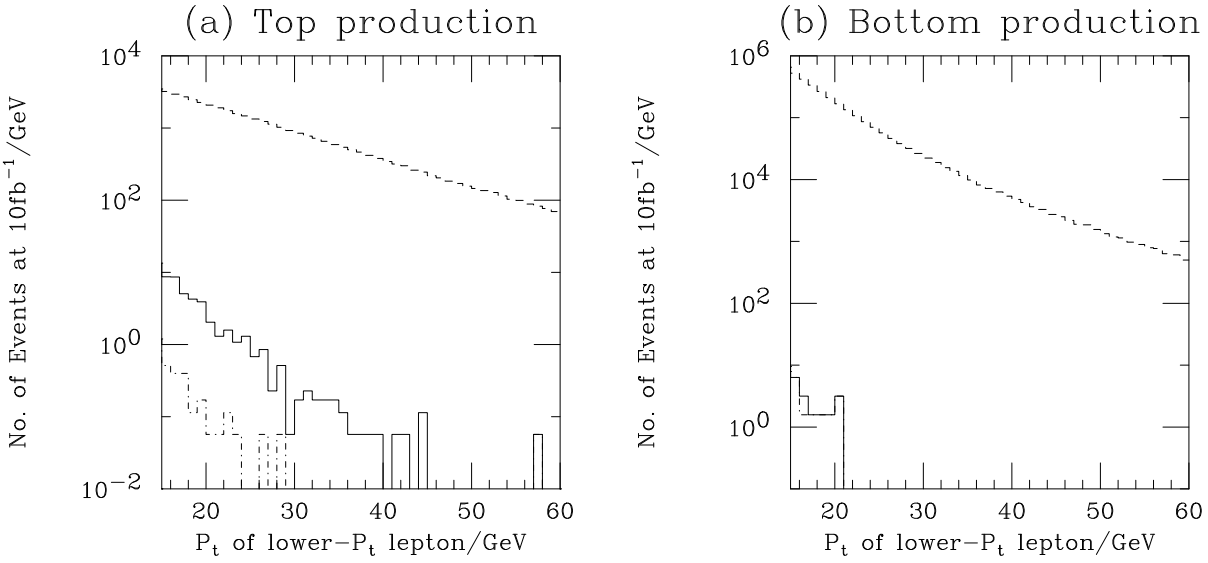

Figure 3.23: Effect of the isolation cuts on the $t\bar{t}$ and $b\bar{b}$ backgrounds at the LHC. The dashed line gives the background before any cuts and the solid line shows the effect of the isolation cut described in the text. The dot-dash line gives the effect of all the cuts, including the cut on the number of jets, for the $b\bar{b}$ background this is almost indistinguishable from the solid line. As a parton-level cut of 40 GeV was used in simulating the $b\bar{b}$ background, the results below 40 GeV for the lepton p_T do not correspond to the full number of background events. The distributions have been normalized to an integrated luminosity of 10 fb^{-1}.

6. A cut on the missing transverse energy, $\not{E}_T < 20$ GeV.

The first two cuts are designed to reduce the background from heavy quark, *i.e.* $b\bar{b}$ and $t\bar{t}$, production which is the major source of background before any cuts. However, as can be seen in Fig. 3.23, after the imposition of the p_T and isolation cuts this background is significantly reduced. It remains the major source of the error on the background however due to the large cross section for $b\bar{b}$ production which makes it impossible to simulate the full luminosity of the LHC with the resources available.

The remaining cuts reduce the background from gauge boson pair production, particularly WZ production, which dominates the Standard Model background after the imposition of the isolation and p_T cuts. Fig. 3.24a shows that the cut on the transverse mass, *i.e.* removing the region 60 GeV $< M_T <$ 85 GeV for each of the like sign leptons, will reduce the background from WZ production, which is the largest of the gauge boson pair production backgrounds. The cut on the missing transverse energy, $\not{E}_T < 20$ GeV, will also significantly reduce the background from WZ production, as can be seen in Fig. 3.24b. The effect of these cuts is shown in Fig. 3.25. Again the simulation of the gauge boson pair production backgrounds does not include Wγ production which may be an important source of background, but should be significantly reduced by the cuts.

The effect of all these cuts on the background is shown in Table 3.3. This gives a total background after all the cuts of 4.9 ± 1.6 events, for 10 fb^{-1} integrated luminosity. If we take a conservative approach and take a background of 6.5 events, *i.e.* a 1σ fluctuation

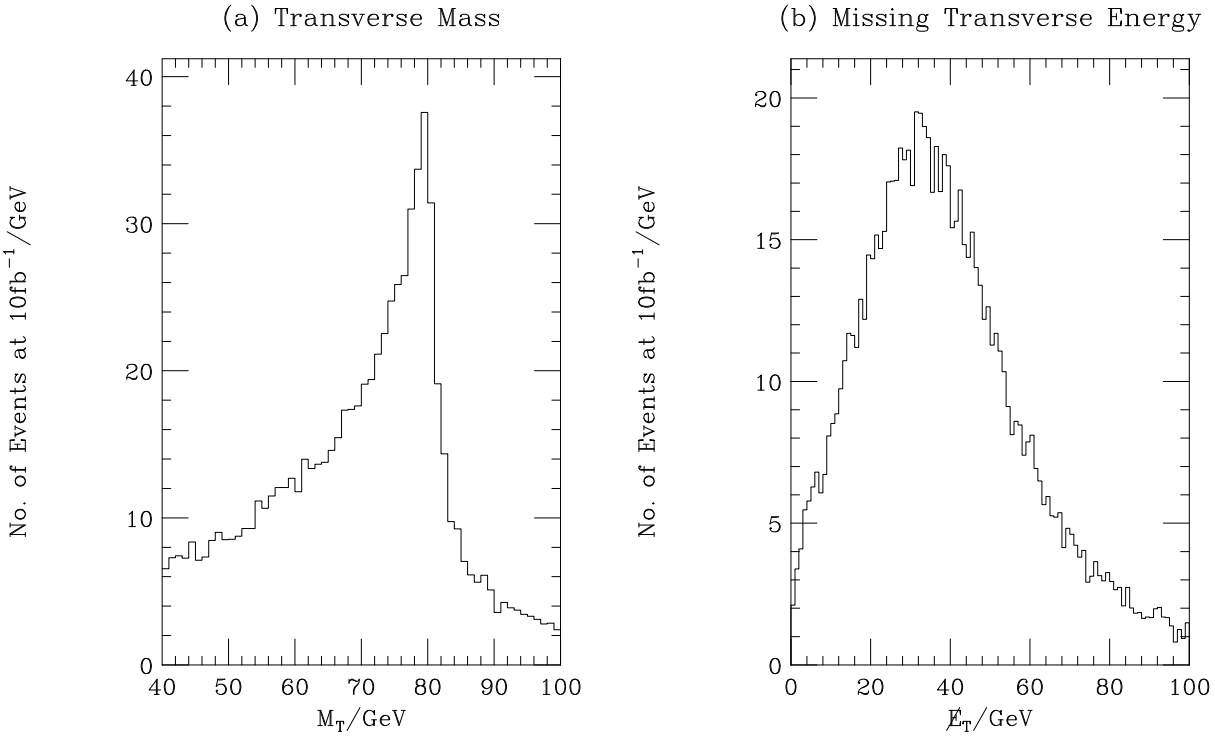

Figure 3.24: The transverse mass and missing transverse energy in WZ events at the LHC. The distributions are normalized to an integrated luminosity of 10 fb^{-1}.

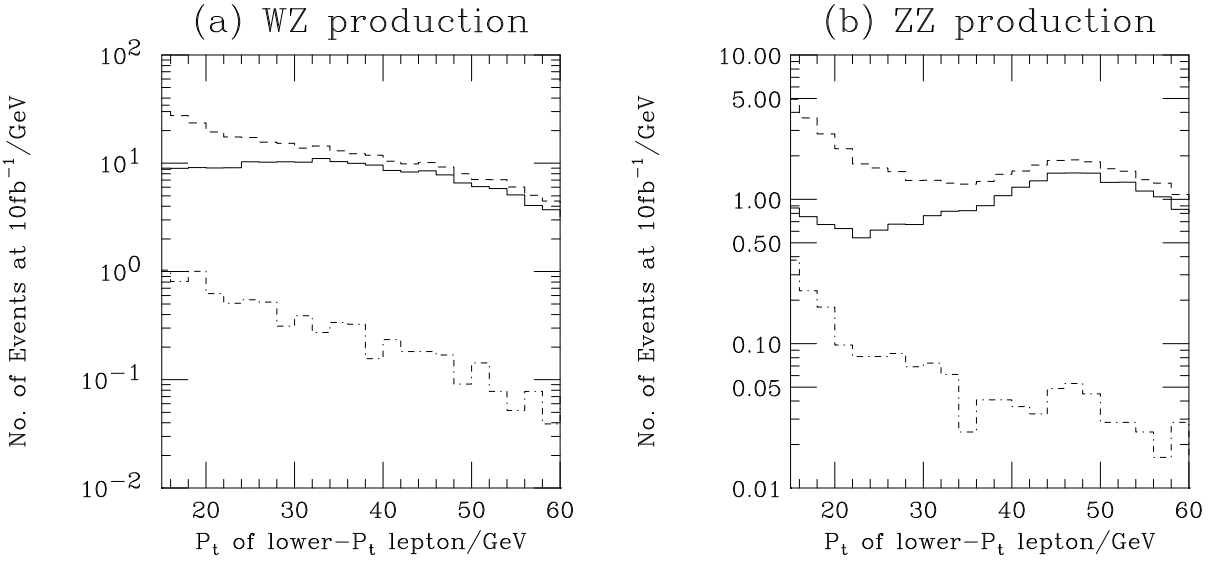

Figure 3.25: Effect of the isolation cuts on the WZ and ZZ backgrounds at the LHC. The dashed line gives the background before any cuts and the solid line shows the effect of the isolation cut described in the text. The dot-dash line gives the effect of all the cuts, including the cut on the number of jets. The distributions are normalized to an integrated luminosity of 10 fb^{-1}.

Background process	Number of Events			
	After p_T cut	After isolation and p_T cuts	After isolation, p_T, M_T, $\not{E}_T$ cuts and OSSF lepton veto.	After all cuts
WW	3.6 ± 0.5	0.0 ± 0.06	0.0 ± 0.06	0.0 ± 0.06
WZ	239 ± 2.5	198.6 ± 2.3	3.8 ± 0.3	3.8 ± 0.3
ZZ	55.4 ± 0.7	45.2 ± 0.6	1.04 ± 0.09	1.04 ± 0.09
$t\bar{t}$	$(4.4 \pm 0.2) \times 10^3$	0.28 ± 0.13	0.06 ± 0.06	0.06 ± 0.06
bb	$(4.4 \pm 0.9) \times 10^4$	0.0 ± 1.6	0.0 ± 1.6	0.0 ± 1.6
Single top	36.6 ± 1.5	0.0 ± 0.004	0.0 ± 0.004	0.0 ± 0.004
Total	$(4.9 \pm 0.9) \times 10^4$	244.1 ± 2.9	4.9 ± 1.6	4.9 ± 1.6

Table 3.3: Backgrounds to like-sign dilepton production at the LHC. The numbers of events are based on an integrated luminosity of 10 fb^{-1}. We have calculated an error on the cross section by varying the scale between half and twice the hard scale, apart from the gauge boson pair cross section where we do not have this information and the effect of varying the scale is expected to be small anyway. The error on the number of events is the error on the cross section and the statistical error from the Monte Carlo simulation added in quadrature. If no events passed the cut the statistical error was taken to be the same as if one event had passed the cuts.

above the central value of our calculation a 5σ statistical fluctuation would correspond to 16 events, for an integrated luminosity of 10 fb^{-1}. Fig. 3.23 shows that this is a conservative upper bound.

We adopted the same procedure described in the previous section to obtain the acceptance for the $\not{R}_p$ signal given the cuts we have imposed. The discovery potential of the LHC is shown in Fig. 3.26, for $\lambda'_{211} = 10^{-2}$ with different integrated luminosities, and in Fig. 3.27, for an integrated luminosity of 10 fb^{-1} with different values of λ'_{211}. This is considerably greater than the discovery potential of the Tevatron at high M_0 and $M_{1/2}$ due to the larger centre-of-mass energy of the LHC and hence the larger cross sections. In particular, the search potential with one year's running at high luminosity, *i.e.* 100 fb^{-1}, covers large regions of the M_0, $M_{1/2}$ plane. At very large values of $M_{1/2}$ this extends to regions where the sparticle pair production cross section is small due to the high masses of the SUSY particles.

At small values of M_0 and $M_{1/2}$ there are regions of SUGRA parameter space which cannot be probed for any couplings due to the cuts we have applied. However these regions can be excluded by either LEP or the Tevatron and we will therefore ignore them in the rest of this analysis. If we neglect these regions, the LHC can observe a resonant slepton with a mass of up to 510 (710) GeV for a coupling of $\lambda'_{211} = 0.02$ with 10 (100) fb^{-1} integrated luminosity and for a coupling $\lambda'_{211} = 0.05$ a resonant slepton can be observed with a mass of up to 750 (950) GeV with 10 (100) fb^{-1} integrated luminosity.

As with the Tevatron analysis, we have neglected the background from sparticle pair production. This is reasonable in an initial search for an excess of like-sign dilepton pairs over the Standard Model expectation. If such an excess were observed it would be

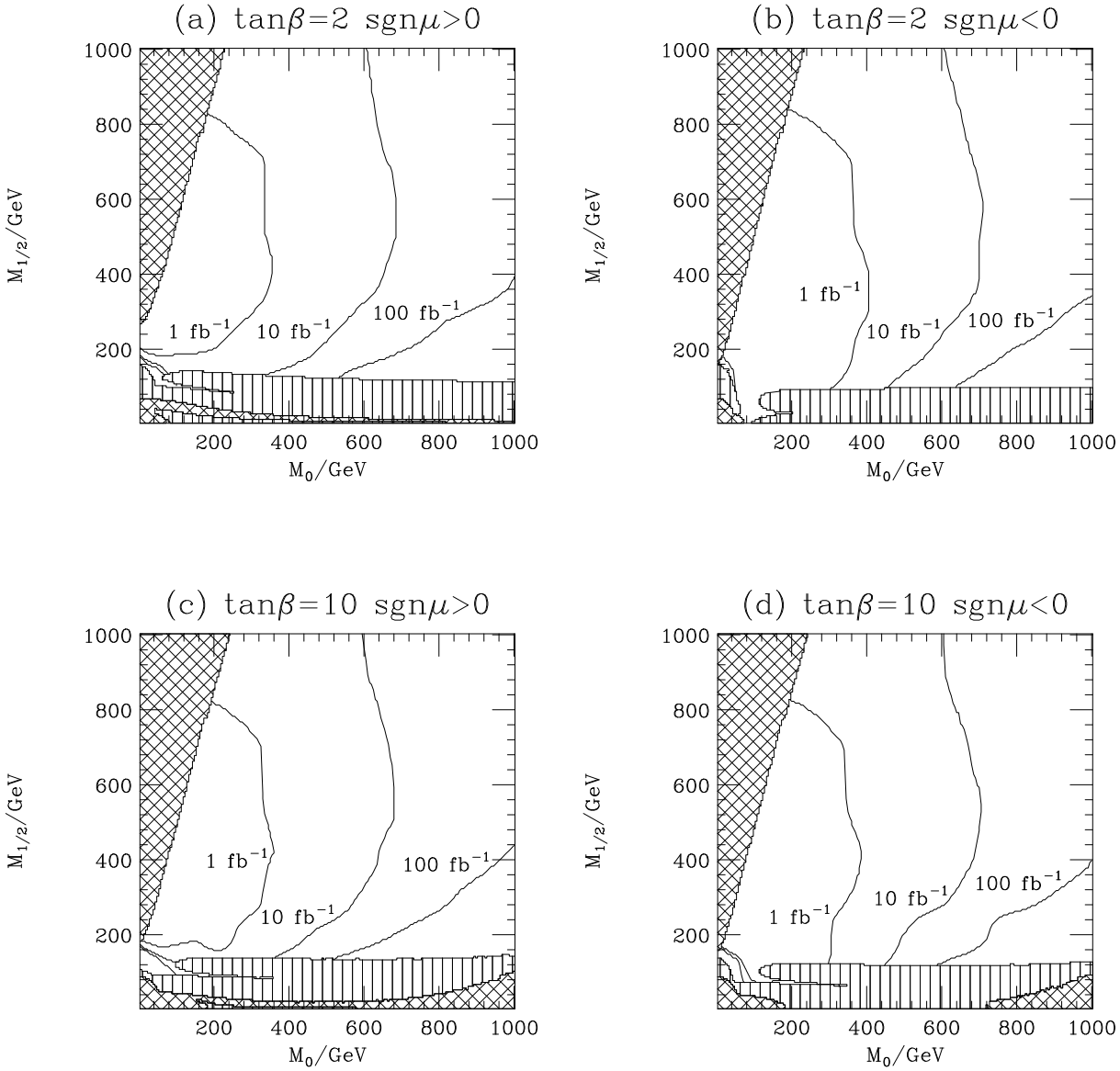

Figure 3.26: Contours showing the discovery potential of the LHC in the M_0, $M_{1/2}$ plane for $\lambda'_{211} = 10^{-2}$ and $A_0 = 0$ GeV. These contours are a 5σ excess of the signal above the background. Here we have imposed cuts on the isolation and p_T of the leptons, the transverse mass and the missing transverse energy described in the text, and a veto on the presence of OSSF leptons. We have only considered the Standard Model background. The striped and hatched regions are described in the caption of Fig. 3.9.

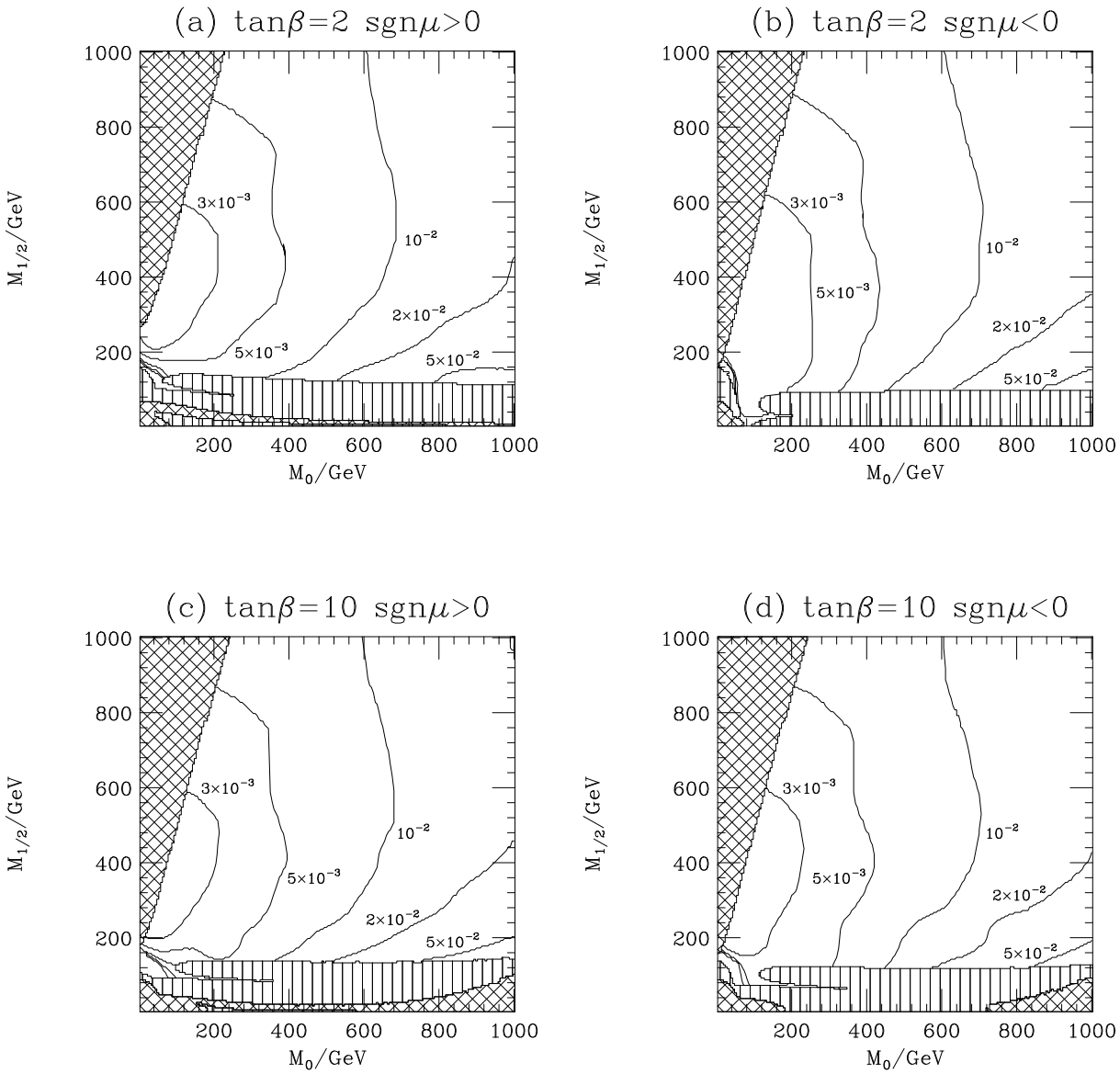

Figure 3.27: Contours showing the discovery potential of the LHC in the M_0, $M_{1/2}$ plane for $A_0 = 0$ GeV and an integrated luminosity of 10 fb^{-1} with different values of λ'_{211}. These contours are a 5σ excess of the signal above the background. Here we have imposed cuts on the isolation and p_T of the leptons, the transverse mass and the missing transverse energy described in the text, and a veto on the presence of OSSF leptons. We have only considered the Standard Model background. The striped and hatched regions are described in the caption of Fig. 3.9.

necessary to establish which process was producing the effect. In the next section, we will present the cuts necessary to reduce the background from sparticle pair production and enable a resonant slepton signature to be established over all the backgrounds.

SUSY Backgrounds

The background from sparticle pair production is much more important at the LHC than the Tevatron given the much higher cross sections for sparticle pair production. The nature of the sparticles produced is also different due to the higher energies. In the regions of SUGRA parameter space where the pair production cross section at the Tevatron is large the lightest SUSY particles, *i.e.* the electroweak gauginos, are predominately produced. This is because the production of the heavier squarks and gluinos is suppressed by the higher parton–parton centre-of-mass energies required. However given the higher centre-of-mass energy of the LHC the production of the coloured sparticles which occurs via the strong interaction dominates the cross section. This means that a cut on the number of jets in an event will be more effective in reducing the background from sparticle pair production. The following cut was applied:

- Vetoing all events when there are more than two jets each with $p_T > 50$ GeV.

As the sparticle pair production background at the LHC is larger than at the Tevatron we needed to simulate more events in order to obtain a reliable estimate of the acceptance for this background. This meant that with the available resources we were forced to use a coarser scan of the M_0, $M_{1/2}$ plane. We used a 16 point grid and simulated a different number of events at each point depending on the value of $M_{1/2}$ as the sparticle pair production cross section decreases as $M_{1/2}$ increases. We simulated 10^5, 10^5, 10^6, and 10^7 events at each of four points in M_0 for $M_{1/2} = 875$ GeV, $M_{1/2} = 625$ GeV, $M_{1/2} = 375$ GeV and $M_{1/2} = 125$ GeV, respectively.

Our estimate of the discovery potential of the LHC after this cut, including all the backgrounds is given in Fig. 3.28, for $\lambda_{211} = 10^{-2}$ with different integrated luminosities, and in Fig. 3.29, for an integrated luminosity of 10 fb^{-1} with different values of the $\not{R}_p$ Yukawa couplings. As with the Tevatron, the discovery potential is reduced in two regions relative to that shown in Figs. 3.26 and 3.27. The reduction at high $M_{1/2}$ is due to the smaller signal after the imposition of the jet cut, whereas the reduction at small $M_{1/2}$ is due to the larger background. However there are still large regions of SUGRA parameter space in which this process is visible above the background, particularly at large $M_{1/2}$ where there is less sensitivity to sparticle pair production. Due to the larger backgrounds from sparticle pair production there are large regions, at small $M_{1/2}$, where the signal is detectable above the background although the S/B is small. In general there is a region extending around 200 GeV in $M_{1/2}$ above the bottom of the 5σ discovery contour for 100 fb^{-1} where $S/B < 1$.

If we again neglect the region at small M_0 and $M_{1/2}$, which cannot be probed for any $\not{R}_p$ Yukawa couplings given our cuts, we can obtain a mass reach for the LHC with a given $\not{R}_p$ Yukawa coupling. Slepton masses of 460 (600) GeV can be discovered with 10 (100) fb^{-1} integrated luminosity for a coupling $\lambda'_{211} = 0.05$ and slepton masses of

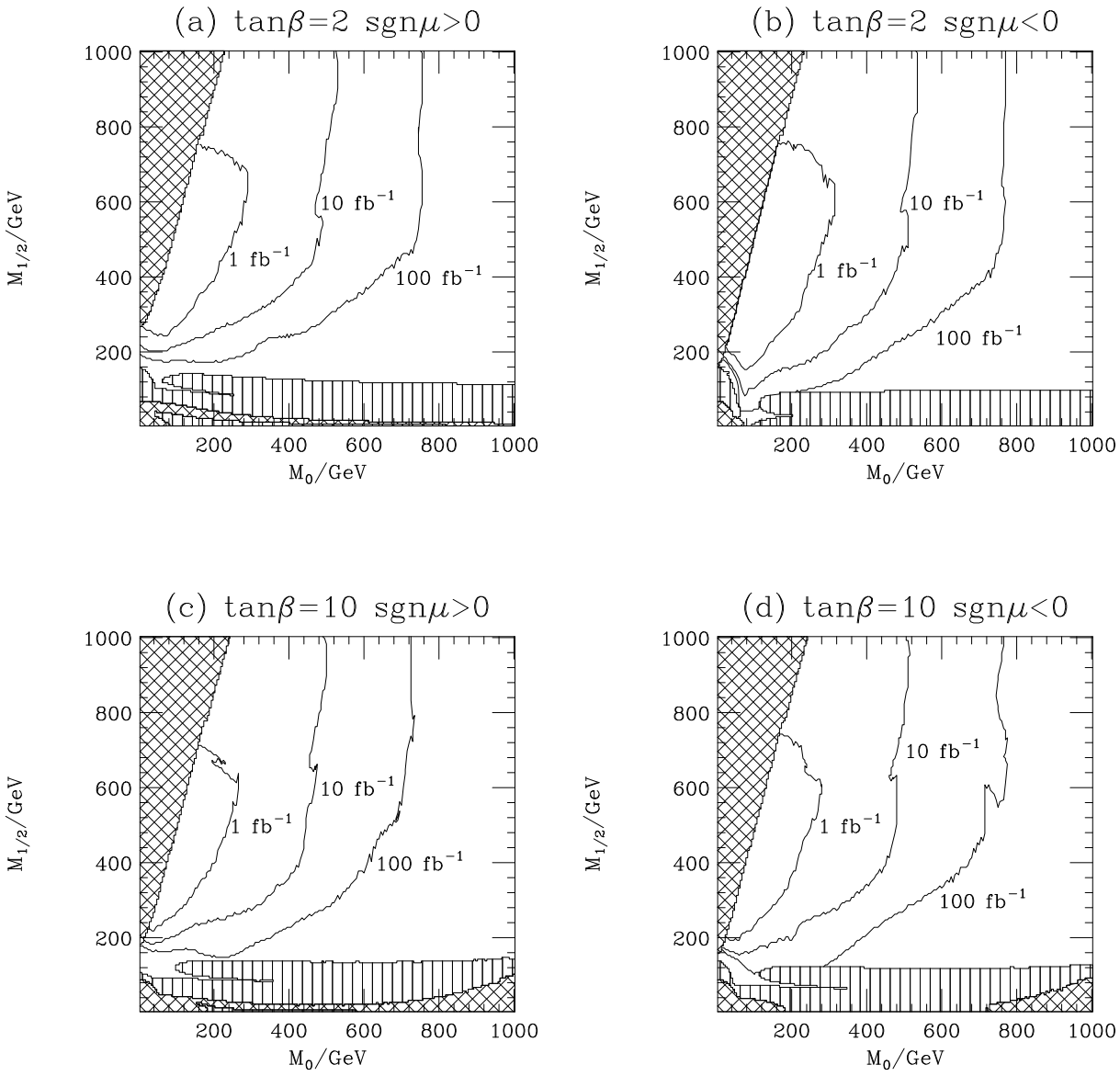

Figure 3.28: Contours showing the discovery potential of the LHC in the M_0, $M_{1/2}$ plane for $\lambda'_{211} = 10^{-2}$ and $A_0 = 0$ GeV. These contours are a 5σ excess of the signal above the background. Here, in addition to the cuts on the isolation and p_T of the leptons, the transverse mass and the missing transverse energy described in the text, and a veto on the presence of OSSF leptons, we have imposed a cut on the presence of more than two jets. We have included the sparticle pair production background as well as the Standard Model backgrounds. The striped and hatched regions are described in the caption of Fig. 3.9.

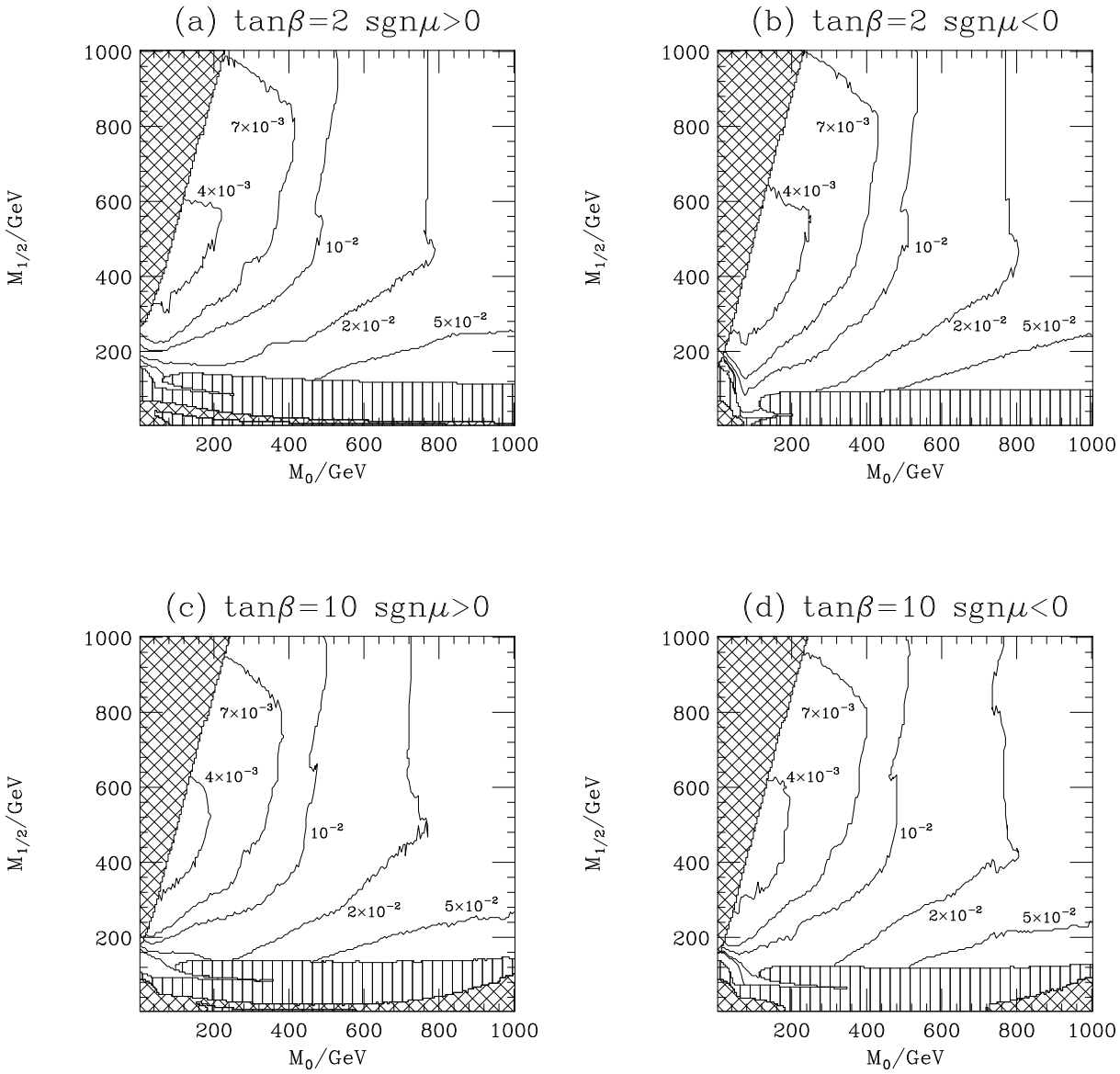

Figure 3.29: Contours showing the discovery potential of the LHC in the M_0, $M_{1/2}$ plane for $A_0 = 0$ GeV and an integrated luminosity of 10 fb^{-1} with different values of λ'_{211}. These contours are a 5σ excess of the signal above the background. Here, in addition to the cuts on the isolation and p_T of the leptons, the transverse mass and the missing transverse energy described in the text, and a veto on the presence of OSSF leptons, we have imposed a cut on the presence of more than two jets. We have included the sparticle pair production background as well as the Standard Model backgrounds. The striped and hatched regions are described in the caption of Fig. 3.9.

610 (820) GeV can be observed with 10 (100) fb^{-1} integrated luminosity for a coupling $\lambda'_{211} = 0.1$.

3.3.4 Mass Reconstruction

There are many possible models which lead to an excess of like-sign dilepton pairs over the prediction of the Standard Model. Indeed, we have seen that within the $\not{R}_p$ extension of the MSSM such an excess could be due to either sparticle pair production followed by $\not{R}_p$ decays of the LSPs, or resonant charged slepton production followed by a supersymmetric gauge decay of the slepton. The cut on the number of jets described above gives one way of discriminating between these two scenarios.

An additional method of distinguishing between these two scenarios is to try to reconstruct the masses of the decaying sparticles for resonant slepton production. In principle this is straightforward. The neutralino decay to a quark–antiquark pair and a charged lepton will give two jets (or more after the emission of QCD radiation) and a charged lepton. These decay products should be relatively close together. Therefore to reconstruct the neutralino we took the highest two p_T jets in the event and combined them with the charged lepton which was closest in (η, ϕ) space. We only used events in which both jets had $p_T > 10$ GeV in addition to passing all the cuts described in the previous sections, *i.e.* both the cuts required to suppress the Standard Model and SUSY backgrounds. This gives a neutralino candidate. The masses of these candidates are shown, for a sample point in SUSY parameter space, for both the Tevatron, Fig. 3.30, and the LHC, Fig. 3.31. In both cases, in addition to showing the result for the coupling $\lambda'_{211} = 10^{-2}$, we show a coupling for which the signal is exactly 5σ above the background at this point to demonstrate what can be seen if the signal is only just detectable. Both figures show that the reconstructed neutralino mass is in good agreement with the simulated value, although the situation may be worse once detector effects have been included.

We can then combine this neutralino candidate with the remaining lepton in the event to give a slepton candidate, under the assumption that the like-sign leptons were produced in the processes $\tilde{\ell}^+ \to \ell^+ \tilde{\chi}_1^0$. The mass distribution of these slepton candidates is shown in Fig. 3.32 for the Tevatron and Fig. 3.33 for the LHC. Again there is good agreement between the position of the peak in the distribution and the value of the smuon mass used in the simulation.

The data for both the neutralino and smuon mass reconstructions is binned in 10 GeV bins. We have used the events in the central bin and the two bins on either side to reconstruct the neutralino and smuon masses. These reconstructed masses are given in Table 3.4. For both the points we have shown, the reconstructed mass lies between 5 GeV and 15 GeV below the simulated sparticle masses. This is due to the loss of some of the energy of the jets produced in the neutralino decay from the cones used to define the jets. It is common to include this effect in the jet energy correction, so this shift would probably not be observed in a full experimental simulation.

The agreement between the results of the simulation and the input values is good provided that the Standard Model background is dominant over the background from sparticle pair production and that the lightest neutralino is predominantly produced in the smuon decay. This is the case at the points used in Figs. 3.30-3.33. At the point

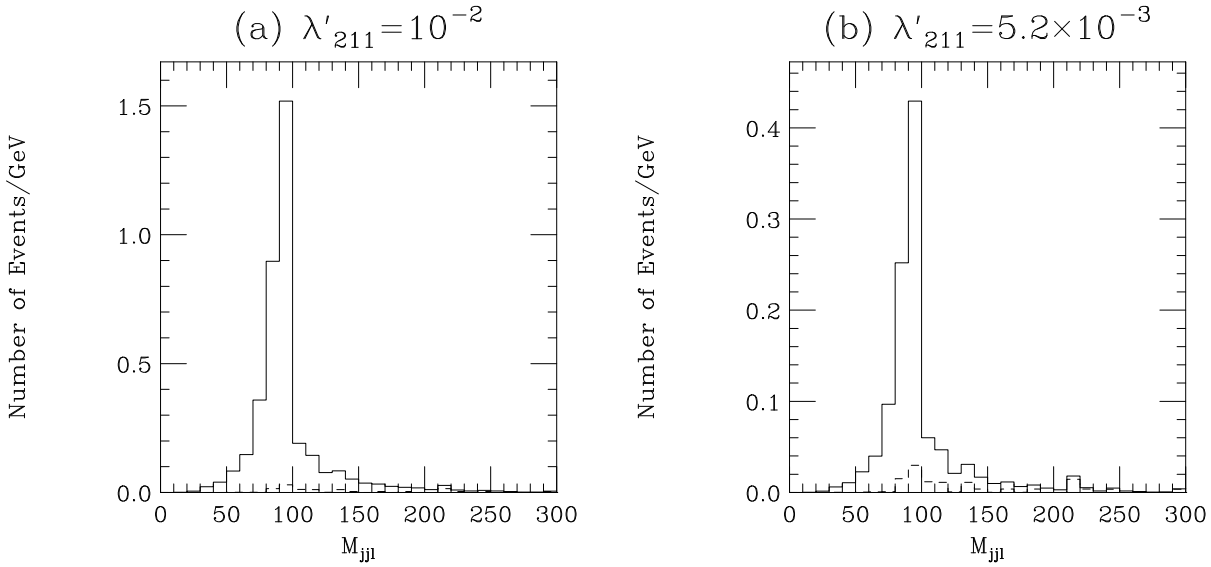

Figure 3.30: The reconstructed neutralino mass at the Tevatron for $M_0 = 50$ GeV, $M_{1/2} = 250$ GeV, $\tan\beta = 2$, $\mathrm{sgn}\,\mu > 0$ and $A_0 = 0$ GeV. The value of the coupling in (b) is chosen such that after the cuts applied in Section 3.3.3 the signal is 5σ above the background. At this point the lightest neutralino mass is $M_{\tilde{\chi}_1^0} = 98.9$ GeV. We have normalized the distributions to an integrated luminosity of 2 fb^{-1}. The dashed line shows the background and the solid line shows the sum of the signal and the background.

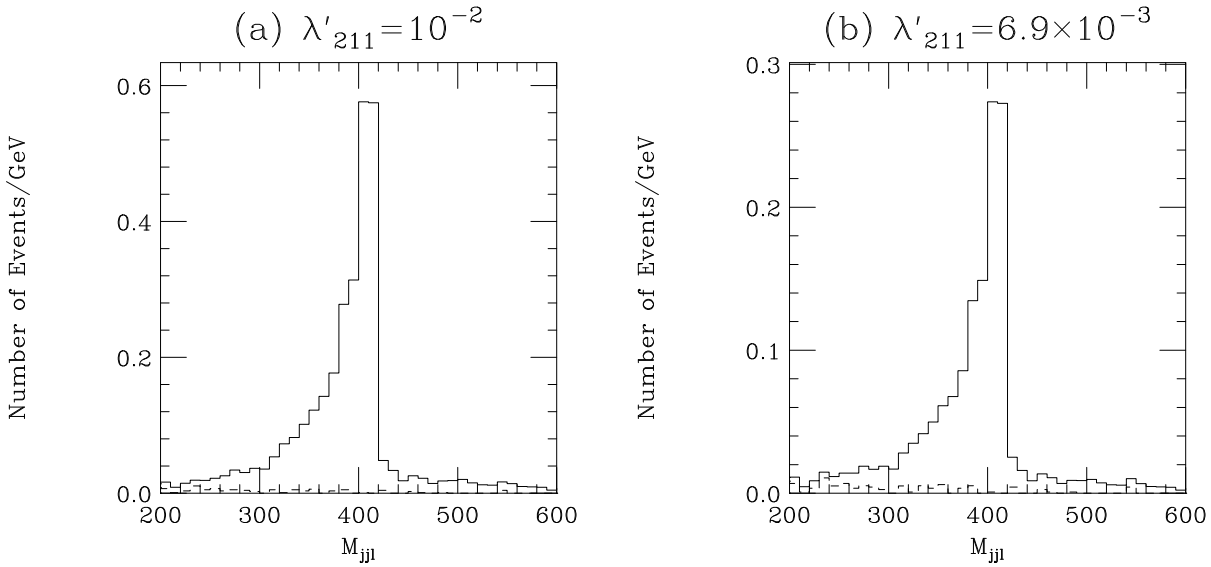

Figure 3.31: The reconstructed neutralino mass at the LHC for $M_0 = 350$ GeV, $M_{1/2} = 950$ GeV, $\tan\beta = 10$, $\mathrm{sgn}\,\mu < 0$ and $A_0 = 0$ GeV. The value of the coupling in (b) is chosen such that after the cuts applied in Section 3.3.3 the signal is 5σ above the background. At this point the lightest neutralino mass is $M_{\tilde{\chi}_1^0} = 418.0$ GeV. We have normalized the distributions to an integrated luminosity of 10 fb^{-1}. The dashed line shows the background and the solid line shows the sum of the signal and the background.

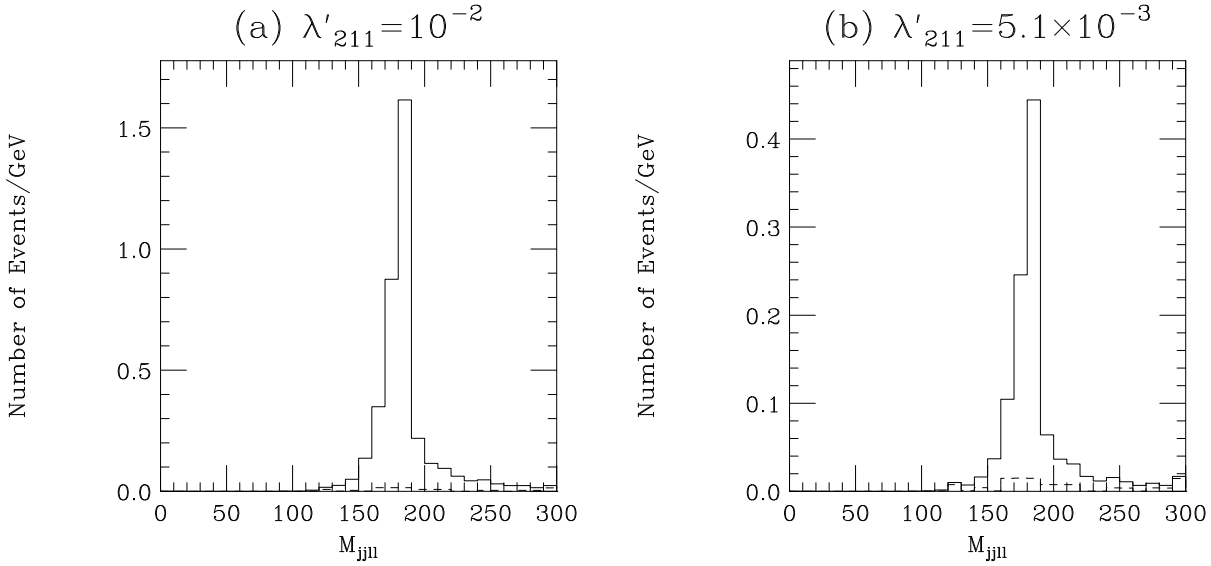

Figure 3.32: The reconstructed slepton mass at the Tevatron for $M_0 = 50$ GeV, $M_{1/2} = 250$ GeV, $\tan\beta = 2$, $\mathrm{sgn}\,\mu > 0$ and $A_0 = 0$ GeV. The value of the coupling in (b) is chosen such that after the cuts applied in Section 3.3.3 the signal is 5σ above the background. At this point the smuon mass is $M_{\tilde{\mu}_\mathrm{L}} = 189.1$ GeV. We have normalized the distributions to an integrated luminosity of 2 fb^{-1}. The dashed line shows the background and the solid line shows the sum of the signal and the background.

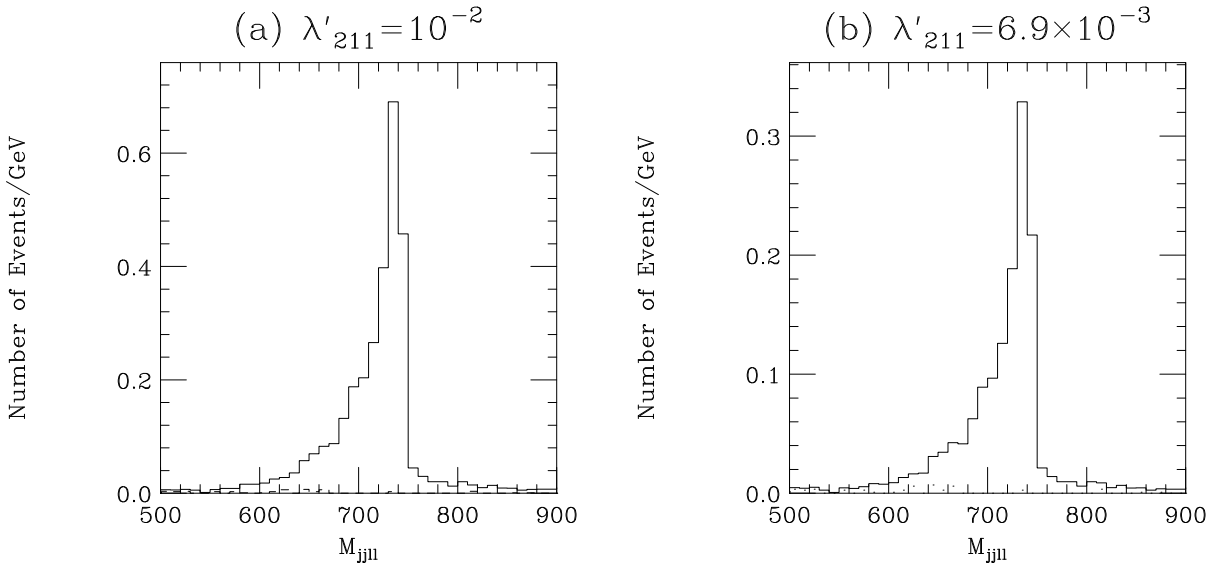

Figure 3.33: The reconstructed slepton mass at the LHC for $M_0 = 350$ GeV, $M_{1/2} = 950$ GeV, $\tan\beta = 10$, $\mathrm{sgn}\,\mu < 0$ and $A_0 = 0$ GeV. The value of the coupling in (b) is chosen such that after the cuts applied in Section 3.3.3 the signal is 5σ above the background. At this point the smuon mass is $M_{\tilde{\mu}_\mathrm{L}} = 745.9$ GeV. We have normalized the distributions to an integrated luminosity of 10 fb^{-1}. The dashed line shows the background and the solid line shows the sum of the signal and the background.

Experiment	λ'_{211}	Cuts	Point	Neutralino mass/ GeV		Slepton mass/ GeV	
				Actual	Recon.	Actual	Recon.
Tevatron	10^{-2}	no	A	98.9	90.3	189.1	181.6
Tevatron	5.2×10^{-3}	no	A	98.9	91.8	189.1	182.3
LHC	10^{-2}	no	B	418.0	404.1	745.0	734.1
LHC	6.9×10^{-2}	no	B	418.0	405.1	745.0	732.6
LHC	10^{-2}	no	C	147.6	142.7	432.0	421.3
LHC	10^{-2}	yes	C	147.6	143.4	432.0	423.3

Table 3.4: Reconstructed neutralino and slepton masses. The following SUGRA points were used in these simulations: point A has $M_0 = 50$ GeV, $M_{1/2} = 250$ GeV, $\tan\beta = 2$, $\mathrm{sgn}\,\mu > 0$ and $A_0 = 0$ GeV; point B has $M_0 = 350$ GeV, $M_{1/2} = 950$ GeV, $\tan\beta = 10$, $\mathrm{sgn}\,\mu < 0$ and $A_0 = 0$ GeV; point C has $M_0 = 350$ GeV, $M_{1/2} = 350$ GeV, $\tan\beta = 10$, $\mathrm{sgn}\,\mu < 0$ and $A_0 = 0$ GeV. The Tevatron and LHC results are based on an integrated luminosity of 2 fb^{-1} and 10 fb^{-1}, respectively.

$M_0 = 50$ GeV, $M_{1/2} = 250$ GeV, $\tan\beta = 2$, $\mathrm{sgn}\,\mu > 0$ and $A_0 = 0$ GeV the branching ratio for the decay of the smuon to the lightest neutralino is $\mathrm{BR}(\tilde{\mu}_\mathrm{L} \to \tilde{\chi}^0_1 \mu^+) = 98\%$. Similarly, at the point $M_0 = 350$ GeV, $M_{1/2} = 950$ GeV, $\tan\beta = 10$, $\mathrm{sgn}\,\mu < 0$ and $A_0 = 0$ GeV, the dominant decay mode of the smuon is to the lightest neutralino with a branching ratio of $\mathrm{BR}(\tilde{\mu}_\mathrm{L} \to \tilde{\chi}^0_1 \mu^+) = 99\%$.

It can however be the case that there is a significant background from sparticle pair production and a substantial contribution from the production of charginos and heavier neutralinos. This is shown in Fig. 3.34a for the neutralino mass reconstruction and Fig. 3.35a for the smuon mass reconstruction. Figs. 3.34a and 3.35a show that there is a significant background in both distributions. At this point, *i.e.* $\lambda'_{211} = 10^{-2}$, $M_0 = 350$ GeV, $M_{1/2} = 350$ GeV, $\tan\beta = 10$, $\mathrm{sgn}\,\mu < 0$ and $A_0 = 0$ GeV, the smuon dominantly decays to the lightest chargino, with branching ratio $\mathrm{BR}(\tilde{\mu}_\mathrm{L} \to \tilde{\chi}^-_1 \nu_\mu) = 50.9\%$. The other important decay modes are to the next-to-lightest neutralino, with branching ratio $\mathrm{BR}(\tilde{\mu}_\mathrm{L} \to \tilde{\chi}^0_2 \mu^+) = 28.0\%$, and to the lightest neutralino, with branching ratio $\mathrm{BR}(\tilde{\mu}_\mathrm{L} \to \tilde{\chi}^0_1 \mu^+) = 20.9\%$.

In the neutralino distribution there is still a peak at the simulated neutralino mass, although there is a large tail at higher masses. This tail is mainly due to the larger sparticle pair production background. The production of charginos and the heavier neutralinos does not significantly effect this distribution as the heavier gauginos will cascade decay to the LSP due to the small $\not{R}_\mathrm{p}$ coupling.

In the slepton distribution in addition to the larger background there is also a spurious peak in the mass distribution due to the production of the lightest chargino and the $\tilde{\chi}^0_2$. As we are not including all of the decay products of the chargino or $\tilde{\chi}^0_2$ in the mass reconstruction, the reconstructed slepton mass in signal events where a chargino or heavier neutralino is produced is below the true value.

We can improve the extraction of both the neutralino and slepton masses by imposing some additional cuts. The aim of these cuts is to require that the neutralino candidate and the second lepton are produced back-to-back, because in most of the signal events

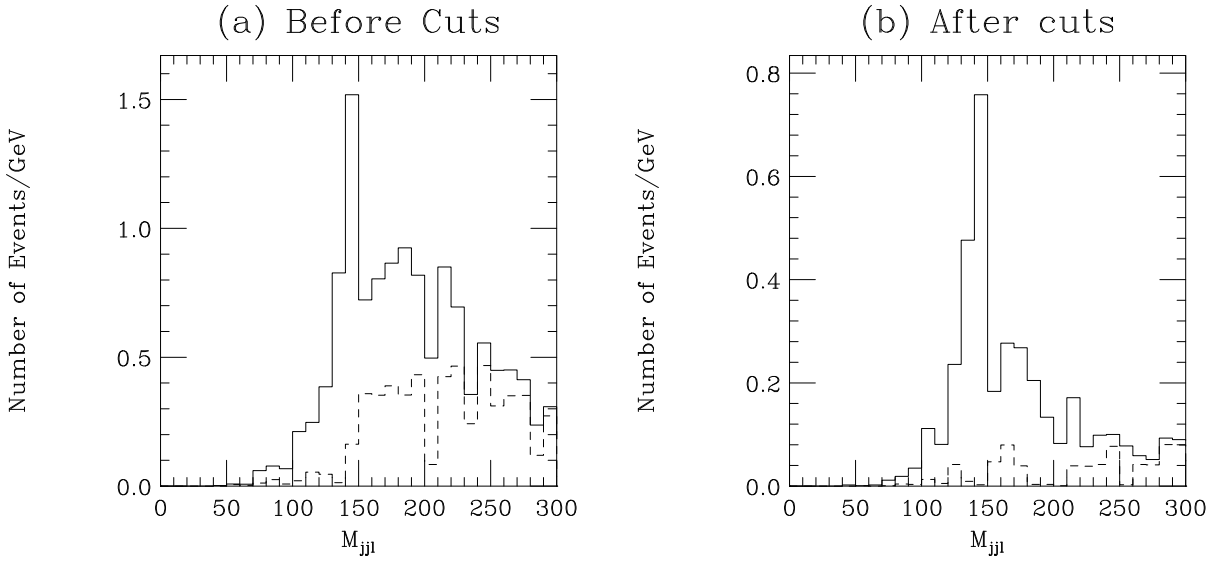

Figure 3.34: The reconstructed neutralino mass at the LHC for $\lambda'_{211} = 10^{-2}$, $M_0 = 350$ GeV, $M_{1/2} = 350$ GeV, $\tan\beta = 10$, $\mathrm{sgn}\,\mu < 0$ and $A_0 = 0$ GeV. At this point the lightest neutralino mass is $M_{\tilde{\chi}^0_1} = 147.6$ GeV. We have normalized the distributions to an integrated luminosity of 10 fb^{-1}. The cuts used are described in the text. The dashed line shows the background and the solid line shows the sum of the signal and the background.

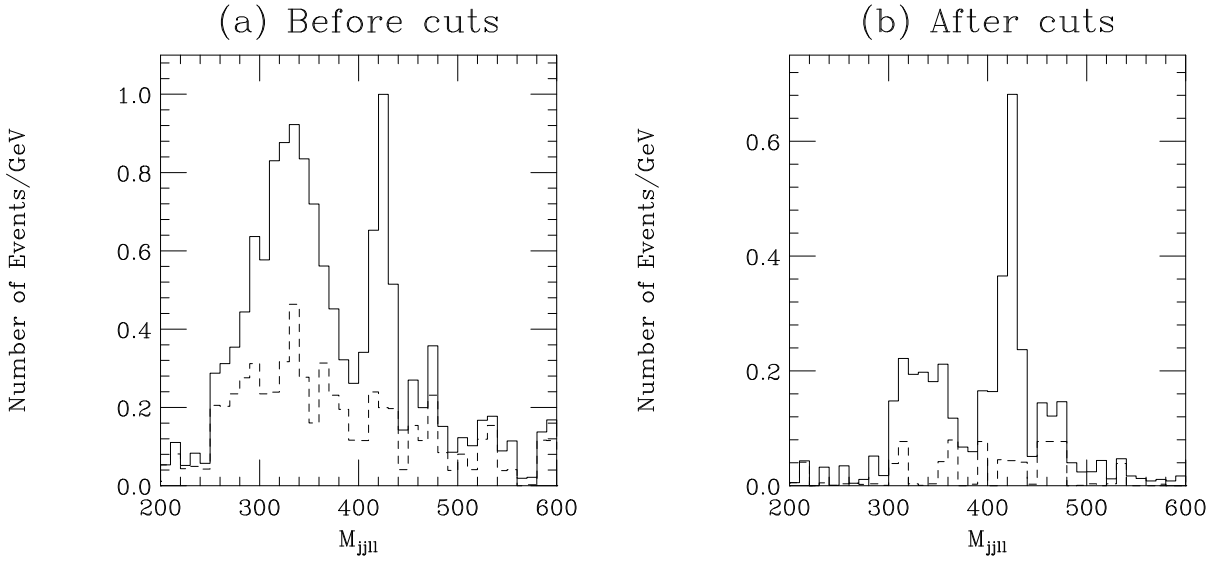

Figure 3.35: The reconstructed slepton mass at the LHC for $\lambda'_{211} = 10^{-2}$, $M_0 = 350$ GeV, $M_{1/2} = 350$ GeV, $\tan\beta = 10$, $\mathrm{sgn}\,\mu < 0$ and $A_0 = 0$ GeV. At this point the smuon mass is $M_{\tilde{\mu}_L} = 432.0$ GeV. We have normalized the distributions to an integrated luminosity of 10 fb^{-1}. The cuts used are described in the text. The dashed line shows the background and the solid line shows the sum of the signal and the background.

the resonant smuon will only have a small transverse momentum due to the initial-state parton shower. We therefore require the transverse momenta of the neutralino candidate and the second lepton to satisfy $|p_T^{\mathrm{jj}\ell_1} - p_T^{\ell_2}| < 20$ GeV, and the azimuthal angles to satisfy $||\phi_{\mathrm{jj}\ell_1} - \phi_{\ell_2}| - 180^0| < 15^0$. $p_T^{\mathrm{jj}\ell_1}$ is the transverse momentum of the combination of the hardest two jets in the event and the lepton closest to the jets in (η, ϕ) space, *i.e.* the transverse momentum of the neutralino candidate. Similarly $\phi_{\mathrm{jj}\ell_1}$ is the azimuthal angle of the combination of the hardest two jets in the event and the lepton closest to the jets in (η, ϕ) space, *i.e.* the azimuthal angle of the neutralino candidate.

Figs. 3.34b and 3.35b show that this significantly reduces the background and the spurious peak in the slepton mass distribution. At these points it is also possible to reconstruct the lightest neutralino, chargino and sneutrino masses using the decay chain $\tilde{\nu} \to \tilde{\chi}_1^+ \ell^+$ followed by the decay of the chargino $\tilde{\chi}_1^+ \to \ell^+ \nu_\ell \tilde{\chi}_1^0$ and the $\not{R}_{\mathrm{p}}$ decay of the lightest neutralino to a lepton and two jets [6, 68]. The reconstructed neutralino and slepton masses, before and after the imposition of the new cuts, are given in Table 3.4. The same procedure as before was used to extract the sparticle masses. There is reasonable agreement between the simulated and reconstructed sparticle masses although again the reconstructed values lie between 5 and 15 GeV below the values used in the simulations, due to the loss of energy from the cones used to define the jets in the neutralino decay.

3.4 Summary

We have considered both the $\not{R}_{\mathrm{p}}$ and gauge decay modes of resonant sleptons. The $\not{R}_{\mathrm{p}}$ decay modes can only be used to discover these processes for large values of the couplings due to the large QCD background.

However the like-sign dilepton signature of these processes can be observed above the background for much lower values of the $\not{R}_{\mathrm{p}}$ Yukawa couplings. We have performed a detailed analysis of the background to like-sign dilepton production at both Run II of the Tevatron and the LHC. We find a background from Standard Model processes of 0.43 ± 0.16 events for 2 fb^{-1} integrated luminosity at the Tevatron and 4.9 ± 1.6 events for 10 fb^{-1} integrated luminosity at the LHC, after a set of cuts. If we only consider this background there are large regions of SUGRA parameter space where resonant slepton production followed by a supersymmetric gauge decay of the slepton is visible above the SM background even for the small values of the $\not{R}_{\mathrm{p}}$ couplings we considered.

This is presumably the strategy which would be adopted in any initial experimental search, *i.e.* looking for an excess of a given type of event over the Standard Model prediction. If such an excess were observed it would then be necessary to identify which of the many possible models of beyond the Standard Model physics was correct.

In the $\not{R}_{\mathrm{p}}$ MSSM such an excess of like-sign dileptons can come from two possible sources: from sparticle pair production followed by the decay of the LSP, and from resonant sparticle production. We have considered the background to resonant slepton production from sparticle pair production and found that after an additional cut on the number of jets the signal from resonant slepton production is visible above the combined Standard Model and SUSY pair production background for large ranges of SUGRA parameter space.

Finally we have studied the possibility of measuring the mass of the resonant slepton and the neutralino into which it decays. Our results suggest that this should be possible even if the signal is only just detectable above the background.

Resonant slepton production offers a potentially interesting channel for the discovery of $\not{R}_p$ SUSY and can be used, provided the $\not{R}_p$ couplings are not too small, to discover supersymmetry over a larger range of SUSY parameter space than supersymmetric particle pair production due to the larger kinematic reach.

Chapter 4

KARMEN Anomaly

4.1 Introduction

The KARMEN experiment is designed to search for neutrino oscillations by looking for the appearance of ν_e from the oscillation $\nu_\mu \to \nu_e$ and of $\bar{\nu}_e$ from the oscillation $\bar{\nu}_\mu \to \bar{\nu}_e$ [120]. While the KARMEN experiment has detected no deviations from the Standard Model predictions which are consistent with neutrino oscillations, their results do contain an anomaly [121].

We will first describe the KARMEN experiment and the nature of the anomaly followed by a possible explanation of this anomaly in terms of R-parity violating supersymmetry. This is followed by a discussion of other possible constraints on this model and possible future experimental tests of our model.

The basic idea of the KARMEN experiment is that a proton beam hits a target producing pions. These pions are quickly stopped in the target and then decay, $\pi^+ \to \mu^+\nu_\mu$. This gives a source of mono-energetic ν_μ, from the two-body pion decay, the spectrum of which is shown in Fig. 4.1a. The muons then decay, $\mu^+ \to e^+\nu_e\bar{\nu}_\mu$, giving equal numbers of ν_e and $\bar{\nu}_\mu$. The energy spectrum of these neutrinos is also shown in Fig. 4.1a.

The experiment uses the ISIS proton beam at the Rutherford Appleton Laboratory. This is a pulsed proton beam which has two pulses separated by 330 ns. The pulse structure of the proton beam is shown in Fig. 4.1b. The pairs of pulses are separated by 20 ms. When the beam hits the target pions are promptly produced, followed by ν_μ from the pion decays due to the short lifetime of the charged pion. This means the detector will first detect two pulses of ν_μ during the first 0.5 μs, after the proton beam hits the target, followed by the ν_e and $\bar{\nu}_\mu$ from the muon decays, which occur with a lifetime of 2.2 μs. This gives the expected time distribution for neutrino detection by the KARMEN experiment shown in Fig. 4.1b.

The ν_μ can thus be separated from the other two types of neutrino by measuring the time at which they are detected relative to the time of the beam hitting the target. A full description of the experiment can be found in [120, 121].

The expectation of the experiment is to see the initial pulse followed by an exponential fall-off with a time constant of 2.2 μs consistent with the muon decay. However, in addition to this signal an additional component is seen which is consistent with a Gaussian centered at a time 3.6 ± 0.25 μs after the beam hits the target [121]. This effect was seen in the

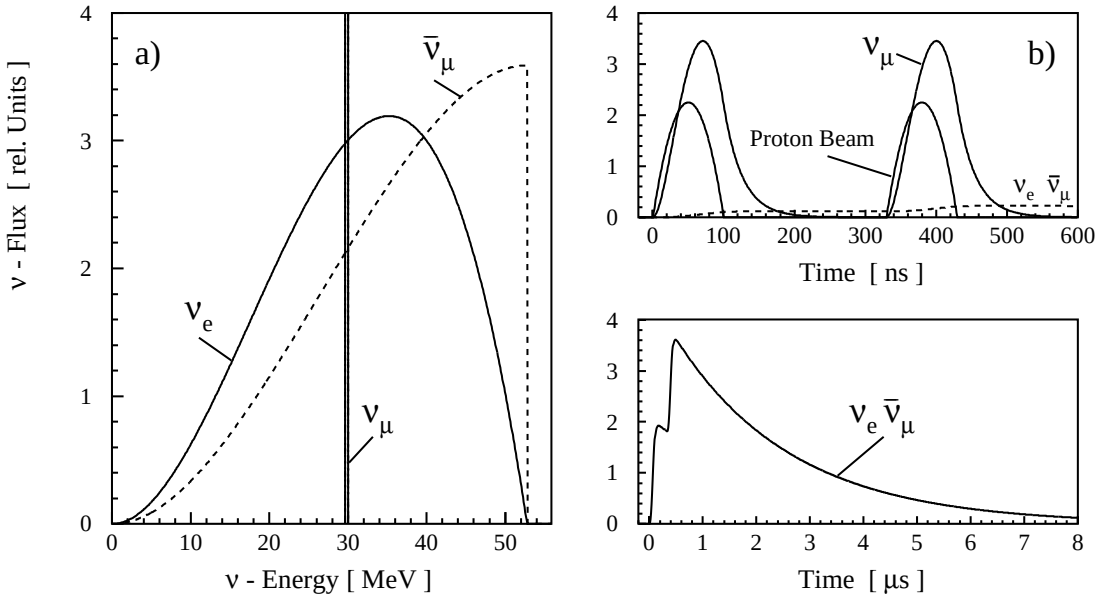

Figure 4.1: The energy spectrum (a) and time structure (b) of the neutrinos produced in the KARMEN experiment. In (b) the neutrino production is shown on two different time scales for the ν_μ neutrinos, and the $\bar{\nu}_\mu$ and ν_e neutrinos. (Taken from [122]).

first run of the KARMEN experiment [121] and has since been confirmed by a new run with improved shielding to eliminate the background from cosmic-rays [123, 124].[1]

The explanation of this anomaly proposed by the KARMEN collaboration in [121] was that a new hypothetical particle, X, was produced at the target and deposits energy in the detector when it decays. The arrival time, *i.e.* the time of the Gaussian component observed by the KARMEN experiment, can be used to estimate the velocity of the particle giving $v_{\rm X} = \left(5.2 \pm \begin{smallmatrix} 2.2 \\ 1.4 \end{smallmatrix}\right) \times 10^6$ ms^{-1}. If we assume that the particle X is produced in the decay of the pion, *i.e.* $\pi^+ \to \mu^+ {\rm X}$, its mass is $m_{\rm X} = 33.9$ MeV (just below the kinematic limit for the decay) and the momentum of the particle in the pion rest frame is $p_{\rm X} = 0.6$ MeV [121]. The new particle could also be produced by the interaction of the proton beam with the target, which we will not consider here. The energy observed in the detector is $\sim 11 - 35$ MeV, which is a lot greater than the kinetic energy of the X particle and must therefore come from the decay of the X particle, if it is produced in the pion decay, $\pi^+ \to \mu^+ {\rm X}$. Since the particle passes through over 7 metres of steel, between the target and the KARMEN detector, it must also be neutral. A time-of-flight likelihood analysis adopting the hypothesis that the anomaly is due to a decaying particle has a negative natural log-likelihood ratio of 9, *i.e.* a less than 1 in 10^4 chance of being a statistical fluctuation.

We can consider various possible candidates for the particle X and its decay modes which lead to the observed energy deposit in the experiment. There have been a number of different explanations of the anomaly [125–128]:

[1] The KARMEN collaboration has recently announced new results which are discussed in the Addendum.

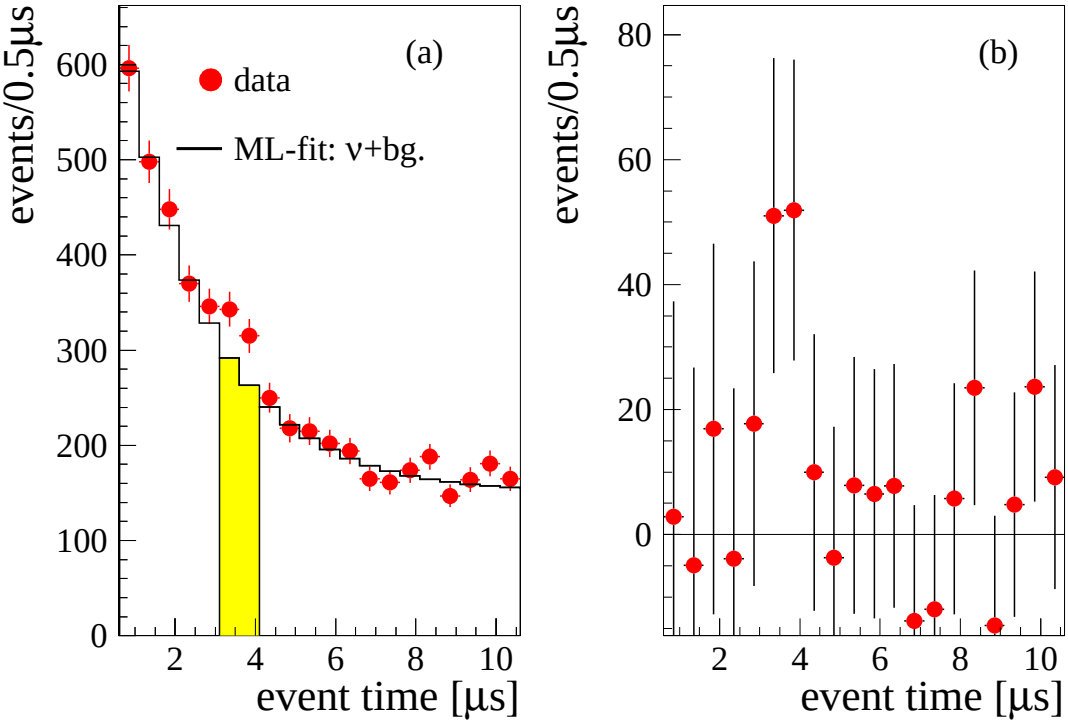

Figure 4.2: Time distribution of the events detected by KARMEN between $0.6 - 10.6$ μs after the proton beam hits the target. The solid line in (a) is the result of a fit to the cosmic ray background (assumed to be constant in time) and the neutrino-induced events from muon decay. The excess number of events after the events from the cosmic ray background and the neutrinos from muon events have been subtracted is shown in (b). These plots are taken from [134].

- One suggestion in [121] was that X could be the tau neutrino, but as they point out this is excluded by the limit on the tau neutrino mass from ALEPH [129]. It was shown in [125] that an $SU(2)_L$ doublet neutrino was excluded. This was reinforced by an improvement [130] in the limit for the branching ratio,[2]

$$\mathrm{BR}(\pi^+ \to \mu^+ \mathrm{X}) < 1.2 \times 10^{-8} \qquad (95\%\ \mathrm{C.L.}), \tag{4.1}$$

  versus the minimum value of $\sim 2 \times 10^{-8}$ required in the doublet-neutrino scenario. A sterile neutrino has also been considered, however [125, 133] showed that while a sterile neutrino was consistent with the current laboratory data, within strict limits on the mixing parameters, it may conflict with the cosmological bounds.

- In [126] the solution proposed was based on an anomalous muon decay, $\mu^+ \to \mathrm{e}^+\mathrm{X}$, as opposed to the pion decay of [121]. X was taken to be a scalar boson with mass 103.9 MeV and kinetic energy 1.7 MeV. This gives too large a value for the energy

[2]There have subsequently been two further improvements in this bound. The first bound [131] only applies for small X lifetimes in the range $\sim 10^{-9} - 10^{-3}$ s and is therefore not relevant for this study. The second [132] is an improvement in the results of [130] and now excludes branching ratios $\mathrm{BR}(\pi^+ \to \mu^+\mathrm{X}) < 6.0 \times 10^{-10}$ (95% C.L.). We will use this bound in the rest of this thesis.

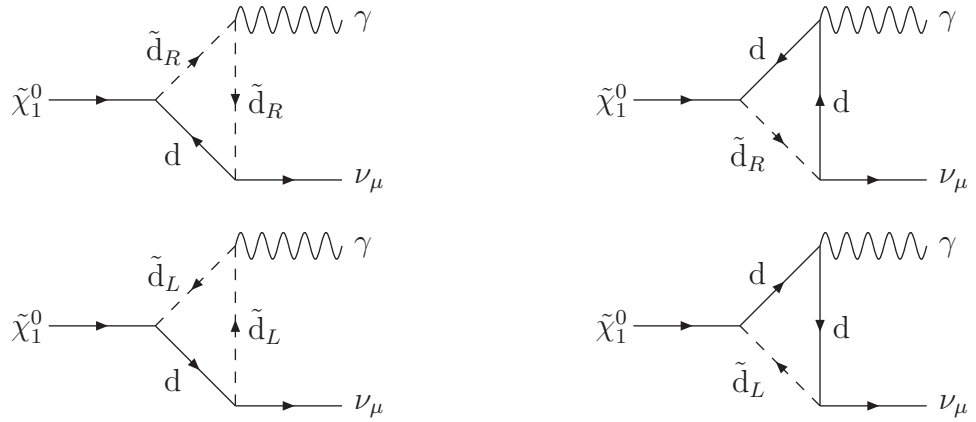

Figure 4.3: Radiative $\not{R}_p$ decay of a neutralino.

release in the X decay and the required branching ratio is constrained by the bound $\mathrm{BR}(\mu^+ \to e^+ X) < 5.7 \times 10^{-4}$ (90% C.L.) [135]. It is therefore necessary to add two more scalar bosons to the model into which X can cascade decay to reduce the energy deposit in the detector [126]. This model is viable but is somewhat contrived.

- Another suggestion [127] was that the massive particle could be the lightest neutralino in a SUSY model. This neutralino then has to decay via an R-parity violating interaction. In [127] the neutralino was assumed to be a photino or a zino. The pion decay can proceed via the $\not{R}_p$ operator $L_2 Q_1 \overline{D}_1$,

$$\pi^+ \longrightarrow \mu^+ \tilde{\gamma}. \tag{4.2}$$

  In [127] only one non-zero $\not{R}_p$ operator was considered and hence the neutralino has to decay radiatively

$$\tilde{\gamma} \longrightarrow \gamma \nu_\mu, \tag{4.3}$$

  via the Feynman diagrams shown in Fig. 4.3. However the new data from the KARMEN experiment appears to suggest that a three-body decay of the new particle, X, is favoured [123].

- A similar model to [127] with a three-body decay for the neutralino has been proposed in [136]. In [136] the neutralino decay was due to neutralino/neutrino mixing from the bilinear term in the $\not{R}_p$ superpotential, Eqn.1.63. This explanation of the KARMEN anomaly requires the Higgs mixing term in the superpotential $\mu H_1 H_2$ to be unnaturally small, $\mu \leq 30$ MeV. Furthermore, this scenario implies a MeV mass for the tau neutrino which is ruled out by cosmological and astrophysical arguments [137, 138].

- In any model with a single particle X, produced in the decay $\pi^+ \to \mu^+ X$, there is fine-tuning between the mass of the X particle and the difference between the pion and muon masses in order to reproduce the experimental results. This fine-tuning is approximately one part in 10^4, *i.e.* $1 - M_X/(m_\pi - m_\mu) = 1.8 \times 10^{-4}$, where m_μ is

the muon mass and m_π is the charged pion mass.

In [128] a brane-word model was proposed which alleviates this problem. In this model the particle X is a sterile neutrino which is part of a tower of Kaluza-Klein excitations associated with a singlet fermion, with respect to the Standard Model gauge group, propagating in $4 + d$ dimensions. If the mass splitting of the Kaluza-Klein tower is small it is more plausible that one of these Kaluza-Klein excitations has the correct mass to explain the experimental results than if there is only a single particle, X. The problem with this model is that the neighbouring states must not be detectable.

We shall present a model which extends the model of [127] by including a three-body decay of the neutralino via trilinear R-parity violation. The details of this model are discussed in the next section. We then consider other possible constraints on this model both from low energy experiments, Section 4.3, and present day collider experiments, Section 4.4. We also suggest possible tests of this model in future experiments.

4.2 The Model

We propose, as in [127], that X is the lightest neutralino with mass $M_{\tilde{\chi}^0_1} = 33.9$ MeV and that this is the lightest supersymmetric particle in the model. Since X is effectively stable on collider time-scales ($\tau_{\tilde{\chi}^0_1} \gtrsim 0.07\,\mathrm{s}$) our model is experimentally very similar to the MSSM. In the GUT-inspired MSSM $M_1 = \frac{5}{3}\tan^2\theta_W M_2$, where M_1 and M_2 are the SUSY-breaking masses for the bino and wino respectively.[3] Assuming this relation requires that $M_{\tilde{\chi}^0_1} > 32.3$ GeV from current LEP data [139]. Hence, in order to obtain a very light neutralino in the SUSY spectrum we must consider M_1 and M_2 to be independent parameters. A small value of M_2 implies at least one light chargino. This can be seen by considering small values of M_2 and the chargino mass matrix in Eqn. A.4. Such a light chargino is excluded by experiment. We must therefore consider small values of M_1. This implies, from the neutralino mass matrix in Eqn. A.22, that the lightest neutralino is dominantly bino. We will quantify this in Section 4.4 where we present regions in the $(M_1, M_2, \mu, \tan\beta)$ parameter space which are consistent with all the current experimental limits. These solutions are indeed dominantly bino, with a small higgsino component.

Instead of only considering one non-zero R-parity violating coupling we will allow two non-zero couplings. First we allow the coupling λ'_{211} to be non-zero so the pion can decay as in [127],

$$\pi^+ \longrightarrow \mu^+ \tilde{\chi}^0_1. \tag{4.4}$$

The tree-level Feynman diagrams for this decay are shown in Fig. 4.4. In order to allow a three-body decay for the lightest neutralino we consider a non-zero coupling λ_{1j1}, where j is 2 or 3. The neutralino can then undergo a three-body decay

$$\tilde{\chi}^0_1 \longrightarrow \mathrm{e}^- \nu_j \mathrm{e}^+. \tag{4.5}$$

[3] The gaugino mass terms in the SUSY Lagrangian can be found in Appendix A.2.

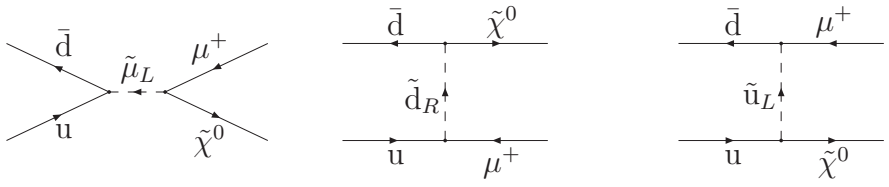

Figure 4.4: Pion decay to muon and neutralino.

Due to the low mass of the neutralino this is the only kinematically allowed three-body decay mode. This decay mode will dominate over the two-body radiative decay mode.

Fig. 4.5 shows the values of the branching ratio, $\mathrm{BR}(\pi^+ \to \mu^+ \tilde{\chi}_1^0)$, and the neutralino lifetime, $\tau_{\tilde{\chi}_1^0}$, which are compatible with the KARMEN data [121]. We can therefore determine the range of couplings λ'_{211}, λ_{131} (or λ_{121}) these solutions correspond to in our model by calculating both the pion branching ratio and the lifetime of the neutralino. We can understand the shape of this curve, *i.e.* Fig. 4.5, in the following way. The number of events detected is the number of neutralinos which decay inside the detector, multiplied by the efficiency for detecting such a decay. For one neutralino, with lifetime τ, the probability of it decaying inside the detector is

$$P_{\mathrm{detected}} = \left[e^{-\frac{t_1}{\tau}} - e^{-\frac{t_2}{\tau}} \right], \tag{4.6}$$

where t_1 is the time the neutralino enters the detector and t_2 is the time it leaves the detector. The total number of events detected by the KARMEN experiment from neutralino decay is

$$N_{\mathrm{detected}} = N_{\mathrm{produced}} \times G \times P_{\mathrm{detected}}, \tag{4.7}$$

where N_{produced} is the number of neutralinos produced and G is a geometrical factor describing the fraction of the total solid angle covered by the KARMEN experiment multiplied by the probability of detecting a decay of the X particle which occurs inside the detector. The number of neutralinos produced is $N_{\mathrm{produced}} = N_\pi \times \mathrm{BR}(\pi^+ \to \mu^+ \tilde{\chi}_1^0)$, where N_π is the number of pions produced at the target. Hence the branching ratio required to solve the KARMEN anomaly is given by

$$\mathrm{BR}(\pi^+ \to \mu^+ \tilde{\chi}_1^0) = \frac{N_{\mathrm{detected}}}{N_\pi \times G} \frac{1}{\left[e^{-\frac{t_1}{\tau}} - e^{-\frac{t_2}{\tau}} \right]}. \tag{4.8}$$

The ratio $\frac{N_{\mathrm{detected}}}{N_\pi \times G} = 1.65 \times 10^{-17}$. The times t_1 and t_2 at which the particle enters and leaves the detector can be calculated from the geometry of the detector and the particle's velocity giving

$$t_1 = 2.925\ \mu\mathrm{s}, \tag{4.9a}$$

$$t_2 = 3.579\ \mu\mathrm{s}. \tag{4.9b}$$

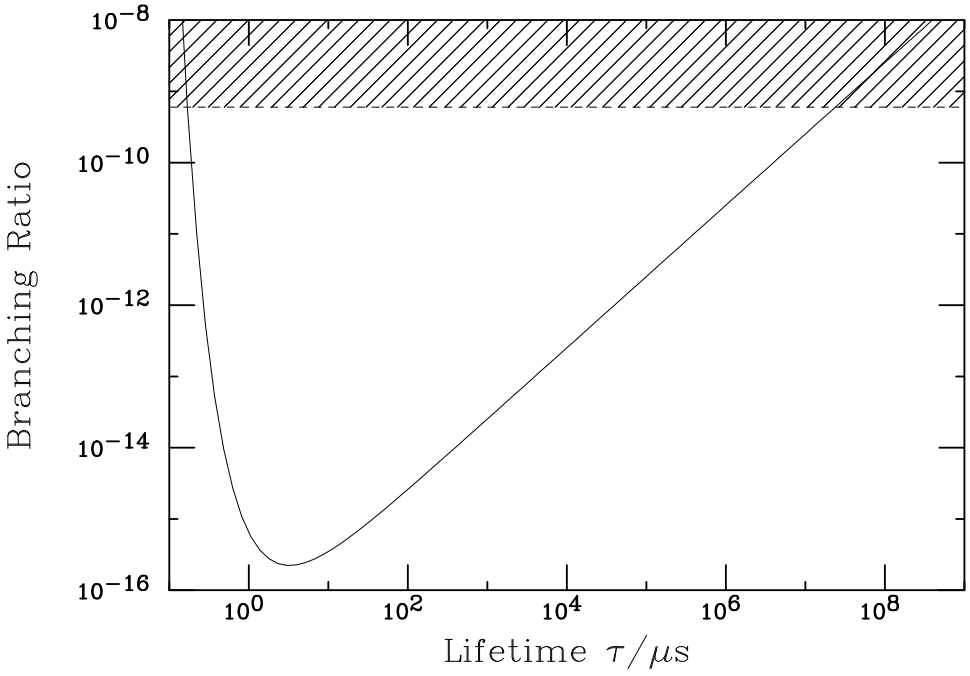

Figure 4.5: Branching ratio for $\pi^+ \to \mu^+ \mathrm{X}$ against lifetime of X required to solve the KARMEN anomaly. The hashed area gives the experimental upper bound, Eqn. 4.1. The results of [131] also exclude an additional region down to branching ratios of less than 10^{-12} for lifetimes between $\sim 10^{-9} - 10^{-3}$ s.

In the limit $\tau \gg t_1,\ t_2$ this reduces to

$$\mathrm{BR}(\pi^+ \to \mu^+ \tilde{\chi}_1^0) \simeq \frac{N_{\mathrm{detected}} \times \tau}{N_\pi \times G\,(t_2 - t_1)}. \tag{4.10}$$

This gives the linear region in Fig. 4.5 for $\tau > 10$ μs.

The calculation of the anomalous pion decay and the neutralino lifetime are presented below. We can use Eqn. 4.8 to calculate the range of the couplings λ'_{211}, λ_{131} (or λ_{121}) which are consistent with the lifetimes and branching ratios required to solve the KARMEN anomaly.

4.2.1 Pion Decay Rate

We can use chiral perturbation theory to calculate the decay rate of the pion via $\not{R}_\mathrm{p}$ as we would to calculate the Standard Model weak decay rate of the pion. To do this we need to obtain an effective Lagrangian for the four-fermion interaction of μ^-, $\bar{\mathrm{u}}$, d, and χ_1^0 with the sfermion degrees of freedom integrated out, just as we would use the Fermi theory with the W degrees of freedom integrated out to perform the calculation of the Standard Model decay rate.

It is easiest to manipulate these Lagrangians in two-component notation. Using this

Coefficient	General coupling	Pure photino	Pure bino
A_μ	$eN'_{l1} + \frac{gN'_{l2}}{\cos\theta_{\rm W}}\left(\frac{1}{2} - \sin^2\theta_{\rm W}\right)$	e	$-\frac{g'Y_{\mu_L}}{2}$
A_u	$-ee_uN'_{l1} - \frac{gN'_{l2}}{\cos\theta_{\rm W}}\left(\frac{1}{2} - e_u\sin^2\theta_{\rm W}\right)$	$-ee_u$	$-\frac{g'Y_{u_L}}{2}$
A_d	$ee_dN'_{l1} - \frac{ge_d\sin^2\theta_{\rm W}N'_{l2}}{\cos\theta_{\rm W}}$	ee_d	$\frac{g'Y_{d_R}}{2}$

Table 4.1: Coefficients for the fermion-sfermion-neutralino Lagrangian. The hypercharges of the MSSM fields are given in Table 1.2.

notation the relevant terms in the fermion-sfermion-neutralino Lagrangian are

$$\mathcal{L}_{\rm f\tilde{f}\tilde{\chi}} = \sqrt{2}\left(A_\mu\tilde{\mu}_L\bar{\psi}_{\tilde{\chi}}\bar{\psi}_{\mu_L} + A_u\tilde{u}_L\bar{\psi}_{\tilde{\chi}}\bar{\psi}_{u_L} + A_d\tilde{d}^*_R\bar{\psi}_{\tilde{\chi}}\bar{\psi}_{d^c_L}\right) + \text{h.c.}, \tag{4.11}$$

where the coefficients are given in Table 4.1. It should be noted that we have only kept the gaugino pieces of the Lagrangian as we are not interested in the higgsino case. Similarly, the relevant pieces of the $\not{R}_{\rm p}$ Lagrangian are

$$\mathcal{L}_{\not{R}_{\rm p}} = \lambda'_{211}\left(\tilde{d}_R\bar{\psi}_{\mu_L}\bar{\psi}_{u_L} + \tilde{u}^*_L\bar{\psi}_{\mu_L}\bar{\psi}_{d^c_L} + \tilde{\mu}^*_L\bar{\psi}_{u_L}\bar{\psi}_{d^c_L}\right) + \text{h.c.}. \tag{4.12}$$

We then proceed by integrating out the heavy sfermion degrees of freedom to obtain an effective Lagrangian

$$\mathcal{L}_{\rm eff} = \lambda'_{211}\sqrt{2}\left(\frac{A_\mu}{M^2_{\tilde{\mu}_L}}\bar{\psi}_{\tilde{\chi}}\bar{\psi}_{\mu_L}\bar{\psi}_{u_L}\bar{\psi}_{d^c_L} + \frac{A_u}{M^2_{\tilde{\rm u}_L}}\bar{\psi}_{\tilde{\chi}}\bar{\psi}_{u_L}\bar{\psi}_{\mu_L}\bar{\psi}_{d^c_L} + \frac{A_d}{M^2_{\tilde{\rm d}_R}}\bar{\psi}_{\tilde{\chi}}\bar{\psi}_{d^c_L}\bar{\psi}_{\mu_L}\bar{\psi}_{u_L}\right) + \text{h.c.}, \tag{4.13}$$

where $M_{\tilde{\mu}_L}$ is the left smuon mass, $M_{\tilde{\rm u}_L}$ is the left up squark mass and $M_{\tilde{\rm d}_R}$ is the right down squark mass.

To enable us to apply the results of chiral perturbation theory we need to rearrange the last two terms in Eqn. 4.13 using a Fierz transformation. This leads to Eqn. 4.14 and some tensor-tensor interaction terms which we can neglect as these do not contribute to the pion decay,

$$\mathcal{L}_{\rm Fierz} = \sqrt{2}\lambda'_{211}\left(\frac{A_\mu}{M^2_{\tilde{\mu}_L}} - \frac{A_u}{2M^2_{\tilde{\rm u}_L}} - \frac{A_d}{2M^2_{\tilde{\rm d}_R}}\right)\bar{\psi}_{\tilde{\chi}}\bar{\psi}_{\mu_L}\bar{\psi}_{u_L}\bar{\psi}_{d^c_L} + \text{h.c.}. \tag{4.14}$$

This equation can be rewritten in terms of four-component Dirac spinors

$$\mathcal{L}_{\rm Fierz} = \sqrt{2}\lambda'_{211}\left(\frac{A_\mu}{M^2_{\tilde{\mu}_L}} - \frac{A_u}{2M^2_{\tilde{\rm u}_L}} - \frac{A_d}{2M^2_{\tilde{\rm d}_R}}\right)\bar{\mu}P_R\tilde{\chi}^0\bar{u}P_Rd + \text{h.c.}, \tag{4.15}$$

where $P_L = \frac{1}{2}(1-\gamma_5)$ is the projection operator for the left-handed component of the fermion field and $P_R = \frac{1}{2}(1+\gamma_5)$ is the projection operator for the right-handed component of the fermion field. The amplitude for the pion decay can be calculated by splitting the

amplitude into a pion matrix element and the matrix element for the final state,

$$\mathcal{A} = \frac{i\lambda'_{211}}{\sqrt{2}}\left(\frac{A_\mu}{M^2_{\tilde{\mu}_L}} - \frac{A_u}{2M^2_{\tilde{\mathrm{u}}_L}} - \frac{A_d}{2M^2_{\tilde{\mathrm{d}}_R}}\right)\bar{u}_\mu(p_1)P_R v_{\tilde{\chi}}(p_2)\int d^4x e^{i(p_1+p_2)\cdot x}\langle 0|\bar{u}\gamma_5 d|\pi^-(p_0)\rangle, \tag{4.16}$$

where p_0 is the pion momentum, p_1 is the muon momentum and p_2 is the neutralino momentum. The pion matrix element is given by the standard chiral perturbation theory identity

$$\langle 0|j^{\mu 5a}(x)|\pi^b(p_0)\rangle = -ip_0^\mu f_\pi \delta^{ab} e^{-ip_0\cdot x}, \tag{4.17}$$

where a and b are the isospin of the pion, $j^{\mu 5a}(x)$ is the axial-vector current and f_π is the pion decay constant. It should be noted that some authors, including the Particle Data Group [22], define f_π to be $\sqrt{2}f_\pi$ compared to our definition. This is because they define Eqn. 4.17 in terms of a charged pion basis rather than the isospin basis we have used here.

Using Eqn. 4.17 we can obtain

$$\langle 0|\bar{u}\gamma^\mu\gamma_5 d|\pi^-(p_0)\rangle = -i\sqrt{2}p_0^\mu f_\pi e^{-ip_0\cdot x}. \tag{4.18}$$

By contracting Eqn. 4.18 with the pion four-momentum and using the Dirac equation for the up and down quarks we obtain,

$$\langle 0|\bar{u}\gamma_5 d|\pi^-(p_0)\rangle = \frac{i\sqrt{2}f_\pi m_\pi^2 e^{-ip_0\cdot x}}{(m_u+m_d)}, \tag{4.19}$$

where m_u and m_d are the up and down quark masses respectively. Hence the amplitude for this process is given by,

$$\mathcal{A} = -\frac{\lambda'_{211}f_\pi m_\pi^2}{(m_u+m_d)}\left(\frac{A_\mu}{M^2_{\tilde{\mu}_L}} - \frac{A_u}{2M^2_{\tilde{\mathrm{u}}_L}} - \frac{A_d}{2M^2_{\tilde{\mathrm{d}}_R}}\right)\bar{u}_\mu(p_1)P_R v_{\tilde{\chi}}(p_2)(2\pi)^4\delta^{(4)}(p_0-p_1-p_2). \tag{4.20}$$

We can therefore obtain the following partial width:

$$\Gamma(\pi\to\mu\tilde{\chi}_1^0) = \frac{\lambda'^2_{211}f_\pi^2 m_\pi^2 p_{\mathrm{cm}}}{8\pi(m_u+m_d)^2}\left(\frac{A_\mu}{M^2_{\tilde{\mu}_L}} - \frac{A_u}{2M^2_{\tilde{\mathrm{u}}_L}} - \frac{A_d}{2M^2_{\tilde{\mathrm{d}}_R}}\right)^2\left(m_\pi^2 - m_\mu^2 - m_{\tilde{\chi}}^2\right), \tag{4.21}$$

where $p_{\mathrm{cm}} = \frac{1}{2m_\pi}\sqrt{\left[m_\pi^2-(m_\mu+m_{\tilde{\chi}})^2\right]\left[m_\pi^2-(m_\mu-m_{\tilde{\chi}})^2\right]}$ and $m_{\tilde{\chi}}$ is the lightest neutralino mass.

The partial width for the Standard Model decay mode $\pi^+\to\ell^+\nu_\ell$ is given by

$$\Gamma(\pi^+\to\ell^+\nu_\ell) = \frac{G_F^2 f_\pi^2 m_\pi m_\ell^2}{4\pi}\left(1-\frac{m_\ell^2}{m_\pi^2}\right)^2. \tag{4.22}$$

In the Standard Model the dominant pion decay mode is to the muon and muon neutrino,

Coefficient	General Formula	Pure Photino	Pure Bino
B_1	$-\left(eN'_{l1} + \frac{gN'_{l2}}{\cos\theta_W}\left[\frac{1}{2} - \sin^2\theta_W\right]\right)$	$-e$	$\frac{Y_{e_L}}{2}$
B_2	$\frac{gN'_{l2}}{2\cos\theta_W}$	0	$\frac{Y_{\nu_L}}{2}$
B_3	$\left(eN'_{l1} - \frac{gN'_{l2}\sin^2\theta_W}{\cos\theta_W}\right)$	e	$-\frac{Y_{e_R}}{2}$

Table 4.2: Coefficients for the neutralino decay.

and at the level of accuracy to which we are working we can approximate the total decay rate by the partial width for $\pi^+ \to \mu^+\nu_\mu$. This gives the branching ratio[4]

$$\begin{aligned}
\mathrm{BR}(\pi^+ \to \mu^+\tilde{\chi}_1^0) &= \frac{\lambda'^2_{211} m_\pi^5 p_{\mathrm{cm}}}{2G_F^2 m_\mu^2 (m_u + m_d)^2}\left(\frac{A_\mu}{M^2_{\tilde{\mu}_L}} - \frac{A_u}{2M^2_{\tilde{\mathrm{u}}_L}} - \frac{A_d}{2M^2_{\tilde{\mathrm{d}}_R}}\right)^2 \frac{\left(m_\pi^2 - m_\mu^2 - m^2_{\tilde{\chi}}\right)}{\left(m_\pi^2 - m_\mu^2\right)^2} \\
&\approx 1.4\times 10^{-4}\left(\frac{\lambda'_{211}}{0.01}\right)^2\left(\frac{150\ \mathrm{GeV}}{M_{\tilde{\mathrm{f}}}}\right)^4 \qquad (4.23) \\
&< 6.0\times 10^{-10}, \qquad (4.24)
\end{aligned}$$

where in Eqn. 4.23 we have assumed that the sfermion masses are degenerate, *i.e.* $M_{\tilde{\mu}_L} = M_{\tilde{\mathrm{u}}_L} = M_{\tilde{\mathrm{d}}_L} = M_{\tilde{\mathrm{f}}}$, and the neutralino is purely bino. In Eqn. 4.24 we have quoted the experimental bound from Eqn. 4.1, which is shown as a hashed region in Fig. 4.5. This bound can be satisfied by either a small $\not{R}_{\mathrm{p}}$ coupling or a large sfermion mass. In principle it could also be satisfied if there was a fine-tuned cancellation between different diagrams for non-degenerate sfermion masses, however we disregard this possibility. This bound on the pion branching ratio can be translated into an upper bound on λ'_{211},

$$\lambda'_{211} < 2.1\times 10^{-5}\left(\frac{M_{\tilde{\mathrm{f}}}}{150\ \mathrm{GeV}}\right)^2. \qquad (4.25)$$

4.2.2 Neutralino Lifetime

We also need to calculate the decay rate for the three-body decay of the neutralino produced in the pion decay via the $L_iL_j\overline{E}_k$ term in the $\not{R}_{\mathrm{p}}$ superpotential, Eqn. 1.63. We calculate this decay rate neglecting the momentum flow through the virtual sfermions, as we did in the pion decay calculation, and the masses of the final-state particles. With these approximations the decay rate is

$$\begin{aligned}
\Gamma(\tilde{\chi} \to \ell_i^+\bar{\nu}_j\ell_k^-) &= \frac{M_{\tilde{\chi}}^5\lambda^2_{ijk}}{3072\pi^3}\left(\frac{B_1^2}{M^4_{\tilde{\ell}_{iL}}} + \frac{B_2^2}{M^4_{\tilde{\nu}_{jL}}} + \frac{B_3^2}{M^4_{\tilde{\ell}_{kR}}}\right. \\
&\quad \left. - \frac{B_1B_2}{M^2_{\tilde{\ell}_{iL}}M^2_{\tilde{\nu}_{jL}}} - \frac{B_1B_3}{M^2_{\tilde{\ell}_{iL}}M^2_{\tilde{\ell}_{kR}}} - \frac{B_2B_3}{M^2_{\tilde{\nu}_{jL}}M^2_{\tilde{\ell}_{kR}}}\right). \qquad (4.26)
\end{aligned}$$

[4]This disagrees slightly with the result given in [127]. We have discussed this with the authors of [127] and have agreed on the above result.

This is obtained by integrating the matrix element given in Appendix B.4, Eqn. B.15, over the available phase space, Eqn. B.14. The coefficients are given in Table 4.2. In the pure bino limit this gives

$$\Gamma(\tilde{\chi} \to \ell_i^+ \bar{\nu}_j \ell_k^-) = \frac{3\alpha M_{\tilde{\chi}}^5 \lambda_{ijk}^2}{1024\pi^2 \cos^2\theta_W M_{\tilde{\mathrm{f}}}^4}, \tag{4.27}$$

assuming a common sfermion mass. This gives the result for the neutralino lifetime

$$\tau_{\mathrm{bino}} = 1.32 \times 10^{-3} \frac{1}{\lambda_{ijk}^2} \left(\frac{M_{\tilde{\mathrm{f}}}}{150\ \mathrm{GeV}}\right)^4 \left(\frac{33.9\,\mathrm{MeV}}{M_{\tilde{\chi}}}\right)^5, \tag{4.28}$$

$$< 23.8\ \mathrm{s}. \tag{4.29}$$

The last inequality comes from using the bound, Eqn. 4.1, on the pion branching ratio and the solutions shown in Fig. 4.5. This can be inverted to give a bound on the coupling

$$\lambda_{131},\ \lambda_{121} > 7.45 \times 10^{-3} \left(\frac{M_{\tilde{\mathrm{f}}}}{150\ \mathrm{GeV}}\right)^2. \tag{4.30}$$

4.2.3 Solutions of the KARMEN Anomaly

The KARMEN collaboration has produced a graph of the branching ratio for $\pi^+ \to \mu^+\mathrm{X}$ against the lifetime of X which is required to explain their data, Fig. 4.5. In our model, each point along the curve in Fig. 4.5 corresponds to a specific anomalous pion branching ratio, Eqn. 4.23, and a specific neutralino lifetime, Eqn. 4.28. If we assume that the scalar fermions are degenerate we can translate these solutions into specific values of the couplings λ'_{211} and λ_{131} (or λ_{121}) for a fixed sfermion mass using Eqn. 4.8. This set of solutions in R-parity violating SUSY parameter space is shown in Fig. 4.6 for $M_{\tilde{\mathrm{f}}} = 150$ GeV (solid line), $M_{\tilde{\mathrm{f}}} = 300$ GeV (dashed line) and $M_{\tilde{\mathrm{f}}} = 1000$ GeV (dot-dash line). The hashed lines at $\lambda,\ \lambda' = \sqrt{4\pi}$ give the perturbative limit. For large sfermion masses (> 1 TeV) there is little room for perturbative solutions. Solutions above and to the left of the stars are excluded by the inequalities in Eqns. 4.25 and 4.30.

Given the perturbative upper bound, $\lambda_{ijk} < \sqrt{4\pi}$, and the lower bound on the sfermion mass from LEP 2, $M_{\tilde{\mathrm{f}}} > 100$ GeV, we also have a lower limit on the lifetime of the neutralino, $\tau_{\mathrm{bino}} > 2.1 \times 10^{-5}$s. There is therefore a range of six orders of magnitude in the lifetime or three orders of magnitude in the coupling for solutions in our model.

4.3 Limits on the R-parity Violating Couplings

There are constraints on the R-parity violating couplings which come from low energy experiments. The best bounds at the 2σ-level on the couplings we are interested in are

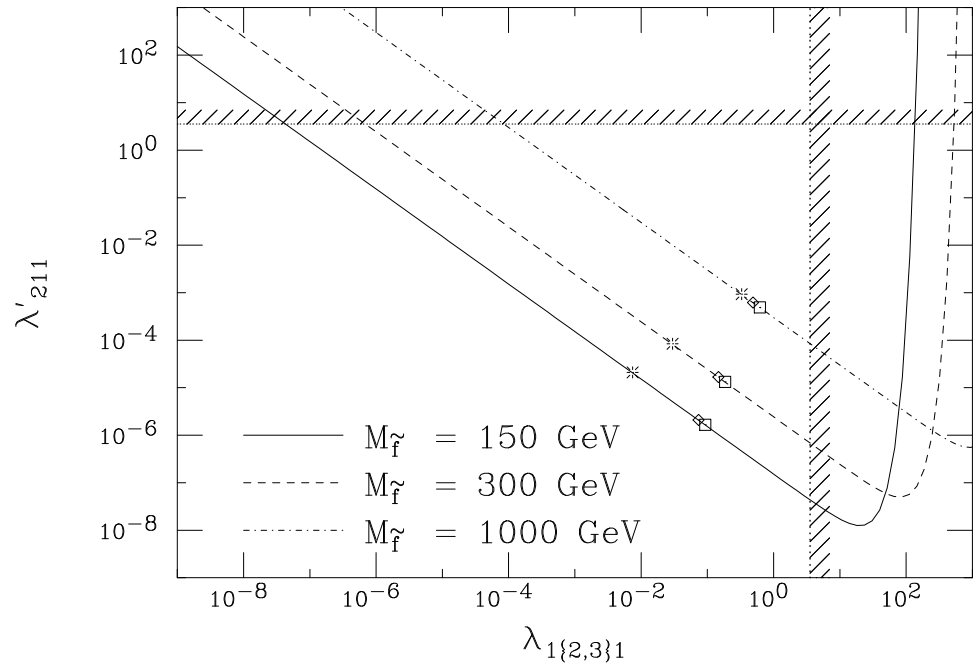

Figure 4.6: Solutions to the KARMEN anomaly in terms of the R-parity violating couplings λ'_{211} and $\lambda_{1\{2,3\}1}$, for different (assumed degenerate) sfermion masses. The hashed lines indicate upper limits on the couplings from perturbativity. The stars and diamonds (squares) give the upper limits on the couplings λ'_{211} and λ_{121} (λ_{131}), respectively. Solutions above and to the left of the stars are excluded, as are solutions below and to the right of the diamonds (squares).

summarized in [21],

$$\begin{aligned}
\lambda'_{211} &< 0.059 \left(\frac{M_{\tilde{d}_R}}{100\ \text{GeV}}\right), \\
\lambda_{121} &< 0.049 \left(\frac{M_{\tilde{\ell}_R}}{100\ \text{GeV}}\right) \Rightarrow \tau_{\text{bino}} > 0.11\,\text{s}, \\
\lambda_{131} &< 0.062 \left(\frac{M_{\tilde{\ell}_R}}{100\ \text{GeV}}\right) \Rightarrow \tau_{\text{bino}} > 0.07\text{s}.
\end{aligned} \tag{4.31}$$

The bound on λ'_{211} is from the measurement of $R_\pi = \Gamma(\pi \to e\nu)/\Gamma(\pi \to \mu\nu)$ [58], the bound on λ_{121} is from charged-current universality [58] and the bound on λ_{131} is from a measurement of $R_\tau = \Gamma(\tau \to e\nu\bar{\nu})/\Gamma(\tau \to \mu\nu\bar{\nu})$ [58].

The bound on λ'_{211} in Eqn. 4.31 is weaker than the constraint on the coupling imposed by the bound on the pion branching ratio, Eqn. 4.1, and therefore we do not consider it further. In Fig. 4.6 the bounds on the couplings λ_{121} and λ_{131} forbid solutions to the right of the diamonds and squares, respectively. This leaves a range of solutions of about one order of magnitude in λ'_{211} and λ_{131} (or λ_{121}), and corresponds to two orders of magnitude in the pion branching ratio and neutralino lifetime. The bounds on the couplings λ_{131} and λ_{121} give a lower bound on the neutralino lifetime, using Eqn. 4.28, which is given in Eqn. 4.31.

We must also consider bounds on the products of the couplings $\lambda'_{211}\lambda_{121}$ and $\lambda'_{211}\lambda_{131}$. In the first case there is an additional contribution to the pion decay $\pi^+ \to \tilde{\mu}^+ \to \mathrm{e}^+\nu_\mathrm{e}$, which changes the prediction for R_π. To calculate this decay rate we first need to obtain an effective Lagrangian for the four-fermion interaction of the u, $\bar{\mathrm{d}}$, ν_e and e. This is

$$\mathcal{L} = -\frac{\lambda'_{211}\lambda_{121}}{M^2_{\tilde{\mu}_L}} \bar{d} P_L u \bar{\nu} P_R e, \tag{4.32}$$

where again the sfermion degrees of freedom have been integrated out.

We can use chiral perturbation theory to calculate the partial width for the decay $\pi^+ \to \mathrm{e}^+\nu_\mathrm{e}$ including this correction to the Standard Model rate. This gives

$$\Gamma(\pi^+ \to \mathrm{e}^+\nu_\mathrm{e}) = \frac{G_F^2 f_\pi^2 m_\pi m_e^2}{4\pi}\left(1 - \frac{m_e^2}{m_\pi^2}\right)^2 \left[1 + \frac{m_\pi^2 \lambda'_{211}\lambda_{121}}{2\sqrt{2} G_F M^2_{\tilde{\mu}_L} m_e (m_u + m_d)}\right]^2. \tag{4.33}$$

We can express this as a correction to the ratio R_π,

$$R_\pi = R_\pi^{\mathrm{SM}} \left[1 + \frac{m_\pi^2 \lambda'_{211}\lambda_{121}}{2\sqrt{2} G_\mathrm{F} M^2_{\tilde{\mu}\mathrm{L}} m_e (m_u + m_d)}\right]^2. \tag{4.34}$$

The corresponding Feynman diagram has a different structure from the t-channel squark exchange which gives the bound on λ'_{211} in Eqn. 4.31. This leads to a much stricter bound on the product of the couplings than on either of the couplings individually. At the 2σ level we obtain

$$\lambda'_{211}\lambda_{121} < 4.6 \times 10^{-7} \left(\frac{M_{\tilde{\mu}_L}}{100\ \mathrm{GeV}}\right)^2. \tag{4.35}$$

Hence in the case of λ_{121} the maximum sfermion mass which will solve the KARMEN anomaly in our model is 400 GeV, using Eqns. 4.10, 4.23 and 4.28.

The couplings λ'_{211} and λ_{131} violate muon and tau lepton number, respectively. This can therefore lead to the decay $\tau \to \mu\gamma$. The experimental bound on this decay has recently improved [140],

$$\mathrm{BR}(\tau \to \mu\gamma) < 1.0 \times 10^{-6} \quad (90\%\ \mathrm{C.L.}). \tag{4.36}$$

As the couplings $\lambda'_{211}\lambda_{131}$ only contribute to this decay at the two-loop level any bound from this decay is significantly weaker than the individual bounds on the couplings, Eqn. 4.31.

There are also severe cosmological bounds on the R-parity violating couplings derived from considerations of GUT-scale lepto/baryogenesis in the early universe [141–144],

$$\lambda,\ \lambda',\ \lambda'' < 5 \times 10^{-7} \left(\frac{M_{\tilde{\mathrm{f}}}}{1\ \mathrm{TeV}}\right). \tag{4.37}$$

It was subsequently shown that it is sufficient for just one lepton flavour to satisfy this

bound [143,144]. In our model both of the couplings must violate this bound. For the case $(\lambda'_{211}, \lambda_{121})$ we must therefore require either all the electron or all the tau lepton number violating couplings to satisfy Eqn. 4.37. For the case $(\lambda'_{211}, \lambda_{131})$ we must demand that all the electron number violating couplings satisfy Eqn. 4.37. Another alternative is that baryogenesis could occur at the weak scale in which case the bounds in Eqn. 4.37 do not apply.

4.4 Experimental Constraints on a Light Neutralino

There are a number of possible experimental constraints on a light neutralino which we will summarize here. We then show that there are regions of $(M_1, M_2, \mu, \tan\beta)$ parameter space in which all these constraints are satisfied for a dominantly bino lightest neutralino with a small higgsino component. We consider this scenario to avoid all of the constraints. In our model M_1 and M_2 are not related by the supersymmetric GUT relation and we treat them as independent free parameters.

4.4.1 Bounds from $e^+e^- \to \nu\bar{\nu}\gamma$

The Standard Model process $e^+e^- \to \nu\bar{\nu}\gamma$ is measured in e^+e^- collisions by looking for the presence of a photon and missing energy and momentum due to the neutrinos escaping the detector [145,146]. As the lightest neutralino lifetime in our model is large enough that the neutralino will escape the detector before decaying there will be an additional contribution to this process from $e^+e^- \to \tilde{\chi}^0_1\tilde{\chi}^0_1\gamma$. The cross section for the process $e^+e^- \to \tilde{\gamma}\tilde{\gamma}\gamma$ was calculated in [147]. We can use this result to obtain the cross section for a purely bino LSP by changing the relevant couplings. The cross section is shown as a function of the centre-of-mass energy in Fig. 4.7. The expected number of events for various experiments is given in Table 4.3 assuming a scalar fermion mass of $M_{\tilde{f}} = 150$ GeV. We used the same cuts on the energy and angle of the photon with respect to the beam direction as in [147].

As can be seen in Table 4.3, no limits on this process can be set by LEP as the expected number of events in much less than one. The recent results from OPAL give 138 observed events, against the Standard Model expectation of 141.1 ± 1.1 events from $e^+e^- \to \nu\bar{\nu}\gamma$ and the non-physics background of 2.3 ± 1.1 events. There is no evidence for any excess given the statistical error of ± 11.9 events on the background. As the lightest neutralino in our model does not couple to the Z boson, the background at $\sqrt{\hat{s}} = M_Z$ is too large to see a signal.

Given the high luminosities at the B-factories KEK-B and BaBar a few events may be expected. The Standard Model cross section at this energy is 2.3 fb, corresponding to 230 ± 15 events at KEK-B and 70 ± 8 events at BaBar[5], where the quoted errors are statistical. The statistical uncertainty on the Standard Model rate still exceeds the signal rate and hence we do not expect any sensitivity to a light neutralino.

At the NLC we expect a substantially higher number of events. The Standard Model cross section for the same cuts is about 0.35 pb for three neutrinos [148] corresponding to 1.1×10^5 events, with a small relative statistical error of 330 events. This can therefore

[5]This corresponds to one year of running based on the luminosities given in [22].

Experiment	Integrated luminosity (pb^{-1})	Energy	Cross section (fb)	Number of events
LEP	6.65	130	5.87	0.04
	5.96	136	6.14	0.04
	9.89	161	7.11	0.07
	10.28	172	7.44	0.08
	54.5	183	7.72	0.42
	75.0	200	8.05	0.60
KEK-B	1×10^5	10.5	6.74×10^{-2}	6.7
BaBar	3×10^4	10.5	6.74×10^{-2}	2.0
NLC	3×10^5	500	6.19	1857

Table 4.3: Cross sections for the production of $\tilde{\chi}_1^0\tilde{\chi}_1^0\gamma$ at $\mathrm{e}^+\mathrm{e}^-$ colliders for (an assumed degenerate) sfermion mass $M_{\tilde{f}} = 150$ GeV and general expectations of the integrated luminosity.

provide a test of our model as the expected number of events from $\mathrm{e}^+\mathrm{e}^- \to \tilde{\chi}_1^0\tilde{\chi}_1^0\gamma$ is more than a 5σ fluctuation of the background.

4.4.2 Bounds from the Invisible Z Width

In our model, as $M_{\tilde{\chi}_1^0} \ll M_\mathrm{Z}/2$, the decay $\mathrm{Z}^0 \to \tilde{\chi}_1^0\tilde{\chi}_1^0$ is kinematically accessible. Due to its small mass with respect to M_Z the neutralino can be considered effectively massless like a neutrino. The lifetime of the lightest neutralino in our model is such that it will decay outside the detector, and therefore the process $\mathrm{Z}^0 \to \tilde{\chi}_1^0\tilde{\chi}_1^0$ contributes to the invisible Z width. The current measurement of the invisible Z width can be expressed as a number of light neutrino species [22],[6]

$$N_\nu = 3.00 \pm 0.08. \tag{4.38}$$

We must therefore require that $\Gamma(Z^0 \to \tilde{\chi}_1^0\tilde{\chi}_1^0) < 0.08\Gamma(Z^0 \to \nu\bar{\nu})$. A purely bino neutralino does not couple to the Z at tree level. The dominant contribution to the decay $Z^0 \to \tilde{\chi}_1^0\tilde{\chi}_1^0$ comes from the higgsino admixtures of the neutralino, N_{13} and N_{14}, in the notation of [18]. This enters with the fourth power in the decay rate $\mathrm{Z}^0 \to \tilde{\chi}_1^0\tilde{\chi}_1^0$. The ratio of the neutralino to neutrino partial widths is

$$\frac{\Gamma(\mathrm{Z} \to \tilde{\chi}_1^0\tilde{\chi}_1^0)}{\Gamma(\mathrm{Z} \to \nu\bar{\nu})} = \left(|N_{14}|^2 - |N_{13}|^2\right)^2, \tag{4.39}$$

giving the constraint

$$\left||N_{14}|^2 - |N_{13}|^2\right|^{1/2} < 0.53 \approx (0.08)^{1/4}. \tag{4.40}$$

[6] There has been a recent improvement [149] in this result, $N_\nu = 2.9835 \pm 0.0083$. This new result disagrees with the Standard Model at the 2σ-level and hence we must take the upper limit to be 3σ above the central value.

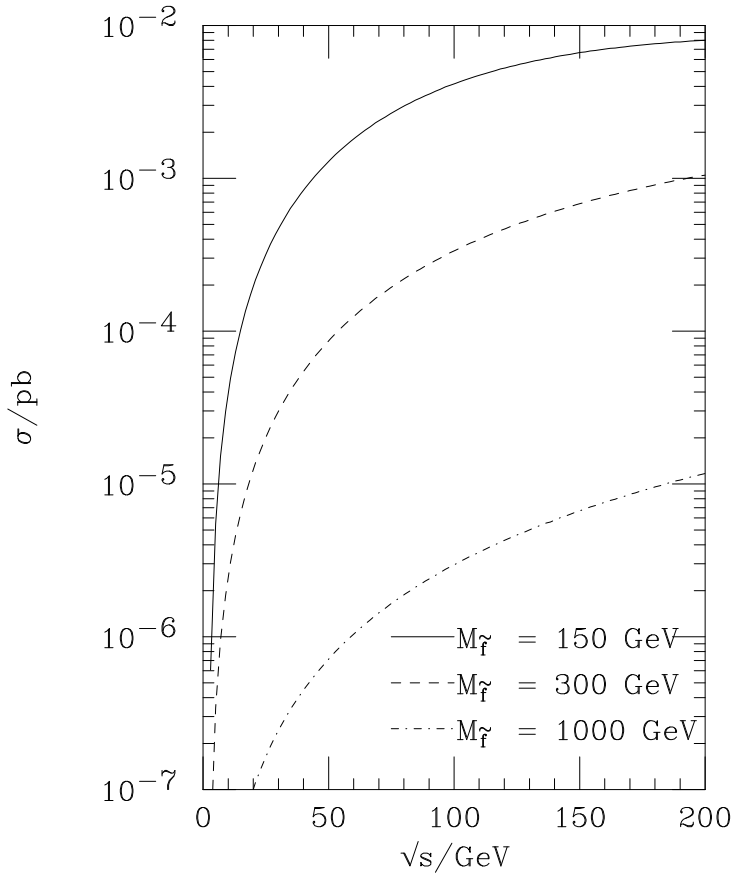

Figure 4.7: Cross section for the production of a purely bino neutralino with mass 33.9 MeV through $e^+e^- \to \tilde{\chi}_1^0\tilde{\chi}_1^0\gamma$.

We shall show below that it is straightforward to find regions which satisfy this in $(M_1, M_2, \mu, \tan\beta)$ parameter space.[7]

4.4.3 Solutions in the MSSM Parameter Space

It is important to establish whether it is possible to have a lightest neutralino with $M_{\tilde{\chi}_1^0} = 33.9$ MeV within the MSSM. We have therefore scanned the MSSM parameter space with independent M_1, M_2, for a neutralino in the mass range

$$33.89 \text{ MeV} < M_{\tilde{\chi}_1^0} < 33.91 \text{ MeV}. \tag{4.41}$$

This gives the neutralino iso-mass curves shown in Fig. 4.8 for $\mu = 300$ GeV and two representative values of $\tan\beta$. We have not been able to find any solutions for $\mu < 0$ GeV. Some fine-tuning is necessary in order to obtain these solutions. This should not be surprising given the requirement of reproducing the lightest neutralino mass needed to solve the KARMEN anomaly. This fine-tuning is a few parts in 10^3 for $\tan\beta = 1$ and a

[7] As these solutions contain $\lesssim$ 15 % higgsino admixture they also satisfy the bound $\left||N_{14}|^2 - |N_{13}|^2\right|^{1/2} < 0.30$ from the improved results of [149].

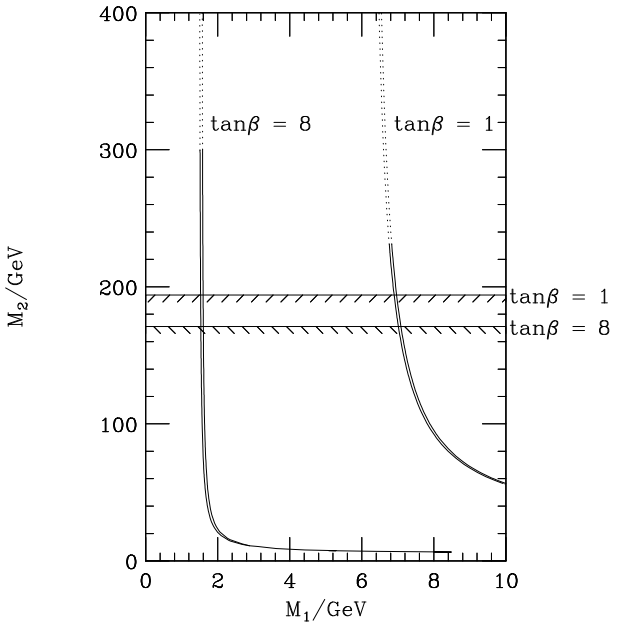

Figure 4.8: Solutions in $(M_1, M_2, \mu, \tan\beta)$ parameter space giving a $M_{\tilde{\chi}_1^0} = 33.9\,\text{MeV}$ neutralino for $\mu = 300$ GeV and 2 representative values of $\tan\beta$. The width of the lines is 0.01 MeV. Below the hashed lines the chargino mass is less than 150 GeV. The dotted lines have $\Delta\rho_{\text{SUSY}} < 10^{-4}$ and the solid lines have $\Delta\rho_{\text{SUSY}} < 5 \times 10^{-4}$.

few parts in 10^2 for $\tan\beta = 8$ [150]. The fine-tuning is reduced for larger M_2 and μ and small M_1 because a light neutralino can then be generated by the see-saw mechanism. It is also reduced for large values of $\tan\beta$ because in the limit $\beta = \pi/2$ there is a zero mass eigenvalue for $M_1 \approx 0$ [150].

We have checked that the higgsino contribution always satisfies the bound in Eqn. 4.40. In order to avoid an observable light chargino we require that $M_{\tilde{\chi}^\pm} > 150$ GeV, which eliminates the region below the hashed lines in Fig. 4.8 for the specified values of $\tan\beta$. The lightest neutralino is dominantly bino along the solution curves given in Fig. 4.8. The next-to-lightest neutralino, $\tilde{\chi}_2^0$, is dominantly wino for $M_2 < 300$ GeV, but for larger values it is mainly higgsino. For $M_2 \gtrsim 110$ GeV, $M_{\tilde{\chi}_2^0} \gtrsim 100$ GeV, and for $M_2 \gtrsim 235$ GeV, $M_{\tilde{\chi}_2^0} \gtrsim 200$ GeV.

4.4.4 Limits from Precision Electroweak Measurements

We would expect the addition of a new light particle to affect the results of the precision electroweak measurements made by the LEP collaborations. We can look at this by calculating the contributions in loop diagrams of the gauginos. To do this we will need to calculate the gaugino loop diagrams in the photon, W and Z propagators, and in the photon–Z mixing. In general we can write the results of these loop diagrams as

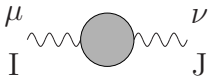

$$= i\Pi_{\text{IJ}}^{\mu\nu}(q). \tag{4.42}$$

Due to the tensor structure of the diagram this can be written as

$$\Pi_{\rm IJ}^{\mu\nu} = \Pi_{\rm IJ}(q^2)g^{\mu\nu} - \Delta(q^2)q^\mu q^\nu. \tag{4.43}$$

We use the conventions of [11, 151] and, as was done there, neglect the terms proportional to $q^\mu q^\nu$ in the W and Z propagators. This is valid as we will only be considering processes with light fermions as the external particles and these terms are suppressed by a factor $m_f^2/M_{\rm Z}^2$ with respect to the $g^{\mu\nu}$ terms after contraction with the external fermion current, where m_f is the fermion mass.

We will therefore consider the loops in the propagators shown in Fig. 4.9. We have calculated these and obtain

$$\begin{aligned}
\Pi_{\rm ZZ}(q) \;=\; & -\frac{g^2}{16\pi^2\cos^2\theta_W}\sum_{i=1}^{4}\sum_{j=1}^{4}\Bigg[2\mathcal{R}e\left\{O''^L_{ij}O''^R_{ij}\right\}M^2_{\tilde\chi^0_i}M^2_{\tilde\chi^0_j}\left(E - b_0(\tilde\chi^0_i\tilde\chi^0_j q)\right) \\
& + \left(|O''^L_{ij}|^2 + |O''^R_{ij}|^2\right)\Bigg(\left[\frac{q^2}{3} - \frac{M^2_{\tilde\chi^0_i}}{2} - \frac{M^2_{\tilde\chi^0_j}}{2}\right]E - 2q^2 b_2(\tilde\chi^0_i\tilde\chi^0_j q) \\
& + M^2_{\tilde\chi^0_i}b_0(\tilde\chi^0_i\tilde\chi^0_j q) + (M^2_{\tilde\chi^0_j} - M^2_{\tilde\chi^0_i})b_1(\tilde\chi^0_i\tilde\chi^0_j q)\Bigg)\Bigg] \\
& - \frac{g^2}{8\pi^2\cos^2\theta_W}\sum_{i=1}^{2}\sum_{j=1}^{2}\Bigg[2\mathcal{R}e\left\{O'^L_{ij}O'^R_{ij}\right\}M^2_{\tilde\chi^+_i}M^2_{\tilde\chi^-_j}\left(E - b_0(\tilde\chi^0_i\tilde\chi^0_j q)\right) \\
& + \left(|O'^L_{ij}|^2 + |O'^R_{ij}|^2\right)\Bigg(\left[\frac{q^2}{3} - \frac{M^2_{\tilde\chi^+_i}}{2} - \frac{M^2_{\tilde\chi^-_j}}{2}\right]E - 2q^2 b_2(\tilde\chi^+_i\tilde\chi^-_j q) \\
& + M^2_{\tilde\chi^+_i}b_0(\tilde\chi^+_i\tilde\chi^-_j q) + (M^2_{\tilde\chi^-_j} - M^2_{\tilde\chi^+_i})b_1(\tilde\chi^+_i\tilde\chi^-_j q)\Bigg)\Bigg],
\end{aligned} \tag{4.44a}$$

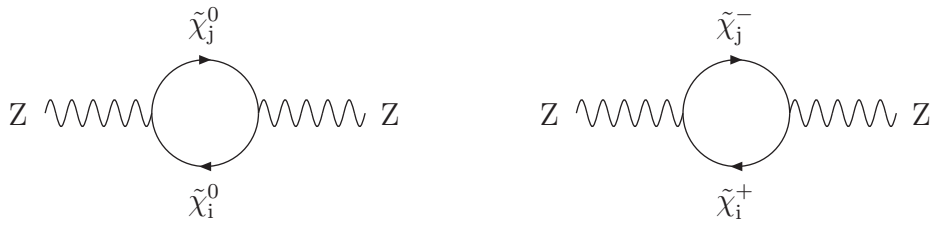

(a) Neutralino and chargino loops in the Z propagator.

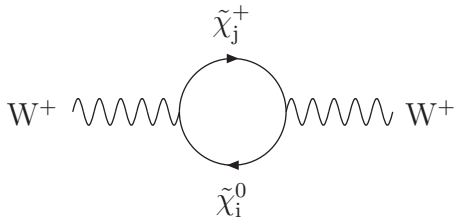

(b) Chargino-neutralino loop in the W propagator.

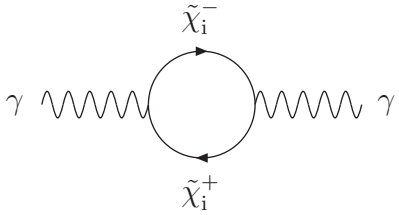

(c) Chargino loop in the photon propagator.

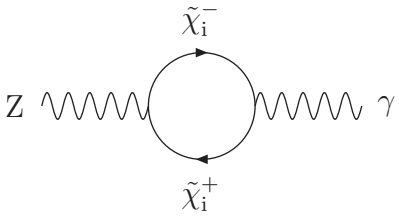

(d) Chargino loop in photon–Z mixing.

Figure 4.9: Gaugino loops in the gauge boson propagators.

$$\Pi_{\rm WW}(q) = -\frac{g^2}{8\pi^2}\sum_{i=1}^{4}\sum_{j=1}^{2}\Bigg[2\mathcal{R}e\left\{O_{ij}^L O_{ij}^R\right\} M_{\tilde{\chi}_i^0}^2 M_{\tilde{\chi}_j^+}^2 \left(E - b_0(\tilde{\chi}_i^0\tilde{\chi}_j^+ q)\right)$$

$$+\left(|O_{ij}^L|^2 + |O_{ij}^R|^2\right)\Bigg(\left[\frac{q^2}{3} - \frac{M_{\tilde{\chi}_i^0}^2}{2} - \frac{M_{\tilde{\chi}_j^+}^2}{2}\right]E - 2q^2 b_2(\tilde{\chi}_i^0\tilde{\chi}_j^+ q)$$

$$+M_{\tilde{\chi}_i^0}^2 b_0(\tilde{\chi}_i^0\tilde{\chi}_j^+ q) + (M_{\tilde{\chi}_j^+}^2 - M_{\tilde{\chi}_i^0}^2) b_1(\tilde{\chi}_i^0\tilde{\chi}_j^+ q)\Bigg)\Bigg], \tag{4.44b}$$

$$\Pi_{\gamma\gamma}(q) = -\frac{e^2}{2\pi^2}\sum_{i=1}^{2}\left[\frac{q^2}{6}E - q^2 b_2(\tilde{\chi}_i^+\tilde{\chi}_i^- q)\right], \tag{4.44c}$$

$$\Pi_{\rm Z\gamma}(q) = \frac{ge}{4\pi^2\cos\theta_W}\sum_{i=1}^{2}\left(O'^L_{ij} + O'^R_{ij}\right)\left[\frac{q^2}{6}E - q^2 b_2(\tilde{\chi}_i^+\tilde{\chi}_i^- q)\right]. \tag{4.44d}$$

The coefficients $O_{ij}^{L,R}$, $O'^{L,R}_{ij}$ and $O''^{L,R}_{ij}$ in the loop diagrams are taken from [18]. We have used the same notation as [11] for the functions in the loop calculations, *i.e.*

$$E = \frac{2}{\epsilon} - \gamma_E + \log(4\pi) - \log(M^2), \tag{4.45a}$$

$$\Delta(m_1^2, m_2^2, q^2) = x m_2^2 + (1-x)m_1^2 - x(1-x)q^2, \tag{4.45b}$$

$$b_0(12q) = b_0(m_1^2, m_2^2, q^2) = \int_0^1 dx \log\left(\frac{\Delta(m_1^2, m_2^2, q^2)}{M^2}\right), \tag{4.45c}$$

$$b_1(12q) = b_1(m_1^2, m_2^2, q^2) = \int_0^1 dx\, x \log\left(\frac{\Delta(m_1^2, m_2^2, q^2)}{M^2}\right), \tag{4.45d}$$

$$b_2(12q) = b_2(m_1^2, m_2^2, q^2) = \int_0^1 dx\, x(1-x) \log\left(\frac{\Delta(m_1^2, m_2^2, q^2)}{M^2}\right), \tag{4.45e}$$

where the calculation has been performed in $d = 4 - \epsilon$ dimensions.

The effect of new physics from these vacuum polarization diagrams is usually parameterized using either the S, T, and U parameters of [151–153] or the ϵ_1, ϵ_2, and ϵ_3 parameters of [154]. The calculation of these parameters is based on an expansion in $q^2/M_{\rm new}^2$, where q^2 is the momentum flow through the gauge boson propagator, typically $M_{\rm Z}^2$ or smaller and $M_{\rm new}^2$ is the scale of the new physics, which is assumed to be well above $M_{\rm Z}^2$. If, however, there are new light particles in the spectrum, as is the case in our model, these approximations are insufficient and in principle the box and vertex

corrections must also be calculated [155].

This full calculation is beyond the scope of our analysis. There is one exception to this which is the ratio of the charged to neutral current neutrino–electron/muon scattering events, the ρ parameter. This is defined at $q^2 = 0$ and hence the expansion is trivial. We have calculated the correction to the ρ parameter from the full set of chargino and neutralino diagrams. The radiative correction to the ρ parameter is given by [22]

$$\Delta\rho = \frac{\Pi_{\rm WW}(0)}{M_{\rm W}^2} - \frac{\Pi_{\rm ZZ}(0)}{M_{\rm Z}^2}. \tag{4.46}$$

The dominant Standard Model contributions to $\Delta\rho$ are from top quark and Higgs boson loops. These contributions can be subtracted, assuming $M_{\rm H} = M_{\rm Z}$, from the experimental results giving the contribution from new physics

$$\Delta\rho_{\rm NEW} = (-1.3 \pm 1.2) \times 10^{-3}. \tag{4.47}$$

This gives the following limit on the contribution to $\Delta\rho$ from new physics at the 2σ level

$$-3.7 \times 10^{-3} < \Delta\rho_{\rm NEW} < 1.1 \times 10^{-3}. \tag{4.48}$$

It is interesting to consider the effect on this limit of varying the Standard Model Higgs. The following result is for $M_{\rm H} = 300$ GeV:

$$-4.6 \times 10^{-3} < \Delta\rho_{\rm NEW} < 0.2 \times 10^{-3}, \tag{4.49}$$

although it should be noted that this is a larger value of the Higgs mass than is possible in the MSSM. We have calculated the contribution to $\Delta\rho$ from the chargino and neutralino loops in Fig. 4.9, using the results given in Eqn. 4.44. We denote this contribution to the ρ parameter by $\Delta\rho_{\rm SUSY}$. We then determine $\Delta\rho_{\rm SUSY}$ along the solution curves given in Fig. 4.8. The dotted lines indicate solutions for which $\Delta\rho_{\rm SUSY} < 10^{-4}$, while the solid lines indicate solutions for which $\Delta\rho_{\rm SUSY} < 5 \times 10^{-4}$. This shows that there is no conflict with the experimental constraint on the ρ parameter, for $M_{\rm H} = M_{\rm Z}$. There may be some constraints on this model for higher values of the Higgs mass although even for Higgs masses above those which are possible in the MSSM there are still areas of SUSY parameter space in which the lightest neutralino mass can solve the KARMEN anomaly.

It is possible to derive bounds on the existence and properties of an additional light particle in the mass spectrum on cosmological grounds and from astrophysical processes. The potential bounds on our model are discussed in [8].

4.5 Future Tests

Experimentally our model looks very much like the MSSM with non-universal gaugino masses and a very light LSP. Hence most future tests of the MSSM will also apply to our model. A specific test would be to identify the existence of a very light neutralino in, for

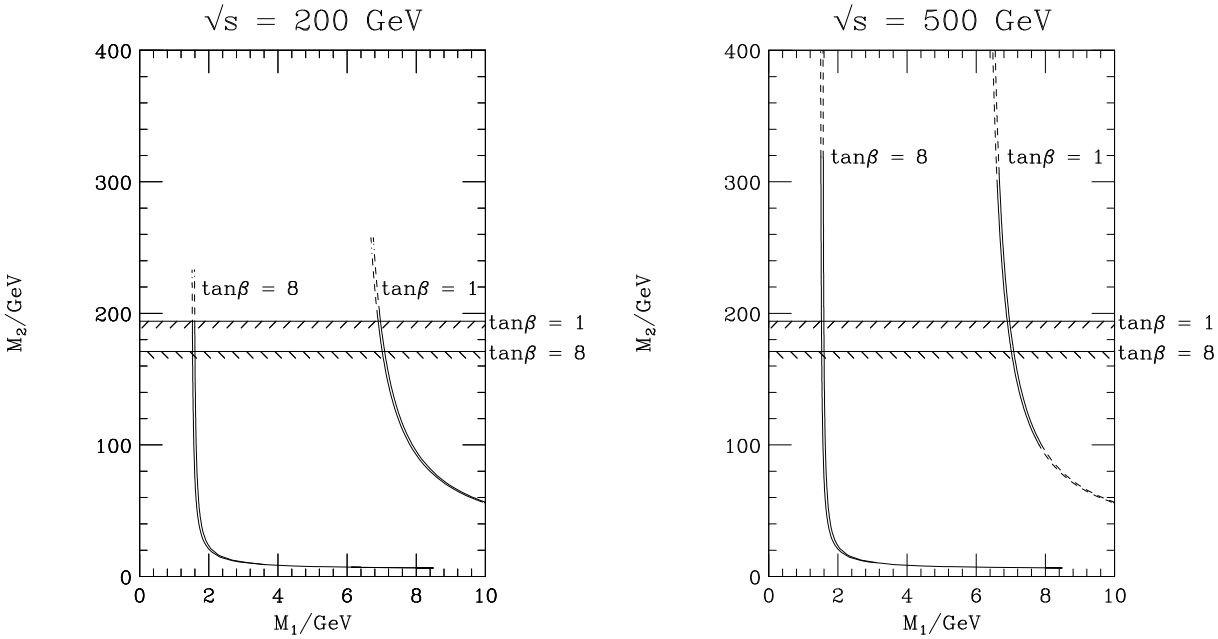

Figure 4.10: Cross sections for $e^+e^- \to \tilde{\chi}^0_2\tilde{\chi}^0_1$ for the solutions in Fig. 4.8. The solid lines correspond to $0.1\,\text{pb} < \sigma < 1\,\text{pb}$, the dashed lines to $10\,\text{fb} < \sigma < 0.1\,\text{pb}$, the dotted lines to $1\,\text{fb} < \sigma < 10\,\text{fb}$, and the dot-dashed lines to $\sigma < 1\,\text{fb}$.

example, neutralino pair production in e^+e^- collisions via,

$$e^+e^- \longrightarrow \tilde{\chi}^0_2\tilde{\chi}^0_1, \tag{4.50}$$

followed by a visible decay of the second-to-lightest neutralino. The cross section for this process is shown in Fig. 4.10 along our MSSM solution curves from Fig. 4.8 for both LEP2 ($\sqrt{s} = 200$ GeV) and the NLC ($\sqrt{s} = 500$ GeV). This process should be observable provided that it is kinematically accessible, *i.e.* $\sqrt{s} > M_{\tilde{\chi}^0_2}$.

As the neutralino is sufficiently long lived in our model that it will escape the detector before decaying the main difference between our model and the MSSM with non-universal gaugino masses is the possibility of resonant sparticle production. As we saw in Chapter 3, the value of the coupling $\lambda'_{211} \lesssim 10^{-4}$ is too small for the observation of resonant slepton production in hadron–hadron collisions. However the values of the couplings λ_{131} (or λ_{121}) $> 10^{-3}$ should allow a test of resonant sneutrino production in e^+e^- collisions provided $M_{\tilde{\nu}} \lesssim \sqrt{s}$. The production of first generation sleptons can also be tested by the processes suggested in [56].

A further upgrade of the KARMEN detector may allow better resolution of the decay of the X particle. In particular there may be tracking so that the angular distribution of the decay products can be measured. We therefore show the differential decay rate of the neutralino in our model as a function of the angle between the electron and positron produced in the neutralino decay in the KARMEN laboratory frame, Fig. 4.11. This differs from the corresponding singlet neutrino decay distribution.

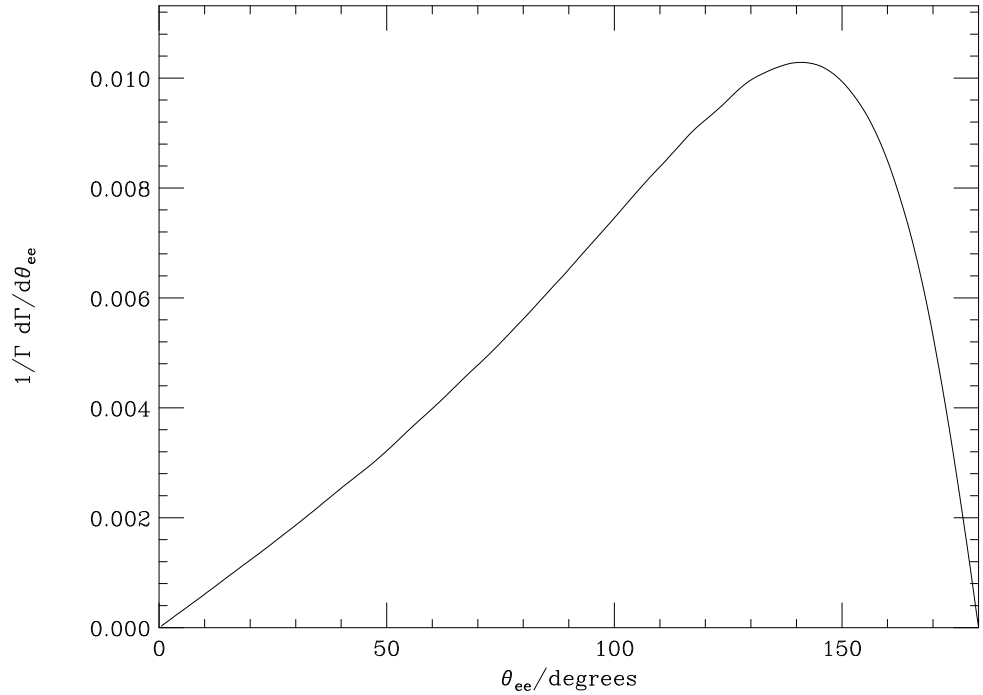

Figure 4.11: $\frac{d\Gamma}{d\theta_{\rm ee}}$ in the KARMEN laboratory frame.

4.6 Summary

There have been many reported experimental deviations from the Standard Model in recent years. Indeed most of these deviations have had much the same statistical significance as the KARMEN time anomaly. However while the statistical significance of most of the deviations has reduced with increased statistics, or the effect has been explained away as a systematic effect, this is not the case for the KARMEN anomaly. In fact the anomaly persists in the second run of the KARMEN experiment, which has a much reduced background [123], with the same characteristics as in the initial run of the experiment [121].

An additional problem in the resolution of this anomaly is that there is no independent experiment with the sensitivity to either confirm or exclude the KARMEN result. Although the LSND experiment also studies the decay of pions and muons at rest, it lacks the time structure of the beam in the KARMEN experiment, which is necessary to extract the anomaly. Since the second run of the KARMEN experiment only collects about ten anomaly events per year, a definitive resolution of the anomaly will require an upgraded detector with improved tracking capabilities.

The different phenomenological models which have been proposed to explain the KARMEN results via the production and decay of a new particle are tightly constrained. The only viable proposals at present are the production of a singlet neutrino which decays through its large mixing with the tau neutrino [125,133], the brane-world model of [128] or model with a neutralino decaying via $\not{R}_{\rm p}$ [127] which we have extended and investigated here.

It is important to note from our study that a light neutralino is only excluded by present day collider experiments if we assume a GUT relation between the SUSY-breaking masses for the gauginos.

Chapter 5

Conclusions

Despite the lack of any experimental evidence there are many compelling theoretical arguments for the existence of supersymmetry. In this thesis we have argued that if we are to discover whether or not supersymmetry is realized in nature we cannot simply consider the simplest possible supersymmetric extension of the Standard Model. Indeed this simplest extension is no better motivated than the R-parity violating models we have considered. In these models lepton or baryon number is violated which leads to very different experimental signatures of supersymmetry which must be investigated if we are to explore all possible channels for the discovery of supersymmetry.

There has however been much less study of these models, particularly experimentally, than of the R_p conserving MSSM. In hadron–hadron collisions studies of these models have been hindered by the lack of a Monte Carlo simulation which includes the $\not{R}_p$ production processes and decays. We have presented the calculations necessary to produce a full simulation of these $\not{R}_p$ processes including colour coherence effects via the angular-ordering procedure. This sees a new type of vertex in which three particles in the fundamental representation of $SU(3)$ interact at a vertex which violates baryon number. The inclusion of these colour coherence effects has proven to be important for an accurate simulation of the QCD radiation in Standard Model processes at previous experiments and we therefore must include it to give a reliable simulation of these $\not{R}_p$ processes. The simulation we produced using these results has already allowed a full simulation of baryon number violating processes at the LHC for the first time [103].

Our studies of the colour coherence properties of different resonant $\not{R}_p$ production processes in hadron–hadron collisions show differences for variables which are sensitive to the colour coherence phenomenon. In particular there are differences between resonant slepton production, which violates lepton number, and resonant squark production, which violates baryon number. We have used this simulation to show that the extraction of a signal for resonant slepton production via the $\not{R}_p$ decay modes of the slepton is much harder than was previously believed due to the emission of QCD radiation. The differences in the distributions of those variables which are sensitive to the presence of colour connections between the initial and final states for these processes and QCD jet production allow us to improve the extraction of a resonant slepton signal by imposing cuts on these variables. However the discovery of resonant slepton production via these $\not{R}_p$ decay modes is still only possible for the largest values of the couplings allowed, given

the current low-energy limits.

We therefore studied the discovery potential of the supersymmetric gauge decay modes of resonantly produced sleptons. These decay modes give a number of different channels for the production of like-sign dilepton pairs, which has a very low Standard Model background. This like-sign dilepton signature is dominated by the production of a neutralino, which decays via $\not{R}_p$, and a lepton in the supersymmetric gauge decay of a resonant charged slepton. We studied the cuts needed to reduce both the Standard Model background and the background from sparticle pair production and improve the extraction of a signal. This gives a large discovery potential for resonant slepton production mechanisms, at both the Tevatron and the LHC, and allows us to probe much smaller values of the $\not{R}_p$ Yukawa couplings than is possible using the $\not{R}_p$ decay modes of the resonant sleptons. We also showed that if such a signal is discovered it should be possible to measure the mass of both the resonant slepton and the lightest neutralino.

Finally, we considered the possibility that we have already seen evidence for the existence of $\not{R}_p$ in the time anomaly reported by the KARMEN collaboration. We have shown that this anomaly could be due to the production via $\not{R}_p$ of the lightest neutralino in charged pion decays. This neutralino could then decay, via $\not{R}_p$, inside the KARMEN detector giving rise to the observed excess. Surprisingly the existence of this light neutralino, decaying via $\not{R}_p$, is not ruled out by any current experimental data. Hopefully a future run of the KARMEN experiment will both improve the statistical significance of this excess and give us further insights into the physics which is producing it. This model can be tested by looking for the production of $\tilde{\chi}_1^0\tilde{\chi}_2^0$ at LEP, or any future e^+e^- collider.

In conclusion we have produced the first full simulation of $\not{R}_p$ violating supersymmetry and have used this simulation to study some possible channels for the discovery of $\not{R}_p$ processes. There are many processes which still needed to be examined. Hopefully this work will allow a more detailed study of these processes, particularly by the experimental community, in the future.

Addendum

While I was in the final stages of preparing this thesis new results [156] were announced by the KARMEN collaboration at the Neutrino 2000 conference. These results show that the results of the KARMEN 2 experiment no longer confirm the anomaly seen in the KARMEN 1 data. However there is still an anomaly for the combined KARMEN 1+2 data set. Given this result the planned experiment to investigate the anomaly has been cancelled.

Appendix A

Feynman Rules and Conventions

A.1 Introduction

There are a number of different conventions which are commonly adopted in the literature for the MSSM Lagrangian. While most authors have chosen to follow the conventions used in [18, 24] other conventions, for example [157], are also commonly used. We will present the conventions we have used in this thesis, which in general follow those of [18, 24]. We then present the Feynman rules used in the various decay rate and cross-section calculations.

We will first present our conventions for the mixing matrices for the charginos, neutralinos and sfermions, together with the conversion between the conventions of [18, 24] and [157]. We then give the Feynman rules we have used from [18, 24] with the inclusion of left/right sfermion mixing. In particular we give the Feynman rules for the interactions of squarks and sleptons with the gauginos, gluinos, electroweak gauge bosons and Higgs bosons of the MSSM.

We conclude by giving the Feynman rules for the R-parity violating superpotential. These Feynman rules are then used in Appendix B to evaluate the decay rates of the sparticles via the different $\not{R}_p$ operators and in Appendix C to calculate the single sparticle production cross sections.

A.2 Mixing

All of the cross-section and decay rate calculations presented in this thesis have been implemented in the HERWIG Monte Carlo event generator [2]. While internally HERWIG uses the conventions of [18, 24, 158], it relies on ISAJET [75] for the calculation of the masses of the sparticles and their R_p conserving decay rates. ISAJET also calculates the mixing matrices for the electroweak gauginos and scalar fermions. ISAJET uses the conventions of [157, 159] and it is essential that the conversion between the two formalisms is correct.

The major problem arises in the conventions for the various mixing matrices, for the charginos and neutralinos, and the left/right mixing of the scalar fermions. We will first consider the conversion between the two formalisms for the gauginos and then for the

left/right sfermion mixing. The ISAJET [157] and Haber and Kane [18] conventions for the sign of the μ and A terms are the same.[1] This corresponds to the following

$$2m_1 = -\mu, \tag{A.1a}$$
$$\mu_1 = -M_1, \tag{A.1b}$$
$$\mu_2 = -M_2, \tag{A.1c}$$

where m_1, μ_1 and μ_2 are in the notation of ISAJET [157] and μ, M_1 and M_2 are in the notation[2] of [18, 24]. Here μ is the mixing parameter in the MSSM superpotential, Eqn. 1.62, for the two Higgs doublets, M_1 is the soft SUSY-breaking mass for the bino and M_2 is the soft SUSY-breaking mass for the winos.

We can compare the Lagrangians of [157] and [18,24] to obtain the conversions between them. We shall use the conventions of [18, 24] for the chargino and neutralino mixing matrices.

A.2.1 Charginos

In the notation of [24], we define the following two-component spinors for the charginos before mixing

$$\psi_j^+ = \left(-i\lambda^+, \psi_{\mathrm{H}_2}^+\right), \tag{A.2a}$$
$$\psi_j^- = \left(-i\lambda^-, \psi_{\mathrm{H}_1}^-\right), \tag{A.2b}$$

where $\lambda^{+,-}$ are the charged winos, $\psi_{\mathrm{H}_1}^-$ is the charged higgsino associated with the Higgs which gives mass to the down-type quarks and $\psi_{\mathrm{H}_2}^+$ is the charged higgsino associated with the Higgs doublet which gives the up-type quarks mass. The mass term in the Lagrangian from Eqn. A.2 of [24] is

$$\mathcal{L}_{\mathrm{chargino}} = -\frac{1}{2}\left(\psi^+, \psi^-\right)\begin{pmatrix} 0 & X^T \\ X & 0 \end{pmatrix}\begin{pmatrix} \psi^+ \\ \psi^- \end{pmatrix} + \mathrm{h.c.}, \tag{A.3}$$

where the mass matrix is given by

$$X = \begin{pmatrix} M_2 & M_{\mathrm{W}}\sqrt{2}\sin\beta \\ M_{\mathrm{W}}\sqrt{2}\cos\beta & \mu \end{pmatrix}. \tag{A.4}$$

In [24] this was diagonalized in two-component notation by defining two-component mass eigenstates

$$\chi_i^+ = V_{ij}\psi_j^+, \tag{A.5a}$$
$$\chi_i^- = U_{ij}\psi_j^-, \tag{A.5b}$$

[1] This also agrees with the conventions of the other major SUSY event generators, SPYTHIA [99] and SUSYGEN [100].

[2] In [18, 24], M' and M are used instead of M_1 and M_2, respectively. However the notation M_1 and M_2 has become more common and we will use this here.

where U and V are unitary matrices chosen such that

$$U^* X V^{-1} = M_D, \tag{A.6}$$

where M_D is the diagonal chargino mass matrix. The four-component mass eigenstates, the charginos, are defined in terms of the two-component fields

$$\tilde{\chi}_1^+ = \begin{pmatrix} \chi_1^+ \\ \bar{\chi}_1^- \end{pmatrix}, \qquad \tilde{\chi}_2^+ = \begin{pmatrix} \chi_2^+ \\ \bar{\chi}_2^- \end{pmatrix}. \tag{A.7}$$

We need to express the chargino mass terms in the Lagrangian in a four-component notation so we can compare this Lagrangian with the conventions of [157]. We define the four-component spinors as in [24],

$$\widetilde{W} = \begin{pmatrix} -i\lambda^+ \\ i\bar{\lambda}^- \end{pmatrix}, \qquad \widetilde{H} = \begin{pmatrix} \psi_{\mathrm{H}_2}^+ \\ \bar{\psi}_{\mathrm{H}_1}^- \end{pmatrix}. \tag{A.8}$$

Using this notation we can express the Lagrangian in four-component notation

$$\mathcal{L}_{\text{chargino}} = -\left(\overline{\widetilde{W}}, \overline{\widetilde{H}}\right) \left[X P_L + X^T P_R\right] \begin{pmatrix} \widetilde{W} \\ \widetilde{H} \end{pmatrix}. \tag{A.9}$$

This is now in a similar form to the chargino mass term in Eqn. 2.1[3] of [157],

$$\mathcal{L}_{\text{chargino}} = -\left(\bar{\lambda}, \bar{\chi}\right) \left[M_{\text{charge}} P_L + M_{\text{charge}}^T P_R\right] \begin{pmatrix} \lambda \\ \chi \end{pmatrix}, \tag{A.10}$$

where

$$M_{\text{charge}} = \begin{pmatrix} \mu_2 & -gv' \\ -gv & 2m_1 \end{pmatrix} = -\begin{pmatrix} M_2 & \sqrt{2} M_{\mathrm{W}} \cos\beta \\ \sqrt{2} M_{\mathrm{W}} \sin\beta & \mu \end{pmatrix}, \tag{A.11}$$

where v and v' are the vacuum expectation values for the Higgs fields which give mass to the up- and down-type quarks, respectively. We now come to the problem in comparing the notations of [24] and [157]. The wino and higgsino fields of [157] are charge conjugates of those used in [24], so the following transformation is required

$$\widetilde{W} = \lambda^c, \tag{A.12a}$$

$$\widetilde{H} = \chi^c. \tag{A.12b}$$

This gives the chargino mass matrix in the form

$$\mathcal{L}_{\text{chargino}} = \left(\overline{\widetilde{W}}, \overline{\widetilde{H}}\right) \left[M'_{\text{charge}} P_L + M'^T_{\text{charge}} P_R\right] \begin{pmatrix} \widetilde{W} \\ \widetilde{H} \end{pmatrix}, \tag{A.13}$$

[3] This Lagrangian is taken from [160] which corrected a sign error in the off-diagonal terms in [157].

where

$$M'_{\rm charge} = \begin{pmatrix} -\mu_2 & gv \\ gv' & -2m_1 \end{pmatrix} = \begin{pmatrix} M_2 & \sqrt{2}M_{\rm W}\sin\beta \\ \sqrt{2}M_{\rm W}\cos\beta & \mu \end{pmatrix}. \tag{A.14}$$

This agrees with Eqn. A.9, apart from the overall sign. We need to express the fields in terms of the ISAJET mixing matrices. The ISAJET mixing matrices are [157], Eqns. 2.10 and 2.11,

$$\begin{pmatrix} \widetilde{W}_+ \\ \widetilde{W}_- \end{pmatrix}_L = \begin{pmatrix} \theta_x\cos\gamma_L & -\theta_x\sin\gamma_L \\ \sin\gamma_L & \cos\gamma_L \end{pmatrix} \begin{pmatrix} \lambda \\ \chi \end{pmatrix}_L, \tag{A.15a}$$

$$\begin{pmatrix} (-1)^{\theta_+}\widetilde{W}_+ \\ (-1)^{\theta_-}\widetilde{W}_- \end{pmatrix}_R = \begin{pmatrix} \theta_y\cos\gamma_R & -\theta_y\sin\gamma_R \\ \sin\gamma_R & \cos\gamma_R \end{pmatrix} \begin{pmatrix} \lambda \\ \chi \end{pmatrix}_R, \tag{A.15b}$$

where the mixing angles γ_L and γ_R, and the sign functions θ_x, θ_y, θ_+, and θ_- are defined in [157].

We can transform these equations into the notation of Haber and Kane with the identification

$$\tilde{\chi}_1 = \widetilde{W}^c_-, \tag{A.16a}$$

$$\tilde{\chi}_2 = \widetilde{W}^c_+. \tag{A.16b}$$

This gives

$$P_L \begin{pmatrix} \widetilde{W} \\ \widetilde{H} \end{pmatrix} = P_L \begin{pmatrix} -\sin\gamma_R & -\theta_y\cos\gamma_R \\ -\cos\gamma_R & \theta_y\sin\gamma_R \end{pmatrix} \begin{pmatrix} (-1)^{\theta_-}\tilde{\chi}_1 \\ (-1)^{\theta_+}\tilde{\chi}_2 \end{pmatrix}, \tag{A.17a}$$

$$P_R \begin{pmatrix} \widetilde{W} \\ \widetilde{H} \end{pmatrix} = P_R \begin{pmatrix} -\sin\gamma_L & -\theta_x\cos\gamma_L \\ -\cos\gamma_L & \theta_x\sin\gamma_L \end{pmatrix} \begin{pmatrix} \tilde{\chi}_1 \\ \tilde{\chi}_2 \end{pmatrix}. \tag{A.17b}$$

These mixing matrices are now in a form that allows us to compare them with the notation of [24], Eqn. A.13,

$$P_L \begin{pmatrix} \widetilde{W} \\ \widetilde{H} \end{pmatrix} = P_L \begin{pmatrix} V^*_{11} & V^*_{21} \\ V^*_{12} & V^*_{22} \end{pmatrix} \begin{pmatrix} \tilde{\chi}_1 \\ \tilde{\chi}_2 \end{pmatrix}, \tag{A.18a}$$

$$P_R \begin{pmatrix} \widetilde{W} \\ \widetilde{H} \end{pmatrix} = P_R \begin{pmatrix} U_{11} & U_{21} \\ U_{12} & U_{22} \end{pmatrix} \begin{pmatrix} \tilde{\chi}_1 \\ \tilde{\chi}_2 \end{pmatrix}. \tag{A.18b}$$

By comparing Eqns.A.17 and A.18 we can obtain the mixing matrices in the notation of [24]

$$U = \begin{pmatrix} -\sin\gamma_L & -\cos\gamma_L \\ -\theta_x\cos\gamma_L & \theta_x\sin\gamma_L \end{pmatrix}, \tag{A.19a}$$

$$V = \begin{pmatrix} -\sin\gamma_R(-1)^{\theta_-} & -\cos\gamma_R(-1)^{\theta_+} \\ -\theta_y\cos\gamma_R(-1)^{\theta_-} & \theta_y\sin\gamma_R(-1)^{\theta_+} \end{pmatrix}. \tag{A.19b}$$

It should be noted that we adopt the opposite sign convention for the chargino masses due to the sign differences in the two Lagrangians.

A.2.2 Neutralinos

We define a two-component fermion field for the neutralinos before mixing

$$\psi_j^0 = \left(-i\lambda', -i\lambda^3, \psi_{\mathrm{H}_1}^0, \psi_{\mathrm{H}_2}^0\right), \tag{A.20}$$

where λ' is the bino, λ^3 is the neutral wino, $\psi_{\mathrm{H}_1}^0$ is the higgsino for the Higgs giving mass to the down-type quarks and $\psi_{\mathrm{H}_2}^0$ is the higgsino for the Higgs giving mass to the up-type quarks. The Lagrangian for the neutralino masses from Eqn. A.18 of [24] is

$$\mathcal{L}_{\mathrm{neutralino}} = -\frac{1}{2}\left(\psi^0\right)^T Y \psi^0 + \mathrm{h.c.}, \tag{A.21}$$

where

$$Y = \begin{pmatrix} M_1 & 0 & -M_{\mathrm{Z}}\sin\theta_W\cos\beta & M_{\mathrm{Z}}\sin\theta_W\sin\beta \\ 0 & M_2 & M_{\mathrm{Z}}\cos\theta_W\cos\beta & -M_{\mathrm{Z}}\cos\theta_W\sin\beta \\ -M_{\mathrm{Z}}\sin\theta_W\cos\beta & M_{\mathrm{Z}}\cos\theta_W\cos\beta & 0 & -\mu \\ M_{\mathrm{Z}}\sin\theta_W\sin\beta & -M_{\mathrm{Z}}\cos\theta_W\sin\beta & -\mu & 0 \end{pmatrix}. \tag{A.22}$$

In [24] the Lagrangian was diagonalized in this two-component notation to give the mass eigenstates. The diagonalization was performed by defining two-component fields

$$\chi_i^0 = N_{ij}\psi_j^0, \qquad i,j = 1,\ldots,4, \tag{A.23}$$

where N is a unitary matrix satisfying $N^* Y N^{-1} = N_D$, and N_D is the diagonal neutralino mass matrix. The four-component mass eigenstates, the neutralinos, can be defined in terms of the two-component fields, *i.e.*

$$\tilde{\chi}_i^0 = \begin{pmatrix} \chi_i^0 \\ \bar{\chi}_i^0 \end{pmatrix}. \tag{A.24}$$

Rather than adopting this approach we need to express the neutralino mass terms in four-component notation before performing the diagonalization in order to compare this Lagrangian with that of [157]. We use the standard procedure of [24] to express this in four-component notation by defining four-component Majorana fields

$$\widetilde{B} = \begin{pmatrix} -i\lambda' \\ i\bar{\lambda}' \end{pmatrix}, \quad \widetilde{W}_3 = \begin{pmatrix} -i\lambda^3 \\ i\bar{\lambda}^3 \end{pmatrix}, \quad \widetilde{H}_1 = \begin{pmatrix} \psi_{\mathrm{H}_1}^0 \\ \bar{\psi}_{\mathrm{H}_1}^0 \end{pmatrix}, \quad \widetilde{H}_2 = \begin{pmatrix} \psi_{\mathrm{H}_2}^0 \\ \bar{\psi}_{\mathrm{H}_2}^0 \end{pmatrix}, \tag{A.25}$$

where $\widetilde{B}$ is the bino field, $\widetilde{W}_3$ is the neutral wino field, $\widetilde{H}_1$ is the field for the higgsino associated with the Higgs boson which gives mass to the down-type quarks and $\widetilde{H}_2$ is the field for the higgsino associated with the Higgs boson which gives mass to the up-type quarks.

This gives the Lagrangian in four-component notation

$$\mathcal{L}_{\text{neutralino}} = -\frac{1}{2}\left(\overline{\widetilde{B}}, \overline{\widetilde{W}}_3, \overline{\widetilde{H}}_1, \overline{\widetilde{H}}_2\right)[YP_L + YP_R]\begin{pmatrix}\widetilde{B}\\ \widetilde{W}_3\\ \widetilde{H}_1\\ \widetilde{H}_2\end{pmatrix}. \tag{A.26}$$

We can now compare this with the relevant Lagrangian, in four-component notation, given in [157]. This Lagrangian is from [157], Eqn. 2.2,[4]

$$\mathcal{L}_{\text{neutralino}} = -\frac{1}{2}\left(\bar{h}^0, \bar{h}'^0, \bar{\lambda}_3, \bar{\lambda_0}\right)[M_{\text{neutral}}P_L + M_{\text{neutral}}P_R]\begin{pmatrix}h^0\\ h'^0\\ \lambda_3\\ \lambda_0\end{pmatrix}, \tag{A.27}$$

where h^0 is the higgsino partner of the Higgs which gives mass to the up-type quarks, h'^0 is the higgsino partner of the Higgs which gives mass to the down-type quarks, λ_3 is the neutral wino, λ_0 is the bino and the mass matrix is given by

$$M_{\text{neutral}} = \begin{pmatrix} 0 & -2m_1 & -\frac{1}{\sqrt{2}}gv & \frac{1}{\sqrt{2}}g'v \\ -2m_1 & 0 & \frac{1}{\sqrt{2}}gv' & -\frac{1}{\sqrt{2}}g'v' \\ -\frac{1}{\sqrt{2}}gv & \frac{1}{\sqrt{2}}gv' & \mu_2 & 0 \\ \frac{1}{\sqrt{2}}g'v & -\frac{1}{\sqrt{2}}g'v' & 0 & \mu_1 \end{pmatrix}. \tag{A.28}$$

It is easier to compare this with Eqn. A.26 after reordering the entries and reexpressing it in terms of M_{Z}, β and θ_W. This gives

$$\mathcal{L}_{\text{neutralino}} = \frac{1}{2}\left(\bar{\lambda_0}, \bar{\lambda}_3, \bar{h}'^0, \bar{h}^0\right)[M'_{\text{neutral}}P_L + M'_{\text{neutral}}P_R]\begin{pmatrix}\lambda_0\\ \lambda_3\\ h'^0\\ h^0\end{pmatrix}, \tag{A.29}$$

where

$$M'_{\text{neutral}} = \begin{pmatrix} M_1 & 0 & M_{\text{Z}}\sin\theta_W\cos\beta & -M_{\text{Z}}\sin\theta_W\sin\beta \\ 0 & M_2 & -M_{\text{Z}}\cos\theta_W\cos\beta & M_{\text{Z}}\cos\theta_W\sin\beta \\ M_{\text{Z}}\sin\theta_W\cos\beta & -M_{\text{Z}}\cos\theta_W\cos\beta & 0 & -\mu \\ -M_{\text{Z}}\sin\theta_W\sin\beta & M_{\text{Z}}\cos\theta_W\sin\beta & -\mu & 0 \end{pmatrix}. \tag{A.30}$$

This equation then agrees with Eqn. A.26 up to an overall sign provided we make the

[4] This Lagrangian is taken from [160] which corrects a sign error in [157].

following identification

$$\widetilde{B} = \lambda_0, \tag{A.31a}$$
$$\widetilde{W}_3 = \lambda_3, \tag{A.31b}$$
$$\widetilde{H}_1 = -h'^0, \tag{A.31c}$$
$$\widetilde{H}_2 = -h^0. \tag{A.31d}$$

The convention from ISAJET for the mixing taken from Eqn. 2.12 of [157] is

$$\begin{pmatrix} (-i\gamma_5)^{\theta_1}\widetilde{Z}_1 \\ (-i\gamma_5)^{\theta_2}\widetilde{Z}_2 \\ (-i\gamma_5)^{\theta_3}\widetilde{Z}_3 \\ (-i\gamma_5)^{\theta_4}\widetilde{Z}_4 \end{pmatrix} = \begin{pmatrix} v_1^{(1)} & v_2^{(1)} & v_3^{(1)} & v_4^{(1)} \\ v_1^{(2)} & v_2^{(2)} & v_3^{(2)} & v_4^{(2)} \\ v_1^{(3)} & v_2^{(3)} & v_3^{(3)} & v_4^{(3)} \\ v_1^{(4)} & v_2^{(4)} & v_3^{(4)} & v_4^{(4)} \end{pmatrix} \begin{pmatrix} h^0 \\ h'^0 \\ \lambda_3 \\ \lambda_0 \end{pmatrix}, \tag{A.32}$$

where $\widetilde{Z}_i$ are the mass eigenstates obtained by diagonalizing the mass matrix given in Eqn. A.28, $v_j^{(i)}$ are the elements of the mixing matrix and θ_i is zero (one) if the mass of $\widetilde{Z}_i$ is positive (negative).

After reordering we get

$$\begin{pmatrix} (-i\gamma_5)^{\theta_1}\widetilde{Z}_1 \\ (-i\gamma_5)^{\theta_2}\widetilde{Z}_2 \\ (-i\gamma_5)^{\theta_3}\widetilde{Z}_3 \\ (-i\gamma_5)^{\theta_4}\widetilde{Z}_4 \end{pmatrix} = \begin{pmatrix} v_4^{(1)} & v_3^{(1)} & -v_2^{(1)} & -v_1^{(1)} \\ v_4^{(2)} & v_3^{(2)} & -v_2^{(2)} & -v_1^{(2)} \\ v_4^{(3)} & v_3^{(3)} & -v_2^{(3)} & -v_1^{(3)} \\ v_4^{(4)} & v_3^{(4)} & -v_2^{(4)} & -v_1^{(4)} \end{pmatrix} \begin{pmatrix} \widetilde{B} \\ \widetilde{W} \\ \widetilde{H}_1 \\ \widetilde{H}_2 \end{pmatrix}. \tag{A.33}$$

We can therefore obtain the mixing matrix in the notation of [24] by making the identification

$$N_{i1} = v_4^{(i)}, \tag{A.34a}$$
$$N_{i2} = v_3^{(i)}, \tag{A.34b}$$
$$N_{i3} = -v_2^{(i)}, \tag{A.34c}$$
$$N_{i4} = -v_1^{(i)}. \tag{A.34d}$$

Again we need to adopt the opposite sign convention for the neutralino masses.

A.2.3 Left/Right Sfermion Mixing

In addition to the mixing of the neutralinos and charginos we also need to consider the left/right mixing of the sfermions. In general as the off-diagonal terms in the mass matrices are proportional to the fermion mass these effects are only important for the third generation sfermions, *i.e.* stop, sbottom and stau. As the top mass is much larger than any of the other Standard Model fermion masses these effects are particularly important for the top squarks.

The following mass matrix for the top squarks uses the conventions of [24][5] and is taken from Eqn. 4.17 of [24],

$$M_{\tilde{t}}^2 = \begin{pmatrix} M_{\tilde{Q}}^2 + M_{\rm Z}^2 \cos 2\beta \left(\frac{1}{2} - \frac{2}{3}\sin^2\theta_W\right) + m_t^2 & m_t\left(A_t - \mu\cot\beta\right) \\ m_t\left(A_t - \mu\cot\beta\right) & M_{\tilde{U}}^2 + \frac{2}{3}m_{\rm Z}^2\cos 2\beta\sin^2\theta_W + m_t^2 \end{pmatrix}, \tag{A.35}$$

where $M_{\tilde{Q}}$ and $M_{\tilde{U}}$ are soft SUSY-breaking masses for the left and right top squarks, respectively. A_t is the trilinear soft SUSY-breaking term for the interaction of the left and right stop squarks with the Higgs boson. This compares with the ISAJET matrix from [159]

$$M_{\tilde{t}}^2 = \begin{pmatrix} M_{\tilde{t}_L}^2 + M_{\rm Z}^2 \cos 2\beta \left(\frac{1}{2} - \frac{2}{3}\sin^2\theta_W\right) + m_t^2 & -m_t\left(A_t - \mu\cot\beta\right) \\ -m_t\left(A_t - \mu\cot\beta\right) & M_{\tilde{t}_R}^2 + \frac{2}{3}m_{\rm Z}^2\cos 2\beta\sin^2\theta_W + m_t^2 \end{pmatrix}, \tag{A.36}$$

where $M_{\tilde{t}_L}^2 = M_{\tilde{Q}}^2$ and $M_{\tilde{t}_R}^2 = M_{\tilde{U}}^2$. There is a difference in the sign of the off-diagonal terms. This means that, as the sign convention for the μ and A terms are the same, there is a difference in the relative phases of the two fields in the different conventions. Hence we should apply the following change in the ISAJET output

$$\theta_t \longrightarrow -\theta_t, \tag{A.37}$$

i.e. change the sign of the stop mixing angle. The same argument also applies to the sbottom and stau mixing angles.

We adopt the following convention for the sfermion mixing matrices

$$\begin{pmatrix} \tilde{q}_{iL} \\ \tilde{q}_{iR} \end{pmatrix} = \begin{pmatrix} \cos\theta_q^i & \sin\theta_q^i \\ -\sin\theta_q^i & \sin\theta_q^i \end{pmatrix} \begin{pmatrix} \tilde{q}_{i1} \\ \tilde{q}_{i2} \end{pmatrix}, \tag{A.38}$$

where $\tilde{q}_{iL}$ and $\tilde{q}_{iR}$ are the left and right squark fields, for the ith quark, where i is u, d, s, c, b, and t. $\tilde{q}_{i1}$ and $\tilde{q}_{i2}$ are the squark fields for the mass eigenstates, for the quark i, and θ_q^i is the mixing angle obtained by diagonalizing the mass matrix. We denote the mixing matrix above as $Q_{\alpha\beta}^i$ where i is the quark, β is the mass eigenstate and α is the left/right eigenstate.

Similarly we denote the lepton mixing as above with the matrix $L_{\alpha\beta}^i$ where i is e^-, ν_e, μ^-, ν_μ, τ^- and ν_τ, β is the mass eigenstate and α is the left/right eigenstate. As we do not include the right-handed neutrino we will neglect the left/right mixing for the sneutrinos.

A.3 Gaugino Interactions with the Sfermions

The Lagrangians for the interactions of the electroweak gauginos with the sfermions and fermions are derived in [24] without left/right mixing of the sfermions. We will therefore

[5] This is the same as [161], SPYTHIA [99] and SUSYGEN [100].

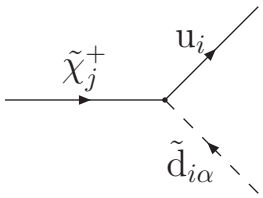

$$-\frac{ig}{2}\left[a(\tilde{\mathrm{d}}_{i\alpha})(1-\gamma_5)+b(\tilde{\mathrm{d}}_{i\alpha})(1+\gamma_5)\right]$$

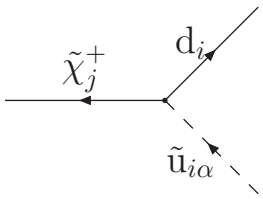

$$-\frac{ig}{2}\left[a(\tilde{\mathrm{u}}_{i\alpha})(1-\gamma_5)+b(\tilde{\mathrm{u}}_{i\alpha})(1+\gamma_5)\right]C$$

Figure A.1: Feynman rules for $\mathrm{q}\tilde{\mathrm{q}}\tilde{\chi}^+$.

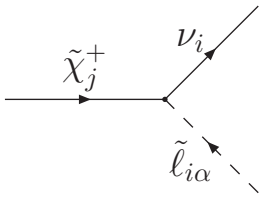

$$-\frac{ig}{2}b(\tilde{\ell}_{i\alpha})(1+\gamma_5)$$

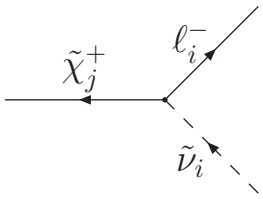

$$-\frac{ig}{2}\left[a(\tilde{\nu}_i)(1-\gamma_5)+b(\tilde{\nu}_i)(1+\gamma_5)\right]C$$

Figure A.2: Feynman rules for $\ell\tilde{\ell}\tilde{\chi}^+$.

take the results for the Lagrangians in the left/right sfermion basis and transform them into the mass basis we will use in the decay rate and cross-section calculations.

We will first consider the interactions of the sfermions and the charginos. The relevant Lagrangian, without left/right sfermion mixing, is

$$\begin{aligned}\mathcal{L}_{\mathrm{q}\tilde{\mathrm{q}}\tilde{\chi}^+} &= -g\left[\bar{u}P_R U_{l1}\tilde{\chi}_l^+\tilde{d}_L+\bar{d}P_R V_{l1}\chi_l^c\tilde{u}_L\right]\\ &\quad+\frac{gm_d}{\sqrt{2}M_{\mathrm{W}}\cos\beta}\left[\bar{u}P_R U_{l2}\tilde{\chi}_l^+\tilde{d}_R+\bar{d}P_L U_{l2}^*\tilde{\chi}_l^c\tilde{u}_L\right]\\ &\quad+\frac{gm_u}{\sqrt{2}M_{\mathrm{W}}\sin\beta}\left[\bar{u}P_L V_{l2}^*\tilde{\chi}_l^+\tilde{d}_L+\bar{d}P_R V_{l2}\tilde{\chi}_l^c\tilde{u}_R\right]+\mathrm{h.c.},\end{aligned}\tag{A.39}$$

for one generation of quarks. This is taken from [24], Eqn. 5.3. In Eqn. A.39 there is an implied summation over the chargino mass eigenstates. If we now substitute for the left

Coefficient	Coupling	Coefficient	Coupling
$a(\tilde{\ell}_{i\alpha})$	0	$b(\tilde{\ell}_{i\alpha})$	$U_{l1}L_{1\alpha}^{2i-1} - \frac{m_{\ell_i}U_{l2}L_{2\alpha}^{2i-1}}{\sqrt{2}M_{\rm W}\cos\beta}$
$a(\tilde{\nu}_i)$	$-\frac{m_{\ell_i}U_{l2}^*}{\sqrt{2}M_{\rm W}\cos\beta}$	$b(\tilde{\nu}_i)$	V_{l1}
$a(\tilde{\rm d}_{i\alpha})$	$-\frac{m_{u_i}V_{l2}^*Q_{1\alpha}^{2i-1}}{\sqrt{2}M_{\rm W}\sin\beta}$	$b(\tilde{\rm d}_{i\alpha})$	$U_{l1}Q_{1\alpha}^{2i-1} - \frac{m_{d_i}U_{l2}Q_{2\alpha}^{2i-1}}{\sqrt{2}M_{\rm W}\cos\beta}$
$a(\tilde{\rm u}_{i\alpha})$	$-\frac{m_{d_i}U_{l2}^*Q_{1\alpha}^{2i}}{\sqrt{2}M_{\rm W}\cos\beta}$	$b(\tilde{\rm u}_{i\alpha})$	$V_{l1}Q_{1\alpha}^{2i} - \frac{m_{u_i}V_{l2}Q_{2\alpha}^{2i}}{\sqrt{2}M_{\rm W}\sin\beta}$

Table A.1: Couplings for the chargino Feynman rules.

and right squark eigenstates in terms of the mass eigenstates we obtain

$$\begin{aligned}\mathcal{L}_{\rm q\tilde{q}\tilde{\chi}^+} &= -g\bar{u}_i\left[\left(U_{l1}Q_{1\alpha}^{2i-1} - \frac{m_{d_i}U_{l2}Q_{2\alpha}^{2i-1}}{\sqrt{2}M_{\rm W}\cos\beta}\right)P_R - \frac{m_{u_i}V_{l2}^*Q_{1\alpha}^{2i-1}}{\sqrt{2}M_{\rm W}\sin\beta}P_L\right]\tilde{\chi}_l^+\tilde{d}_{i\alpha} \\ &\quad -g\bar{d}_i\left[\left(V_{l1}Q_{1\alpha}^{2i} - \frac{m_{u_i}V_{l2}Q_{2\alpha}^{2i}}{\sqrt{2}M_{\rm W}\sin\beta}\right)P_R - \frac{m_{d_i}U_{l2}^*Q_{1\alpha}^{2i}}{\sqrt{2}M_{\rm W}\cos\beta}P_L\right]\tilde{\chi}_l^c\tilde{u}_{i\alpha}, \quad \text{(A.40)}\end{aligned}$$

where i is the generation of the squark and α is the mass eigenstate. In Eqn. A.40 there is an implicit summation over the squark and chargino mass eigenstates. This leads to the Feynman rules given in Fig. A.1, with the coefficients given in Table A.1.

The Feynman rules for the sleptons, Fig. A.2, can be obtained by changing the relevant masses and couplings, *i.e.* replacing the squark mixing matrices with the slepton mixing matrices and making the replacement

$$e_d \to -1, \quad e_u \to 0, \quad m_d \to m_e, \quad m_u \to 0. \quad \text{(A.41)}$$

The Lagrangian for the interaction of neutralinos with squarks is given in Eqn. 5.5 of [24],

$$\begin{aligned}\mathcal{L}_{\rm q\tilde{q}\tilde{\chi}^0} &= -\sqrt{2}\bar{u}\left\{\frac{gm_uN_{l4}^*}{2M_{\rm W}\sin\beta}P_L + \left[ee_uN_{l1}' + \frac{gN_{l2}'}{\cos\theta_W}\left(\frac{1}{2} - e_u\sin^2\theta_W\right)\right]P_R\right\}\tilde{\chi}_l^0\tilde{u}_L \\ &\quad +\sqrt{2}\bar{u}\left[\left(ee_uN'^*_{l1} - \frac{ge_u\sin^2\theta_WN'^*_{l2}}{\cos\theta_W}\right)P_L - \frac{gm_uN_{l4}}{2M_{\rm W}\sin\beta}P_R\right]\tilde{\chi}_l^0\tilde{u}_R \\ &\quad -\sqrt{2}\bar{d}\left\{\frac{gm_dN_{l3}^*}{2M_{\rm W}\cos\beta}P_L + \left[ee_dN_{l1}' - \frac{gN_{l2}'}{\cos\theta_W}\left(\frac{1}{2} + e_d\sin^2\theta_W\right)\right]P_R\right\}\tilde{\chi}_l^0\tilde{d}_L \\ &\quad +\sqrt{2}\bar{d}\left[\left(ee_dN'^*_{l1} - \frac{ge_d\sin^2\theta_WN'^*_{l2}}{\cos\theta_W}\right)P_L - \frac{gm_dN_{l3}}{2M_{\rm W}\cos\beta}P_R\right]\tilde{\chi}_l^0\tilde{d}_R \\ &\quad +\text{h.c.}, \quad \text{(A.42)}\end{aligned}$$

Coefficient	Coupling
$a(\tilde{\mathrm{d}}_{i\alpha})$	$\frac{gm_{d_i}N^*_{l3}}{2M_{\mathrm{W}}\cos\beta}Q^{2i-1}_{1\alpha} - Q^{2i-1}_{2\alpha}\left(ee_dN'^*_{l1} - \frac{ge_d\sin^2\theta_W N'^*_{l2}}{\cos\theta_W}\right)$
$b(\tilde{\mathrm{d}}_{i\alpha})$	$\frac{gm_{d_i}N_{l3}}{2M_{\mathrm{W}}\cos\beta}Q^{2i-1}_{2\alpha} + Q^{2i-1}_{1\alpha}\left(ee_dN'_{l1} - \frac{gN'_{l2}\left(\frac{1}{2}+e_d\sin^2\theta_W\right)}{\cos\theta_W}\right)$
$a(\tilde{\mathrm{u}}_{i\alpha})$	$\frac{gm_{u_i}N^*_{l4}}{2M_{\mathrm{W}}\sin\beta}Q^{2i}_{1\alpha} - Q^{2i}_{2\alpha}\left(ee_uN'^*_{l1} - \frac{ge_u\sin^2\theta_W N'^*_{l2}}{\cos\theta_W}\right)$
$b(\tilde{\mathrm{u}}_{i\alpha})$	$\frac{gm_{u_i}N_{l4}}{2M_{\mathrm{W}}\sin\beta}Q^{2i}_{2\alpha} + Q^{2i}_{1\alpha}\left(ee_uN'_{l1} + \frac{gN'_{l2}\left(\frac{1}{2}-e_u\sin^2\theta_W\right)}{\cos\theta_W}\right)$
$a(\tilde{\ell}_{i\alpha})$	$\frac{gm_{\ell_i}N^*_{l3}}{2M_{\mathrm{W}}\cos\beta}L^{2i-1}_{1\alpha} + L^{2i-1}_{2\alpha}\left(eN'^*_{l1} - \frac{g\sin^2\theta_W N'^*_{l2}}{\cos\theta_W}\right)$
$b(\tilde{\ell}_{i\alpha})$	$\frac{gm_{\ell_i}N_{l3}}{2M_{\mathrm{W}}\cos\beta}L^{2i-1}_{2\alpha} - L^{2i-1}_{1\alpha}\left(eN'_{l1} + \frac{gN'_{l2}\left(\frac{1}{2}-\sin^2\theta_W\right)}{\cos\theta_W}\right)$
$a(\tilde{\nu}_i)$	0
$b(\tilde{\nu}_i)$	$\frac{gN'_{l2}}{2\cos\theta_W}$

Table A.2: Couplings for the neutralino Feynman rules.

for one generation of squarks. Here there is an implied summation over the neutralino mass eigenstates.

This Lagrangian can be expressed in terms of the squark mass eigenstates,

$$\begin{aligned}
\mathcal{L}_{\mathrm{q\tilde{q}\tilde{\chi}^0}} \;=\; & \sqrt{2}\bar{u}_i\left\{-\left[\left\{ee_uN'_{l1} + \frac{gN'_{l2}}{\cos\theta_W}\left(\frac{1}{2} - e_u\sin^2\theta_W\right)\right\}Q^{2i}_{1\alpha} + \frac{gm_{u_i}N_{l4}}{2M_{\mathrm{W}}\sin\beta}Q^{2i}_{2\alpha}\right]P_R\right. \\
& \left. + \left[-\frac{gm_{u_i}N^*_{l4}}{2M_{\mathrm{W}}\sin\beta}Q^{2i}_{1\alpha} + \left(ee_uN'^*_{l1} - \frac{ge_u\sin^2\theta_W N'^*_{l2}}{\cos\theta_W}\right)Q^{2i}_{2\alpha}\right]P_L\right\}\tilde{\chi}^0_l\tilde{u}_{i\alpha} \\
& + \sqrt{2}\bar{d}_i\left\{\left[-\frac{gm_{d_i}N^*_{l3}}{2M_{\mathrm{W}}\cos\beta}Q^{2i-1}_{1\alpha} + \left(ee_dN'^*_{l1} - \frac{ge_d\sin^2\theta_W N'^*_{l2}}{\cos\theta_W}\right)Q^{2i-1}_{2\alpha}\right]P_L\right. \\
& \left. - \left[\left\{ee_dN'_{l1} - \frac{gN'_{l2}}{\cos\theta_W}\left(\frac{1}{2} + e_d\sin^2\theta_W\right)\right\}Q^{2i-1}_{1\alpha} + \frac{gm_{d_i}N_{l3}}{2M_{\mathrm{W}}\cos\beta}Q^{2i-1}_{2\alpha}\right]P_R\right\}\tilde{\chi}^0_l\tilde{d}_{i\alpha} \\
& + \mathrm{h.c.}, \qquad\qquad (A.43)
\end{aligned}$$

where i is the generation of the squark (assuming no mixing between the generations) and α is its mass eigenstate. Again there is an implied summation over the squark and neutralino mass eigenstates.

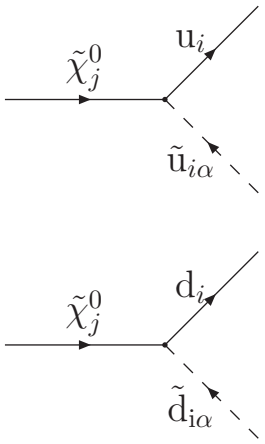

$$\frac{-i}{\sqrt{2}}\Big[a(\tilde{\mathrm{u}}_{i\alpha})(1-\gamma_5)+b(\tilde{\mathrm{u}}_{i\alpha})(1+\gamma_5)\Big]$$

$$\frac{-i}{\sqrt{2}}\Big[a(\tilde{\mathrm{d}}_{i\alpha})(1-\gamma_5)+b(\tilde{\mathrm{d}}_{i\alpha})(1+\gamma_5)\Big]$$

Figure A.3: Feynman rules for $\mathrm{q}\tilde{\mathrm{q}}\tilde{\chi}^0$.

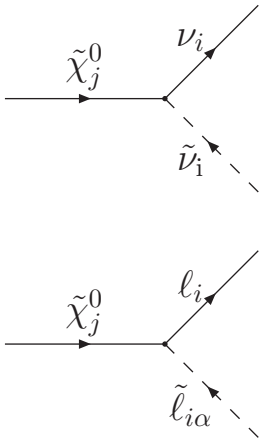

$$\frac{-i}{\sqrt{2}}b(\tilde{\nu}_i)(1+\gamma_5)$$

$$\frac{-i}{\sqrt{2}}\Big[a(\tilde{\ell}_{i\alpha})(1-\gamma_5)+b(\tilde{\ell}_{i\alpha})(1+\gamma_5)\Big]$$

Figure A.4: Feynman rules for $\ell\tilde{\ell}\tilde{\chi}^0$.

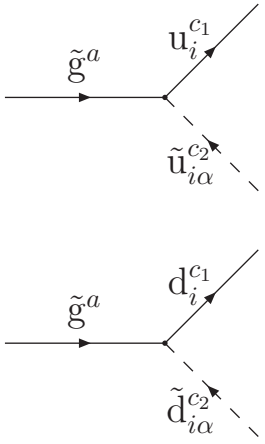

$$\frac{-ig_s\mathbf{t}^a_{c_1c_2}}{\sqrt{2}}\Big[a(\tilde{\mathrm{u}}_{i\alpha})(1-\gamma_5)+b(\tilde{\mathrm{u}}_{i\alpha})(1+\gamma_5)\Big]$$

$$\frac{-ig_s\mathbf{t}^a_{c_1c_2}}{\sqrt{2}}\Big[a(\tilde{\mathrm{d}}_{i\alpha})(1-\gamma_5)+b(\tilde{\mathrm{d}}_{i\alpha})(1+\gamma_5)\Big]$$

Figure A.5: Feynman rules for $\mathrm{q}\tilde{\mathrm{q}}\tilde{\mathrm{g}}$. The colours of the gluino, quark and squark are a, c_1 and c_2, respectively.

Coefficient	Coupling	Coefficient	Coupling
$a(\tilde{\mathrm{u}}_{i\alpha})$	$-Q^{2i}_{2\alpha}$	$b(\tilde{\mathrm{u}}_{i\alpha})$	$Q^{2i}_{1\alpha}$
$a(\tilde{\mathrm{d}}_{i\alpha})$	$-Q^{2i-1}_{2\alpha}$	$b(\tilde{\mathrm{d}}_{i\alpha})$	$Q^{2i-1}_{1\alpha}$

Table A.3: Couplings for the gluino Feynman rules.

We can obtain the Feynman rules from Eqn. A.43, which gives the Feynman rules shown in Fig. A.3, where the couplings are given in Table A.2. The Feynman rules for the interactions of leptons and sleptons with the neutralinos, Fig. A.4, can be obtained by taking the Feynman rules for the squarks and replacing the relevant masses and mixings, as in Eqn. A.41.

A.4 Gluino Interactions with the Squarks

The Lagrangian for the interaction of the gluino and the squarks in given in Eqn. C.89 of [18],

$$\mathcal{L}_{\mathrm{q\tilde{q}\tilde{g}}} = -\sqrt{2} g_s \mathbf{t}^a_{c_1 c_2} \left[\bar{\tilde{g}}_a P_L q^{c_2} \tilde{q}^{c_1 *}_L + \bar{q}^{c_1} P_R \tilde{g}_a \tilde{q}^{c_2}_L - \bar{\tilde{g}}_a P_R q^{c_2} \tilde{q}^{c_1 *}_R - \bar{q}^{c_1} P_L \tilde{g}_a \tilde{q}^{c_2}_R \right], \tag{A.44}$$

where for simplicity we have only considered one flavour of quark. Again we can replace the left/right eigenstates with the mass eigenstates giving

$$\mathcal{L}_{\mathrm{q\tilde{q}\tilde{g}}} = -\sqrt{2} g_s \mathbf{t}^a_{c_1 c_2} \left[\bar{\tilde{g}}_a P_L q^{c_2} Q^i_{1\alpha} \tilde{q}^{c_1 *}_{i\alpha} + \bar{q}^{c_1} P_R \tilde{g}_a Q^i_{1\alpha} \tilde{q}^{c_2}_{i\alpha} - \bar{\tilde{g}}_a P_R q^{c_2} Q^i_{2\alpha} \tilde{q}^{c_1 *}_{i\alpha} - \bar{q}^{c_1} P_L \tilde{g}_a Q^i_{2\alpha} \tilde{q}^{c_2}_{i\alpha} \right] \tag{A.45}$$

The Feynman rules for this process are given in Fig. A.5, and the relevant couplings are in Table A.3.

A.5 Gauge Boson Interactions with the Sfermions and Fermions

We also need the Feynman rules for the interactions of squark–antisquark pairs with the gauge bosons of the MSSM. The relevant Lagrangian is given in Eqn. C.66 of [18],

$$\begin{aligned}
\mathcal{L}_{\tilde{\mathrm{q}}\bar{\mathrm{q}}\mathrm{V}} \;=\; & \frac{-ig}{\sqrt{2}} \left[W^+_\mu \tilde{u}^*_L \overleftrightarrow{\partial^\mu} \tilde{d}_L + W^-_\mu \tilde{d}^*_L \overleftrightarrow{\partial^\mu} \tilde{u}_L \right] - \frac{ig}{\cos\theta_W} Z_\mu \left[\left(\frac{1}{2} - e_u \sin^2\theta_W \right) \tilde{u}^*_L \overleftrightarrow{\partial^\mu} \tilde{u}_L \right. \\
& \left. - \left(\frac{1}{2} + e_d \sin^2\theta_W \right) \tilde{d}^*_L \overleftrightarrow{\partial^\mu} \tilde{d}_L - e_u \sin^2\theta_W \tilde{u}^*_R \overleftrightarrow{\partial^\mu} \tilde{u}_R - e_d \sin^2\theta_W \tilde{d}^*_R \overleftrightarrow{\partial^\mu} \tilde{d}_R \right] \\
& - ieA_\mu \left[e_u \left(\tilde{u}^*_L \overleftrightarrow{\partial^\mu} \tilde{u}_L + \tilde{u}^*_R \overleftrightarrow{\partial^\mu} \tilde{u}_R \right) + e_d \left(\tilde{d}^*_L \overleftrightarrow{\partial^\mu} \tilde{d}_L + \tilde{d}^*_R \overleftrightarrow{\partial^\mu} \tilde{d}_R \right) \right].
\end{aligned} \tag{A.46}$$

Squark couplings			
$Z_{u_i}^{\alpha\beta}$	$\frac{1}{2}\left(-Q_{1\alpha}^{2i}Q_{1\beta}^{2i}+2e_u\sin^2\theta_W\delta_{\alpha\beta}\right)$	$Z_{d_i}^{\alpha\beta}$	$\frac{1}{2}\left(Q_{1\alpha}^{2i-1}Q_{1\beta}^{2i-1}+2e_d\sin^2\theta_W\delta_{\alpha\beta}\right)$
Slepton couplings			
$Z_{\nu_i}^{\alpha\beta}$	$-\frac{1}{2}\delta_{\alpha=1,\beta=1}$	$Z_{\ell_i}^{\alpha\beta}$	$\frac{1}{2}\left(L_{1\alpha}^{2i-1}L_{1\beta}^{2i-1}-2\sin^2\theta_W\delta_{\alpha\beta}\right)$
Quark couplings			
Z_{u_L}	$-\frac{1}{4}\left(1-2e_u\sin^2\theta_W\right)$	Z_{d_L}	$\frac{1}{4}\left(1+2e_d\sin^2\theta_W\right)$
Z_{u_R}	$\frac{1}{2}e_u\sin^2\theta_W$	Z_{d_R}	$\frac{1}{2}e_d\sin^2\theta_W$
Lepton couplings			
Z_{ν_L}	$-\frac{1}{4}$	Z_{ℓ_L}	$\frac{1}{4}\left(1-2\sin^2\theta_W\right)$
Z_{ν_R}	0	Z_{ℓ_R}	$-\frac{1}{2}\sin^2\theta_W$

Table A.4: Couplings of squarks, sleptons, quarks and leptons to the Z^0.

This can be expressed in terms of the mass eigenstates giving,

$$\begin{aligned}\mathcal{L}_{\tilde{\mathrm{q}}\tilde{\mathrm{q}}\mathrm{V}} &= -\frac{ig}{\sqrt{2}}\left[Q_{1\alpha}^{2i}Q_{1\beta}^{2i-1}W_\mu^+\tilde{u}_{i\alpha}^*\overleftrightarrow{\partial^\mu}\,\tilde{d}_{i\beta}+Q_{1\alpha}^{2i-1}Q_{1\beta}^{2i}W_\mu^-\tilde{d}_{i\alpha}^*\overleftrightarrow{\partial^\mu}\,\tilde{u}_{i\beta}\right]\\ &\quad -\frac{ig}{\cos\theta_W}Z_\mu\left[-e_u\sin^2\theta_W\tilde{u}_{i\alpha}^*\overleftrightarrow{\partial^\mu}\,\tilde{u}_{i\alpha}-e_d\sin^2\theta_W\tilde{d}_{i\alpha}^*\overleftrightarrow{\partial^\mu}\,\tilde{d}_{i\alpha}+\frac{1}{2}Q_{1\alpha}^{2i}Q_{1\beta}^{2i}\tilde{u}_{i\alpha}^*\overleftrightarrow{\partial^\mu}\,\tilde{u}_{i\beta}\right.\\ &\quad \left.-\frac{1}{2}Q_{1\alpha}^{2i-1}Q_{1\beta}^{2i-1}\tilde{d}_{i\alpha}^*\overleftrightarrow{\partial^\mu}\,\tilde{d}_{i\beta}\right]-ieA_\mu\left[e_u\tilde{u}_{i\alpha}^*\overleftrightarrow{\partial^\mu}\,\tilde{u}_{i\alpha}+e_d\tilde{d}_{i\alpha}^*\overleftrightarrow{\partial^\mu}\,\tilde{d}_{i\alpha}\right], \qquad \text{(A.47)}\end{aligned}$$

where there is now an implied summation over the squark mass eigenstates. Hence we obtain the Feynman rules in Fig. A.6, where the couplings for the $Z\tilde{\mathrm{q}}\tilde{\mathrm{q}}^*$ vertex are given in Table A.4. The Feynman rules for the interactions of the sleptons with the gauge bosons can be obtained by replacing the relevant couplings and are given in Fig. A.7. The couplings for these processes are also given in Table A.4. For completeness, we include the Lagrangian for the interactions of the quarks with the gauge bosons which is given in Eqn. C.61 of [18],

$$\begin{aligned}\mathcal{L}_{\mathrm{qqV}} &= \frac{-g}{\sqrt{2}}\left[W_\mu^+\bar{u}\gamma^\mu P_L d+W_\mu^-\bar{d}\gamma^\mu P_L u\right]-eA_\mu\left(e_u\bar{u}\gamma^\mu u+e_d\bar{d}\gamma^\mu d\right)\\ &\quad -\frac{g}{\cos\theta_W}Z_\mu\left\{\bar{u}\gamma^\mu\left[\left(\frac{1}{2}-e_u\sin^2\theta_W\right)P_L-e_u\sin^2\theta_W P_R\right]u\right.\\ &\quad \left.-\bar{d}\gamma^\mu\left[\left(\frac{1}{2}+e_d\sin^2\theta_W\right)P_L+e_d\sin^2\theta_W P_R\right]d\right\}. \qquad \text{(A.48)}\end{aligned}$$

The relevant Feynman rules for both the quarks and the leptons, which can be obtained by replacing the relevant couplings, are given in Fig. A.8. We have neglected the effect of quark mixing in these Feynman rules.

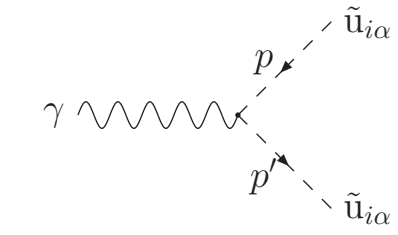

$$-iee_u(p+p')^\mu$$

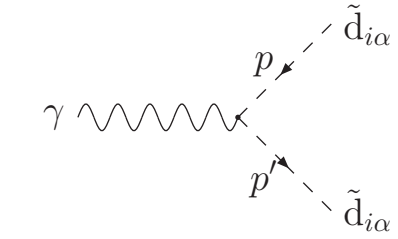

$$-iee_d(p+p')^\mu$$

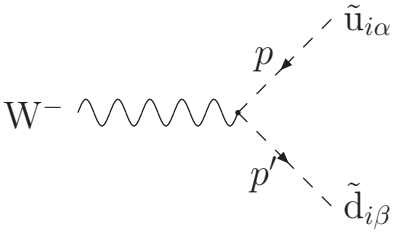

$$\frac{-ig}{\sqrt{2}} Q_{1\alpha}^{2i} Q_{1\beta}^{2i-1} (p+p')^\mu$$

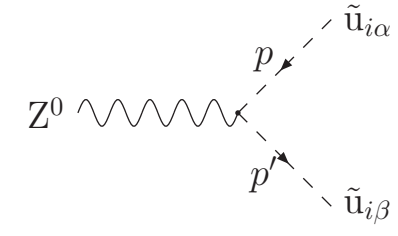

$$\frac{ig}{\cos\theta_W} Z_{u_i}^{\alpha\beta} (p+p')^\mu$$

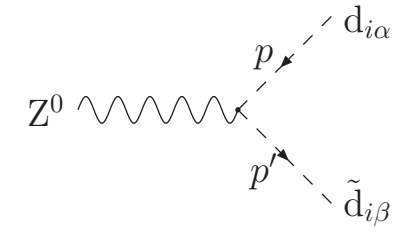

$$\frac{ig}{\cos\theta_W} Z_{d_i}^{\alpha\beta} (p+p')^\mu$$

Figure A.6: Feynman rules for the interactions of the squarks and the gauge bosons. The couplings of the W and Z to the squarks are given in Table A.4. The momenta of the outgoing squarks, p and p', should be taken in the direction of the arrows.

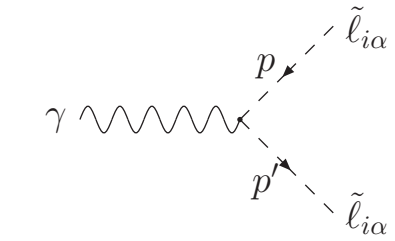

$$ie(p+p')^\mu$$

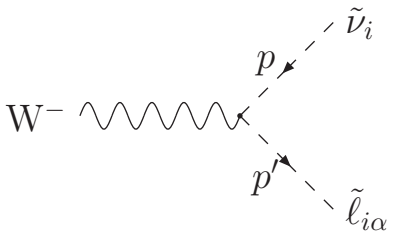

$$\frac{-ig}{\sqrt{2}} L_{1\alpha}^{2i-1} (p+p')^\mu$$

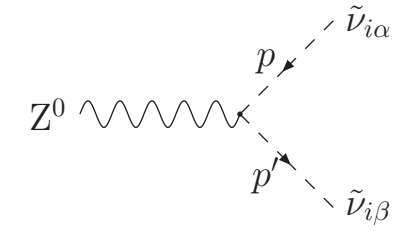

$$\frac{ig}{\cos\theta_W} Z_{\nu_i}^{\alpha\beta} (p+p')^\mu$$

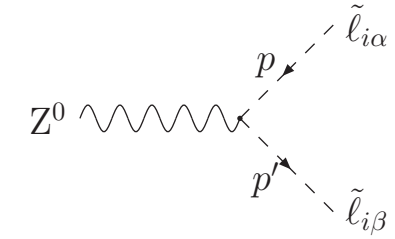

$$\frac{ig}{\cos\theta_W} Z_{e_i}^{\alpha\beta} (p+p')^\mu$$

Figure A.7: Feynman rules for the interactions of the sleptons and the gauge bosons. The couplings of the sleptons to the gauge bosons are given in Table A.4 and the momenta of the outgoing sleptons, p and p', should be taken in the directions of the arrows.

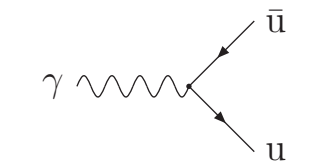

$$-iee_u\gamma^\mu$$

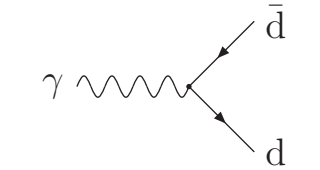

$$-iee_d\gamma^\mu$$

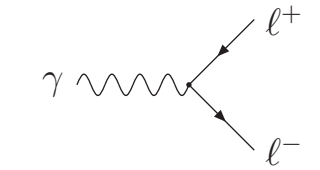

$$ie\gamma^\mu$$

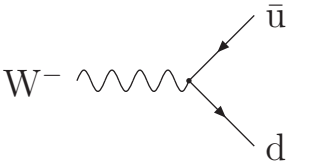

$$\frac{-ig}{2\sqrt{2}}\gamma^\mu(1-\gamma_5)$$

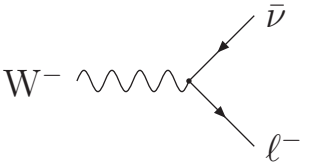

$$\frac{-ig}{2\sqrt{2}}\gamma^\mu(1-\gamma_5)$$

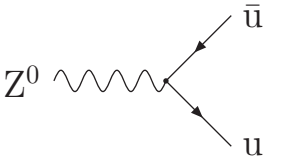

$$\frac{ig}{\cos\theta_W}\gamma^\mu\left[Z_{u_L}(1-\gamma_5)+Z_{u_R}(1+\gamma_5)\right]$$

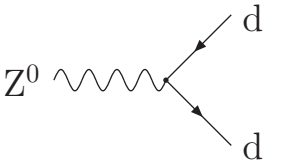

$$\frac{ig}{\cos\theta_W}\gamma^\mu\left[Z_{d_L}(1-\gamma_5)+Z_{d_R}(1+\gamma_5)\right]$$

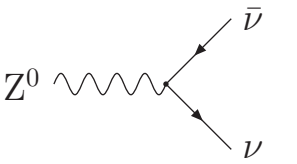

$$\frac{ig}{\cos\theta_W}\gamma^\mu Z_{\nu_L}(1-\gamma_5)$$

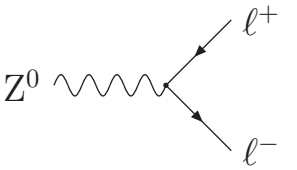

$$\frac{ig}{\cos\theta_W}\gamma^\mu\left[Z_{\ell_L}(1-\gamma_5)+Z_{\ell_R}(1+\gamma_5)\right]$$

Figure A.8: Feynman rules for the interactions of the quarks and the gauge bosons.

A.6 Higgs Boson Interactions with the Sfermions and Fermions

The Lagrangian for the interaction of the Higgs bosons of the MSSM with the sfermions is given in [24]. This Lagrangian is given below without left/right sfermion mixing,[6] this is taken from Eqn. 4.19 of [24],

$$
\begin{aligned}
\mathcal{L}_{\mathrm{H}\tilde{\mathrm{q}}\tilde{\mathrm{q}}^*} = & -\frac{gM_{\mathrm{Z}}}{\cos\theta_W}\left[H_1^0\cos(\alpha+\beta) - H_2^0\sin(\alpha+\beta)\right] \\
& \left[\left(\frac{1}{2} - e_u\sin^2\theta_W\right)\tilde{u}_L^*\tilde{u}_L + e_u\sin^2\theta_W\tilde{u}_R^*\tilde{u}_R\right. \\
& \left. - \left(\frac{1}{2} + e_d\sin^2\theta_W\right)\tilde{d}_L^*\tilde{d}_L + e_d\sin^2\theta_W\tilde{d}_R^*\tilde{d}_R\right] \\
& - \frac{gm_d^2}{M_{\mathrm{W}}\cos\beta}\left(\tilde{d}_L^*\tilde{d}_L + \tilde{d}_R^*\tilde{d}_R\right)\left(H_1^0\cos\alpha - H_2^0\sin\alpha\right) \\
& - \frac{gm_u^2}{M_{\mathrm{W}}\sin\beta}\left(\tilde{u}_L^*\tilde{u}_L + \tilde{u}_R^*\tilde{u}_R\right)\left(H_1^0\sin\alpha + H_2^0\cos\alpha\right) \\
& - \frac{gm_d}{2M_{\mathrm{W}}\cos\beta}\left(\tilde{d}_R^*\tilde{d}_L + \tilde{d}_L^*\tilde{d}_R\right)\left[\left(A_d\cos\alpha - \mu\sin\alpha\right)H_1^0 - \left(\mu\cos\alpha + A_d\sin\alpha\right)H_2^0\right] \\
& - \frac{gm_u}{2M_{\mathrm{W}}\sin\beta}\left(\tilde{u}_R^*\tilde{u}_L + \tilde{u}_L^*\tilde{u}_R\right)\left[\left(A_u\sin\alpha - \mu\cos\alpha\right)H_1^0 + \left(\mu\sin\alpha + A_u\cos\alpha\right)H_2^0\right] \\
& - \frac{igm_d}{2M_{\mathrm{W}}}\left(A_d\tan\beta + \mu\right)\left(\tilde{d}_R^*\tilde{d}_L - \tilde{d}_L^*\tilde{d}_R\right)H_3^0 \\
& - \frac{igm_u}{2M_{\mathrm{W}}}\left(A_u\cot\beta + \mu\right)\left(\tilde{u}_R^*\tilde{u}_L - \tilde{u}_L^*\tilde{u}_R\right)H_3^0 \\
& + \frac{g}{\sqrt{2}M_{\mathrm{W}}}\left(m_d^2\tan\beta + m_u^2\cot\beta - M_{\mathrm{W}}^2\sin 2\beta\right)\left(H^+\tilde{u}_L^*\tilde{d}_L + H^-\tilde{d}_L^*\tilde{u}_L\right) \\
& + \frac{gm_um_d\left(\cot\beta + \tan\beta\right)}{\sqrt{2}M_{\mathrm{W}}}\left(H^+\tilde{u}_R^*\tilde{d}_R + H^-\tilde{d}_R^*\tilde{u}_R\right) \\
& + \frac{gm_d}{\sqrt{2}M_{\mathrm{W}}}\left(A_d\tan\beta + \mu\right)\left(H^+\tilde{u}_L^*\tilde{d}_R + H^-\tilde{d}_R^*\tilde{u}_L\right) \\
& + \frac{gm_u}{\sqrt{2}M_{\mathrm{W}}}\left(A_d\tan\beta + \mu\right)\left(H^+\tilde{u}_R^*\tilde{d}_L + H^-\tilde{d}_L^*\tilde{u}_R\right),
\end{aligned}
\tag{A.49}
$$

where α is the mixing angle for the CP-even Higgs bosons, H_0^2 is the lighter CP-even Higgs boson field, H_0^1 is the heavier CP-even Higgs boson field, H_0^3 is the pseudo-scalar Higgs boson field and all the other terms have been defined previously. As before, this

[6] We have neglected the terms arising from the presence of an additional Higgs singlet.

Lagrangian is only for one generation of squarks.

We can express this Lagrangian in terms of the squark mass eigenstates giving

$$
\begin{aligned}
\mathcal{L}_{\mathrm{H\tilde{q}\tilde{q}^*}} &= -\frac{gM_{\mathrm{Z}}}{\cos\theta_W}\left[H_1^0\cos(\alpha+\beta)-H_2^0\sin(\alpha+\beta)\right] \\
&\quad\Bigg[\left\{\left(\frac{1}{2}-e_u\sin^2\theta_W\right)Q_{1\alpha}^{2i}Q_{1\beta}^{2i}+e_u\sin^2\theta_W Q_{2\alpha}^{2i}Q_{2\beta}^{2i}\right\}\tilde{u}_{i\alpha}^*\tilde{u}_{i\beta} \\
&\quad-\left\{\left(\frac{1}{2}+e_d\sin^2\theta_W\right)Q_{1\alpha}^{2i-1}Q_{1\beta}^{2i-1}-e_d\sin^2\theta_W Q_{2\alpha}^{2i-1}Q_{2\beta}^{2i-1}\right\}\tilde{d}_{i\alpha}^*\tilde{d}_{i\beta}\Bigg] \\
&\quad-\frac{gm_d^2}{M_{\mathrm{W}}\cos\beta}\left(Q_{1\alpha}^{2i-1}Q_{1\beta}^{2i-1}+Q_{2\alpha}^{2i-1}Q_{2\beta}^{2i-1}\right)\left(H_1^0\cos\alpha-H_2^0\sin\alpha\right)\tilde{d}_{i\alpha}^*\tilde{d}_{i\beta} \\
&\quad-\frac{gm_u^2}{M_{\mathrm{W}}\sin\beta}\left(Q_{1\alpha}^{2i}Q_{1\beta}^{2i}+Q_{2\alpha}^{2i}Q_{2\beta}^{2i}\right)\left(H_1^0\sin\alpha+H_2^0\cos\alpha\right)\tilde{u}_{i\alpha}^*\tilde{u}_{i\beta} \\
&\quad-\frac{gm_d}{2M_{\mathrm{W}}\cos\beta}\left(Q_{2\alpha}^{2i-1}Q_{1\beta}^{2i-1}+Q_{1\alpha}^{2i-1}Q_{2\beta}^{2i-1}\right) \\
&\quad\left[\left(A_{d_i}\cos\alpha-\mu\sin\alpha\right)H_1^0-\left(\mu\cos\alpha+A_{d_i}\sin\alpha\right)H_2^0\right]\tilde{d}_{i\alpha}^*\tilde{d}_{i\beta} \\
&\quad-\frac{gm_u}{2M_{\mathrm{W}}\sin\beta}\left(Q_{2\alpha}^{2i}Q_{1\beta}^{2i}+Q_{1\alpha}^{2i}Q_{2\beta}^{2i}\right) \\
&\quad\left[\left(A_{u_i}\sin\alpha-\mu\cos\alpha\right)H_1^0+\left(\mu\sin\alpha+A_{u_i}\cos\alpha\right)H_2^0\right]\tilde{u}_{i\alpha}^*\tilde{u}_{i\alpha} \\
&\quad-\frac{igm_d}{2M_{\mathrm{W}}}\left(A_{d_i}\tan\beta+\mu\right)\left(Q_{2\alpha}^{2i-1}Q_{1\beta}^{2i-1}-Q_{1\alpha}^{2i-1}Q_{2\beta}^{2i-1}\right)H_3^0\tilde{d}_{i\alpha}^*\tilde{d}_{i\beta} \\
&\quad-\frac{igm_u}{2M_{\mathrm{W}}}\left(A_{u_i}\cot\beta+\mu\right)\left(Q_{2\alpha}^{2i}Q_{1\beta}^{2i}-Q_{1\alpha}^{2i}Q_{2\beta}^{2i}\right)H_3^0\tilde{u}_{i\alpha}^*\tilde{u}_{i\beta} \\
&\quad+\frac{g}{\sqrt{2}M_{\mathrm{W}}}\left(m_d^2\tan\beta+m_u^2\cot\beta-M_{\mathrm{W}}^2\sin 2\beta\right) \\
&\quad\left(H^+Q_{1\alpha}^{2i}Q_{1\beta}^{2i-1}\tilde{u}_{i\alpha}^*\tilde{d}_{i\beta}+H^-Q_{1\alpha}^{2i-1}Q_{1\beta}^{2i}\tilde{d}_{i\alpha}^*\tilde{u}_{i\beta}\right) \\
&\quad+\frac{gm_um_d\left(\cot\beta+\tan\beta\right)}{\sqrt{2}M_{\mathrm{W}}}\left(H^+Q_{2\alpha}^{2i}Q_{2\beta}^{2i-1}\tilde{u}_{i\alpha}^*\tilde{d}_{i\beta}+H^-Q_{2\alpha}^{2i-1}Q_{2\beta}^{2i}\tilde{d}_{i\alpha}^*\tilde{u}_{i\beta}\right) \\
&\quad+\frac{gm_d}{\sqrt{2}M_{\mathrm{W}}}\left(A_{d_i}\tan\beta+\mu\right)\left(H^+Q_{1\alpha}^{2i}Q_{2\beta}^{2i-1}\tilde{u}_{i\alpha}^*\tilde{d}_{i\beta}+H^-Q_{2\alpha}^{2i-1}Q_{1\beta}^{2i}\tilde{d}_{i\alpha}^*\tilde{u}_{i\beta}\right) \\
&\quad+\frac{gm_u}{\sqrt{2}M_{\mathrm{W}}}\left(A_{d_i}\tan\beta+\mu\right)\left(H^+Q_{2\alpha}^{2i}Q_{1\beta}^{2i-1}\tilde{u}_{i\alpha}^*\tilde{d}_{i\beta}+H^-Q_{1\alpha}^{2i-1}Q_{2\beta}^{2i}\tilde{d}_{i\alpha}^*\tilde{u}_{i\beta}\right),
\end{aligned}
\tag{A.50}
$$

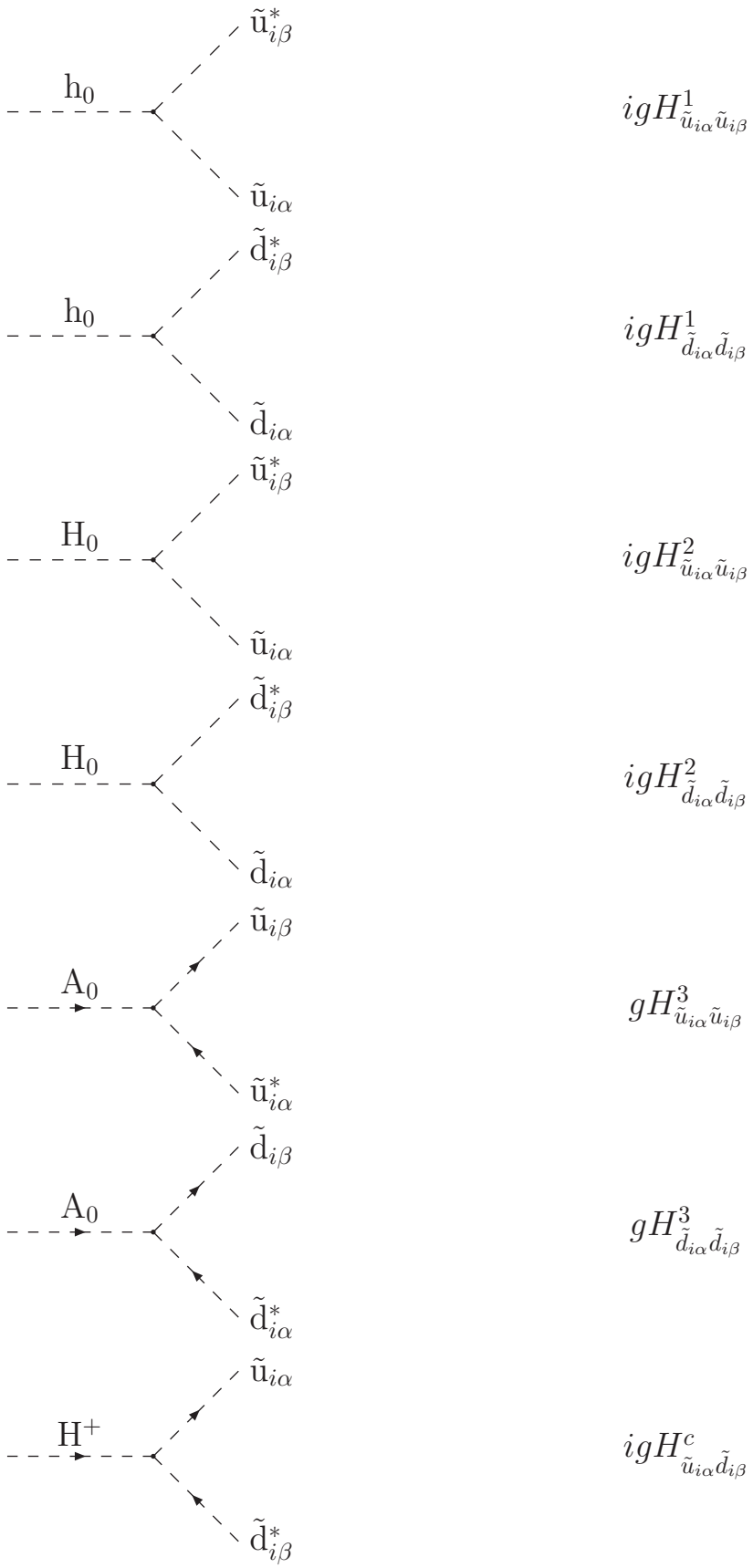

Figure A.9: Feynman rules for the interactions of the Higgs bosons and the squarks. The sign of the $A_0\tilde{q}_{i\alpha}\tilde{q}_{i\beta}$ vertex changes under a change of sign of the squark momenta. The couplings of the Higgs bosons to the squarks are given in Table. A.5.

Coefficient	Coupling
$H^1_{\tilde{d}_{i\alpha}\tilde{d}_{i\beta}}$	$-\frac{M_{\rm Z}\sin(\alpha+\beta)}{\cos\theta_W}\left[Q^{2i-1}_{1\alpha}Q^{2i-1}_{1\beta}(\frac{1}{2}+e_d\sin^2\theta_W)-e_d\sin^2\theta_W Q^{2i-1}_{2\alpha}Q^{2i-1}_{2\beta}\right]$ $+\frac{m^2_{d_i}\sin\alpha}{M_{\rm W}\cos\beta}\left[Q^{2i-1}_{1\alpha}Q^{2i-1}_{1\beta}+Q^{2i-1}_{2\alpha}Q^{2i-1}_{2\beta}\right]$ $+\frac{m_{d_i}}{2M_{\rm W}\cos\beta}\left(A_{d_i}\sin\alpha+\mu\cos\alpha\right)\left[Q^{2i-1}_{2\alpha}Q^{2i-1}_{1\beta}+Q^{2i-1}_{1\alpha}Q^{2i-1}_{2\beta}\right]$
$H^1_{\tilde{u}_{i\alpha}\tilde{u}_{i\beta}}$	$\frac{M_{\rm Z}\sin(\alpha+\beta)}{\cos\theta_W}\left[Q^{2i}_{1\alpha}Q^{2i}_{1\beta}(\frac{1}{2}-e_u\sin^2\theta_W)+e_u\sin^2\theta_W Q^{2i}_{2\alpha}Q^{2i}_{2\beta}\right]$ $-\frac{m^2_{u_i}\cos\alpha}{M_{\rm W}\sin\beta}\left[Q^{2i}_{1\alpha}Q^{2i}_{1\beta}+Q^{2i}_{2\alpha}Q^{2i}_{2\beta}\right]$ $-\frac{m_{u_i}}{2M_{\rm W}\sin\beta}\left(A_{u_i}\cos\alpha+\mu\sin\alpha\right)\left[Q^{2i}_{2\alpha}Q^{2i}_{1\beta}+Q^{2i}_{1\alpha}Q^{2i}_{2\beta}\right]$
$H^2_{\tilde{d}_{i\alpha}\tilde{d}_{i\beta}}$	$\frac{M_{\rm Z}\cos(\alpha+\beta)}{\cos\theta_W}\left[Q^{2i-1}_{1\alpha}Q^{2i-1}_{1\beta}(\frac{1}{2}+e_d\sin^2\theta_W)-e_d\sin^2\theta_W Q^{2i-1}_{2\alpha}Q^{2i-1}_{2\beta}\right]$ $-\frac{m^2_{d_i}\cos\alpha}{M_{\rm W}\cos\beta}\left[Q^{2i-1}_{1\alpha}Q^{2i-1}_{1\beta}+Q^{2i-1}_{2\alpha}Q^{2i-1}_{2\beta}\right]$ $+\frac{m_{d_i}}{2M_{\rm W}\cos\beta}\left(\mu\sin\alpha-A_{d_i}\cos\alpha\right)\left[Q^{2i-1}_{2\alpha}Q^{2i-1}_{1\beta}+Q^{2i-1}_{1\alpha}Q^{2i-1}_{2\beta}\right]$
$H^2_{\tilde{u}_{i\alpha}\tilde{u}_{i\beta}}$	$-\frac{M_{\rm Z}\cos(\alpha+\beta)}{\cos\theta_W}\left[Q^{2i}_{1\alpha}Q^{2i}_{1\beta}(\frac{1}{2}-e_u\sin^2\theta_W)+e_u\sin^2\theta_W Q^{2i}_{2\alpha}Q^{2i}_{2\beta}\right]$ $-\frac{m^2_{u_i}\sin\alpha}{M_{\rm W}\sin\beta}\left[Q^{2i}_{1\alpha}Q^{2i}_{1\beta}+Q^{2i}_{2\alpha}Q^{2i}_{2\beta}\right]$ $-\frac{m_{u_i}}{2M_{\rm W}\sin\beta}\left(A_{u_i}\sin\alpha-\mu\cos\alpha\right)\left[Q^{2i}_{2\alpha}Q^{2i}_{1\beta}+Q^{2i}_{1\alpha}Q^{2i}_{2\beta}\right]$
$H^3_{\tilde{d}_{i\alpha}\tilde{d}_{i\beta}}$	$\delta_{\alpha\neq\beta}\frac{m_{d_i}}{2M_{\rm W}}\left(A_{d_i}\tan\beta+\mu\right)$
$H^3_{\tilde{u}_{i\alpha}\tilde{u}_{i\beta}}$	$\delta_{\alpha\neq\beta}\frac{m_{u_i}}{2M_{\rm W}}\left(A_{u_i}\cot\beta+\mu\right)$
$H^c_{\tilde{u}_{i\alpha}\tilde{d}_{i\beta}}$	$\frac{1}{\sqrt{2}M_{\rm W}}\left[Q^{2i}_{1\alpha}Q^{2i-1}_{1\beta}\left(m^2_{d_i}\tan\beta+m^2_{u_i}\cot\beta-M^2_{\rm W}\sin 2\beta\right)\right.$ $+Q^{2i}_{2\alpha}Q^{2i-1}_{2\beta}m_{u_i}m_{d_i}\left(\cot\beta+\tan\beta\right)$ $\left.+Q^{2i}_{1\alpha}Q^{2i-1}_{2\beta}m_{d_i}\left(A_{d_i}\tan\beta+\mu\right)+Q^{2i}_{2\alpha}Q^{2i-1}_{1\beta}m_{u_i}\left(A_{u_i}\cot\beta+\mu\right)\right]$

Table A.5: Higgs couplings to the squarks.

Coefficient	Coupling
$H^1_{\tilde{\ell}_{i\alpha}\tilde{\ell}_{i\beta}}$	$-\frac{M_{\rm Z}\sin(\alpha+\beta)}{\cos\theta_W}\left[L^{2i-1}_{1\alpha}L^{2i-1}_{1\beta}(\frac{1}{2}-\sin^2\theta_W)+\sin^2\theta_W L^{2i-1}_{2\alpha}L^{2i-1}_{2\beta}\right]$ $+\frac{m^2_{\ell_i}\sin\alpha}{M_{\rm W}\cos\beta}\left[L^{2i-1}_{1\alpha}L^{2i-1}_{1\beta}+L^{2i-1}_{2\alpha}L^{2i-1}_{2\beta}\right]$ $+\frac{m_{\ell_i}}{2M_{\rm W}\cos\beta}\left(\mu\cos\alpha+A_{e_i}\sin\alpha\right)\left[L^{2i-1}_{2\alpha}L^{2i-1}_{1\beta}+L^{2i-1}_{1\alpha}L^{2i-1}_{2\beta}\right]$
$H^1_{\tilde{\nu}_i\tilde{\nu}_i}$	$\frac{M_{\rm Z}\sin(\alpha+\beta)}{2\cos\theta_W}$
$H^2_{\tilde{\ell}_{i\alpha}\tilde{\ell}_{i\beta}}$	$\frac{M_{\rm Z}\cos(\alpha+\beta)}{\cos\theta_W}\left[L^{2i-1}_{1\alpha}L^{2i-1}_{1\beta}(\frac{1}{2}-\sin^2\theta_W)+\sin^2\theta_W L^{2i-1}_{2\alpha}L^{2i-1}_{2\beta}\right]$ $-\frac{m^2_{\ell_i}\cos\alpha}{M_{\rm W}\cos\beta}\left[L^{2i-1}_{1\alpha}L^{2i-1}_{1\beta}+L^{2i-1}_{2\alpha}L^{2i-1}_{2\beta}\right]$ $+\frac{m_{\ell_i}}{2M_{\rm W}\cos\beta}\left(\mu\sin\alpha-A_{e_i}\cos\alpha\right)\left[L^{2i-1}_{2\alpha}L^{2i-1}_{1\beta}+L^{2i-1}_{1\alpha}L^{2i-1}_{2\beta}\right]$
$H^2_{\tilde{\nu}_i\tilde{\nu}_i}$	$-\frac{M_{\rm Z}\cos(\alpha+\beta)}{2\cos\theta_W}$
$H^3_{\tilde{\ell}_{i\alpha}\tilde{\ell}_{i\beta}}$	$\delta_{\alpha\neq\beta}\frac{m_{\ell_i}}{2M_{\rm W}}\left(A_{e_i}\tan\beta+\mu\right)$
$H^c_{\tilde{\nu}\tilde{\ell}_{i\alpha}}$	$\frac{1}{\sqrt{2}M_{\rm W}}\left[L^{2i-1}_{1\alpha}\left(m^2_{\ell_i}\tan\beta-M^2_{\rm W}\sin 2\beta\right)+L^{2i-1}_{2\alpha}m_{\ell_i}\left(A_{e_i}\tan\beta+\mu\right)\right]$

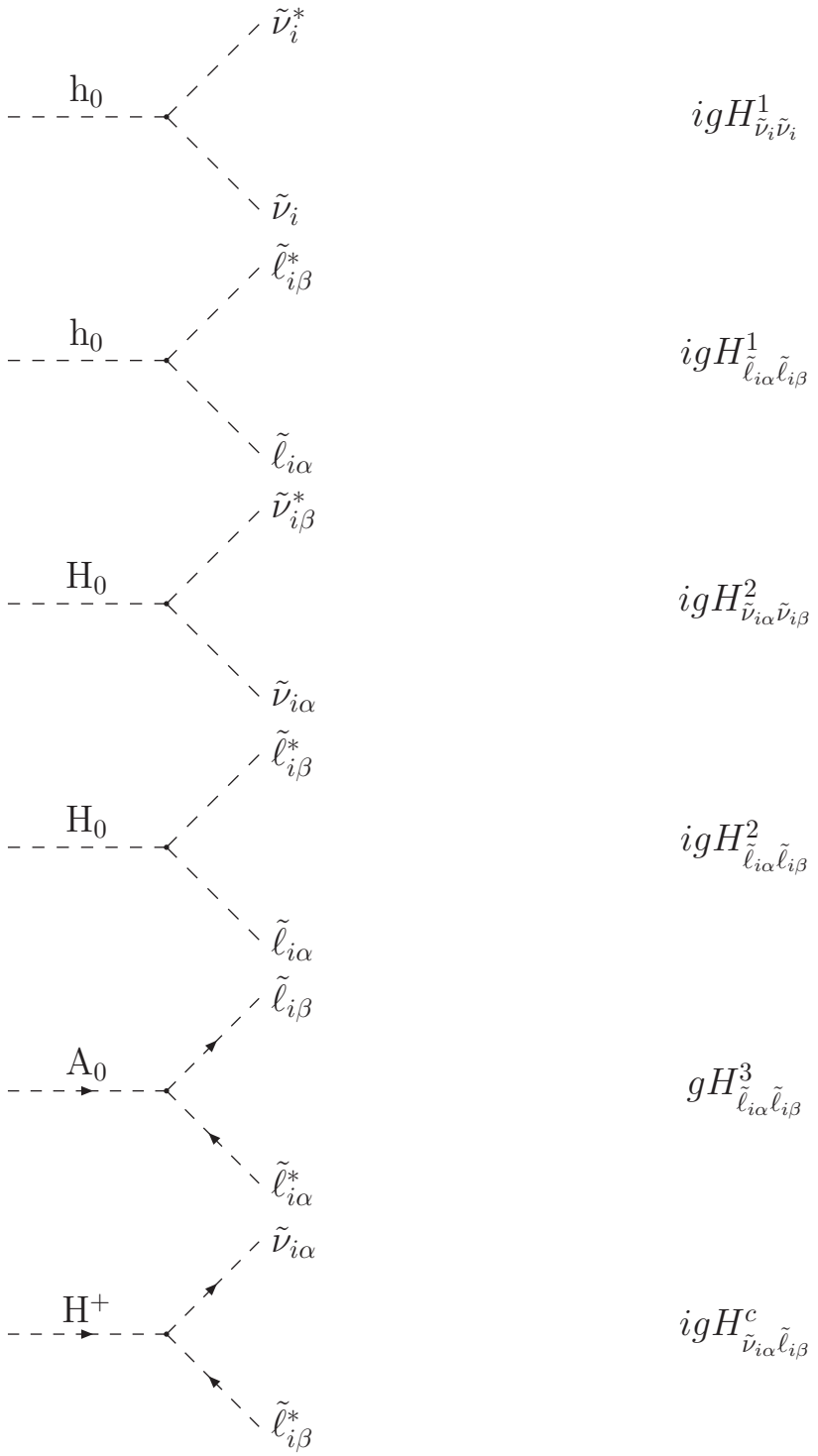

Figure A.10: Feynman rules for the interactions of the Higgs bosons and the sleptons. The sign of the $A_0\tilde{\ell}_{i\alpha}\tilde{\ell}_{i\beta}$ vertex changes under a change of sign of the slepton momenta. The couplings of the Higgs bosons to the sleptons are given in Table. A.6.

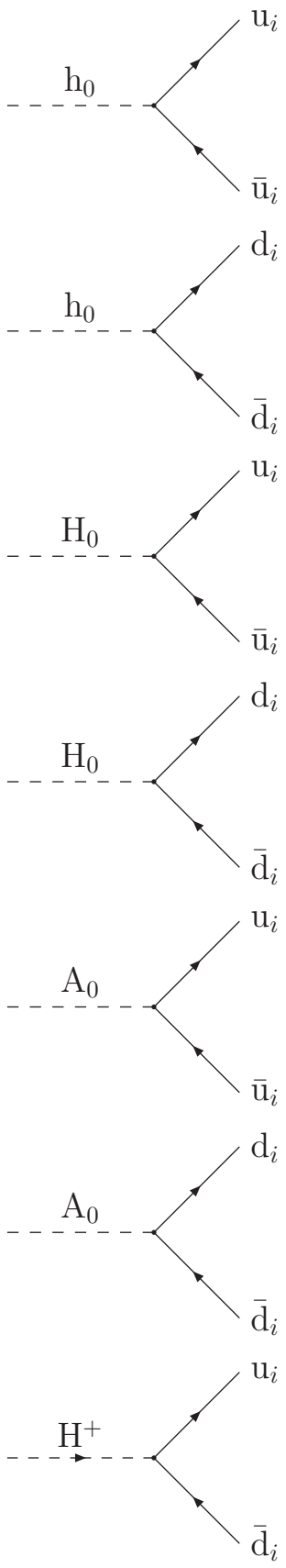

$$-igU_i^1$$

$$-igD_i^1$$

$$-igU_i^2$$

$$-igD_i^2$$

$$-gU_i^3\gamma_5$$

$$-gD_i^3\gamma_5$$

$$ig\left[D_i^c\left(1+\gamma_5\right)+U_i^c\left(1-\gamma_5\right)\right]$$

Figure A.11: Feynman rules for the interactions of the Higgs bosons and the quarks. The couplings of the Higgs bosons to the quarks are given in Table. A.7.

U_i^1	$\dfrac{m_{u_i}\cos\alpha}{2M_{\rm W}\sin\beta}$	D_i^1	$-\dfrac{m_{d_i}\sin\alpha}{2M_{\rm W}\cos\beta}$
U_i^2	$\dfrac{m_{u_i}\sin\alpha}{2M_{\rm W}\sin\beta}$	D_i^2	$\dfrac{m_{d_i}\cos\alpha}{2M_{\rm W}\cos\beta}$
U_i^3	$\dfrac{m_{u_i}\cot\beta}{2M_{\rm W}}$	D_i^3	$\dfrac{m_{d_i}\tan\beta}{2M_{\rm W}}$
U_i^c	$\dfrac{m_{u_i}\cot\beta}{2\sqrt{2}M_{\rm W}}$	D_i^c	$\dfrac{m_{d_i}\tan\beta}{2\sqrt{2}M_{\rm W}}$

Table A.7: Higgs couplings to the quarks.

where there is an implied summation over the squark mass eigenstates. The α in the sines and cosines is the mixing angle for the CP-even Higgs bosons, whereas that appearing in the subscripts is the mass eigenstate of the squark. We can derive the Feynman rules for the interactions of the Higgs bosons with the squarks, Fig. A.9, from this Lagrangian. The relevant couplings are given in Table A.5. In the Feynman rules we have used the notation h_0 for the lighter scalar Higgs, H_0 for the heavier scalar Higgs and A_0 for the pseudo-scalar Higgs. These correspond to H_0^2, H_0^1 and H_0^3 respectively in the notation used above. The Feynman rules for the interactions of the sleptons can be derived by replacing the relevant couplings in the above Lagrangian. This gives the Feynman rules shown in Fig. A.10, with the couplings given in Table A.6.

Again for completeness we will include the Feynman rules for the interaction of the Higgs bosons of the MSSM with the fermions. The relevant Lagrangian from Eqn. 4.10 of [24] is,

$$\begin{aligned}\mathcal{L}_{\mathrm{Hq\bar{q}}} \;=\; & -\frac{gm_u}{2M_{\rm W}\sin\beta}\left[\bar{u}u\left(H_1^0\sin\alpha+H_2^0\cos\alpha\right)-i\bar{u}\gamma_5 uH_3^0\cos\beta\right] \\ & -\frac{gm_d}{2M_{\rm W}\cos\beta}\left[\bar{d}d\left(H_1^0\cos\alpha-H_2^0\sin\alpha\right)-i\bar{d}\gamma_5 dH_3^0\sin\beta\right] \\ & +\frac{g}{2\sqrt{2}M_{\rm W}}\left\{H^+\bar{u}\left[\left(m_d\tan\beta+m_u\cot\beta\right)+\left(m_d\tan\beta-m_u\cot\beta\right)\gamma_5\right]d+\mathrm{h.c.}\right\}.\end{aligned} \tag{A.51}$$

This gives the Feynman rules shown in Fig. A.11, using the couplings given in Table A.7.

A.7 R-parity Violating Feynman Rules

Here we present the Feynman rules for R-parity violating supersymmetry with arbitrary left/right sfermion mixing. In general these terms in the superpotential, Eqn. 1.63, give rise to a number of interactions, the Yukawa-type coupling of two fermions and a sfermion, and scalar-scalar interaction terms. As we are only interested in the Yukawa-type terms we will only consider the Feynman rules which couple two fermions and a sfermion. We derive the Feynman rules from the superpotential including mixing between the left and

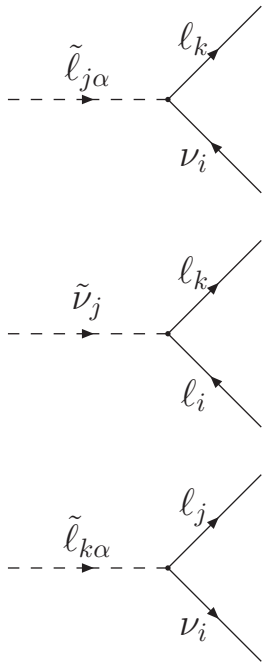

$$-\frac{i\lambda_{ijk}L_{1\alpha}^{2j-1}}{2}(1-\gamma_5)$$

$$\frac{i\lambda_{ijk}}{2}(1-\gamma_5)$$

$$-\frac{i\lambda_{ijk}L_{2\alpha}^{2k-1}}{2}(1+\gamma_5)C$$

Figure A.12: Feynman rules for LLE. The standard rules for charge conjugation matrices apply. In this case the ν_i should be transposed in the last diagram.

right sfermions. Due to our definition of the couplings in the superpotential, Eqn. 1.63, there are differences in our Feynman rules and hence cross sections and decay rates when compared with [162].

We follow the standard procedure defined in [18] to obtain the Lagrangian from the superpotential. We will consider the superpotential term by term. The first term in the $\not{R}_{\rm p}$ superpotential, Eqn. 1.63, *i.e.* the LLE term, gives the Lagrangian

$$\mathcal{L}_{\rm LLE} = -\lambda_{ijk}\left(\tilde{\ell}^*_{kR}\bar{\nu}^c_i P_L \ell_j + \tilde{\ell}_{jL}\bar{\ell}_k P_L \nu_i - \tilde{\nu}_j \bar{\ell}_k P_L \ell_i + \text{h.c.}\right), \tag{A.52}$$

where we have used the antisymmetries of the coupling λ_{ijk}, *i.e.* $\lambda_{ijk} = -\lambda_{jik}$. This Lagrangian therefore only applies for $i > j$.

After the inclusion of left/right sfermion mixing this gives the Lagrangian

$$\mathcal{L}_{\rm LLE} = -\lambda_{ijk}\left(L_{2\alpha}^{2k-1}\tilde{\ell}^*_{k\alpha}\bar{\nu}^c_i P_L \ell_j + L_{1\alpha}^{2j-1}\tilde{\ell}_{j\alpha}\bar{\ell}_k P_L \nu_i - \tilde{\nu}_j \bar{\ell}_k P_L \ell_i + \text{h.c.}\right), \tag{A.53}$$

where there is an implied summation over the slepton mass eigenstates. This Lagrangian gives the Feynman rules shown in Fig. A.12.

We can apply the same procedure to obtain the Lagrangian for the second term in

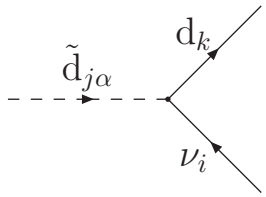

$$-\frac{i\lambda'_{ijk}Q^{2j-1}_{1\alpha}}{2}(1-\gamma_5)$$

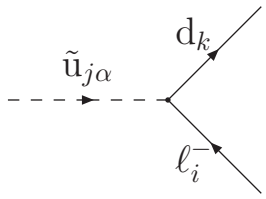

$$\frac{i\lambda'_{ijk}Q^{2j}_{1\alpha}}{2}(1-\gamma_5)$$

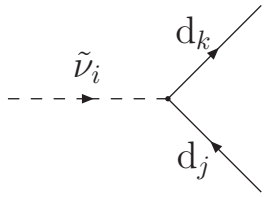

$$-\frac{i\lambda'_{ijk}}{2}(1-\gamma_5)$$

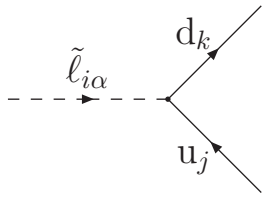

$$\frac{i\lambda'_{ijk}L^{2i-1}_{1\alpha}}{2}(1-\gamma_5)$$

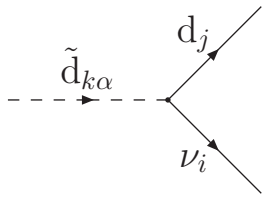

$$-\frac{i\lambda'_{ijk}Q^{2k-1}_{2\alpha}}{2}(1+\gamma_5)C$$

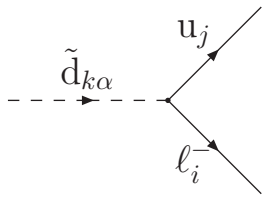

$$\frac{i\lambda'_{ijk}Q^{2k-1}_{2\alpha}}{2}(1+\gamma_5)C$$

Figure A.13: Feynman rules for LQD. The standard rules for charge conjugation matrices apply. In this case the lepton in the last two rules should be transposed.

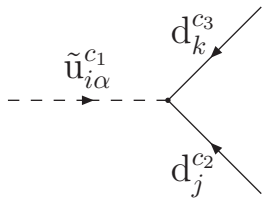

$$\frac{i\lambda''_{ijk}Q_{2\alpha}^{2i}\varepsilon_{c_1c_2c_3}}{2}C^\dagger(1+\gamma_5)$$

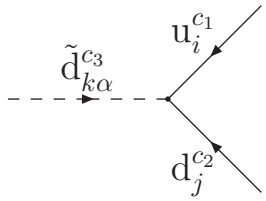

$$\frac{i\lambda''_{ijk}Q_{2\alpha}^{2k-1}\varepsilon_{c_1c_2c_3}}{2}C^\dagger(1+\gamma_5)$$

Figure A.14: Feynman rules for UDD. The standard rules for charge conjugation matrices apply. In this case the d_j should be transposed.

Eqn. 1.63, *i.e.* the LQD term,

$$\begin{aligned}\mathcal{L}_{\mathrm{LQD}} &= -\lambda'_{ijk}\Big(\tilde{d}^*_{kR}\bar{\nu}^c_i P_L d_j - \tilde{d}^*_{kR}\bar{\ell}^c_i P_L u_j + \tilde{d}_{jL}\bar{d}_k P_L \nu_i \\ &\quad -\tilde{u}_{jL}\bar{d}_k P_L \ell_i + \tilde{\nu}_i \bar{d}_k P_L d_j - \tilde{\ell}_{iL}\bar{d}_k P_L u_j + \mathrm{h.c.}\Big),\end{aligned} \tag{A.54}$$

where again there is an implied summation over the sfermion mass eigenstates. We can include the left/right sfermion mixing in the Lagrangian, giving

$$\begin{aligned}\mathcal{L}_{\mathrm{LQD}} &= -\lambda'_{ijk}\Big(Q_{2\alpha}^{2k-1}\tilde{d}^*_{k\alpha}\bar{\nu}^c_i P_L d_j - Q_{2\alpha}^{2k-1}\tilde{d}^*_{k\alpha}\bar{\ell}^c_i P_L u_j + Q_{1\alpha}^{2j-1}\tilde{d}_{j\alpha}\bar{d}_k P_L \nu_i \\ &\quad -Q_{1\alpha}^{2j}\tilde{u}_{j\alpha}\bar{d}_k P_L \ell_i + \tilde{\nu}_i \bar{d}_k P_L d_j - L_{1\alpha}^{2i-1}\tilde{\ell}_{i\alpha}\bar{d}_k P_L u_j + \mathrm{h.c.}\Big).\end{aligned} \tag{A.55}$$

This gives the Feynman rules in Fig. A.13.

The last term in the superpotential, Eqn. 1.63, gives the Lagrangian

$$\mathcal{L}_{\mathrm{UDD}} = -\lambda''_{ijk}\varepsilon_{c_1c_2c_3}\Big(\tilde{u}^{*c_1}_{iR}\bar{d}^{c_3}_k P_L d^{cc_2}_j + \tilde{d}^{*c_3}_{kR}\bar{u}^{c_1}_i P_L d^{cc_2}_j + \mathrm{h.c.}\Big), \tag{A.56}$$

where c_1, c_2 and c_3 are the colour indices.

We can include the left/right mixing in this equation, giving

$$\mathcal{L}_{\mathrm{UDD}} = -\lambda''_{ijk}\varepsilon_{c_1c_2c_3}\Big(Q_{2\alpha}^{2i}\tilde{u}^{*c_1}_{i\alpha}\bar{d}^{c_3}_k P_L d^{cc_2}_j + Q_{2\alpha}^{2k-1}\tilde{d}^{*c_3}_{k\alpha}\bar{u}^{c_1}_i P_L d^{cc_2}_j + \mathrm{h.c.}\Big). \tag{A.57}$$

The Feynman rules from this Lagrangian are shown in Fig. A.14.

Appendix B

Decay Rate Calculations

B.1 Introduction

In this appendix we present the matrix elements for the decays of the sfermions, charginos, neutralinos and gluinos via $\not{R}_{\rm p}$. The next appendix gives the matrix elements for the $\not{R}_{\rm p}$ production cross sections, most of which can simply be obtained by crossing the various decay matrix elements. Throughout we allow for more than one $\not{R}_{\rm p}$ coupling to be non-zero.

In order to simplify the notation for the matrix elements, for both the decay rates presented in this appendix and the cross sections in Appendix C, we introduce the following functions

$$R(\tilde{a}, m^2_{bc}) \equiv \frac{1}{(m^2_{bc} - M^2_{\tilde{a}})^2 + \Gamma^2_{\tilde{a}} M^2_{\tilde{a}}}, \tag{B.1a}$$

$$S(\tilde{a}, \tilde{b}, m^2_{cd}, m^2_{ef}) \equiv R(\tilde{a}, m^2_{cd}) R(\tilde{b}, m^2_{ef}) \left[(m^2_{cd} - M^2_{\tilde{a}})(m^2_{ef} - M^2_{\tilde{b}}) + \Gamma_{\tilde{a}} \Gamma_{\tilde{b}} M_{\tilde{a}} M_{\tilde{b}} \right], \tag{B.1b}$$

where $m^2_{bc} = (p_b + p_c)^2$, and $M_{\tilde{a}}$ and $\Gamma_{\tilde{a}}$ are the mass and the width of the sfermion $\tilde{a}$, respectively. The various terms in the matrix elements can be more easily expressed in terms of

$$\begin{aligned} \Psi(\tilde{a}, 1, 2, 3) \equiv\ & R(\tilde{a}, m^2_{12}) \left(m^2_{12} - m^2_1 - m^2_2 \right) \\ & \Big[\left(a^2(\tilde{a}) + b^2(\tilde{a}) \right) \left(M^2_0 + m^2_3 - m^2_{12} \right) + 4 a(\tilde{a}) b(\tilde{a}) m_3 M_0 \Big], \end{aligned} \tag{B.2a}$$

$$\begin{aligned} \Upsilon(\tilde{a}, 1, 2, 3) \equiv\ & S(\tilde{a}_1, \tilde{a}_2, m^2_{12}, m^2_{12}) \left(m^2_{12} - m^2_1 - m^2_2 \right) \\ & \Big[\left(a(\tilde{a}_1) a(\tilde{a}_2) + b(\tilde{a}_1) b(\tilde{a}_2) \right) \left(M^2_0 + m^2_3 - m^2_{12} \right) \\ & + 2 \left(a(\tilde{a}_1) b(\tilde{a}_2) + a(\tilde{a}_2) b(\tilde{a}_1) \right) m_3 M_0 \Big], \end{aligned} \tag{B.2b}$$

$$\begin{aligned} \Phi(\tilde{a}, \tilde{b}, 1, 2, 3) \equiv\ & S(\tilde{a}, \tilde{b}, m^2_{12}, m^2_{23}) \Big[m_1 m_3 a(\tilde{a}) a(\tilde{b}) \left(m^2_{12} + m^2_{23} - m^2_1 - m^2_3 \right) \\ & + m_1 M_0 b(\tilde{a}) a(\tilde{b}) \left(m^2_{23} - m^2_2 - m^2_3 \right) \\ & + m_3 M_0 a(\tilde{a}) b(\tilde{b}) \left(m^2_{12} - m^2_1 - m^2_2 \right) \\ & + b(\tilde{a}) b(\tilde{b}) \left(m^2_{12} m^2_{23} - m^2_1 m^2_3 - M^2_0 m^2_2 \right) \Big], \end{aligned} \tag{B.2c}$$

Operator	Process	Product of the colour factor and coupling C^a_{bc}
LLE	$\tilde{\ell}^-_{j\alpha} \longrightarrow \bar{\nu}_i \ell^-_k$	$\lvert\lambda_{ijk}\rvert^2 \lvert L^{2j-1}_{1\alpha}\rvert^2$
LLE	$\tilde{\ell}^-_{k\alpha} \longrightarrow \nu_i \ell^-_j$	$\lvert\lambda_{ijk}\rvert^2 \lvert L^{2k-1}_{2\alpha}\rvert^2$
LLE	$\tilde{\nu}_j \longrightarrow \ell^+_i \ell^-_k$	$\lvert\lambda_{ijk}\rvert^2$
LQD	$\tilde{\ell}^-_{i\alpha} \longrightarrow \bar{\mathrm{u}}_j \mathrm{d}_k$	$N_c \lvert\lambda'_{ijk}\rvert^2 \lvert L^{2i-1}_{1\alpha}\rvert^2$
LQD	$\tilde{\nu}_i \longrightarrow \bar{\mathrm{d}}_j \mathrm{d}_k$	$N_c \lvert\lambda'_{ijk}\rvert^2$
LQD	$\tilde{\mathrm{d}}_{j\alpha} \longrightarrow \bar{\nu}_i \mathrm{d}_k$	$\lvert\lambda'_{ijk}\rvert^2 \lvert Q^{2j-1}_{1\alpha}\rvert^2$
LQD	$\tilde{\mathrm{u}}_{j\alpha} \longrightarrow \ell^+_i \mathrm{d}_k$	$\lvert\lambda'_{ijk}\rvert^2 \lvert Q^{2j}_{1\alpha}\rvert^2$
LQD	$\tilde{\mathrm{d}}_{k\alpha} \longrightarrow \nu_i \mathrm{d}_j$	$\lvert\lambda'_{ijk}\rvert^2 \lvert Q^{2k-1}_{2\alpha}\rvert^2$
LQD	$\tilde{\mathrm{d}}_{k\alpha} \longrightarrow \ell^-_i \mathrm{u}_j$	$\lvert\lambda'_{ijk}\rvert^2 \lvert Q^{2k-1}_{2\alpha}\rvert^2$
UDD	$\tilde{\mathrm{u}}_{i\alpha} \longrightarrow \bar{\mathrm{d}}_j \bar{\mathrm{d}}_k$	$(N_c-1)! \lvert\lambda''_{ijk}\rvert^2 \lvert Q^{2i}_{2\alpha}\rvert^2$
UDD	$\tilde{\mathrm{d}}_{k\alpha} \longrightarrow \bar{\mathrm{u}}_i \bar{\mathrm{d}}_j$	$(N_c-1)! \lvert\lambda''_{ijk}\rvert^2 \lvert Q^{2k-1}_{2\alpha}\rvert^2$

Table B.1: Coefficients for the sfermion $\not{R}_\mathrm{p}$ decays.

where $\tilde{a}_1$ and $\tilde{a}_2$ are the mass eigenstates of the relevant SUSY particle. The functions a and b are gaugino-sfermion-fermion coupling constants and are given in the following tables in Appendix A: Table A.1 for the charginos, Table A.2 for the neutralinos and Table A.3 for the gluino. The couplings are defined such that $a(\tilde{c}^*) = b(\tilde{c})$ and $b(\tilde{c}^*) = a(\tilde{c})$. In all the above expressions M_0 is the mass of the decaying sparticle and 1, 2, 3, are the decay products. As we will consider the decays for arbitrary couplings we will use the indices $i, j, k = 1, 2, 3$ to represent the generations of the particles and the indices $\alpha, \beta = 1, 2$ to represent the mass eigenstates of the sfermions. We have not included the right-handed neutrino and therefore we will neglect the left/right mixing for the sneutrinos.

B.2 Sfermions

Here we present the matrix elements for the two-body sfermion decays including left/right mixing. In general the spin- and colour-averaged matrix elements have the form

$$|\overline{\mathcal{M}}(a \to b, c)|^2 = C^a_{bc}(M_a^2 - m_b^2 - m_c^2), \tag{B.3}$$

where C^a_{bc} is the product of the colour factor and the coupling for the process. These factors are tabulated for the various sfermion decays in Table B.1 where N_c denotes the number of colours.

In all these terms the Roman indices represent the generation of the particle and the

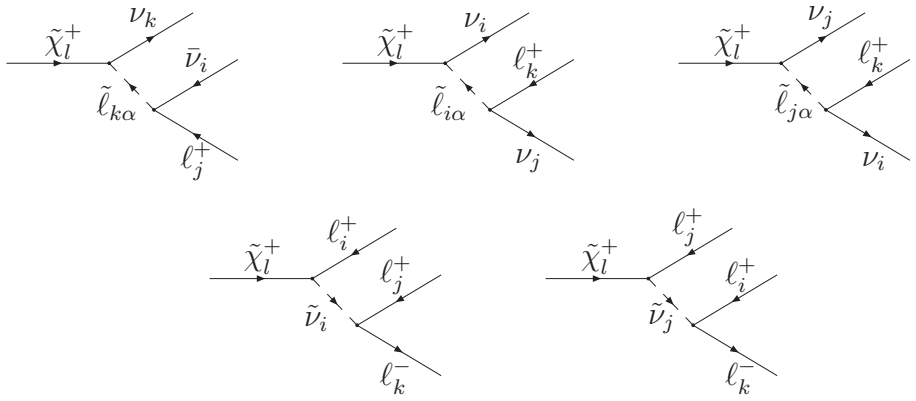

Figure B.1: LLE decays of the $\tilde{\chi}^+$.The index $l = 1, 2$ gives the mass eigenstate of the chargino, the index $\alpha = 1, 2$ gives the mass eigenstate of the slepton and the indices $i, j, k = 1, 2, 3$ give the generations of the particles.

Greek indices the mass eigenstate of the sfermions when there is mixing. The decay rate can be obtained by integrating over the two body phase space. This gives

$$\Gamma(a \to b, c) = \frac{|\overline{\mathcal{M}}(a \to b, c)|^2 p_{\rm cm}}{8\pi M_a^2}, \tag{B.4}$$

where $p_{\rm cm}$ is the final-state momentum in the rest frame of the decaying particle,

$$p_{\rm cm}^2 = \frac{1}{4M_a^2}\left[M_a^2 - (m_b + m_c)^2\right]\left[M_a^2 - (m_b - m_c)^2\right].$$

B.3 Charginos

Most of the chargino $\not{R}_{\rm p}$ decay rates have already been calculated [33] in the case of no left/right sfermion mixing for the first two operators in the $\not{R}_{\rm p}$ superpotential. We recalculate these rates with left/right sfermion mixing. First we consider the LLE decays of the chargino. There are three possible decay modes:

1. $\tilde{\chi}_l^+ \longrightarrow \bar{\nu}_i \ell_j^+ \nu_k$;
2. $\tilde{\chi}_l^+ \longrightarrow \nu_i \nu_j \ell_k^+$;
3. $\tilde{\chi}_l^+ \longrightarrow \ell_i^+ \ell_j^+ \ell_k^-$.

The Feynman diagrams for these decays are shown in Fig. B.1. The spin-averaged matrix elements are given by:

$$|\overline{\mathcal{M}}(\tilde{\chi}_l^+ \to \bar{\nu}_i \ell_j^+ \nu_k)|^2 = \frac{g^2 \lambda_{ijk}^2}{2}\left[\sum_{\alpha=1,2} |L_{2\alpha}^{2k-1}|^2 \Psi(\tilde{\ell}_{k\alpha}^*, \nu_i, \ell_j, \nu_k) + 2L_{21}^{2k-1} L_{22}^{2k-1} \Upsilon(\tilde{\ell}_k^*, \nu_i, \ell_j, \nu_k)\right]; \tag{B.5}$$

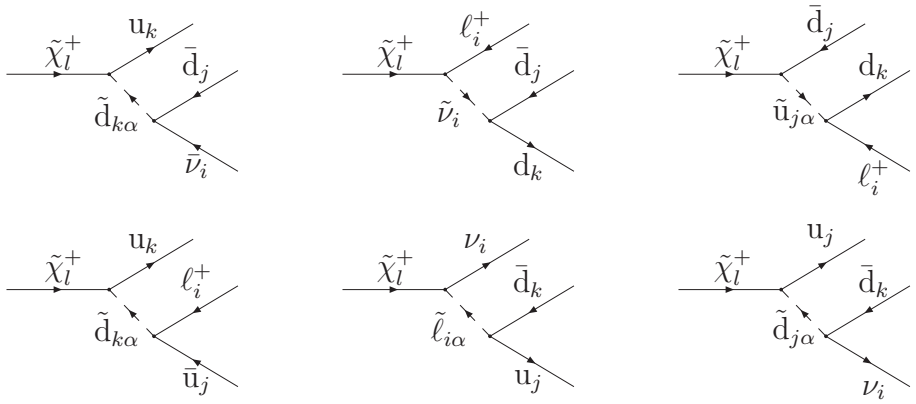

Figure B.2: LQD decays of the $\tilde{\chi}^+$.The index $l = 1, 2$ gives the mass eigenstate of the chargino, the index $\alpha = 1, 2$ gives the mass eigenstate of the sfermion and the indices $i, j, k = 1, 2, 3$ give the generations of the particles.

$$
\begin{aligned}
|\overline{\mathcal{M}}(\tilde{\chi}_l^+ \to \nu_i \nu_j \ell_k^+)|^2 &= \frac{g^2 \lambda_{ijk}^2}{2} \Bigg[\sum_{\alpha=1,2} |L_{1\alpha}^{2i-1}|^2 \Psi(\tilde{\ell}_{i\alpha}, \nu_j, \ell_k, \nu_i) \\
&\quad + \sum_{\alpha=1,2} |L_{1\alpha}^{2j-1}|^2 \Psi(\tilde{\ell}_{j\alpha}, \nu_i, \ell_k, \nu_j) \\
&\quad 2 L_{11}^{2i-1} L_{12}^{2i-1} \Upsilon(\tilde{\ell}_i, \nu_j, \ell_k, \nu_i) + 2 L_{11}^{2j-1} L_{12}^{2j-1} \Upsilon(\tilde{\ell}_j, \nu_i, \ell_k, \nu_j) \\
&\quad + \sum_{\alpha=1,2} \sum_{\beta=1,2} 2 L_{1\alpha}^{2i-1} L_{1\beta}^{2j-1} \Phi(\tilde{\ell}_{j\beta}, \tilde{\ell}_{i\alpha}, \nu_i, \ell_k, \nu_j) \Bigg]; \qquad \text{(B.6)} \\
|\overline{\mathcal{M}}(\tilde{\chi}_l^+ \to \ell_i^+ \ell_j^+ \ell_k^-)|^2 &= \frac{g^2 \lambda_{ijk}^2}{2} \Bigg[\Psi(\tilde{\nu}_i, \ell_j, \ell_k, \ell_i) + \Psi(\tilde{\nu}_j, \ell_i, \ell_k, \ell_j) \\
&\quad + 2\Phi(\tilde{\nu}_j, \tilde{\nu}_i, \ell_i, \ell_k, \ell_j) \Bigg]. \qquad \text{(B.7)}
\end{aligned}
$$

We go beyond the results of [33] to include the decay $\tilde{\chi}^+ \longrightarrow \bar{\nu}_i \ell_j^+ \nu_k$.

We now consider the LQD decays of the chargino. There are four possible decay modes:

1. $\tilde{\chi}_l^+ \longrightarrow \bar{\nu}_i \bar{\mathrm{d}}_j \mathrm{u}_k$;
2. $\tilde{\chi}_l^+ \longrightarrow \ell_i^+ \bar{\mathrm{u}}_j \mathrm{u}_k$;
3. $\tilde{\chi}_l^+ \longrightarrow \ell_i^+ \bar{\mathrm{d}}_j \mathrm{d}_k$;
4. $\tilde{\chi}_l^+ \longrightarrow \nu_i \mathrm{u}_j \bar{\mathrm{d}}_k$.

The Feynman diagrams for these decays are shown in Fig. B.2. The spin- and colour-averaged matrix elements are given by

$$|\overline{\mathcal{M}}(\tilde{\chi}_l^+ \to \bar{\nu}_i \bar{\mathrm{d}}_j \mathrm{u}_k)|^2 = \frac{g^2 \lambda'^2_{ijk} N_c}{2} \left[\sum_{\alpha=1,2} |Q_{2\alpha}^{2k-1}|^2 \Psi(\tilde{\mathrm{d}}^*_{k\alpha}, \nu_i, \mathrm{d}_j, \mathrm{u}_k) + 2 Q_{21}^{2k-1} Q_{22}^{2k-1} \Upsilon(\tilde{\mathrm{d}}^*_k, \nu_i, \mathrm{d}_j, \mathrm{u}_k) \right]; \quad \text{(B.8)}$$

$$|\overline{\mathcal{M}}(\tilde{\chi}_l^+ \to \ell_i^+ \bar{\mathrm{u}}_j \mathrm{u}_k)|^2 = \frac{g^2 \lambda'^2_{ijk} N_c}{2} \left[\sum_{\alpha=1,2} |Q_{2\alpha}^{2k-1}|^2 \Psi(\tilde{\mathrm{d}}^*_{k\alpha}, \ell_i, \mathrm{u}_j, \mathrm{u}_k) + 2 Q_{21}^{2k-1} Q_{22}^{2k-1} \Upsilon(\tilde{\mathrm{d}}^*_k, \ell_i, \mathrm{u}_j, \mathrm{u}_k) \right]; \quad \text{(B.9)}$$

$$|\overline{\mathcal{M}}(\tilde{\chi}_l^+ \to \ell_i^+ \bar{\mathrm{d}}_j \mathrm{d}_k)|^2 = \frac{g^2 \lambda'^2_{ijk} N_c}{2} \left[\Psi(\tilde{\nu}_i, \mathrm{d}_j, \mathrm{d}_k, \ell_i) + \sum_{\alpha=1,2} |Q_{1\alpha}^{2j}|^2 \Psi(\tilde{\mathrm{u}}_{j\alpha}, \ell_i, \mathrm{d}_k, \mathrm{d}_j) \right.$$
$$\left. + 2 Q_{11}^{2j} Q_{12}^{2j} \Upsilon(\tilde{\mathrm{u}}_j, \ell_i, \mathrm{d}_k, \mathrm{d}_j) + 2 \sum_{\alpha=1,2} Q_{1\alpha}^{2j} \Phi(\tilde{\mathrm{u}}_{j\alpha}, \tilde{\nu}_i, \ell_i, \mathrm{d}_k, \mathrm{d}_j) \right]; \quad \text{(B.10)}$$

$$|\overline{\mathcal{M}}(\tilde{\chi}_l^+ \to \nu_i \mathrm{u}_j \bar{\mathrm{d}}_k)|^2 = \frac{g^2 \lambda'^2_{ijk} N_c}{2} \left[\sum_{\alpha=1,2} |L_{1\alpha}^{2i-1}|^2 \Psi(\tilde{\ell}_{i\alpha}, \mathrm{u}_j, \mathrm{d}_k, \nu_i) + \sum_{\alpha=1,2} |Q_{1\alpha}^{2j-1}|^2 \Psi(\tilde{\mathrm{d}}_{j\alpha}, \nu_i, \mathrm{d}_k, \mathrm{u}_j) \right.$$
$$+ 2 L_{11}^{2i-1} L_{12}^{2i-1} \Upsilon(\tilde{\ell}_i, \mathrm{u}_j, \mathrm{d}_k, \nu_i) + 2 Q_{11}^{2j-1} Q_{12}^{2j-1} \Upsilon(\tilde{\mathrm{d}}_j, \nu_i, \mathrm{d}_k, \mathrm{u}_j)$$
$$\left. + 2 \sum_{\alpha=1,2} \sum_{\beta=1,2} L_{1\alpha}^{2i-1} Q_{1\beta}^{2j-1} \Phi(\tilde{\mathrm{d}}_{j\beta}, \tilde{\ell}_{i\alpha}, \nu_i, \mathrm{d}_k, \mathrm{u}_j) \right]. \quad \text{(B.11)}$$

We now come to the baryon number violating decays. We do not assume that there is only one non-zero $\not{R}_\mathrm{p}$ coupling. This means that more than one coupling contributes to these decays. It may seem that this will only matter in the case where more than one λ'' coupling is taken to be non-zero, however there can be more than one diagram even with only one coupling non-zero, *e.g.* λ''_{112} will give two diagrams for each of the decay modes. In this case one of these diagrams is obtained from the other simply by crossing the identical fermions in the final state.

There are two possible decay modes:

1. $\tilde{\chi}_l^+ \longrightarrow \mathrm{u}_i \mathrm{u}_j \mathrm{d}_k$;
2. $\tilde{\chi}_l^+ \longrightarrow \bar{\mathrm{d}}_i \bar{\mathrm{d}}_j \bar{\mathrm{d}}_k$.

The Feynman diagrams for these decays are shown in Fig. 2.8. The spin- and colour-averaged matrix elements for these processes with left/right sfermion mixing are given

by:

$$
\begin{aligned}
&|\overline{\mathcal{M}}(\tilde{\chi}_l^+ \to \mathrm{u}_i\mathrm{u}_j\mathrm{d}_k)|^2 = \\
&\quad \frac{g^2 N_c!}{2(1+\delta_{ij})}\Bigg[\lambda''^2_{jik}\sum_{\alpha=1,2}|Q_{2\alpha}^{2i-1}|^2\Psi(\tilde{\mathrm{d}}^*_{i\alpha},\mathrm{u}_j,\mathrm{d}_k,\mathrm{u}_i)+\lambda''^2_{ijk}\sum_{\alpha=1,2}|Q_{2\alpha}^{2j-1}|^2\Psi(\tilde{\mathrm{d}}^*_{j\alpha},\mathrm{u}_i,\mathrm{d}_k,\mathrm{u}_j) \\
&\quad +2\lambda''^2_{jik}Q_{21}^{2i-1}Q_{22}^{2i-1}\Upsilon(\tilde{\mathrm{d}}^*_i,\mathrm{u}_j,\mathrm{d}_k,\mathrm{u}_i)+2\lambda''^2_{ijk}Q_{21}^{2j-1}Q_{22}^{2j-1}\Upsilon(\tilde{\mathrm{d}}^*_j,\mathrm{u}_i,\mathrm{d}_k,\mathrm{u}_j) \\
&\quad +2\lambda''_{ijk}\lambda''_{jik}\sum_{\alpha=1,2}\sum_{\beta=1,2}Q_{2\alpha}^{2i-1}Q_{2\beta}^{2j-1}\Phi(\tilde{\mathrm{d}}^*_{j\beta},\tilde{\mathrm{d}}^*_{i\alpha},\mathrm{u}_i,\mathrm{d}_k,\mathrm{u}_j)\Bigg]; \qquad \text{(B.12)}
\end{aligned}
$$

$$
\begin{aligned}
&|\overline{\mathcal{M}}(\tilde{\chi}_l^+ \to \bar{\mathrm{d}}_i\bar{\mathrm{d}}_j\bar{\mathrm{d}}_k)|^2 = \\
&\quad \frac{g^2 N_c!}{2(1+\delta_{ij}+\delta_{jk}+\delta_{ik})}\Bigg[\lambda''^2_{ijk}\sum_{\alpha=1,2}|Q_{2\alpha}^{2i}|^2\Psi(\tilde{\mathrm{u}}^*_{i\alpha},\mathrm{d}_j,\mathrm{d}_k,\mathrm{d}_i) \\
&\quad +\lambda''^2_{jki}\sum_{\alpha=1,2}|Q_{2\alpha}^{2j}|^2\Psi(\tilde{\mathrm{u}}^*_{j\alpha},\mathrm{d}_i,\mathrm{d}_k,\mathrm{d}_j) \\
&\quad +\lambda''^2_{kij}\sum_{\alpha=1,2}|Q_{2\alpha}^{2k}|^2\Psi(\tilde{\mathrm{u}}^*_{k\alpha},\mathrm{d}_i,\mathrm{d}_j,\mathrm{d}_k)+2\lambda''^2_{ijk}Q_{21}^{2i}Q_{22}^{2i}\Upsilon(\tilde{\mathrm{u}}^*_i,\mathrm{d}_j,\mathrm{d}_k,\mathrm{d}_i) \\
&\quad +2\lambda''^2_{jki}Q_{21}^{2j}Q_{22}^{2j}\Upsilon(\tilde{\mathrm{u}}^*_j,\mathrm{d}_i,\mathrm{d}_k,\mathrm{d}_j)+2\lambda''^2_{kij}Q_{21}^{2k}Q_{22}^{2k}\Upsilon(\tilde{\mathrm{u}}^*_{k\alpha},\mathrm{d}_i,\mathrm{d}_j,\mathrm{d}_k) \\
&\quad -2\lambda''_{ijk}\lambda''_{jki}\sum_{\alpha=1,2}\sum_{\beta=1,2}Q_{2\alpha}^{2i}Q_{2\beta}^{2j}\Phi(\tilde{\mathrm{u}}^*_{j\beta},\tilde{\mathrm{u}}^*_{i\alpha},\mathrm{d}_i,\mathrm{d}_k,\mathrm{d}_j) \\
&\quad -2\lambda''_{ijk}\lambda''_{kij}\sum_{\alpha=1,2}\sum_{\beta=1,2}Q_{2\alpha}^{2i}Q_{2\beta}^{2k}\Phi(\tilde{\mathrm{u}}^*_{k\beta},\tilde{\mathrm{u}}^*_{i\alpha},\mathrm{d}_i,\mathrm{d}_j,\mathrm{d}_k) \\
&\quad -2\lambda''_{jki}\lambda''_{kij}\sum_{\alpha=1,2}\sum_{\beta=1,2}Q_{2\alpha}^{2j}Q_{2\beta}^{2k}\Phi(\tilde{\mathrm{u}}^*_{k\beta},\tilde{\mathrm{u}}^*_{j\alpha},\mathrm{d}_j,\mathrm{d}_i,\mathrm{d}_k)\Bigg]. \qquad \text{(B.13)}
\end{aligned}
$$

The coefficients in the chargino matrix elements are given in Table A.1. When the chargino mass matrix is diagonalized it is possible to get negative eigenvalues in which case the physical field is $\gamma_5\chi$ rather than χ. This means that the coefficients $a(\tilde{\nu}_i)$, $a(\tilde{\mathrm{u}}_{i\alpha})$, and $a(\tilde{\mathrm{d}}_{i\alpha})$ change sign if the chargino mass is negative.

The partial widths can be obtained from these matrix elements by integrating over any two of m_{12}^2, m_{23}^2 and m_{13}^2. The partial width is given by [22]

$$
\Gamma(0\to 1,2,3) = \frac{1}{(2\pi)^3}\frac{1}{32M_0^3}\int_{(m_{12}^2)_{\min}}^{(m_{12}^2)_{\max}} dm_{12}^2 \int_{(m_{23}^2)_{\min}}^{(m_{23}^2)_{\max}} dm_{23}^2\,|\overline{\mathcal{M}}|^2, \qquad \text{(B.14)}
$$

where

- $(m_{12}^2)_{\max} = (M_0 - m_3)^2$,
- $(m_{12}^2)_{\min} = (m_1 + m_2)^2$,
- $(m_{23}^2)_{\max} = (E_2^* + E_3^*)^2 - \left(\sqrt{E_2^{*2} - m_2^2} - \sqrt{E_3^{*2} - m_3^2}\right)^2$,

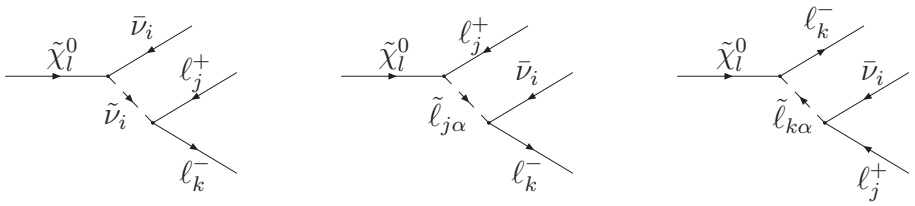

Figure B.3: LLE decays of the $\tilde{\chi}^0$. The index $l = 1, \ldots, 4$ gives the mass eigenstate of the neutralino, the index $\alpha = 1, 2$ gives the mass eigenstate of the slepton and the indices $i, j, k = 1, 2, 3$ give the generations of the particles.

- $(m_{23}^2)_{\min} = (E_2^* + E_3^*)^2 - \left(\sqrt{E_2^{*2} - m_2^2} + \sqrt{E_3^{*2} - m_3^2}\right)^2$,
- $E_2^* = \left(m_{12}^2 - m_1^2 + m_2^2\right)/2m_{12}$ and $E_3^* = \left(M_0^2 - m_{12}^2 - m_3^2\right)/2m_{12}$ are the energies of particles 2 and 3 in the m_{12} rest frame.

These double integrals are complicated and in general, for massive final-state particles, cannot be performed analytically. However the kinematic functions defined in Eqn. B.2 only depend on two of the possible kinematic variables. This is because there are only two independent variables with the third given by momentum conservation, *i.e.* $m_{12}^2 + m_{13}^2 + m_{23}^2 = M_0^2 + m_1^2 + m_2^2 + m_3^2$. We can therefore split the matrix element up into terms containing these functions and integrate each term over different kinematic variables. This allows us to perform the first integral for each of these terms analytically leaving the second integral to be performed numerically. Thus we obtain a number of one-dimensional integrals which must be performed numerically rather than one two-dimensional integral. It is more efficient to calculate these one-dimensional integrals rather than the two-dimensional integral.

B.4 Neutralinos

The total three-body decay rate of a photino was first computed in [105] in the limit where the sfermion is much heavier than the decaying photino and assuming massless final-state particles. In [63] the general photino matrix element squared was given, allowing for the computation of final-state distributions. In [64, 162] this was extended to the general case of a neutralino. In [162] arbitrary sfermion mixing was included as well. We have recalculated the rates with only left/right sfermion mixing (neglecting inter-generational sfermion mixing.) We use a different convention for both the $\not{R}_p$ superpotential and the MSSM Lagrangian, which is more appropriate for implementation in HERWIG. The LLE, LQD and UDD decay modes are shown in Figs. B.3, B.4 and 2.9, respectively.

There are four decay modes:

1. $\tilde{\chi}_l^0 \longrightarrow \bar{\nu}_i \ell_j^+ \ell_k^-$;
2. $\tilde{\chi}_l^0 \longrightarrow \bar{\nu}_i \bar{\mathrm{d}}_j \mathrm{d}_k$;
3. $\tilde{\chi}_l^0 \longrightarrow \ell_i^+ \bar{\mathrm{u}}_j \mathrm{d}_k$;
4. $\tilde{\chi}_l^0 \longrightarrow \bar{\mathrm{u}}_i \bar{\mathrm{d}}_j \bar{\mathrm{d}}_k$,

as well as their charge conjugates, since the neutralino is a Majorana fermion. The spin- and colour-averaged matrix elements are given below[1]

$$
\begin{aligned}
&|\overline{\mathcal{M}}(\tilde{\chi}_l^0 \to \bar{\nu}_i \ell_j^+ \ell_k^-)|^2 = \\
&\quad \lambda_{ijk}^2 \Bigg[\Psi(\tilde{\nu}_i, \ell_j, \ell_k, \nu_i) + \sum_{\alpha=1,2} |L_{1\alpha}^{2j-1}|^2 \Psi(\tilde{\ell}_{j\alpha}, \nu_i, \ell_k, \ell_j) \\
&\quad + \sum_{\alpha=1,2} |L_{2\alpha}^{2k-1}|^2 \Psi(\tilde{\ell}_{k\alpha}^*, \nu_i, \ell_j, \ell_k) \\
&\quad + 2L_{11}^{2j-1} L_{12}^{2j-1} \Upsilon(\tilde{\ell}_j, \nu_i, \ell_k, \ell_j) + 2L_{21}^{2k-1} L_{22}^{2k-1} \Upsilon(\tilde{\ell}_k^*, \nu_i, \ell_j, \ell_k) \\
&\quad - \sum_{\alpha=1,2} 2L_{1\alpha}^{2j-1} \Phi(\tilde{\ell}_{j\alpha}, \tilde{\nu}_i, \nu_i, \ell_k, \ell_j) - \sum_{\alpha=1,2} 2L_{2\alpha}^{2k-1} \Phi(\tilde{\ell}_{k\alpha}^*, \tilde{\nu}_i, \nu_i, \ell_j, \ell_k) \\
&\quad - \sum_{\alpha=1,2} \sum_{\beta=1,2} 2L_{1\alpha}^{2j-1} L_{2\beta}^{2k-1} \Phi(\tilde{\ell}_{k\beta}^*, \tilde{\ell}_{j\alpha}, \ell_j, \nu_i, \ell_k) \Bigg],
\end{aligned}
\tag{B.15}
$$

$$
\begin{aligned}
&|\overline{\mathcal{M}}(\tilde{\chi}_l^0 \to \bar{\nu}_i \bar{\mathrm{d}}_j \mathrm{d}_k)|^2 = \\
&\quad \lambda'^2_{ijk} N_c \Bigg[\Psi(\tilde{\nu}_i, \mathrm{d}_j, \mathrm{d}_k, \nu_i) + \sum_{\alpha=1,2} |Q_{1\alpha}^{2j-1}|^2 \Psi(\tilde{\mathrm{d}}_{j\alpha}, \nu_i, \mathrm{d}_k, \mathrm{d}_j) \\
&\quad + \sum_{\alpha=1,2} |Q_{2\alpha}^{2k-1}|^2 \Psi(\tilde{\mathrm{d}}_{k\alpha}^*, \nu_i, \mathrm{d}_j, \mathrm{d}_k) \\
&\quad + 2Q_{11}^{2j-1} Q_{12}^{2j-1} \Upsilon(\tilde{\mathrm{d}}_j, \nu_i, \mathrm{d}_k, \mathrm{d}_j) + 2Q_{21}^{2k-1} Q_{22}^{2k-1} \Upsilon(\tilde{\mathrm{d}}_k^*, \nu_i, \mathrm{d}_j, \mathrm{d}_k) \\
&\quad - \sum_{\alpha=1,2} 2Q_{1\alpha}^{2j-1} \Phi(\tilde{\mathrm{d}}_{j\alpha}, \tilde{\nu}_i, \nu_i, \mathrm{d}_k, \mathrm{d}_j) - \sum_{\alpha=1,2} 2Q_{2\alpha}^{2k-1} \Phi(\tilde{\mathrm{d}}_{k\alpha}^*, \tilde{\nu}_i, \nu_i, \mathrm{d}_j, \mathrm{d}_k) \\
&\quad - \sum_{\alpha=1,2} \sum_{\beta=1,2} 2Q_{1\alpha}^{2j-1} Q_{2\beta}^{2k-1} \Phi(\tilde{\mathrm{d}}_{k\beta}^*, \tilde{\mathrm{d}}_{j\alpha}, \mathrm{d}_j, \nu_i, \mathrm{d}_k) \Bigg],
\end{aligned}
\tag{B.16}
$$

$$
\begin{aligned}
&|\overline{\mathcal{M}}(\tilde{\chi}_l^0 \to \ell_i^+ \bar{u}_j d_k)|^2 = \\
&\quad \lambda'^2_{ijk} N_c \Bigg[\sum_{\alpha=1,2} |L_{1\alpha}^{2i-1}|^2 \Psi(\tilde{\ell}_{i\alpha}, \mathrm{u}_j, \mathrm{d}_k, \ell_i) + \sum_{\alpha=1,2} |Q_{1\alpha}^{2j}|^2 \Psi(\tilde{\mathrm{u}}_{j\alpha}, \ell_i, \mathrm{d}_k, \mathrm{u}_j) \\
&\quad + \sum_{\alpha=1,2} |Q_{2\alpha}^{2k-1}|^2 \Psi(\tilde{\mathrm{d}}_{k\alpha}^*, \ell_i, \mathrm{u}_j, \mathrm{d}_k) + 2L_{11}^{2i-1} L_{12}^{2i-1} \Upsilon(\tilde{\ell}_i, \mathrm{u}_j, \mathrm{d}_k, \ell_i) \\
&\quad + 2Q_{11}^{2j} Q_{12}^{2j} \Upsilon(\tilde{\mathrm{u}}_j, \ell_i, \mathrm{d}_k, \mathrm{u}_j) + 2Q_{21}^{2k-1} Q_{22}^{2k-1} \Upsilon(\tilde{\mathrm{d}}_k^*, \ell_i, \mathrm{u}_j, \mathrm{d}_k) \\
&\quad - \sum_{\alpha=1,2} \sum_{\beta=1,2} 2L_{1\alpha}^{2i-1} Q_{1\beta}^{2j} \Phi(\tilde{\mathrm{u}}_{j\beta}, \tilde{\ell}_{i\alpha}, \ell_i, \mathrm{d}_k, \mathrm{u}_j) \\
&\quad - \sum_{\alpha=1,2} \sum_{\beta=1,2} 2L_{1\alpha}^{2i-1} Q_{2\beta}^{2k-1} \Phi(\tilde{\mathrm{d}}_{k\beta}^*, \tilde{\ell}_{i\alpha}, \ell_i, \mathrm{u}_j, \mathrm{d}_k) \\
&\quad - \sum_{\alpha=1,2} \sum_{\beta=1,2} 2Q_{1\alpha}^{2j} Q_{2\beta}^{2k-1} \Phi(\tilde{\mathrm{d}}_{k\beta}^*, \tilde{\mathrm{u}}_{j\alpha}, \mathrm{u}_j, \ell_i, \mathrm{d}_k) \Bigg],
\end{aligned}
\tag{B.17}
$$

[1] We have a slight disagreement with [162] concerning the sign of the width of the sfermions. This is numerically insignificant since when the sfermion is on-shell HERWIG treats this as a two-body decay. The authors of [162] agree with our signs. We thank Paolo Gondolo for discussions of this point.

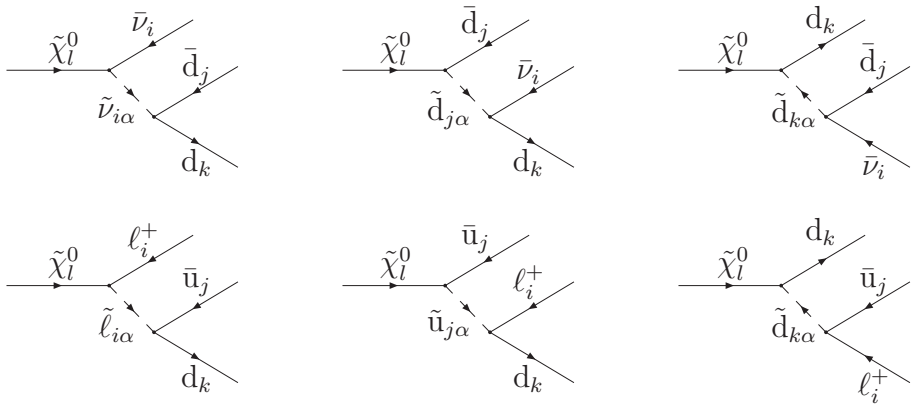

Figure B.4: LQD decays of the $\tilde{\chi}^0$.The index $l = 1, \ldots, 4$ gives the mass eigenstate of the neutralino, the index $\alpha = 1, 2$ gives the mass eigenstate of the sfermion and the indices $i, j, k = 1, 2, 3$ give the generations of the particles.

$$
\begin{aligned}
&|\overline{\mathcal{M}}(\tilde{\chi}^0_l \to \bar{u}_i \bar{d}_j \bar{d}_k)|^2 = \\
&\quad \lambda''^2_{ijk} N_c! \Bigg[\sum_{\alpha=1,2} |Q^{2i}_{2\alpha}|^2 \Psi(\tilde{\mathrm{u}}^*_{i\alpha}, \mathrm{d}_j, \mathrm{d}_k, \mathrm{u}_i) + \sum_{\alpha=1,2} |Q^{2j-1}_{2\alpha}|^2 \Psi(\tilde{\mathrm{d}}^*_{j\alpha}, \mathrm{u}_i, \mathrm{d}_k, \mathrm{d}_j) \\
&\quad + \sum_{\alpha=1,2} |Q^{2k-1}_{2\alpha}|^2 \Psi(\tilde{\mathrm{d}}^*_{k\alpha}, \mathrm{u}_i, \mathrm{d}_j, \mathrm{d}_k) + 2 Q^{2i}_{21} Q^{2i}_{22} \Upsilon(\tilde{\mathrm{u}}^*_i, \mathrm{d}_j, \mathrm{d}_k, \mathrm{u}_i) \\
&\quad + 2 Q^{2j-1}_{21} Q^{2j-1}_{22} \Upsilon(\tilde{\mathrm{d}}^*_j, \mathrm{u}_i, \mathrm{d}_k, \mathrm{d}_j) + 2 Q^{2k-1}_{21} Q^{2k-1}_{22} \Upsilon(\tilde{\mathrm{d}}^*_k, \mathrm{u}_i, \mathrm{d}_j, \mathrm{d}_k) \\
&\quad - \sum_{\alpha=1,2} \sum_{\beta=1,2} 2 Q^{2i}_{2\alpha} Q^{2j-1}_{2\beta} \Phi(\tilde{\mathrm{d}}^*_{j\beta}, \tilde{\mathrm{u}}^*_{i\alpha}, \mathrm{u}_i, \mathrm{d}_k, \mathrm{d}_j) \\
&\quad - \sum_{\alpha=1,2} \sum_{\beta=1,2} 2 Q^{2i}_{2\alpha} Q^{2k-1}_{2\beta} \Phi(\tilde{\mathrm{d}}^*_{k\beta}, \tilde{\mathrm{u}}^*_{i\alpha}, \mathrm{u}_i, \mathrm{d}_j, \mathrm{d}_k) \\
&\quad - \sum_{\alpha=1,2} \sum_{\beta=1,2} 2 Q^{2j-1}_{2\alpha} Q^{2k-1}_{2\beta} \Phi(\tilde{\mathrm{d}}^*_{k\beta}, \tilde{\mathrm{d}}^*_{j\alpha}, \mathrm{d}_j, \mathrm{u}_i, \mathrm{d}_k) \Bigg].
\end{aligned}
\tag{B.18}
$$

The relevant coefficients are given in Table A.2. Again, when the neutralino mass matrix is diagonalized, negative eigenvalues can be obtained and the fields must be rotated. This changes the sign of some of the coefficients in Table A.2: the coefficients $a(\tilde{c})$ change sign, and hence the coefficients $b(\tilde{c}^*)$ also change sign. The partial widths can be obtained by integrating the matrix elements in the same way as for the chargino decays.

B.5 Gluinos

These decay rates are calculated here with left/right mixing. There are three possible decay modes, two via the LQD operator and one via the UDD operator:

1. $\tilde{\mathrm{g}} \longrightarrow \bar{\nu}_i \bar{\mathrm{d}}_j \mathrm{d}_k$;
2. $\tilde{\mathrm{g}} \longrightarrow \ell^+_i \bar{\mathrm{u}}_j \mathrm{d}_k$;

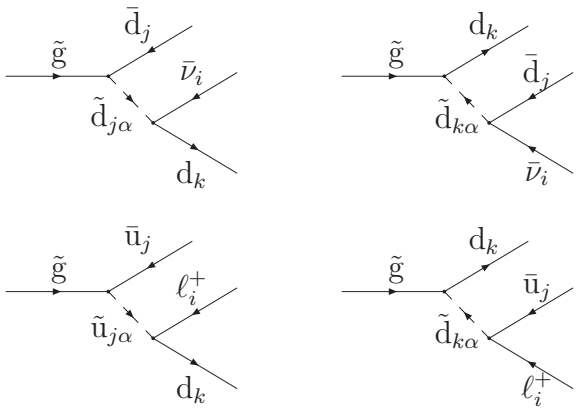

Figure B.5: LQD decays of the $\tilde{g}$. The index $\alpha = 1, 2$ gives the mass eigenstate of the sfermion and the indices $i, j, k = 1, 2, 3$ give the generations of the particles.

3. $\tilde{g} \longrightarrow u_i d_j d_k$.

Since the gluino is a Majorana fermion the charge conjugate decay modes are also possible. The Feynman diagrams for these processes are shown in Fig. B.5 and Fig. 2.11, respectively. The spin- and colour-averaged matrix elements with left/right sfermion mixing are given by

$$
\begin{aligned}
&|\overline{\mathcal{M}}(\tilde{g} \to \bar{\nu}_i \bar{d}_j d_k)|^2 = \\
&\quad \frac{\lambda'^2_{ijk} g_s^2}{2} \Bigg[\sum_{\alpha=1,2} |Q^{2j-1}_{1\alpha}|^2 \Psi(\tilde{d}_{j\alpha}, \nu_i, d_k, d_j) + \sum_{\alpha=1,2} |Q^{2k-1}_{2\alpha}|^2 \Psi(\tilde{d}^*_{k\alpha}, \nu_i, d_j, d_k) \\
&\quad + 2 Q^{2j-1}_{11} Q^{2j-1}_{12} \Upsilon(\tilde{d}_j, \nu_i, d_k, d_j) + 2 Q^{2k-1}_{21} Q^{2k-1}_{22} \Upsilon(\tilde{d}^*_k, \nu_i, d_j, d_k) \\
&\quad - \sum_{\alpha=1,2} \sum_{\beta=1,2} 2 Q^{2j-1}_{1\alpha} Q^{2k-1}_{2\beta} \Phi(\tilde{d}^*_{k\beta}, \tilde{d}_{j\alpha}, d_j, \nu_i, d_k) \Bigg],
\end{aligned}
\tag{B.19}
$$

$$
\begin{aligned}
&|\overline{\mathcal{M}}(\tilde{g} \to \ell_i^+ \bar{u}_j d_k)|^2 = \\
&\quad \frac{\lambda'^2_{ijk} g_s^2}{2} \Bigg[\sum_{\alpha=1,2} |Q^{2j}_{1\alpha}|^2 \Psi(\tilde{u}_{j\alpha}, \ell_i, d_k, u_j) + 2 Q^{2j}_{11} Q^{2j}_{12} \Upsilon(\tilde{u}_j, \ell_i, d_k, u_j) \\
&\quad + \sum_{\alpha=1,2} |Q^{2k-1}_{2\alpha}|^2 \Psi(\tilde{d}^*_{k\alpha}, \ell_i, u_j, d_k) + 2 Q^{2k-1}_{21} Q^{2k-1}_{22} \Upsilon(\tilde{d}^*_k, \ell_i, u_j, d_k) \\
&\quad - \sum_{\alpha=1,2} \sum_{\beta=1,2} 2 Q^{2j}_{1\alpha} Q^{2k-1}_{2\beta} \Phi(\tilde{d}^*_{k\beta}, \tilde{u}_{j\alpha}, u_j, \ell_i, d_k) \Bigg],
\end{aligned}
\tag{B.20}
$$

$$
\begin{aligned}
&|\overline{\mathcal{M}}(\tilde{\mathrm{g}} \to \bar{\mathrm{u}}_i \bar{\mathrm{d}}_j \bar{\mathrm{d}}_k)|^2 = \\
&\quad \frac{\lambda''^2_{ijk}(N_c-1)!}{2} \Bigg[\sum_{\alpha=1,2} |Q^{2i}_{2\alpha}|^2 \Psi(\tilde{\mathrm{u}}^*_{i\alpha}, \mathrm{d}_j, \mathrm{d}_k, \mathrm{u}_i) + 2Q^{2i}_{21} Q^{2i}_{22} \Upsilon(\tilde{\mathrm{u}}^*_i, \mathrm{d}_j, \mathrm{d}_k, \mathrm{u}_i) \\
&\quad + \sum_{\alpha=1,2} |Q^{2j-1}_{2\alpha}|^2 \Psi(\tilde{\mathrm{d}}^*_{j\alpha}, \mathrm{u}_i, \mathrm{d}_k, \mathrm{d}_j) + 2Q^{2j-1}_{21} Q^{2j-1}_{22} \Upsilon(\tilde{\mathrm{d}}^*_j, \mathrm{u}_i, \mathrm{d}_k, \mathrm{d}_j) \\
&\quad + \sum_{\alpha=1,2} |Q^{2k-1}_{2\alpha}|^2 \Psi(\tilde{\mathrm{d}}^*_{k\alpha}, \mathrm{u}_i, \mathrm{d}_j, \mathrm{d}_k) + 2Q^{2k-1}_{21} Q^{2k-1}_{22} \Upsilon(\tilde{\mathrm{d}}^*_k, \mathrm{u}_i, \mathrm{d}_j, \mathrm{d}_k) \\
&\quad + \frac{1}{N_c-1} \sum_{\alpha=1,2} \sum_{\beta=1,2} 2Q^{2i}_{2\alpha} Q^{2j-1}_{2\beta} \Phi(\tilde{\mathrm{d}}^*_{j\beta}, \tilde{\mathrm{u}}^*_{i\alpha}, \mathrm{u}_i, \mathrm{d}_k, \mathrm{d}_j) \\
&\quad + \frac{1}{N_c-1} \sum_{\alpha=1,2} \sum_{\beta=1,2} 2Q^{2i}_{2\alpha} Q^{2k-1}_{2\beta} \Phi(\tilde{\mathrm{d}}^*_{k\beta}, \tilde{\mathrm{u}}^*_{i\alpha}, \mathrm{u}_i, \mathrm{d}_j, \mathrm{d}_k) \\
&\quad + \frac{1}{N_c-1} \sum_{\alpha=1,2} \sum_{\beta=1,2} 2Q^{2j-1}_{2\alpha} Q^{2k-1}_{2\beta} \Phi(\tilde{\mathrm{d}}^*_{k\beta}, \tilde{\mathrm{d}}^*_{j\alpha}, \mathrm{d}_j, \mathrm{u}_i, \mathrm{d}_k) \Bigg]. \qquad \text{(B.21)}
\end{aligned}
$$

The coefficients for these matrix elements are given in Table A.3. As the gluino mass is not obtained by diagonalizing a mass matrix it cannot be negative. The partial widths can be obtained integrating the matrix elements in the same way as for the chargino decays.

Appendix C

Cross-section Calculations

C.1 Introduction

Here we present all the matrix elements for $2 \to 2$ scattering processes via single sparticle exchange. We disregard those possibilities where the sfermion resonance is not kinematically probed, *e.g.*

$$\mathrm{d}_j + \bar{\mathrm{d}}_k \to \tilde{\nu}_i \to \tilde{\nu}_i + \mathrm{Z}^0. \tag{C.1}$$

All of the single neutralino, chargino and gluino production cross sections can be obtained by crossing from the decay matrix elements we have already presented in Appendix B. This crossing will lead to the invariants m_{12}^2, m_{23}^2, and m_{13}^2 being replaced by the usual invariants s, t and u. There is also an overall sign change due to exchanging fermions between the initial and final states. Furthermore it should be remembered that the decay matrix elements have been averaged over the spin and colour of the initial particle.

The cross sections for the remaining processes are presented below. In all cases the formulae have been averaged over the initial spins and colours. The initial-state masses have all been set to zero, except where they appear in a coupling constant. In t- and u-channel fermion propagators the fermion masses have been neglected as well.

C.2 LQD Processes

C.2.1 Resonant Slepton Production followed by Weak Decay

There are three processes which can occur via the production of a resonant slepton followed by a weak decay of this slepton. These are:

1. $\mathrm{d}_j\bar{\mathrm{d}}_k \longrightarrow \tilde{\ell}_i^*\mathrm{W}^-$;
2. $\mathrm{u}_j\bar{\mathrm{d}}_k \longrightarrow \tilde{\nu}_i^*\mathrm{W}^+$;
3. $\mathrm{u}_j\bar{\mathrm{d}}_k \longrightarrow \tilde{\tau}_1^*\mathrm{Z}^0$.

We have not included processes where the resonance is not accessible, *e.g.* $\mathrm{u}_j\bar{\mathrm{d}}_k \longrightarrow \tilde{\tau}_2^*\mathrm{Z}^0$. The matrix elements are given below:

$$
\begin{aligned}
&|\overline{\mathcal{M}}(\mathrm{d}_j\bar{\mathrm{d}}_k \to \tilde{\ell}^*_{i\alpha}\mathrm{W}^-)|^2 = \\
&\quad \frac{g^2\lambda'^2_{ijk}|L^{2i-1}_{1\alpha}|^2}{2M^2_{\mathrm{W}}N_c}\left[\hat{s}^2p^2_{\mathrm{cm}}R(\tilde{\nu}_i,\hat{s}) + \frac{1}{4\hat{u}^2}\left(2M^2_{\mathrm{W}}(\hat{u}\hat{t} - M^2_{\tilde{\ell}_{i\alpha}}M^2_{\mathrm{W}}) + \hat{u}^2\hat{s}\right)\right. \\
&\quad \left. -\frac{\hat{s}\left(\hat{s} - M^2_{\tilde{\nu}_i}\right)R(\tilde{\nu}_i,\hat{s})}{2\hat{u}}\left(M^2_{\mathrm{W}}(2M^2_{\tilde{\ell}_{i\alpha}} - \hat{u}) + \hat{u}(\hat{s} - M^2_{\tilde{\ell}_{i\alpha}})\right)\right]; \qquad \text{(C.2)}
\end{aligned}
$$

$$
\begin{aligned}
&|\overline{\mathcal{M}}(\mathrm{u}_j\bar{\mathrm{d}}_k \to \tilde{\nu}^*_i\mathrm{W}^+)|^2 = \\
&\quad \frac{g^2\lambda'^2_{ijk}}{2M^2_{\mathrm{W}}N_c}\left[\sum_{\alpha=1,2}|L^{2i-1}_{1\alpha}|^4\hat{s}^2p^2_{\mathrm{cm}}R(\tilde{\ell}_{i\alpha},\hat{s}) + 2|L^{2i-1}_{11}|^2|L^{2i-1}_{12}|^2\hat{s}^2p^2_{\mathrm{cm}}S(\tilde{\ell}_{i1},\tilde{\ell}_{i2},\hat{s},\hat{s})\right. \\
&\quad + \frac{1}{4\hat{u}^2}\left(2M^2_{\mathrm{W}}(\hat{u}\hat{t} - M^2_{\tilde{\nu}_i}M^2_{\mathrm{W}}) + \hat{u}^2\hat{s}\right) \\
&\quad \left. -\sum_{\alpha=1,2}\frac{|L^{2i-1}_{1\alpha}|^2\hat{s}\left(\hat{s} - M^2_{\tilde{\ell}_{i\alpha}}\right)R(\tilde{\ell}_{i\alpha},\hat{s})}{2\hat{u}}\left(M^2_{\mathrm{W}}(2M^2_{\tilde{\nu}_i} - \hat{u}) + \hat{u}(\hat{s} - M^2_{\tilde{\nu}_i})\right)\right]; \qquad \text{(C.3)}
\end{aligned}
$$

$$
\begin{aligned}
&|\overline{\mathcal{M}}(\mathrm{u}_j\bar{\mathrm{d}}_k \to \tilde{\ell}^*_{i1}\mathrm{Z}^0)|^2 = \\
&\quad \frac{g^2\lambda'^2_{ijk}}{N_cM^2_{\mathrm{Z}}\cos^2\theta_W}\left[\sum_{\alpha=1,2}|L^{2i-1}_{1\alpha}|^2|Z^{\alpha1}_{\ell_i}|^2\hat{s}^2p^2_{\mathrm{cm}}R(\tilde{\ell}_{i\alpha},\hat{s})\right. \\
&\quad + \frac{|L^{2i-1}_{11}|^2Z^2_{u_L}}{\hat{u}^2}\left(2M^2_{\mathrm{Z}}(\hat{u}\hat{t} - M^2_{\tilde{\ell}_{i1}}M^2_{\mathrm{Z}}) + \hat{u}^2\hat{s}\right) \\
&\quad + \frac{|L^{2i-1}_{11}|^2Z^2_{d_R}}{\hat{t}^2}\left(2M^2_{\mathrm{Z}}(\hat{u}\hat{t} - M^2_{\tilde{\ell}_{i1}}M^2_{\mathrm{Z}}) + \hat{t}^2\hat{s}\right) + 2L^{2i-1}_{11}L^{2i-1}_{12}Z^{11}_{\ell_i}Z^{21}_{\ell_i}\hat{s}^2p^2_{\mathrm{cm}}S(\tilde{\ell}_{i1},\tilde{\ell}_{i2},\hat{s},\hat{s}) \\
&\quad + \sum_{\alpha=1,2}\frac{L^{2i-1}_{1\alpha}L^{2i-1}_{11}Z^{\alpha1}_{\ell_i}Z_{u_L}\hat{s}\left(\hat{s} - M^2_{\tilde{\ell}_{i\alpha}}\right)R(\tilde{\ell}_{i\alpha},\hat{s})}{\hat{u}}\left(M^2_{\mathrm{Z}}(2M^2_{\tilde{\ell}_{i1}} - \hat{u}) + \hat{u}(s - M^2_{\tilde{\ell}_{i1}})\right) \\
&\quad - \sum_{\alpha=1,2}\frac{L^{2i-1}_{1\alpha}L^{2i-1}_{11}Z^{\alpha1}_{\ell_i}Z_{d_R}\hat{s}\left(\hat{s} - M^2_{\tilde{\ell}_{i\alpha}}\right)R(\tilde{\ell}_{i\alpha},\hat{s})}{\hat{t}}\left(M^2_{\mathrm{Z}}(2M^2_{\tilde{\ell}_{i1}} - \hat{t}) + \hat{t}(s - M^2_{\tilde{\ell}_{i1}})\right) \\
&\quad \left. + \frac{2|L^{2i-1}_{11}|^2Z_{u_L}Z_{d_R}}{\hat{u}\hat{t}}\left(2M^2_{\mathrm{Z}}(M^2_{\tilde{\ell}_{i1}} - \hat{t})(M^2_{\tilde{\ell}_{i1}} - \hat{u}) - \hat{s}\hat{t}\hat{u}\right)\right], \qquad \text{(C.4)}
\end{aligned}
$$

where in all the above equations

$$
p^2_{\mathrm{cm}} = \frac{1}{4\hat{s}}\left[\hat{s} - (m_1+m_2)^2\right]\left[\hat{s} - (m_1-m_2)^2\right],
$$

and m_1, m_2 are the masses of the final-state particles. The couplings for these processes can be found in Table A.4.

In the Monte Carlo simulation all of the cross-section integrals are performed using the multi-channel Monte Carlo integration technique described in Chapter 2.

C.2.2 Resonant Slepton Production followed by $\not{R}_p$ Decay

There are four processes in which we can produce a resonant slepton via $\not{R}_p$ which then decays back to Standard Model particles via a $\not{R}_p$ decay. These are:

1. $d_j\bar{d}_k \longrightarrow d_l\bar{d}_m$;
2. $u_j\bar{d}_k \longrightarrow u_l\bar{d}_m$;
3. $d_j\bar{d}_k \longrightarrow \ell_l^-\ell_m^+$;
4. $u_j\bar{d}_k \longrightarrow \nu_l\ell_m^+$.

The first two of these processes only require non-zero LQD couplings whereas the second two require both non-zero LQD and LLE couplings. The matrix elements are presented below for an arbitrary number of non-zero $\not{R}_p$ couplings:

$$\begin{aligned}|\overline{\mathcal{M}}(d_j\bar{d}_k \to d_l\bar{d}_m)|^2 &= \frac{1}{4}\sum_{i,n=1,3}\lambda'_{ijk}\lambda'_{ilm}\lambda'_{njk}\lambda'_{nlm}S(\tilde{\nu}_i,\tilde{\nu}_n,\hat{s},\hat{s})\hat{s}\left(\hat{s}-m^2_{d_l}-m^2_{d_m}\right)\\ &\quad+\frac{1}{4}\sum_{i,n=1,3}\lambda'_{ijl}\lambda'_{ikm}\lambda'_{njl}\lambda'_{nkm}\frac{(m^2_{d_l}-\hat{t})(m^2_{d_m}-\hat{t})}{(\hat{t}-M^2_{\tilde{\nu}_i})(\hat{t}-M^2_{\tilde{\nu}_n})};\end{aligned} \tag{C.5}$$

$$\begin{aligned}|\overline{\mathcal{M}}(u_j\bar{d}_k \to u_l\bar{d}_m)|^2 &= \frac{1}{4}\sum_{\alpha,\beta=1,2}\sum_{i,n=1,3}\lambda'_{ijk}\lambda'_{ilm}\lambda'_{njk}\lambda'_{nlm}|L^{2i-1}_{1\alpha}|^2|L^{2n-1}_{1\beta}|^2\\ &\quad S(\tilde{\ell}_{i\alpha},\tilde{\ell}_{n\beta},\hat{s},\hat{s})\hat{s}\left(\hat{s}-m^2_{u_l}-m^2_{d_m}\right);\end{aligned} \tag{C.6}$$

$$|\overline{\mathcal{M}}(d_j\bar{d}_k \to \ell_l^-\ell_m^+)|^2 = \frac{1}{4N_c}\sum_{i,n=1,3}\lambda'_{ijk}\lambda'_{njk}\lambda_{ilm}\lambda_{nlm}S(\tilde{\nu}_i,\tilde{\nu}_n,\hat{s},\hat{s})\hat{s}\left(\hat{s}-m^2_{\ell_m}-m^2_{\ell_l}\right); \tag{C.7}$$

$$\begin{aligned}|\overline{\mathcal{M}}(u_j\bar{d}_k \to \nu_l\ell_m^+)|^2 &= \frac{1}{4N_c}\sum_{\alpha,\beta=1,2}\sum_{i,n=1,3}\lambda'_{ijk}\lambda'_{njk}\lambda_{ilm}\lambda_{nlm}|L^{2i-1}_{1\alpha}|^2|L^{2n-1}_{1\beta}|^2\\ &\quad S(\tilde{\ell}_{i\alpha},\tilde{\ell}_{n\beta},\hat{s},\hat{s})\hat{s}\left(\hat{s}-m^2_{\ell_m}\right).\end{aligned} \tag{C.8}$$

C.2.3 Resonant Slepton Production followed by Higgs Decay

There are a number of processes which can occur via the production of a resonant slepton followed by the decay of the resonant slepton to either a neutral or charged Higgs:

1. $\mathrm{d}_j\bar{\mathrm{d}}_k \longrightarrow \tilde{\ell}^*_{i\alpha}\mathrm{H}^-$;
2. $\mathrm{u}_j\bar{\mathrm{d}}_k \longrightarrow \tilde{\nu}^*_i\mathrm{H}^+$;
3. $\mathrm{u}_j\bar{\mathrm{d}}_k \longrightarrow \tilde{\ell}^*_{i\beta}\mathrm{h}_0/\mathrm{H}_0/\mathrm{A}_0$.

As we only include processes where there is a possibility of a resonant production mechanism, the process $\mathrm{d}_j\bar{\mathrm{d}}_k \longrightarrow \tilde{\nu}^*_i\mathrm{h}_0/\mathrm{H}_0/\mathrm{A}_0$ is not included. For the same reason we also have not included the processes $\mathrm{u}_j\bar{\mathrm{d}}_k \longrightarrow \tilde{\ell}^*_{iL}\mathrm{h}_0/\mathrm{H}_0/\mathrm{A}_0$ for the first two slepton generations. This is because HERWIG does not include left/right sfermion mixing for the first two generation sleptons and the initial state only couples to the left-handed slepton. The process $\mathrm{u}_j\bar{\mathrm{d}}_k \longrightarrow \tilde{\ell}^*_{i2}\mathrm{h}_0/\mathrm{H}_0/\mathrm{A}_0$ is also not included for the third generation ($i = 3$) as there is no accessible resonance.

Since the matrix elements have the same form for all the neutral Higgs processes we use the notation H^l_0 where l=1,2,3 is h_0, H_0 and A_0, respectively. The matrix elements for these processes are given below:

$$|\overline{\mathcal{M}}(\mathrm{d}_j\bar{\mathrm{d}}_k \to \tilde{\ell}^*_{i\alpha}\mathrm{H}^-)|^2 = \frac{g^2\lambda'^2_{ijk}}{4N_c}\left[|H^c_{\tilde{\nu}\tilde{\ell}_{i\alpha}}|^2\hat{s}R(\tilde{\nu}_i,\hat{s}) + \frac{4|L^{2i-1}_{1\alpha}|^2|D^c_j|^2}{\hat{u}^2}\left(\hat{u}\hat{t} - M^2_{\tilde{\ell}_{i\beta}}M^2_{\mathrm{H}^-}\right)\right]; \tag{C.9}$$

$$|\overline{\mathcal{M}}(\mathrm{u}_j\bar{\mathrm{d}}_k \to \tilde{\nu}^*_i\mathrm{H}^+)|^2 = \frac{g^2\lambda'^2_{ijk}}{4N_c}\left[\sum_{\alpha=1,2}|L^{2i-1}_{i\alpha}|^2|H^c_{\tilde{\nu}\tilde{\ell}_{i\alpha}}|^2\hat{s}R(\tilde{\ell}_{i\alpha},\hat{s}) + 2L^{2i-1}_{i1}L^{2i-1}_{i2}H^c_{\nu\tilde{\ell}_{i1}}H^c_{\nu\tilde{\ell}_{i2}}\hat{s}S(\tilde{\ell}_{i1},\tilde{\ell}_{i2},\hat{s},\hat{s}) + \frac{4|U^c_j|^2}{\hat{u}^2}\left(\hat{u}\hat{t} - M^2_{\tilde{\nu}_i}M^2_{\mathrm{H}^+}\right)\right]; \tag{C.10}$$

$$|\overline{\mathcal{M}}(\mathrm{u}_j\bar{d}_k \to \tilde{\ell}^*_{i\beta}\mathrm{H}^l_0)|^2 = \frac{g^2\lambda'^2_{ijk}}{4N_c}\left[\sum_{\alpha=1,2}|L^{2i-1}_{i\alpha}|^2|H^l_{\tilde{\ell}_{i\alpha}\tilde{\ell}_{i\beta}}|^2\hat{s}R(\tilde{\ell}_{i\alpha},\hat{s}) + 2L^{2i-1}_{i1}L^{2i-1}_{i2}H^l_{\tilde{\ell}_{i1}\tilde{\ell}_{i\beta}}H^l_{\tilde{\ell}_{i2}\tilde{\ell}_{i\beta}}\hat{s}S(\tilde{\ell}_{i1},\tilde{\ell}_{i2},\hat{s},\hat{s}) + \frac{|L^{2i-1}_{1\beta}|^2|D^l_j|^2}{\hat{u}^2}\left(\hat{u}\hat{t} - M^2_{\tilde{\ell}_{i\beta}}M^2_{\mathrm{H}^l_0}\right) + \frac{|L^{2i-1}_{1\beta}|^2|D^l_k|^2}{\hat{t}^2}\left(\hat{u}\hat{t} - M^2_{\tilde{\ell}_{i\beta}}M^2_{\mathrm{H}^l_0}\right)\right]. \tag{C.11}$$

The couplings involved in the various processes can be found in Tables A.6 and A.7.

C.3 UDD Processes

C.3.1 Resonant Squark Production followed by Weak Decay

There are four processes which can occur via the production of a resonant squark followed by a weak decay of this squark:

1. $\mathrm{d}_j\mathrm{d}_k \longrightarrow \tilde{\mathrm{d}}^*_{i\beta}\mathrm{W}^-$;

2. $\mathrm{u}_i\mathrm{d}_j \longrightarrow \tilde{\mathrm{u}}^*_{k\beta}\mathrm{W}^+$;

3. $\mathrm{d}_j\mathrm{d}_k \longrightarrow \tilde{\mathrm{t}}^*_1\mathrm{Z}^0$;

4. $\mathrm{u}_i\mathrm{d}_j \longrightarrow \tilde{\mathrm{b}}^*_1\mathrm{Z}^0$.

Again we do not include processes where the resonance is not accessible, *i.e.* $\mathrm{d}_j\mathrm{d}_k \longrightarrow \tilde{\mathrm{t}}^*_2\mathrm{Z}^0$ and $\mathrm{u}_i\mathrm{d}_j \longrightarrow \tilde{\mathrm{b}}^*_2\mathrm{Z}^0$. The matrix elements for these processes are given by

$$
\begin{aligned}
&|\overline{\mathcal{M}}(\mathrm{d}_j\mathrm{d}_k \to \tilde{\mathrm{d}}^*_{i\beta}\mathrm{W}^-)|^2 = \\
&\quad \frac{g^2{\lambda''}^2_{ijk}(N_c-1)!|Q^{2i-1}_{1\beta}|^2\hat{s}^2p^2_{\mathrm{cm}}}{2N_cM^2_{\mathrm{W}}}\left[\sum_{\alpha=1,2}|Q^{2i}_{2\alpha}|^2|Q^{2i}_{1\alpha}|^2R(\tilde{\mathrm{u}}_{i\alpha},\hat{s})\right. \qquad \text{(C.12)}\\
&\quad \left.+2Q^{2i}_{21}Q^{2i}_{22}Q^{2i}_{11}Q^{2i}_{12}S(\tilde{\mathrm{u}}_{i1},\tilde{\mathrm{u}}_{i2},\hat{s},\hat{s})\right], \\
&|\overline{\mathcal{M}}(\mathrm{u}_i\mathrm{d}_j \to \tilde{\mathrm{u}}^*_{k\beta}\mathrm{W}^+)|^2 = \\
&\quad \frac{g^2{\lambda''}^2_{ijk}(N_c-1)!\hat{s}^2p^2_{\mathrm{cm}}|Q^{2i}_{1\beta}|^2}{2N_cM^2_{\mathrm{W}}}\left[\sum_{\alpha=1,2}|Q^{2i-1}_{2\alpha}|^2|Q^{2i-1}_{1\alpha}|^2R(\tilde{\mathrm{d}}_{k\alpha},\hat{s})\right. \\
&\quad \left.+2Q^{2i-1}_{21}Q^{2i-1}_{22}Q^{2i-1}_{11}Q^{2i-1}_{12}S(\tilde{\mathrm{d}}_{k1},\tilde{\mathrm{d}}_{k2},\hat{s},\hat{s})\right], \qquad \text{(C.13)}\\
&|\overline{\mathcal{M}}(\mathrm{d}_j\mathrm{d}_k \to \tilde{\mathrm{u}}^*_{i1}\mathrm{Z}^0)|^2 = \\
&\quad \frac{g^2{\lambda''}^2_{ijk}(N_c-1)!}{N_cM^2_{\mathrm{Z}}\cos^2\theta_W}\left[\sum_{\alpha=1,2}|Q^{2i}_{2\alpha}|^2|Z^{\alpha1}_{u_i}|^2\hat{s}^2p^2_{\mathrm{cm}}R(\tilde{\mathrm{u}}_{i\alpha},\hat{s})\right. \\
&\quad +2Q^{2i}_{21}Q^{2i}_{22}Z^{11}_{u_i}Z^{21}_{u_i}\hat{s}^2p^2_{\mathrm{cm}}S(\tilde{\mathrm{u}}_{i1},\tilde{\mathrm{u}}_{i2},\hat{s},\hat{s})+\frac{|Q^{2i}_{21}|^2Z^2_{d_R}}{\hat{u}^2}\left(2M^2_{\mathrm{Z}}(\hat{u}\hat{t}-M^2_{\tilde{\mathrm{u}}_{i1}}M^2_{\mathrm{Z}})+\hat{u}^2\hat{s}\right) \\
&\quad +\frac{|Q^{2i}_{21}|^2Z^2_{d_R}}{\hat{t}^2}\left(2M^2_{\mathrm{Z}}(\hat{u}\hat{t}-M^2_{\tilde{\mathrm{u}}_{i1}}M^2_{\mathrm{Z}})+\hat{t}^2\hat{s}\right) \\
&\quad -\frac{2|Q^{2i}_{21}|^2Z^2_{d_R}}{\hat{u}\hat{t}}\left(2M^2_{\mathrm{Z}}(M^2_{\tilde{\mathrm{u}}_{i1}}-\hat{u})(M^2_{\tilde{\mathrm{u}}_{i1}}-\hat{t})-\hat{s}\hat{t}\hat{u}\right) \\
&\quad +\sum_{\alpha=1,2}\frac{Q^{2i}_{2\alpha}Q^{2i}_{21}Z^{\alpha1}_{u_i}Z_{d_R}}{\hat{u}}\hat{s}(\hat{s}-M^2_{\tilde{\mathrm{u}}_{i\alpha}})R(\tilde{\mathrm{u}}_{i\alpha},\hat{s})\left(M^2_{\mathrm{Z}}(2M^2_{\tilde{\mathrm{u}}_{i1}}-\hat{u})+\hat{u}(\hat{s}-M^2_{\tilde{\mathrm{u}}_{i1}})\right) \\
&\quad \left.+\sum_{\alpha=1,2}\frac{Q^{2i}_{2\alpha}Q^{2i}_{21}Z^{\alpha1}_{u_i}Z_{d_R}}{\hat{t}}\hat{s}(\hat{s}-M^2_{\tilde{\mathrm{u}}_{i\alpha}})R(\tilde{\mathrm{u}}_{i\alpha},\hat{s})\left(M^2_{\mathrm{Z}}(2M^2_{\tilde{\mathrm{u}}_{i1}}-\hat{t})+\hat{t}(\hat{s}-M^2_{\tilde{\mathrm{u}}_{i1}})\right)\right], \qquad \text{(C.14)}
\end{aligned}
$$

$$
\begin{aligned}
&|\overline{\mathcal{M}}(\mathrm{u}_i\mathrm{d}_k \to \tilde{\mathrm{d}}^*_{j1}\mathrm{Z}^0)|^2 = \\
&\quad \frac{g^2\lambda''^2_{ijk}(N_c-1)!}{N_c M_{\mathrm{Z}}^2\cos^2\theta_W}\left[\sum_{\alpha=1,2}|Q^{2j-1}_{2\alpha}|^2|Z^{\alpha 1}_{d_j}|^2\hat{s}^2 p^2_{\mathrm{cm}}R(\tilde{\mathrm{d}}_{j\alpha},\hat{s})\right. \\
&\quad +2Q^{2j-1}_{21}Q^{2j-1}_{22}Z^{11}_{d_j}Z^{21}_{d_j}\hat{s}^2p^2_{\mathrm{cm}}S(\tilde{\mathrm{d}}_{j1},\tilde{\mathrm{d}}_{j2},\hat{s}^2,\hat{s}^2) \\
&\quad +\frac{|Q^{2j-1}_{21}|^2Z^2_{u_R}}{\hat{u}^2}\left(2M_{\mathrm{Z}}^2(\hat{u}\hat{t}-M^2_{\tilde{\mathrm{d}}_{j1}}M_{\mathrm{Z}}^2)+\hat{u}^2\hat{s}\right)+\frac{|Q^{2j-1}_{21}|^2Z^2_{d_R}}{\hat{t}^2}\left(2M_{\mathrm{Z}}^2(\hat{u}\hat{t}-M^2_{\tilde{\mathrm{d}}_{j1}}M_{\mathrm{Z}}^2)+\hat{t}^2\hat{s}\right) \\
&\quad -\frac{2|Q^{2j-1}_{21}|^2Z_{u_R}Z_{d_R}}{\hat{u}\hat{t}}\left(2M_{\mathrm{Z}}^2(M^2_{\tilde{\mathrm{d}}_{j1}}-\hat{u})(M^2_{\tilde{\mathrm{d}}_{j1}}-\hat{t})-\hat{s}\hat{t}\hat{u}\right) \\
&\quad +\sum_{\alpha=1,2}\frac{Q^{2j-1}_{2\alpha}Q^{2j-1}_{21}Z^{\alpha 1}_{d_j}Z_{u_R}}{\hat{u}}\hat{s}(\hat{s}-M^2_{\tilde{\mathrm{d}}_{j\alpha}})R(\tilde{\mathrm{d}}_{j\alpha},\hat{s})\left(M_{\mathrm{Z}}^2(2M^2_{\tilde{\mathrm{d}}_{j1}}-\hat{u})+\hat{u}(\hat{s}-M^2_{\tilde{\mathrm{d}}_{j1}})\right) \\
&\quad \left.+\sum_{\alpha=1,2}\frac{Q^{2j-1}_{2\alpha}Q^{2j-1}_{21}Z^{\alpha 1}_{d_j}Z_{d_R}}{\hat{t}}\hat{s}(\hat{s}-M^2_{\tilde{\mathrm{d}}_{j\alpha}})R(\tilde{\mathrm{d}}_{j\alpha},\hat{s})\left(M_{\mathrm{Z}}^2(2M^2_{\tilde{\mathrm{d}}_{j1}}-\hat{t})+\hat{t}(\hat{s}-M^2_{\tilde{\mathrm{d}}_{j1}})\right)\right],
\end{aligned}
\tag{C.15}
$$

The coefficients for these processes can be found in Table A.4.

C.3.2 Resonant Squark Production followed by $\not{R}_p$ Decay

There are two processes in which a resonant squark is produced via the $\not{B}$ term in the superpotential where these squarks then decay to Standard Model particles:

1. $\mathrm{d}_j\mathrm{d}_k \longrightarrow \mathrm{d}_l\mathrm{d}_m$;
2. $\mathrm{u}_i\mathrm{d}_j \longrightarrow \mathrm{u}_l\mathrm{d}_m$.

The matrix elements are given by

$$
\begin{aligned}
|\overline{\mathcal{M}}(\mathrm{d}_j\mathrm{d}_k \to \mathrm{d}_l\mathrm{d}_m)|^2 &= \frac{(N_c-1)!^2}{4N_c}\sum_{\alpha,\beta=1,2}\sum_{i,n=1,3}\lambda''_{ijk}\lambda''_{ilm}\lambda''_{njk}\lambda''_{nlm}|Q^{2i}_{2\alpha}|^2|Q^{2n}_{2\beta}|^2 \\
&\quad S(\tilde{\mathrm{u}}_{i\alpha},\tilde{\mathrm{u}}_{n\beta},\hat{s},\hat{s})\hat{s}\left(\hat{s}-m^2_{\mathrm{d}_l}-m^2_{\mathrm{d}_m}\right),
\end{aligned}
\tag{C.16}
$$

$$
\begin{aligned}
|\overline{\mathcal{M}}(\mathrm{u}_i\mathrm{d}_j \to \mathrm{u}_l\mathrm{d}_m)|^2 &= \frac{(N_c-1)^2}{4N_c}\sum_{\alpha,\beta=1,2}\sum_{k,n=1,3}\lambda''_{ijk}\lambda''_{lmk}\lambda''_{ijn}\lambda''_{lmn}|Q^{2k-1}_{2\alpha}|^2|Q^{2n-1}_{2\beta}|^2 \\
&\quad S(\tilde{\mathrm{d}}_{i\alpha},\tilde{\mathrm{d}}_{n\beta},\hat{s},\hat{s})\hat{s}\left(\hat{s}-m^2_{\mathrm{u}_l}-m^2_{\mathrm{d}_m}\right).
\end{aligned}
\tag{C.17}
$$

C.3.3 Resonant Squark Production followed by Higgs Decay

There are a number of processes which occur via the production of a resonant squark which subsequently decays to either a neutral or charged Higgs. Again we only consider those processes for which a resonance is possible, *i.e.* we neglect the processes $\mathrm{d}_j\mathrm{d}_k \longrightarrow \tilde{\mathrm{u}}^*_{iR}\mathrm{h}_0/\mathrm{H}_0/\mathrm{A}_0$ and $\mathrm{u}_i\mathrm{d}_j \longrightarrow \tilde{d}^*_{iR}\mathrm{h}_0/\mathrm{H}_0/\mathrm{A}_0$ for the first two generations and the

processes $\mathrm{d}_j\mathrm{d}_k \longrightarrow \tilde{t}^*_{i2}\mathrm{h}_0/\mathrm{H}_0/\mathrm{A}_0$ and $\mathrm{u}_i\mathrm{d}_j \longrightarrow \tilde{b}^*_{i2}\mathrm{h}_0/\mathrm{H}_0/\mathrm{A}_0$ for the third generation, where we consider left/right sfermion mixing as these processes cannot occur via a resonant diagram:

1. $\mathrm{d}_j\mathrm{d}_k \longrightarrow \tilde{\mathrm{d}}^*_{i\beta}\mathrm{H}^-$;
2. $\mathrm{u}_i\mathrm{d}_j \longrightarrow \tilde{\mathrm{u}}^*_{k\beta}\mathrm{H}^+$;
3. $\mathrm{d}_j\mathrm{d}_k \longrightarrow \tilde{\mathrm{u}}^*_{i1}\mathrm{h}_0/\mathrm{H}_0/\mathrm{A}_0$;
4. $\mathrm{u}_i\mathrm{d}_j \longrightarrow \tilde{\mathrm{d}}^*_{i1}\mathrm{h}_0/\mathrm{H}_0/\mathrm{A}_0$.

Due to our notation for the squark mixing matrices in the case of no left/right sfermion mixing the right squark is denoted as the second mass eigenstate. The matrix elements for these processes are given below:

$$
\begin{aligned}
&|\overline{\mathcal{M}}(\mathrm{d}_j\mathrm{d}_k \to \tilde{\mathrm{d}}^*_{i\beta}\mathrm{H}^-)|^2 = \\
&\quad \frac{g^2(N_c-1)!}{4N_c}\left[\sum_{\alpha=1,2}\lambda''^2_{ijk}|Q^{2i}_{2\alpha}|^2|H^c_{\tilde{u}_{i\alpha}\tilde{d}_{i\beta}}|^2\hat{s}R(\tilde{\mathrm{u}}_{i\alpha},\hat{s})\right. \\
&\quad +2\lambda''^2_{ijk}Q^{2i}_{21}Q^{2i}_{22}H^c_{\tilde{u}_{i1}\tilde{d}_{i\beta}}H^c_{\tilde{u}_{i2}\tilde{d}_{i\beta}}\hat{s}S(\tilde{\mathrm{u}}_{i1},\tilde{\mathrm{u}}_{i2},\hat{s},\hat{s}) + \frac{4\lambda''^2_{jik}|U^c_j|^2|Q^{2i-1}_{2\beta}|^2}{\hat{u}^2}\left(\hat{u}\hat{t} - M^2_{\tilde{\mathrm{d}}_{i\beta}}M^2_{\mathrm{H}^-}\right) \\
&\quad \left.+\frac{4\lambda''^2_{kij}|U^c_k|^2|Q^{2i-1}_{2\beta}|^2}{\hat{t}^2}\left(\hat{u}\hat{t} - M^2_{\tilde{\mathrm{d}}_{i\beta}}M^2_{\mathrm{H}^-}\right)\right]; \qquad \text{(C.18)}
\end{aligned}
$$

$$
\begin{aligned}
&|\overline{\mathcal{M}}(\mathrm{u}_i\mathrm{d}_j \to \tilde{\mathrm{u}}^*_{k\beta}\mathrm{H}^+)|^2 = \\
&\quad \frac{g^2(N_c-1)!}{4N_c}\left[\sum_{\alpha=1,2}\lambda''^2_{ijk}|Q^{2k-1}_{2\alpha}|^2H^c_{\tilde{u}_{k\beta}\tilde{d}_{k\alpha}}|^2\hat{s}R(\tilde{\mathrm{d}}_{k\alpha},\hat{s})\right. \\
&\quad +2\lambda''^2_{ijk}Q^{2k-1}_{21}Q^{2k-1}_{22}H^c_{\tilde{u}_{k\beta}\tilde{d}_{k1}}H^c_{\tilde{u}_{k\beta}\tilde{d}_{k2}}\hat{s}S(\tilde{\mathrm{d}}_{k1},\tilde{\mathrm{d}}_{k2},\hat{s},\hat{s}) \\
&\quad \left.+\frac{4\lambda''^2_{kij}|D^c_i|^2|Q^{2k}_{2\beta}|^2}{\hat{u}^2}\left(\hat{u}\hat{t} - M^2_{\tilde{\mathrm{d}}_{k\alpha}}M^2_{\mathrm{H}^+}\right)\right]; \qquad \text{(C.19)}
\end{aligned}
$$

$$
\begin{aligned}
&|\overline{\mathcal{M}}(\mathrm{d}_j\mathrm{d}_k \to \tilde{\mathrm{u}}^*_{i1}\mathrm{H}^l_0)|^2 = \\
&\quad \frac{g^2\lambda''^2_{ijk}(N_c-1)!}{4N_c}\left[\sum_{\alpha=1,2}|Q^{2i}_{2\alpha}|^2|H^l_{\tilde{u}_{i\alpha}\tilde{u}_{i1}}|^2\hat{s}R(\tilde{\mathrm{u}}_{i\alpha},\hat{s})\right. \\
&\quad +2Q^{2i}_{21}Q^{2i}_{22}H^l_{\tilde{u}_{i1}\tilde{u}_{i1}}H^l_{\tilde{u}_{i2}\tilde{u}_{i1}}\hat{s}S(\tilde{\mathrm{u}}_{i1},\tilde{\mathrm{u}}_{i2},\hat{s},\hat{s}) \\
&\quad \left.+\frac{|Q^{2i}_{21}|^2|D^l_j|^2}{\hat{t}^2}\left(\hat{u}\hat{t} - M^2_{\tilde{\mathrm{u}}_{i1}}M^2_{\mathrm{H}^l_0}\right) + \frac{|Q^{2i}_{21}|^2|D^l_k|^2}{\hat{u}^2}\left(\hat{u}\hat{t} - M^2_{\tilde{\mathrm{u}}_{i1}}M^2_{\mathrm{H}^l_0}\right)\right]; \qquad \text{(C.20)}
\end{aligned}
$$

$$
\begin{aligned}
&|\overline{\mathcal{M}}(\mathrm{u}_i\mathrm{d}_k \to \tilde{\mathrm{d}}^*_{j1}\mathrm{H}^l_0)|^2 = \\
&\quad \frac{g^2\lambda''^2_{ijk}(N_c-1)!}{4N_c}\left[\sum_{\alpha=1,2}|Q^{2j-1}_{2\alpha}|^2|H^l_{\tilde{d}_{j\alpha}\tilde{d}_{j1}}|^2\hat{s}R(\tilde{\mathrm{d}}_{j\alpha},\hat{s})\right. \\
&\quad +2Q^{2j-1}_{21}Q^{2j-1}_{22}H^l_{\tilde{d}_{j1}\tilde{d}_{j1}}H^l_{\tilde{d}_{j2}\tilde{d}_{j1}}\hat{s}S(\tilde{\mathrm{d}}_{j1},\tilde{\mathrm{d}}_{j2},\hat{s},\hat{s}) \\
&\quad \left.+\frac{|Q^{2j-1}_{21}|^2|U^l_i|^2}{\hat{t}^2}\left(\hat{u}\hat{t}-M^2_{\tilde{\mathrm{d}}_{j1}}M^2_{\mathrm{H}^{\mathrm{l}}_0}\right)+\frac{|Q^{2j-1}_{21}|^2|D^l_k|^2}{\hat{u}^2}\left(\hat{u}\hat{t}-M^2_{\tilde{\mathrm{d}}_{j1}}M^2_{\mathrm{H}^{\mathrm{l}}_0}\right)\right]. \quad \text{(C.21)}
\end{aligned}
$$

The coefficients for the various processes can be found in Tables A.5 and A.7.

Bibliography

[1] H. Dreiner, P. Richardson and M. H. Seymour, JHEP **0004**, 008 (2000).

[2] HERWIG6.1, G. Corcella *et al.*, (1999), hep-ph/9912396; G. Corcella *et al.*, (2000), hep-ph/0011363. G. Marchesini *et al.*, Comput. Phys. Commun. **67**, 465 (1992).

[3] H. Dreiner, P. Richardson and M. H. Seymour, (2000), hep-ph/0007228.

[4] H. Dreiner, P. Richardson and M. H. Seymour, (1999), hep-ph/9903419.

[5] B. C. Allanach *et al.*, (1999), hep-ph/9906224.

[6] S. Abdullin *et al.*, (1999), hep-ph/0005142.

[7] H. Dreiner, P. Richardson and M. H. Seymour, hep-ph/0001224.

[8] D. Choudhury, H. Dreiner, P. Richardson, and S. Sarkar, Phys. Rev. **D61**, 095009 (2000).

[9] S. L. Glashow, Nucl. Phys. **22**, 579 (1961); S. Weinberg, Phys. Rev. Lett. **19**, 1264 (1967); A. Salam, in *Elementary Particle Theory*, ed. by N. Svaratholm, 1968.

[10] P. W. Higgs, Phys. Lett. **12**, 132 (1964); P. W. Higgs, Phys. Rev. Lett. **13**, 508 (1964); P. W. Higgs, Phys. Rev. **145**, 1156 (1966); F. Englert and R. Brout, Phys. Rev. Lett. **13**, 321 (1964); T. W. B. Kibble, Phys. Rev. **155**, 1554 (1967).

[11] M. E. Peskin and D. V. Schroeder, *An Introduction to Quantum Field Theory* (Reading, USA: Addison-Wesley, 1995).

[12] R. K. Ellis, W. J. Stirling, and B. R. Webber, *QCD and Collider Physics* (Cambridge, UK: Univ. Pr., 1996).

[13] G. 't Hooft, Phys. Rev. **D14**, 3432 (1976); G. 't Hooft, Phys. Rev. Lett. **37**, 8 (1976).

[14] J. Wess and B. Zumino, Phys. Lett. **B49**, 52 (1974).

[15] S. Coleman and J. Mandula, Phys. Rev. **159**, 1251 (1967).

[16] R. Haag, J. T. Lopuszanski, and M. Sohnius, Nucl. Phys. **B88**, 257 (1975).

[17] S. P. Martin, (1997), hep-ph/9709356.

[18] H. E. Haber and G. L. Kane, Phys. Rept. **117**, 75 (1985).

[19] D. Bailin and A. Love, *Supersymmetric Gauge Field Theory and String Theory* (Bristol, UK: IOP, 1994).

[20] J. Wess and J. Bagger, *Supersymmetry and Supergravity* (Princeton, USA: Princeton University Press, 1992).

[21] B. C. Allanach, A. Dedes, and H. K. Dreiner, Phys. Rev. **D60**, 075014 (1999).

[22] C. Caso *et al.*, Eur. Phys. J. **C3**, 1 (1998), and 1999 partial update at http://pdg.lbl.gov.

[23] G. R. Farrar and P. Fayet, Phys. Lett. **B76**, 575 (1978).

[24] J. F. Gunion and H. E. Haber, Nucl. Phys. **B272**, 1 (1986); Erratum-ibid. **B402**, 567, (1993).

[25] S. Ferrara, L. Girardello, and F. Palumbo, Phys. Rev. **D20**, 403 (1979).

[26] H. E. Haber, Nucl. Phys. Proc. Suppl. **62**, 469 (1998).

[27] H. P. Nilles, Phys. Rept. **110**, 1 (1984).

[28] M. Dine and W. Fischler, Phys. Lett. **B110**, 227 (1982); C. R. Nappi and B. A. Ovrut, Phys. Lett. **B113**, 175 (1982); L. Alvarez-Gaume, M. Claudson, and M. B. Wise, Nucl. Phys. **B207**, 96 (1982); M. Dine and A. E. Nelson, Phys. Rev. **D48**, 1277 (1993); M. Dine, A. E. Nelson, and Y. Shirman, Phys. Rev. **D51**, 1362 (1995); M. Dine, A. E. Nelson, Y. Nir, and Y. Shirman, Phys. Rev. **D53**, 2658 (1996).

[29] H. P. Nilles, Phys. Lett. **B115**, 193 (1982); S. Ferrara, L. Girardello, and H. P. Nilles, Phys. Lett. **B125**, 457 (1983).

[30] L. Ibanez and G. G. Ross, Phys. Lett. **B110**, 215 (1982).

[31] J. Ellis, J. S. Hagelin, D. V. Nanopoulos, K. Olive, and M. Srednicki, Nucl. Phys. **B238**, 453 (1984).

[32] A. K. Grant, R. D. Peccei, T. Veletto, and K. Wang, Phys. Lett. **B379**, 272 (1996).

[33] H. Dreiner, S. Lola, and P. Morawitz, Phys. Lett. **B389**, 62 (1996).

[34] M. Carena, G. F. Giudice, S. Lola, and C. E. M. Wagner, Phys. Lett. **B395**, 225 (1997).

[35] P. H. Chankowski, D. Choudhury, and S. Pokorski, Phys. Lett. **B389**, 677 (1996).

[36] D. Choudhury and D. P. Roy, Phys. Rev. **D54**, 6797 (1996).

[37] H. Dreiner and P. Morawitz, Nucl. Phys. **B503**, 55 (1997).

[38] G. Altarelli, J. Ellis, G. F. Giudice, S. Lola, and M. L. Mangano, Nucl. Phys. **B506**, 3 (1997).

[39] D. Choudhury and S. Raychaudhuri, Phys. Lett. **B401**, 54 (1997).

[40] J. Kalinowski, R. Rückl, H. Spiesberger, and P. M. Zerwas, Z. Phys. **C74**, 595 (1997).

[41] H. Dreiner, in *Perspectives on Supersymmetry*, ed. G.L. Kane, World Scientific, (1997), hep-ph/9707435; G. Bhattacharyya, Talk given at Workshop on Physics Beyond the Standard Model, Tegernsee, Germany, (1997), hep-ph/9709395.

[42] F. Abe *et al.*, Phys. Rev. Lett. **63**, 1447 (1989); E. Soderstrom *et al.*, Phys. Rev. Lett. **64**, 2980 (1990); OPAL, M. Z. Akrawy *et al.*, Phys. Lett. **B252**, 290 (1990); CDF, F. Abe *et al.*, Phys. Rev. **D46**, 1889 (1992); DELPHI, P. Abreu *et al.*, Phys. Lett. **B396**, 315 (1997); OPAL, K. Ackerstaff *et al.*, Phys. Lett. **B433**, 195 (1998).

[43] OPAL, P. D. Acton *et al.*, Phys. Lett. **B313**, 333 (1993).

[44] OPAL, G. Abbiendi *et al.*, Eur. Phys. J. **C11**, 619 (1999).

[45] OPAL, G. Abbiendi *et al.*, Eur. Phys. J. **C12**, 1 (2000).

[46] DELPHI, R. Keranen, Prepared for International Workshop on Quantum Effects in the Minimal Supersymmetric Standard Model, Barcelona, Spain, 9-13 Sep 1997; DELPHI, P. Abreu *et al.*, CERN-EP-99-049.

[47] ALEPH, D. Buskulic *et al.*, Phys. Lett. **B349**, 238 (1995).

[48] ALEPH, D. Buskulic *et al.*, Phys. Lett. **B384**, 461 (1996).

[49] ALEPH, R. Barate *et al.*, Eur. Phys. J. **C4**, 433 (1998).

[50] ALEPH, R. Barate *et al.*, Eur. Phys. J. **C7**, 383 (1999).

[51] ALEPH, R. Barate *et al.*, Eur. Phys. J. **C13**, 29 (2000).

[52] L3, M. Acciarri *et al.*, Phys. Lett. **B459**, 354 (1999).

[53] CDF, X. Wu, in *Jerusalem 1997, Proceedings of International Europhysics Conference on High-Energy Physics*, p1229-1234; CDF, M. Chertok, J. P. Done, and T. Kamon, Talk given at 29th International Conference on High-Energy Physics (ICHEP 98), Vancouver, Canada, 23-29 Jul 1998; CDF, F. Abe *et al.*, Phys. Rev. Lett. **83**, 2133 (1999).

[54] D0, B. Abbott *et al.*, Phys. Rev. Lett. **83**, 4476 (1999).

[55] A. Mirea and E. Nagy, (1999), hep-ph/9904354.

[56] B. C. Allanach, H. Dreiner, P. Morawitz, and M. D. Williams, Phys. Lett. **B420**, 307 (1998).

[57] S. Dimopoulos and L. J. Hall, Phys. Lett. **B207**, 210 (1988).

[58] V. Barger, G. F. Giudice, and T. Han, Phys. Rev. **D40**, 2987 (1989).

[59] G. F. Giudice *et al.*, (1996), hep-ph/9602207.

[60] ECFA/DESY LC Physics Working Group, E. Accomando *et al.*, Phys. Rept. **299**, 1 (1998).

[61] J. Erler, J. L. Feng, and N. Polonsky, Phys. Rev. Lett. **78**, 3063 (1997).

[62] J. Kalinowski, R. Rückl, H. Spiesberger, and P. M. Zerwas, Phys. Lett. **B406**, 314 (1997).

[63] J. Butterworth and H. Dreiner, Nucl. Phys. **B397**, 3 (1993).

[64] H. Dreiner and P. Morawitz, Nucl. Phys. **B428**, 31 (1994).

[65] S. Dimopoulos, R. Esmailzadeh, L. J. Hall, and G. D. Starkman, Phys. Rev. **D41**, 2099 (1990).

[66] J. Kalinowski, R. Rückl, H. Spiesberger, and P. M. Zerwas, Phys. Lett. **B414**, 297 (1997).

[67] J. L. Hewett and T. G. Rizzo, (1998), hep-ph/9809525.

[68] G. Moreau, M. Chemtob, F. Deliot, C. Royon, and E. Perez, Phys. Lett. **B475**, 184 (2000); G. Moreau, E. Perez, and G. Polesello, (2000), hep-ph/0002130; G. Moreau, E. Perez, and G. Polesello, (2000), hep-ph/0003012; F. Deliot, G. Moreau and C. Royon, (2000), hep-ph/0007288.

[69] A. Datta, J. M. Yang, B.-L. Young, and X. Zhang, Phys. Rev. **D56**, 3107 (1997).

[70] J.-M. Yang *et al.*, (1997), hep-ph/9802305.

[71] R. J. Oakes, K. Whisnant, J. M. Yang, B.-L. Young, and X. Zhang, Phys. Rev. **D57**, 534 (1998).

[72] E. L. Berger, B. W. Harris, and Z. Sullivan, Phys. Rev. Lett. **83**, 4472 (1999).

[73] H. Dreiner and G. G. Ross, Nucl. Phys. **B365**, 597 (1991).

[74] R. Barbier *et al.*, (1998), hep-ph/9810232.

[75] H. Baer, F. E. Paige, S. D. Protopopescu, and X. Tata, (2000), hep-ph/0001086.

[76] R. K. Ellis, D. A. Ross, and A. E. Terrano, Phys. Rev. Lett. **45**, 1226 (1980).

[77] E. W. N. Glover and D. J. Miller, Phys. Lett. **B396**, 257 (1997); J. M. Campbell, E. W. N. Glover, and D. J. Miller, Phys. Lett. **B409**, 503 (1997); J. M. Campbell, M. A. Cullen, and E. W. N. Glover, Eur. Phys. J. **C9**, 245 (1999); A. Signer and L. Dixon, Phys. Rev. Lett. **78**, 811 (1997); A. Signer, (1997), hep-ph/9705218.

[78] J. Ellis, M. K. Gaillard, and G. G. Ross, Nucl. Phys. **B111**, 253 (1976).

[79] B. R. Webber, Ann. Rev. Nucl. Part. Sci. **36**, 253 (1986).

[80] G. Marchesini and B. R. Webber, Nucl. Phys. **B238**, 1 (1984).

[81] G. Marchesini and B. R. Webber, Nucl. Phys. **B310**, 461 (1988).

[82] V. N. Gribov and L. N. Lipatov, Yad. Fiz. **15**, 1218 (1972); V. N. Gribov and L. N. Lipatov, Yad. Fiz. **15**, 781 (1972); Y. L. Dokshitzer, Sov. Phys. JETP **46**, 641 (1977); G. Altarelli and G. Parisi, Nucl. Phys. **B126**, 298 (1977).

[83] V. V. Sudakov, Sov. Phys. JETP **3**, 65 (1956).

[84] G. Marchesini and B. R. Webber, Nucl. Phys. **B330**, 261 (1990).

[85] I. G. Knowles, Nucl. Phys. **B304**, 767 (1988); I. G. Knowles, Nucl. Phys. **B310**, 571 (1988); I. G. Knowles, Comput. Phys. Commun. **58**, 271 (1990).

[86] JADE, W. Bartel *et al.*, Phys. Lett. **134B**, 275 (1984); JADE, W. Bartel *et al.*, Phys. Lett. **157B**, 340 (1985); TPC/Two Gamma, H. Aihara *et al.*, Z. Phys. **C28**, 31 (1985); OPAL, M. Z. Akrawy *et al.*, Phys. Lett. **B261**, 334 (1991); OPAL, R. Akers *et al.*, Z. Phys. **C68**, 531 (1995).

[87] D0, B. Abbott *et al.*, Phys. Lett. **B414**, 419 (1997).

[88] CDF, F. Abe *et al.*, Phys. Rev. **D50**, 5562 (1994).

[89] Y. L. Dokshitzer, V. A. Khoze and S. I. Troian, in *Perturbative Quantum Chromodynamics*, ed. A.H. Mueller (World Scientific,1989), p. 241; Y. L. Dokshitzer, V. A. Khoze, S. I. Troian and A. H. Mueller, Rev. Mod. Phys. **60**, 373 (1988); C. P. Fong and B. R. Webber, Phys. Lett. **B229**, 289 (1989); C. P. Fong and B. R. Webber, Phys. Lett. **B241**, 255 (1990); C. P. Fong and B. R. Webber, Nucl. Phys. **B355**, 54 (1991); S. Catani, B. R. Webber and G. Marchesini, Nucl. Phys. **B349**, 635 (1991).

[90] K. Odagiri, JHEP **10**, 006 (1998).

[91] R. D. Field and R. P. Feynman, Phys. Rev. **D15**, 2590 (1977).

[92] B. Andersson, G. Gustafson, and B. Soderberg, Z. Phys. **C20**, 317 (1983).

[93] A. Bassetto, M. Ciafaloni, and G. Marchesini, Phys. Lett. **83B**, 207 (1979); G. Marchesini, L. Trentadue, and G. Veneziano, Nucl. Phys. **B181**, 335 (1981).

[94] B. R. Webber, Nucl. Phys. **B238**, 492 (1984).

[95] R. D. Field and S. Wolfram, Nucl. Phys. **B213**, 65 (1983).

[96] T. Sjostrand, Comput. Phys. Commun. **82**, 74 (1994).

[97] G. Ingelman, A. Edin, and J. Rathsman, Comput. Phys. Commun. **101**, 108 (1997).

[98] L. Lonnblad, Comput. Phys. Commun. **71**, 15 (1992).

[99] S. Mrenna, Comput. Phys. Commun. **101**, 232 (1997).

[100] S. Katsanevas and P. Morawitz, Comput. Phys. Commun. **112**, 227 (1998).

[101] M. J. Gibbs, A. Ringwald, B. R. Webber, and J. T. Zadrozny, Z. Phys. **C66**, 285 (1995).

[102] S. Moretti *et al.*, Cavendish-HEP-98/06.

[103] L. Drage, *The Evaluation of Silicon Microstrip Detectors for the ATLAS Semiconductor Tracker and Supersymmetry Studies at the Large Hadron Collider*, PhD thesis, Cambridge University, (1999), RAL-TH-99-014; L. Drage and M. A. Parker, (2000), ATLAS-PHYS-2000-007.

[104] M. Hirsch, H. V. Klapdor-Kleingrothaus, and S. G. Kovalenko, Phys. Rev. Lett. **75**, 17 (1995); M. Hirsch, H. V. Klapdor-Kleingrothaus, and S. G. Kovalenko, Phys. Rev. **D53**, 1329 (1996); K. S. Babu and R. N. Mohapatra, Phys. Rev. Lett. **75**, 2276 (1995).

[105] S. Dawson, Nucl. Phys. **B261**, 297 (1985).

[106] V. Barger, W. Y. Keung, and R. J. N. Phillips, Phys. Rev. Lett. **55**, 166 (1985); C. Albajar, *et al.*, in *Aachen 1990, Proceedings of the Large Hadron Collider Workshop*, vol. 2, p621-653, ed. G. Jarlskog and ed. D. Rein, CERN-90-10; H. Baer, M. Bisset, X. Tata, and J. Woodside, Phys. Rev. **D46**, 303 (1992); H. Baer, X. Tata, and J. Woodside, Phys. Rev. **D45**, 142 (1992); R. M. Barnett, J. F. Gunion, and H. E. Haber, Phys. Lett. **B315**, 349 (1993).

[107] H. Dreiner, M. Guchait, and D. P. Roy, Phys. Rev. **D49**, 3270 (1994); M. Guchait and D. P. Roy, Phys. Rev. **D52**, 133 (1995).

[108] ATLAS, W. W. Armstrong *et al.*, CERN-LHCC-94-43; H. Baer, M. Drees, C. Kao, M. Nojiri, and X. Tata, Phys. Rev. **D50**, 2148 (1994).

[109] H. Baer, C. hao Chen, F. Paige, and X. Tata, Phys. Rev. **D53**, 6241 (1996); S. Abdullin and F. Charles, Nucl. Phys. **B547**, 60 (1999).

[110] K. T. Matchev and D. M. Pierce, Phys. Rev. **D60**, 075004 (1999).

[111] K. T. Matchev and D. M. Pierce, Phys. Lett. **B467**, 225 (1999).

[112] CDF, J. Nachtman, D. Saltzberg, and M. Worcester, (1999), hep-ex/9902010.

[113] H. Baer, M. Drees, F. Paige, P. Quintana, and X. Tata, Phys. Rev. **D61**, 095007 (2000).

[114] N. K. Mondal and D. P. Roy, Phys. Rev. **D49**, 183 (1994); R. M. Godbole, S. Pakvasa, and D. P. Roy, Phys. Rev. Lett. **50**, 1539 (1983); V. Barger, A. D. Martin, and R. J. N. Phillips, Phys. Rev. **D28**, 145 (1983); D. P. Roy, Phys. Lett. **196B**, 395 (1987).

[115] J. M. Campbell and R. K. Ellis, Phys. Rev. **D60**, 113006 (1999).

[116] R. Bonciani, S. Catani, M. L. Mangano, and P. Nason, Nucl. Phys. **B529**, 424 (1998).

[117] S. Frixione and G. Ridolfi, Nucl. Phys. **B507**, 315 (1997).

[118] M. L. Mangano, P. Nason, and G. Ridolfi, Nucl. Phys. **B373**, 295 (1992).

[119] A. D. Martin, R. G. Roberts, W. J. Stirling, and R. S. Thorne, Eur. Phys. J. **C14**, 133 (2000); A. D. Martin, R. G. Roberts, W. J. Stirling, and R. S. Thorne, Eur. Phys. J. **C4**, 463 (1998).

[120] KARMEN, B. Zeitnitz, Prog. Part. Nucl. Phys. **32**, 351 (1994); KARMEN, B. E. Bodmann *et al.*, Phys. Lett. **B332**, 251 (1994).

[121] KARMEN, B. Armbruster *et al.*, Phys. Lett. **B348**, 19 (1995).

[122] KARMEN, K. Eitel, (1997), hep-ex/9706023.

[123] KARMEN, B. Zeitnitz, Talk given at NEUTRINO'98, Takayama, 1998.

[124] KARMEN, R. Maschuw, Talk given at WIN'99, Cape Town, 1999.

[125] V. Barger, R. J. N. Phillips, and S. Sarkar, Phys. Lett. **B352**, 365 (1995).

[126] S. N. Gninenko and N. V. Krasnikov, Phys. Lett. **B434**, 163 (1998).

[127] D. Choudhury and S. Sarkar, Phys. Lett. **B374**, 87 (1996).

[128] A. Lukas and A. Romanino, (2000), hep-ph/0004130.

[129] ALEPH, D. Buskulic *et al.*, Phys. Lett. **B349**, 585 (1995).

[130] M. Daum *et al.*, Phys. Lett. **B361**, 179 (1995).

[131] J. A. Formaggio *et al.*, Phys. Rev. Lett. **84**, 4043 (2000).

[132] J. Koglin, *The KARMEN Time Anomaly: Search for a Neutral Particle of Mass 33.9 MeV in Pion Decay*, PhD thesis, University of Virginia, (2000).

[133] J. Govaerts, J. Deutsch, and P. M. V. Hove, Phys. Lett. **B389**, 700 (1996).

[134] KARMEN, C. Oehler, Talk given at Topics in Neutrino and Astro-Particle Physics, San Miniato, 1999.

[135] R. Bilger *et al.*, Phys. Lett. **B446**, 363 (1999).

[136] M. Nowakowski and A. Pilaftsis, Nucl. Phys. **B461**, 19 (1996).

[137] S. Sarkar, Rept. Prog. Phys. **59**, 1493 (1996).

[138] G. G. Raffelt, *Stars as Laboratories for Fundamental Physics: The Astrophysics of Neutrinos, Axions, and other Weakly Interacting Particles* (Chicago, USA: Univ. Pr., 1996).

[139] ALEPH, R. Barate *et al.*, (1999), hep-ex/9902031.

[140] CLEO, A. Anastassov *et al.*, (1999), hep-ex/9908025.

[141] B. A. Campbell, S. Davidson, J. Ellis, and K. A. Olive, Phys. Lett. **B256**, 457 (1991).

[142] W. Fischler, G. F. Giudice, R. G. Leigh, and S. Paban, Phys. Lett. **B258**, 45 (1991).

[143] H. Dreiner and G. G. Ross, Nucl. Phys. **B410**, 188 (1993).

[144] B. A. Campbell, S. Davidson, J. Ellis, and K. A. Olive, Astropart. Phys. **1**, 77 (1992).

[145] E. Ma and J. Okada, Phys. Rev. Lett. **41**, 287 (1978).

[146] K. J. F. Gaemers, R. Gastmans, and F. M. Renard, Phys. Rev. **D19**, 1605 (1979).

[147] K. Grassie and P. N. Pandita, Phys. Rev. **D30**, 22 (1984).

[148] S. Ambrosanio, private communication (with the use of CompHEP A. Pukhov *et al.*, (1999), hep-ph/9908288); S. Ambrosanio, B. Mele, G. Montagna, O. Nicrosini, and F. Piccinini, Nucl. Phys. **B478**, 46 (1996).

[149] D. Abbaneo *et al.*, (2000), CERN-EP-2000-016.

[150] A. Romanino, private communication.

[151] M. E. Peskin and T. Takeuchi, Phys. Rev. **D46**, 381 (1992).

[152] M. E. Peskin and T. Takeuchi, Phys. Rev. Lett. **65**, 964 (1990).

[153] W. J. Marciano and J. L. Rosner, Phys. Rev. Lett. **65**, 2963 (1990).

[154] G. Altarelli and R. Barbieri, Phys. Lett. **B253**, 161 (1991); G. Altarelli, R. Barbieri, and S. Jadach, Nucl. Phys. **B369**, 3 (1992).

[155] R. Barbieri, M. Frigeni, and F. Caravaglios, Phys. Lett. **B279**, 169 (1992).

[156] K. Eitel, Talk given at Neutrino 2000, Sudbury, 2000.

[157] H. Baer, V. Barger, D. Karatas, and X. Tata, Phys. Rev. **D36**, 96 (1987).

[158] J. F. Gunion, H. E. Haber, G. L. Kane, and S. Dawson, *The Higgs Hunter's Guide* (Reading USA:Addison-Wesley, 1990); Erratum (1993), hep-ph/9302272.

[159] H. Baer, J. Sender, and X. Tata, Phys. Rev. **D50**, 4517 (1994).

[160] X. Tata, (1997), hep-ph/9706307.

[161] A. Bartl, W. Majerotto, and W. Porod, Z. Phys. **C64**, 499 (1994).

[162] E. A. Baltz and P. Gondolo, Phys. Rev. **D57**, 2969 (1998).